Raman interferometry with free-falling and trapped atoms

Von der Fakultät für Mathematik und Physik
der Gottfried Wilhelm Leibniz Universität Hannover

zur Erlangung des Grades

**Doktor der Naturwissenschaften
Dr. rer. nat.**

und der Université Pierre et Marie Curie, Paris VI
sowie der École Doctorale 389 - La Physique de la Particule à la Matière Condensée

zur Erlangung des Grades

Docteur de l'Université Paris 6

genehmigte Dissertation von

Dipl. Phys. Gunnar Tackmann,
geboren am 12.05.1982, in Warburg

2013

Raman interferometry with free-falling and trapped atoms

Abstract

Since about twenty years atom interferometers have been studied for measuring inertial forces to high precision with atoms in free fall. The use of cold atoms was key for a reduction of the size of these devices. New methods of cooling and trapping permit to perform interferometry with guided atoms which opens new perspectives for measuring forces with high spatial resolution. This thesis explored both directions by employing atoms in free fall for rotation sensing and guided atoms for testing gravity at close distances.

The CASI gyroscope is based on a double Raman interferometer with counter-propagating atomic trajectories. This work presents studies on the long term stability of the sensor and an improvement in sensitivity to rotations of one order of magnitude compared to the previous status. A sensitivity of $2 \cdot 10^{-8}$ rad/s after an integration time of 4000 s was achieved using a post-correction technique based on a correlation of the rotation signal to the atomic sample arrival time.

The FORCA-G experiment targets to measure short range forces with high spatial resolution based on Raman interferometers using laser induced tunneling in an optical lattice. Measurements are presented showing a sensitivity to the gravitational acceleration of $2 \cdot 10^{-5}$ $g/\sqrt{\text{Hz}}$. The resulting sensitivity after 150 s of integration will allow for a measurement of Casimir-Polder forces in 5 μm atom-surface separation with 1 % statistical uncertainty. Finally, the implementation of a coherent atomic transport based on an accelerated lattice for future short range force measurements is reported.

Keywords: atom interferometry, Raman transition, Sagnac effect, gyroscope, short range forces, optical lattices

Interférométrie Raman avec des atomes en chute libre et piégés

Résumé

L'application de l'interférométrie atomique pour la mesure précise des forces d'inertie à l'aide d'atomes en chute libre a été étudiée depuis une vingtaine d'années. L'utilisation des atomes froids a conduit à une réduction en taille de ces dispositifs. Des nouvelles méthodes de refroidissement et de piégeage permettent d'augmenter la résolution spatiale en utilisant des atomes guidés. Cette thèse a exploré les deux directions en utilisant des atomes en chute libre pour la mesure des rotations et des atomes guidés pour un test de la gravitation à courte distance.

Le gyromètre CASI est basé sur un double interféromètre Raman aux trajectoires atomiques contrapropageantes. Cet ouvrage présente des études sur la stabilité du capteur et une amélioration de la sensibilité aux rotations d'un ordre de grandeur par rapport à l'état précédent. Une sensibilité de $2 \cdot 10^{-8}$ rad/s après 4000 s de moyennage a été démontrée en exploitant, pour le corriger, la corrélation du signal de rotation avec le temps d'arrivée des échantillons atomiques.

L'expérience FORCA-G vise à réaliser des mesures de forces à faible distance à l'aide d'interféromètres Raman basés sur un effet tunnel induit par laser dans un réseau optique. Des mesures avec une sensibilité aux accélérations de $2 \cdot 10^{-5}\ g/\sqrt{\text{Hz}}$ sont présentées. La sensibilité obtenue après une intégration de 150 s permettra de réaliser des mesures de la force de Casimir-Polder avec une incertitude statistique de 1 % à une distance atome-surface de l'ordre de 5 μm. Par ailleurs, l'implémentation d'un transport cohérent des atomes dans des réseaux optiques accélérés a été effectuée, qui sera utile pour les mesures futures.

Mots clés: interférométrie atomique, transition Raman, effet Sagnac, gyromètre, forces à faible distance, réseaux optiques

Raman-Interferometrie mit freifallenden und gefangenen Atomen

Zusammenfassung

In den vergangenen zwanzig Jahren wurde der Einsatz von Atominterferometern für die Präzisionsmessung inertialer Kräfte mit Hilfe freifallender Atome untersucht. Die Verwendung kalter Atome führte zu einer Kompaktifizierung dieser Apparaturen. Neue Methoden des Kühlens und Fangens erlauben räumlich hochauflösende interferometrische Messungen von Kräften mit geführten Atomen. Die vorliegende Arbeit befasst sich mit beiden Ansätzen, genauer mit der Messung von Rotationen mit Hilfe freifallender Atome sowie mit dem Einsatz von geführten Atomen für Tests der Gravitation auf kürzesten Entfernungen.

Das CASI-Gyroskop basiert auf einem doppelten Raman-Interferometer mit gegenläufigen atomaren Trajektorien. Diese Arbeit stellt Studien der Langzeitstabilität des Sensors und die Erhöhung der Sensitivität für Rotationen um eine Größenordnung im Vergleich zum vorangegangenen Status dar. Es konnte eine Sensitivität von $2 \cdot 10^{-8}$ rad/s nach einer Mittelungszeit von 4000 s unter Verwendung einer nachgelagerten Signalkorrektur basierend auf einer Korrelation des Rotationssignals mit der atomaren Ankunftszeit erreicht werden.

Das FORCA-G-Experiment strebt die räumlich hochauflösende Messung von Kräften auf kurzen Distanzen mit Raman-Interferometern an, die auf laserinduziertem Tunneln in einem optischen Gitter basieren. In dieser Arbeit werden Messungen mit einer Beschleunigungssensitivität von $2 \cdot 10^{-5}$ $g/\sqrt{\mathrm{Hz}}$ dargestellt. Die resultierende Sensitivität nach 150 s Mittelung wird eine Messung von Casimir-Polder-Kräften in einem Abstand von einem Atom zur Oberfläche von 5 μm mit einer statistischen Unsicherheit von 1 % ermöglichen. Abschließend wird die Implementierung eines kohärenten, lichtgitterbasierten Transports kalter Atome für die Anwendung in den anvisierten Messungen auf kurzen Distanzen vorgestellt.

Schlagwörter: Atominterferometrie, Raman-Übergang, Sagnac-Effekt, Gyroskop, Kräfte auf kurzen Distanzen, optische Gitter

Résumé substantiel

Introduction

L'interférométrie a aujourd'hui des nombreuses applications en recherche fondamentale et appliquée, aussi bien dans la haute technologie que dans la vie de tous les jours. Deux exemples des applications en recherche fondamentale et appliquée sont les détecteurs d'ondes gravitationelles ainsi que les cavités laser en anneau pour la mesure à haute résolution de la rotation terrestre, tous les deux basés sur l'interférométrie à optique. Le premier est basé sur une géométrie d'interféromètre inventée par Michelson. Une onde lumineuse est séparée en deux à l'aide d'une séparatrice, les deux ondes sont rétroréfléchies sur des miroirs et superposées sur la même séparatrice. Une variation de la longueur d'un des deux chemins optiques qui constituent les deux bras de l'interféromètre induit, par effet d'interférences des deux ondes partielles, une variation en intensité en sortie de l'interféromètre et peut alors être détectée (voir figure 1).

Une géométrie légèrement différente est celle proposée par Mach et Zehnder, appelée communément géométrie Mach-Zehnder. Elle est composée par une séparation de l'onde incidente, un changement de direction sur chacun des deux chemins et la superposition des deux ondes partielles sur une deuxième séparatrice (voir figure 1). L'intensité en sortie de l'interféromètre, de nouveau, dépend de la phase relative des deux bras de l'interféromètre. Dans cette géométrie, la surface entourée par les deux bras est la clé pour une mesure de rotation. Celle-ci est basée sur l'effet Sagnac, formulé par Georges Sagnac en 1913, qui prédit une dépendance de la phase de cet interféromètre à la rotation de la surface encerclée. C'est sur ce même principe que fonctionnent les gyrolasers en anneau, qui permettent la mesure locale des variations de la rotation terrestre, la plus sensible de nos jours.

Tandis que le modèle ondulatoire de la lumière est utilisé pour décrire les phénomènes d'interférences pour des intensités suffisamment élevées étant considérés jusqu'ici, ceci n'est plus possible, par exemple, dans la limite des intensités fortement réduites. Dans ce cas, la lumière révèle sa nature corpusculaire ce qui nécessite l'application de la mécanique quantique, qui définit la lumière comme flux d'un nombre de particules nommées photons. Dans ce contexte de dualité onde-corpuscule, la nature ondulatoire des particules massives est proposée par
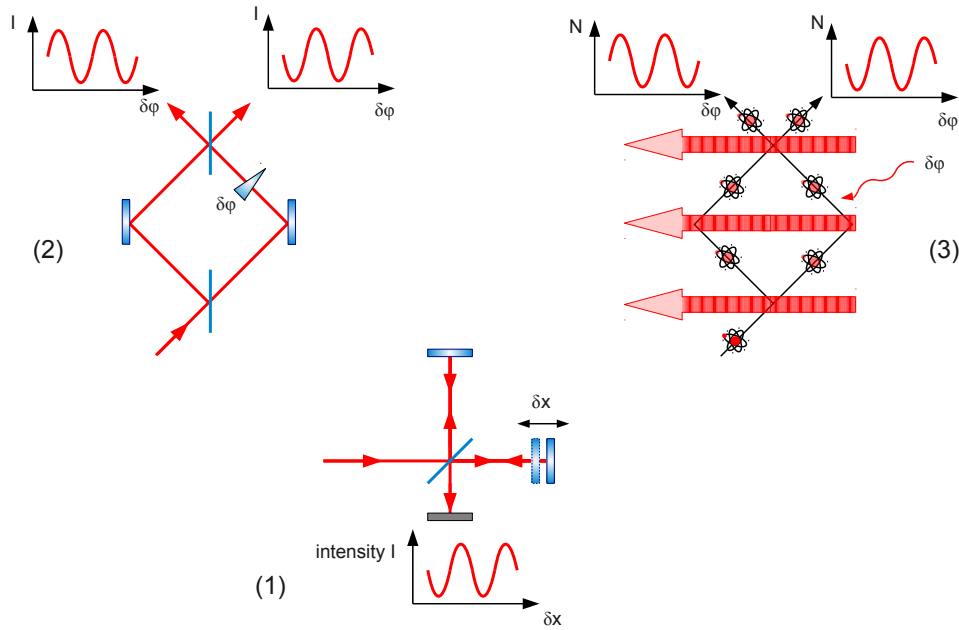
Figure 1: Schémas d'interférométrie. (1) Géométrie Michelson. (2) Géométrie Mach-Zehnder basé sur l'interférence de faisceaux laser. (3) Géométrie Mach-Zehnder basé sur l'interférence d'atomes.

de Broglie en 1923 et 1924. Par conséquent, des effets d'interférences sont aussi attendues aussi pour la matière. Ceci a pu être démontré pour des électrons, des neutrons, des atomes, et même pour des molécules d'une masse qui dépasse 10^3 unités de masse atomique.

L'interférence peut être induite par diffraction des ondes de matière sur des cristaux solides ainsi qu'à l'aide de réseaux solides ou bien de réseaux lumineux qui ionisent des atomes et et impriment une modulation spatiale de la densité, agissant comme des réseaux d'amplitude. Dans le cas des atomes neutres, la diffraction sur des réseaux lumineux de phase s'est révélée être un outil flexible et puissant qui permet de réaliser des interféromètres atomiques par analogie avec, par exemple, l'interféromètre Mach-Zehnder (voir figure 1). Les réseaux lumineux utilisés dans ce type d'interféromètres sont basés sur deux faisceaux laser contrapropageants. Ce processus de diffraction peut être décrit comme absorption d'un photon de l'un des faisceaux et une émission immédiate d'un photon dans l'autre faisceau. La conservation d'impulsion oblige l'atome à gagner une impulsion qui est égale à la somme des reculs des deux photons. Dans ce processus, la différence d'énergie des deux photons correspond à la différence d'énergie cinétique de l'atome. Par ailleurs, il est possible, en choisissant la différence d'énergie des photons égale à la différence d'énergie de deux états atomiques internes, d'induire une transition de type Raman stimulée. Si la différence d'énergie est alors la somme des différences

d'énergie interne et externe, on réalise une séparatrice atomique qui couple les états atomiques internes et externes simultanément.

Dans le cas d'atomes en chute libre, une séparatrice atomique Raman permet de coupler deux états d'impulsion et ainsi de réaliser un interféromètre atomique du type Mach-Zehnder. Cette technique a permis, entre autres, de réaliser des gravimètres absolus qui montrent des performances compétitives avec celles des gravimètres absolus basés sur la mesure de la chute libre d'un réflecteur en dièdre, ce qui représente l'état de l'art de la gravimétrie absolue classique. Aussi basés sur des interféromètres Mach-Zehnder atomiques, des gyromètres atomiques ont été réalisés en lançant les atomes sur des trajectoires balistiques avec une composante de vitesse importante perpendiculaire à la direction du recul de la séparatrice atomique. Dans ce cas, les bras de l'interféromètre Mach-Zehnder entourent une surface ce qui permet de mesurer des rotations grâce à l'effet Sagnac. L'expérience de gyromètre CASI («Cold Atom Sagnac Interferometer»), le premier objet de recherche de cette thèse, est basée sur deux interféromètres Raman aux trajectoires atomiques contrapropageantes. La corrélation des signaux des deux interféromètres permet de déduire le taux de rotation du dispositif expérimental, et ainsi la valeur de la rotation terrestre locale. Ce travail présente les résultats des études de stabilité long terme du signal de rotation du gyromètre. Nous discutons les sources de fluctuations lente du signal et identifions l'effet croisé du recouvrement des deux trajectoires atomiques et les imperfections des fronts d'onde des séparatrices atomiques comme limitation dominante. La mesure du temps d'arrivée des échantillons atomiques dans la zone de détection en sortie de l'interféromètre et une correction du signal de rotation à l'aide de cette information nous permet d'améliorer la sensibilité du gyromètre aux rotations d'un ordre de grandeur par rapport à l'état précédent.

La sensibilité d'un interféromètre atomique croît avec le temps d'interrogation. Tandis que ce temps est limité dans des dispositifs expérimentaux dans des salles de manips standard, de nouveaux projets cherchent à prolonger le temps de propagation libre dans une tour de chute libre, des fontaines géantes ou bien des vols paraboliques. Une approche complémentaire à l'interférométrie des atomes en chute libre est donné par l'interférométrie basée sur des atomes piégés ou guidés. Elle consiste à créer des superpositions d'états spatiaux et à réaliser des interféromètres atomiques basée sur ces états. Ceci permet non seulement de prolonger le temps d'interrogation dans l'interféromètre, mais surtout de miniaturiser les dispositifs expérimentaux et d'augmenter la résolution spatiale de l'interférométrie atomique. Dans l'expérience FORCA-G («FORce de CAsimir et test de Gravité à courte distance »), nous mettons en œuvre des tels interféromètres dans un réseau lumineux vertical. Le couplage des états spatiaux (quasi-)stationnaires, qui décrivent des atomes piégés dans les puits de ce potentiel périodique, est réalisé par des faisceaux laser Raman qui induisent un effet tunnel cohérent entre les puits. Ce couplage permet de réaliser un interféromètre atomique en créant une superpo-

sition d'états spatiaux, de la laisser évoluer pour un temps donné et de coupler les états une deuxième fois. La phase de cet interféromètre dépendra directement de la différence des potentiels dans les deux puits correspondants aux états spatiaux. Ceci permet de mesurer cette différence avec haute précision et une résolution spatiale qui est, en principe, donnée par la séparation de deux puits adjacents définie par la périodicité du réseau. Le projet vise à réaliser des mesures de forces à faible distance à l'aide de cette technique en réalisant des interféromètres atomiques à la proximité d'une surface macroscopique. Dans cette thèse, des études de stabilité de la mesure d'accélération loin d'une surface macroscopique sont présentées. Nous étudions le couplage des états spatiaux par effet tunnel et montrons une résolution spectrale de ce processus en dessous du Hz. Ce couplage nous permet de réaliser un interféromètre piégé et ainsi une mesure de l'accélération locale. Nous analysons la stabilité de cette mesure et identifions les sources dominantes de bruit et de dérive. De plus, l'implémentation d'un transport cohérent pour les futures mesures de forces à faible distance est présentée. Ce processus est basé sur l'accélération et la décélération des atomes dans des réseaux optiques accélérés.

Le chapitre 2 de cette thèse est une présensation des outils théoriques utilisés dans les analyses de stabilité des deux capteurs atomiques. Nous introduisons les états (quasi-)propres des systèmes utilisés dans un interféromètre Raman en chute libre et un interféromètre Raman piégé. Ceci nous conduit au calcul des déphasages d'interféromètres dans les différents types d'interféromètres considérés. Nous nous plaçons ensuite dans le cas particulier de l'atome de ^{87}Rb, qui est l'atome utilisé dans les expériences décrites ici. Nous décrivons les états internes et les déphasages parasites dûs aux déplacements différentiels de ces états. Dans la suite de ce résumé substantiel, le contenu des chapitres 3 et 4 est présenté de façon synthétique, décrivant les principes de mesure, des réalisations expérimentales, les sensibilités obtenues ainsi que les sources dominantes des fluctuations résiduelles pour chacun des deux capteurs.

Gyromètre atomique

Principe de mesure

La mesure de la rotation dans notre gyromètre atomique est basée sur deux interféromètres Raman de type Mach-Zehnder. La séparation, la réflexion et la superposition des ondes de matière sont réalisées à l'aide de trois faisceaux laser Raman horizontaux. Ces derniers sont mis en œuvre dans une configuration rétroréfléchie. Pour la réalisation des interféromètres atomiques, les échantillons atomiques des deux interféromètres atomiques sont lancés simultanément sur des trajectoires contrapropageantes (voir figure 2). Cette configuration permet de déduire le signal de rotation du gyromètre de la somme des signaux des deux interféromètres. Le signal de chaque interféromètre est dominé par trois termes de

phase. La rotation, l'accélération et la différence de séparation des trois miroirs de rétroréflexion. Tous ces termes dépendent de la direction du recul de la séparatrice atomique Raman. Seule la phase de rotation dépend en plus de la vitesse des échantillons atomiques. Les phases d'accélération et de séparation des miroirs ont alors des signes opposés dans les deux interféromètres, tandis que les signes sont les mêmes pour la phase de rotation. En conséquence, la phase de rotation est donnée, en négligeant les termes de phases dûs aux effets des déplacements d'énergie d'états internes, par la somme des deux phases d'interféromètres atomiques.
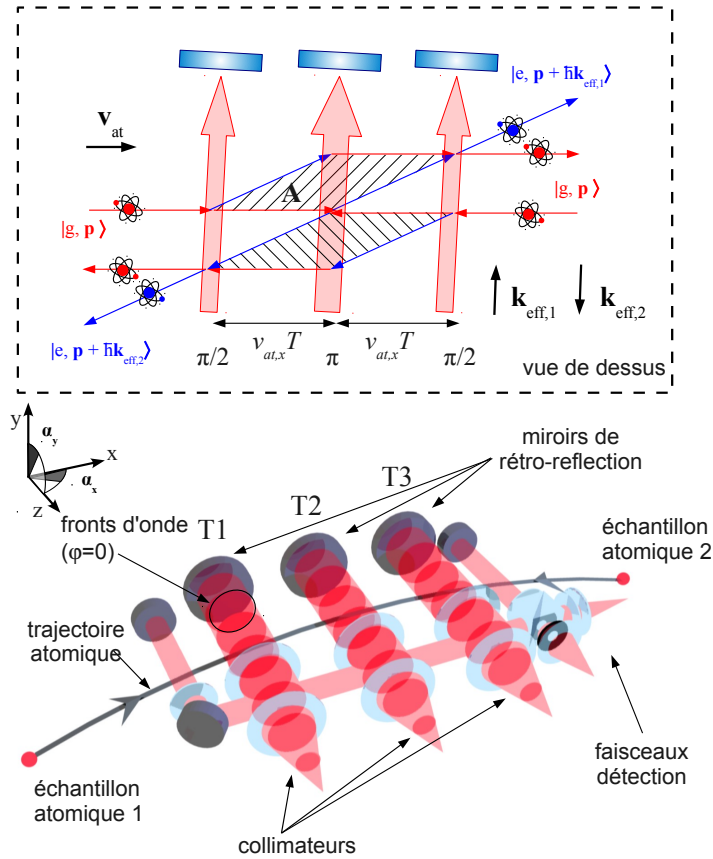

Figure 2: Schéma du gyromètre atomique CASI. Le gyromètre est basé sur deux interféromètres Raman aux trajectoires contrapropageantes. Les ensembles atomiques sont lancés sur des trajectoires paraboliques. Pendant leur chute libre sur ces trajectoires, les atomes sont préparés dans l'état fondamental d'interféromètre avant d'appliquer les impulsions $\pi/2$, π et $\pi/2$ pour séparer, réfléchir et superposer les ondes de matière. La probabilité de transition de l'état fondamental à l'état excité permet ensuite de déduire la phase des interféromètres atomiques et, en corrélant les deux signaux, le signal de rotation du dispositif. La vue par dessus *(cadre pointillé)* montre la surface entourée par les bras des interféromètres qui entraîne la sensibilité aux rotations par effet Sagnac.

L'interaction des atomes avec les faisceaux Raman en configuration contra-propageantes, dans laquelle les deux faisceaux Raman proviennent des directions opposées grâce à la rétroréflexion des faisceaux, permet de transmettre un recul important aux atomes et ainsi d'être très sensible à la rotation et à l'accélération. En même temps, elle implique la transmission d'une phase dite spatiale des faisceaux Raman à la phase atomique et ainsi aux phases des interféromètres. Cette phase est définie pour chaque atome à partir des fronts d'onde Raman et des positions de l'atome pendant l'application des impulsions des séparations atomiques. Trois conséquences peuvent découler de cet effet croisé : (i) un biais sur le signal de rotation, (ii) un bruit de la phase interférométrique, donc du signal de rotation et (iii) une perte de contraste des signaux des interféromètres. Le biais de phase dans la mesure de la rotation est nul pour une superposition parfaite des trajectoires atomiques. En revanche, si la superposition est imparfaite et que les fronts d'ondes des faisceaux Raman montrent une dépendance spatiale, un biais apparaît sur le signal de rotation. De plus, une fluctuation lente ou rapide de la superposition des trajectoires ou de l'alignement des faisceaux Raman peut induire une fluctuation du signal de rotation, donc une dérive lente ou un bruit d'un cycle de mesure à l'autre. Ces deux premiers effets sont liés aux barycentres des échantillons atomiques. Si, en plus, une dispersion de phase à travers des nuages atomiques apparaît, ceci peut réduire les contrastes des signaux des interféromètres atomiques.

Dans le cas de notre gyromètre, les trois faisceaux Raman sont appliqués dans trois zones disjointes. Les fronts d'onde effectifs des séparatrices Raman sont définis par les éléments optiques situés entre la position de l'interaction lumineuse-atomique et la rétroréflexion, soit par les hublots de l'enceinte à vide ainsi que par les miroirs de rétroréflexion. Les aberrations optiques sont fortement réduites grâce à l'utilisation d'éléments optiques de haute qualité. La planéité des surfaces de ces éléments est spécifiée à moins d'un dixième de la longueur d'onde. Cependant, les perturbations liées au défaut de planéité résiduel sont attendus de constituer une limitation de la stabilité à court terme du gyromètre.

Un impact plus important est dû à l'alignement relatif des trois faisceaux Raman qui est défini par l'orientation relative des trois miroirs de rétroréflexion et à l'influence des hublots de l'enceinte. Cet alignement nous permet de compenser la réfraction des faisceaux Raman par les hublots de l'enceinte et ainsi d'optimiser le contraste des interféromètres. Nous réalisons l'alignement en utilisant les signaux des deux interféromètres en différentes configurations d'impulsion de séparatrices atomiques. Néanmoins, l'imperfection résiduelle de cet alignement induit, dans l'effet croisé avec les fluctuations lentes de la superposition des trajectoires atomiques, une dérive sur le signal de rotation.

Dans la suite, le dispositif expérimental du gyromètre atomique est présenté. Ensuite, les sources de fluctuations lentes du signal de rotation sont discutées et l'effet croisé des fluctuations de la position des sources atomiques et l'alignement imparfait des fronts d'onde est identifié comme source dominante.

Réalisation expérimentale

Les interféromètres atomiques du gyromètre sont réalisés dans une enceinte à vide disposant d'une zone d'interférométrie ainsi que de deux zones de sources atomiques et d'une branche de pompage. Une paire de bobines sur deux cartes imprimées sert à réaliser un champ magnétique de quantification selon la direction du recul des séparatrices Raman. L'ensemble de ce montage est entouré par un blindage magnétique qui sert à réduire les influences des champs magnétiques externes. Ce blindage comportant l'appareil de gyromètre est posé sur une plateforme d'isolation pour diminuer l'influence des vibrations de l'environnement.

Toutes les étapes expérimentales nécessitent des sources lasers monofréquences à longueur d'onde de 780 nm et d'une largeur de raie en dessous du MHz et une puissance optique de l'ordre du Watt. Ces besoins sont couverts par des sources laser à cavité externe étendue (LCE, angl. «external cavity diode laser, ECDL») en configuration MOPA (angl. «master oscillator power amplifier»).

Les sources atomiques sont basées sur des pièges magnéto-optiques (PMO, angl. «magneto-optical trap, MOT») bi-dimensionels qui chargent des PMO à trois dimensions. Le piégeage est réalisé dans le minimum d'un champ magnétique quadrupolaire à l'aide de faisceaux lasers désaccordés dans le rouge de la raie D2 du ^{87}Rb. Le PMO 3D est chargé pendant une durée de 0,2 s avec un taux de chargement d'environ 10^9 atomes par seconde. Ensuite, les ensembles atomiques sont lancés, en choisissant les désaccords appropriés des six faisceaux de refroidissement, sur des trajectoires paraboliques bien définies. Sur la première étape de ce vol, les nuages sont refroidis par refroidissement à gradient de polarisation, dans ce qu'on appelle une mélasse mouvante. Nous obtenons alors deux échantillons atomiques d'environ 10^8 atomes et une température d'environ 8 μK à 10 μK.

Les ensembles atomiques sont ensuite, sur leurs vols paraboliques, séléctionnés dans leur état externe et interne par une première impulsion Raman dans la première zone d'interaction. En poussant les atomes, qui n'ont pas été transférés par cette impulsion, en dehors de la zone d'interférométrie avec un faisceaux résonant, nous obtenons des ensembles d'un équivalent de température d'environ 1 μK dans la direction du recul de la séparatrice Raman dans l'état fondamental interne. Après cette étape, les ondes de matière sont séparées, réfléchies et superposées dans les trois zones d'interaction en appliquant des impulsions Raman $\pi/2$, π et $\pi/2$. Les états de sortie des deux interféromètres sont déterminés dans une détection de fluorescence sélective en état interne. Ce cycle de l'interféromètre est répété deux fois par seconde.

La détection de chaque signal de l'interféromètre consiste en trois impulsions laser résonantes qui sont appliquées consécutivement. Une partie de l'intensité diffusée par les atomes lors chacune de ces impulsions est collectée par un doublet de deux lentilles et détectée par une photodiode. Cet enchaînement nous permet de déterminer la probabilité de transition de l'état interne atomique, qui, en sortie de l'interféromètre, dépend de la phase interférométrique d'une manière sinusoïdale.

Nous pouvons alors déterminer la phase de chaque interféromètre à partir de ce signal. En même temps, nous pouvons, en utilisant la troisième impulsion de la détection, mesurer le temps d'arrivée des échantillons atomiques dans la zone de détection.

La détermination de la phase de rotation est réalisée à partir d'une technique de modulation du signal d'accélération. Nous modulons l'orientation verticale commune des miroirs de rétroréflexion et ainsi la phase d'accélération vue par les interféromètres. Les signaux d'interféromètres résultants de cette modulation sont fortement corrélés. La représentation paramétrique des signaux de probabilité de transition des deux interféromètres est donnée par une ellipse dont l'orientation est définie par la phase de rotation. Nous l'extrayons de cette représentation par un ajustement d'ellipse (angl. «ellipse fitting»). Cette technique est généralement utilisée dans le cas où deux signaux d'interféromètres montrent un bruit important et corrélé d'un coup à l'autre. Dans notre cas, la méthode d'ajustement d'ellipse nous permet de déterminer la phase de rotation en supprimant les fluctuations lentes de l'accélération ainsi que les dérives d'offset des signaux de probabilité de transition. Par rapport à la détermination directe de la phase de l'interféromètre à partir de la frange caractéristique du signal, nous perdons un facteur 1,4 en sensibilité. En revanche, cette méthode est extrêmement robuste, fiable et simple à appliquer.

La phase de rotation extraite par la méthode d'ajustement d'ellipse dépend non seulement de la rotation du dispositif expérimental, mais aussi des déplacements différentiels de l'état interne de l'interféromètre. Ces déplacements sont induits par l'effet Zeeman quadratique ainsi que par le déplacement lumineux différentiel par effet Stark dynamique. Pour annuler les biais sur le signal de rotation ainsi que les fluctuations lentes et les dérives induites par ces effets, nous alternons les mesures avec des orientations de surfaces opposées (angl. «k-reversal technique»). Par ce moyen, la phase de rotation est inversée d'un coup à l'autre tandis que les phases parasites dues aux effets non-inertiels gardent le même signe ce qui permet de discriminer les effets parasites en corrélant deux coups consécutifs.

Stabilité à long terme de la mesure de rotation

Nous étudions ensuite la stabilité à long terme de la mesure de rotation dans notre gyromètre. La lecture de la phase de rotation à l'aide de l'ajustement d'ellipse et l'alternance de l'orientation de la surface supprime le plupart des biais ainsi que l'influence des fluctuations lentes de ces contributions. Cette suppression n'est pas valable pour des contributions de phase qui dépendent du signe du recul de la séparatrice Raman. Les effets que nous devont alors considérer sont le déplacement lumineux à deux photons, une phase induite par un gradient de champ magnétique ainsi que les fronts d'onde des faisceaux Raman.

Le déplacement à deux photons (angl. «two-photon light shift, TPLS») est dû à

la configuration rétroréfléchie des faisceaux Raman. D'une part, cette configuration nous permet de choisir la direction du recul de la séparatrice et ainsi l'orientation de la surface entourée. D'autre part, nous obtenons un couplage non-résonant à deux photons donné, dans notre cas, par la transition entraînée par les paires de faisceaux copropageants et par la paire de faisceaux contrapropageants non-résonant. Bien que cet effet ne peut pas être supprimé en alternant l'orientation de la surface de l'interféromètre, il est en principe le même pour les deux interféromètres avec un signe opposé. Par conséquent, l'influence de ce déplacement lumineux est fortement diminuée dans le signal de rotation. Seules les imperfections de la superposition des deux trajectoires atomiques induisent un déséquilibre des contributions dans les deux interféromètres. Ceci nous permet de réaliser une estimation du biais du signal de rotation. Dans une estimation prudente nous trouvons une fluctuation lente attendue au niveau de $2 \cdot 10^{-8}$ rad/s.

Un gradient du champ magnétique selon la trajectoire atomique a un impact direct sur le signal de rotation par l'effet Zeeman quadratique. Cet effet est néanmoins largement supprimé par l'alternance de l'orientation de la surface des interféromètres. Cependant, les gradients du champ magnétique dans les autres directions peuvent induire des biais du signal de rotation. Pour s'assurer que des fluctuations du champ magnétique ne sont pas la source dominante de fluctuations lentes, nous avons réalisé une mesure longue de rotation en alternant deux valeurs du champ magnétique biais d'interférométrie. Comme l'influence des gradients au signal de rotation dépend de l'intensité du champ, une fluctuation lente de cette influence est différente pour différentes valeurs du champ magnétique et la différence des signaux de rotation pour différentes valeurs du champ magnétique fluctue. Une telle fluctuation n'est pas observée dans notre mesure à long terme. Ceci exclut les fluctuations dues aux gradients du champ magnétique comme source de fluctuations dominante.

Les fluctuations du signal de rotation dues aux effets des fronts d'onde des faisceaux Raman sont présentes seulement si les positions d'application des impulsions Raman dans les trois zones d'interaction ne sont pas identiques pour les deux interféromètres. Ceci peut être le cas si la superposition des trajectoires atomiques est imparfaite ou les instants ou les transitions Raman sont appliquées ne sont pas adpatés à la géométrie des trajectoires. Ce dernier effet peut être généré délibérément en variant les instants d'application des impulsions Raman. Nous observons une claire dépendance de la phase de rotation par rapport au délai des impulsions d'une manière linéaire. De plus, cette dépendance varie en fonction de l'alignement relatif des trois miroirs de rétroréflexion. Nous en déduisons que le biais est dominé par une aberration des front d'onde linéaire qui est l'alignement des trois miroirs Raman. En changeant l'orientation horizontale d'un des trois miroirs, nous pouvons diminuer cet effet. Prenant en compte la précision de la mesure de la phase de rotation et sa dérive au cours de plusieurs mesures qui servent à diminuer cette influence, nous déduisons une incertitude de l'alignement
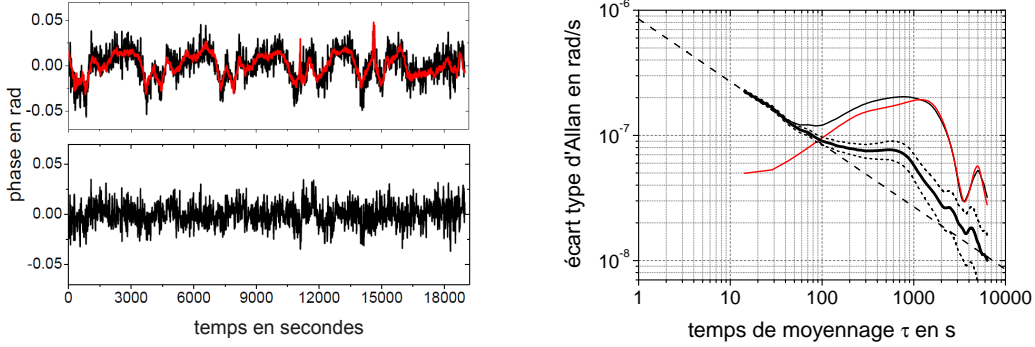
Figure 3: Stabilité long terme du gyromètre. *A gauche :* La phase de rotation est donnée pour une mesure d'une durée d'environ 5 heures *(en haut, ligne noire)*. Elle montre un comportement clairement périodique et est bien corrélée avec une combinaison linéaire des mesures des temps d'arrivée des échantillons atomiques trouvée par ajustement numérique *(en haut, ligne rouge)*. Cette combinaison permet une correction de la phase de rotation et ainsi de diminuer l'influence de l'effet croisé des dérives de position de la source atomique et les fronts d'onde des séparatrices Raman *(en bas, ligne noire)*. *A droite :* La phase de rotation permet de déduire l'incertitude statistique du signal de rotation en fonction de la durée de moyennage. Le graphe représente les écarts type d'Allan du signal de rotation *(ligne noire, fine)*, la combinaison linéaire des mesures des temps d'arrivée atomique *(ligne rouge)* et le signal de rotation corrigé *(ligne noire, épaisse)*. L'erreur statistique de l'écart type d'Allan est tracée en *ligne noire, épaisse et pointée*. La *ligne noire et pointillée* démontre un moyennage de $8,5 \cdot 10^{-7}$ rad/(s$\sqrt{\text{Hz}}$).

total $(\alpha_{x,1} - 2\alpha_{x,2} + \alpha_{x,3})$ selon l'axe horizontal de moins de 3 μrad. Ici, $\alpha_{x,i}$ avec $i = 1, 2, 3$ sont les orientations horizontales des miroirs T1, T2 et T3.

Pour estimer les fluctuations du recouvrement des nuages atomiques aux instants des impulsions Raman, nous étudions les fluctuations de vitesse et de position des sources atomiques. Nous trouvons que les fluctuations en position initiale des PMO sont l'effet dominant. Ceci peut causer des fluctuations du recouvrement de l'ordre du millimètre dans la direction horizontale. Cependant, ces fluctuations se traduisent aussi par des fluctuations des temps d'arrivée des échantillons atomiques dans les zones de détection. Aussi avons-nous enregistré les temps d'arrivée au cours des mesures, que nous avons pu corréler aux fluctuations de la phase de l'interféromètre. Nous avons finalement exploité cette corrélation pour corriger les mesures de la phase de l'interféromètre, et ainsi amélioré la stabilité long terme de la mesure de rotation. Nous avons obtenu une sensibilité court terme sur la mesure de rotation de de $8,5 \cdot 10^{-7}$ rad/(s$\sqrt{\text{Hz}}$). Nous atteignons après 4000 s de moyennage une sensibilité de $2 \cdot 10^{-8}$ rad/s.

Capteur atomique de force à faible distance

Principe de mesure

La mesure de forces à faible distance dans le projet FORCA-G est basée sur l'interférométrie Raman avec des atomes piégés dans un réseau optique unidimensionnel et vertical. Dans ce système, les états (quasi-)stationnaires sont donnés par des états Wannier-Stark. En combinaison avec les états internes d'interférométrie $|g\rangle$ et $|e\rangle$ de l'atome de ^{87}Rb, ces états forment une échelle de Wannier-Stark (voir figure 4). La différence d'énergie entre ces états est donnée par le gradient du potentiel gravitationnel plus la différence d'énergie des états internes. Nous pouvons induire un effet tunnel cohérent du site avec l'indice m au site $m' = m + \Delta m$ en choisissant la fréquence relative des deux faisceaux Raman ν_R égale à la fréquence de transition de l'état interne ν_{eg} plus un multiple Δm de la fréquence de Bloch du système ν_B donnée par

$$\nu_B = \frac{m_a g \lambda_l}{2h},$$

où g est l'accélération gravitationnelle, m_a est la masse d'un atome de ^{87}Rb, h est la constante de Planck et λ_l est la longueur d'onde du laser à l'aide duquel nous réalisons le réseau optique. Inversement, nous pouvons, en mesurant la probabilité de transition autour d'une telle résonance, déterminer la fréquence de Bloch et, ainsi, l'accélération subie par les atomes piégés dans le réseau. En réalisant cette mesure à la proximité d'une surface macroscopique, les forces à faible distance sont, en général, mesurées comme perturbation de l'accélélation gravitationnelle locale. Cette mesure de fréquence peut être réalisée avec une simple impulsion ou bien avec une séquence d'impulsion Raman ce qui correspond à un interféromètre Raman piégé.

Nous démontrons l'effet tunnel nécessaire ainsi que la réalisation de l'interférométrie atomique dans ce système loin d'une surface macroscopique. Dans ce cas, tous les atomes piégés dans le réseau optique contribuent à la mesure indépendamment de la position dans le réseau. Ceci nous permet d'étudier la stabilité de la mesure de la fréquence de Bloch et ainsi de la mesure de l'accélération locale.

Réalisation expérimentale

Le piégeage des atomes de ^{87}Rb est réalisé dans un réseau vertical créé par une onde stationnaire d'un faisceau laser d'une longueur d'onde de $\lambda_l = 532$ nm. Comme cette lumière est désaccordée dans le bleu par rapport aux raies D1 et D2, les atomes sont piégés dans les minima d'intensité. Pour assurer un confinement transverse, nous superposons un faisceau d'une longueur d'onde $\lambda_{dip} = 1064$ nm à l'axe optique du réseau pour réaliser un piège dipolaire. Cette superposition ainsi que l'alignement des faisceaux Raman sont réaliés avec des miroirs dichroïques (voir
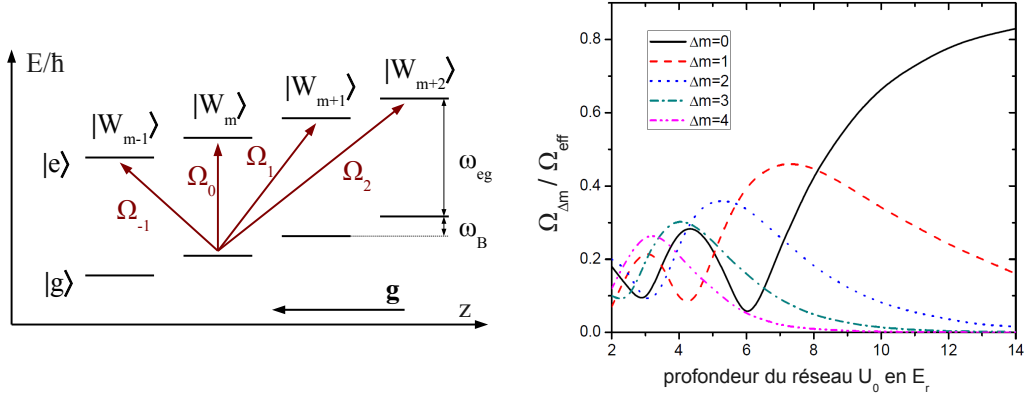
Figure 4: Couplage sur l'échelle Wannier-Stark. *A gauche :* Les états Wannier-Stark $|W_m\rangle$ décrivent les fonctions d'onde des atomes piégés dans le réseau vertical. Ensemble avec les états internes $|g\rangle$ et $|e\rangle$, ils forment une échelle dite Wannier-Stark. *A droite :* L'intensité de couplage dépend fortement de la profondeur du résau optique. Le graphe représente les fréquences de Rabi $\Omega_{\Delta m}$ pour des couplage des sites m et $m' = m + \Delta m$ en rapport avec la fréquence de Rabi pour une particule libre Ω_{eff} en fonction de la profondeur du réseau U_0, donnée en énergie de recul du réseau à longueur d'onde $\lambda_l = 532$ nm. Le vecteur d'onde effectif du couplage est donné par $k_{\text{eff}} \approx 4\pi/(780$ nm$)$.

figure 5). Les faisceaux Raman sont appliqués dans une configuration rétroréfléchie. Pour choisir la direction du vecteur d'onde effectif, seul l'un des faisceaux est réfléchi tandis que l'autre est filtré à l'aide d'une séparatrice polarisante.

Le dispositif expérimental est basé sur les mêmes techniques que celui du gyromètre atomique. L'interféromètre atomique est réalisé dans une enceinte à vide qui possède plusieurs hublots pour l'accès optique. La partie de l'enceinte dans laquelle a lieu l'interféromètre est entourée par un blindage magnétique et le champ magnétique résiduel est par ailleurs minimisé à l'aide de trois paires de bobines autour les trois axes. Un axe de quantification verticale pour le contrôle de l'état interne est défini par une paire de bobines. La source atomique est une combinaison d'un PMO 2D et 3D. Les lasers utilisés pour le piégeage magnéto-optique, préparation et détection ainsi que les lasers Raman sont des LCE. Le laser à 532 nm est un laser monofréquence à milieu amplificateur solide doublé en fréquence. Pour la génération de la lumière à 1064 nm, nous utilisons un laser fibré.

Les atomes sont piégés dans le PMO 3D avant de les refroidir dans une mélasse optique à environ 2 μK. Ceci permet de charger jusqu'à $5 \cdot 10^4$ atomes dans le piège mixte constitué par le réseau vertical et le piège dipolaire transverse. Ici, les atomes sont pompés optiquement dans l'état interférométrique fondamental. Ensuite, nous appliquons la séquence d'impulsions Raman avant de relâcher les atomes en éteignant les lasers du piège mixte. L'état interne est mesuré dans une détection de fluorescence sélective en état interne ce qui nous permet de déterminer la probabilité de transition de notre séquence.
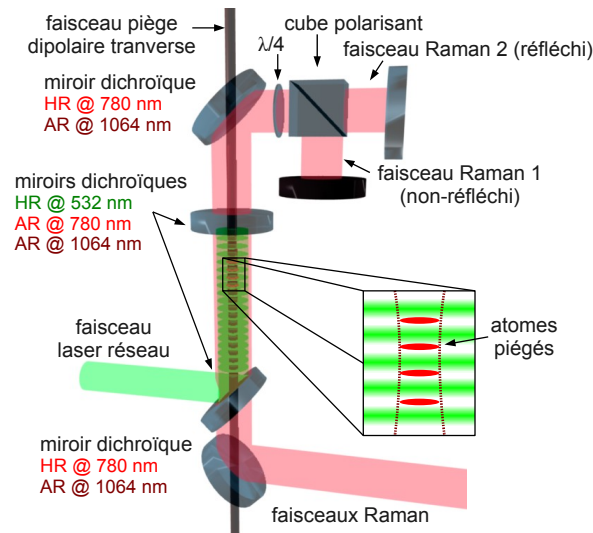
Figure 5: Schéma de l'expérience FORCA-G. Le réseau optique unideminsionnel et vertical est réalisé en rétroréfléchissant un faisceaux laser monofréquence à longueur d'onde $\lambda_l = 532$ nm. Le confinement transverse est assuré à l'aide d'un piège dipolaire généré par un faisceau en onde propageante de longueur d'onde de $\lambda_{dip} = 1064$ nm. Les faisceaux du piège mixte ainsi que les faisceaux Raman sont superposés avec des miroirs dichroïques.

Spectroscopie Wannier-Stark à haute résolution

L'interférométrie dans le réseau vertical est basée sur un couplage cohérent entre des états de Wannier-Stark. Nous étudions donc l'effet tunnel induit par les lasers Raman et la résolution spectrale que l'on peut atteindre avec ce processus. La force du couplage de cet effet tunnel dépend du rapport entre les longueurs d'onde du réseau et du laser de couplage ainsi que de la profondeur du réseau. L'évaluation numérique de l'intensité de couplage pour différentes transitions entre états de Wannier-Stark, correspondant à un couplage de chaque puits à un puits séparé de $\Delta m \lambda_l / 2$, est donnée dans la figure 4. Les différences d'intensité de couplage en fonction de Δm conduisent à des différences d'amplitude dans les pics des spectres de Wanner-Stark. Ces spectres sont obtenus en mesurant la probabilité de transition après l'application d'une seule impulsion des lasers Raman. En choisissant l'intensité de cette impulsion telle que les oscillations de Rabi de toutes les transitions n'excèdent pas le premier maximum, nous retrouvons, quantitativement, le rapport des intensités de couplage des différents ordres (voir figure 6).

La résolution de cette spectroscopie est limitée par deux effets. Le premier est un élargissement induit par l'inhomogénéité du déplacement différentiel du faisceau du piège dipolaire transverse. Pour des durées d'impulsion élevées, nous trouvons une largeur spectrale minimale d'environ 3 Hz. Pour contrecarrer cet effet, un faisceau d'annulation du déplacement lumineux différentiel est superposé et ajusté
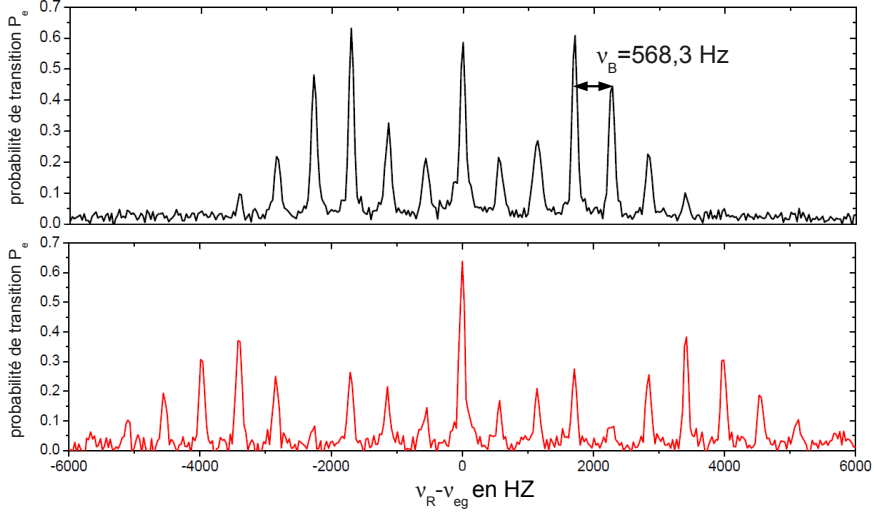
Figure 6: Spectres de Wannier-Stark. La probabilité de transition P_e de l'état interne fondamental à l'état excité est représentée pour une profondeur de réseau de $U_0 = 3.9E_r$ *(en haut)* et $U_0 = 1.6E_r$ *(en bas)*. Les résonances correspondent aux transitions Δm, qui sont séparée spectralement par la fréquence de Bloch $\nu_B = 568, 3$ Hz.

en taille avec le faisceau du piège dipolaire transverse. Ce faisceau induit un déplacement lumineaux différentiel opposé à celui du piège dipolaire et permet alors de compenser le déplacement lumineux et son inhomogénéité. Comme cet effet est indépendant de l'ordre Δm, nous avons étudié la largeur de la raie de transition en fonction de la durée d'impulsion en appliquant une impulsion micro-onde qui couple seulement l'état atomique interne. En présence du faisceau compensateur, nous trouvons une résolution à la limite de Fourier pour les durées d'impulsion jusqu'à 1,5 s (voir figure 7).

Tandis que l'inhomogénéité du déplacement lumineux cause un élargissement spectrale pour une seule impulsion, dans le cas d'une séquence Ramsey consistant en deux impulsions $\pi/2$ séparées un interval de temps T, cette inhomogénéité engendre une perte de contraste des franges de Ramsey. Sans faisceau compensateur, le contraste décroît à zéro pour des temps de Ramsey de quelques centaines de millisecondes. La compensation du déplacement lumineux permet de réaliser des séquences de Ramsey d'une durée de plus d'une seconde. L'évolution du contraste en fonction de T d'une séquence de Ramsey micro-onde nous permet d'estimer l'élargissement résiduel à moins de 0,5 Hz.

La largeur spectrale des transitions de l'ordre $\Delta m = 3$ est également étudiée. Tandis que la largeur décroit avec l'inverse de la durée d'impulsion comme dans le cas du couplage micro-onde, nous trouvons un facteur 2 par rapport à la limite de Fourier. Cet élargissement qui est indépendant de la durée d'impulsion est attribué à des inhomogénéités d'intensité des faisceaux Raman. Ces dernières causent une compensation imparfaite des déplacement lumineux des faisceaux Raman et donc
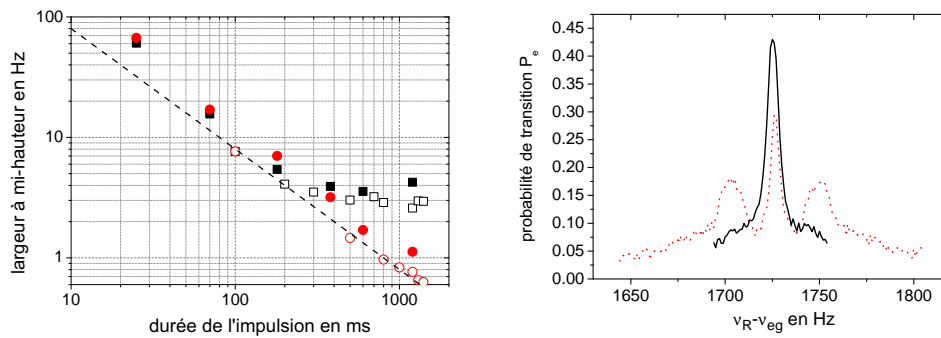
Figure 7: Résolution spectrale. *A gauche :* La largeur à mi-hauteur est représentée pour des spectres d'une seule impulsion π pour des transitions micro-onde *(symboles en contour)* et Raman sur la transition $\Delta m = 3$ *(symboles remplies)*. La largeur décroît avec la durée d'impulsion croissante en présence du faisceau compensateur *(carrées)* tandis que la largeur est limitée à 3 Hz sans compencation du déplacement lumineux différentiel *(cercles)*. *A droite :* Nous observons des bandes latérales correspondant à une excitation ou une désexcitation d'état de vibration dans le piège dipolaire transverse pour un alignement imparfait du vecteur effectif des faisceaux Raman à l'axe optique du réseau verticale *(ligne rouge et pointillée)*. Ce couplage est effectivement supprimé dans le cas d'un alignement parfaitement colinéaire *(ligne noire)*.

une inhomogénéité de déplacement lumineux qui est proportionnelle à la fréquence de Rabi.

Le couplage des états Wannier-Stark peut être accompagné d'un couplage d'états transverses de vibration dans le piège dipolaire de confinement transverse. Cette transition est excitée par une composante non-nulle du vecteur d'onde effectif des faisceaux Raman dans la direction perpendiculaire à l'axe optique du réseau. Comme les atomes sont répartis sur plusieurs états de vibration transverse, nous observons deux bandes latérales qui correspondent à une excitation (bande bleue) et une désexcitation (bande rouge) d'état de vibration. Ces bandes latérales sont efficacement supprimées dans le cas d'un alignement fin des faiscaux Raman sur l'axe optique du réseau vertical (voir figure 7).

Stabilité de la mesure

La fréquence de Bloch, et donc la valeur de l'accélération vue par les atomes piégés, sont mesurées à l'aide d'un interféromètre Wannier-Stark de type Ramsey. Pour supprimer l'influence des fluctuations lentes de l'offset de la probabilité de transition induites par le mécanisme de détection ainsi que les fluctuations lentes des déplacements différentiels des états internes, nous employons une séquence à quatres configurations. D'une part, la mesure de la probabilité de transition

est réalisée en alternance sur les deux flancs de la frange centrale Ramsey d'une résonance Δm en modulant la valeur de fréquence relative des lasers Raman. La valeur de la fréquence correspondante à la transition en question est alors trouvée à l'aide d'une boucle d'asservissement pilotée par l'ordinateur de l'expérience. Cette boucle règle les valeurs de fréquences à droite et à gauche de la raie pour atteindre la même valeur de la probabilité de transition sur les deux flancs de frange. La valeur de la fréquence correspondant à la position de la frange centrale est alors donnée par la valeur située entre ces deux dernières. D'autre part, cette mesure du multiple de la fréquence de Bloch $\Delta m \nu_B$ plus la fréquence de la transition entre états hyperfins est réalisée en alternance sur les transitions $\pm\Delta m$. Le multiple $\Delta m \nu_B$ est alors obtenu en effectuant la demi-différence des deux valeurs de fréquence, ce qui permet de s'affranchir du déplacement de fréquence lié à la transition hyperfine si ses fluctuations sont lentes par rapport au temps de cycle de la mesure.

Nous réalisons une mesure de moyennage du septième multiple de la fréquence de Bloch et analysons la stabilité à l'aide de l'écart type d'Allan (voir figure 8). Nous en déduisons une stabilité à court terme de $5,8 \cdot 10^{-5}$ à une seconde de moyennage. La valeur de fréquence du multiple $\Delta m = -7$ montre un moyennage de $\tau^{-1/2}$ avec la durée de moyennage de τ pendant une durée de 30 secondes et une dérive après cette durée. Comme l'incertitude statistique de la valeur de la fréquence de Bloch déduite des ordres $\Delta m = \pm 7$ décroît aussi pour des temps plus longs que 1000 s, la dérive de fréquence observée peut être attribuée aux déplacements d'énergie des états internes. La précision de la mesure de la fréquence de Bloch peut alors être améliorée en moyennant. La même mesure est réalisée sur l'ordre $\Delta m = \pm 3$. Comme nous trouvons la même stabilité que dans le cas du septième multiple, la fluctuation de la fréquence de Bloch peut être exclue comme source dominante des fluctuations à court terme.

L'origine des dérives de déplacement d'énergie interne est analysée à l'aide d'une séquence Ramsey micro-onde. Ceci nous permet d'identifier une dérive en position des faisceaux du piège dipolaire et du compensateur du déplacement lumineux différentiel étant la source dominante pour des dérives en fréquence à long terme tandis que cet effet ainsi que l'influence des fluctuations en intensité de ces deux faisceaux ont un impact négligeable sur la stabilité court terme. Nous étudions également l'influence du déplacement lumineux différentiel des faisceaux Raman. Nous trouvons une fluctuation lente dont la plus grande partie peut être attribuée aux fluctuations de polarisation qui font varier le rapport d'intensité des deux faisceaux et ainsi le déplacement lumineux résiduel. Encore une fois, la stabilité à court terme n'est pas limitée par cette influence.

Une étude complémentaire est faite en utilisant un interféromètre Ramsey symétrisé qui combine des transitions entre puits et celles dans les mêmes puits. Nous créons une superposition à l'aide d'une impulsion Raman $\pi/2$ et inversons l'état interne pendant la durée de Ramsey pour symétriser le temps passé dans chacun des bras de l'interféromètre dans chacun des deux états internes. Cette
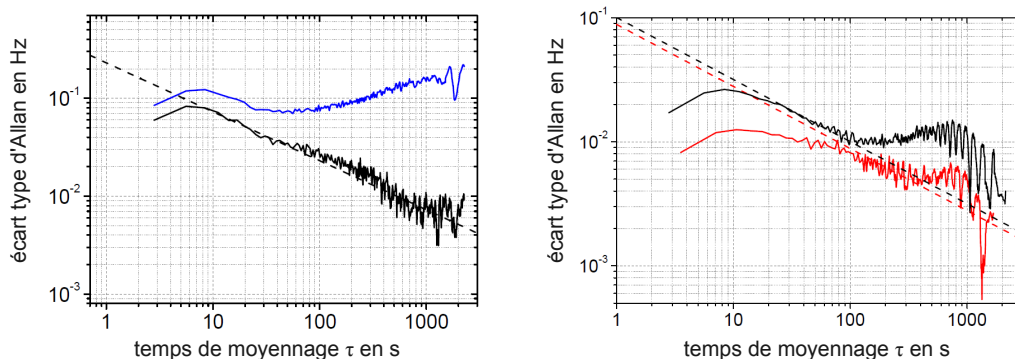
Figure 8: Stabilité de la mesure de fréquence de Bloch. *A gauche :* L'écart type d'Allan des mesures de la fréquence de Bloch est représentée pour la résonance $\Delta m = -7$ *(ligne bleue)* et pour la mesure alternée sur les résonances $\Delta m = \pm 7$ *(ligne noire)* avant les modifications techniques. *A droite :* La même mesure pour une séquence de Ramsey de $\tau_{\pi/2} = 10$ ms et $T = 400$ ms *(ligne noire)* et de $\tau_{\pi/2} = 120$ ms et $T = 850$ ms *(ligne rouge).* Les lignes pointillées représentent les moyennages qui résuident l'incertitude statistique avec $\tau^{-1/2}$.

séquence permet de supprimer le déplacement lumineux dû au piège mixte tandis que le déplacement lumineux résiduel des faisceaux Raman ne peut être éliminé. Nous retrouvons alors un comportement similaire au cas des études Ramsey micro-onde.

Ayant exclu les fluctuations de la fréquence de Bloch et les fluctuations dues aux déplacements de l'état interne de la limitation de la stabilité à court terme, nous estimons l'impact des vibrations du dispositif expérimental sur la stabilité de la mesure. Celles-ci peuvent induire une phase spatiale différente des faisceaux Raman à la position des atomes dans les deux impulsions Raman de la séquence Ramsey. Nous estimons l'impact de cette contribution en mesurant les vibrations du montage des miroirs de rétroréflexion. Nous effectuons une mesure du spectre des vibrations et le calcul du bruit de phase attendu à l'aide du formalisme de la fonction de sensibilité. Si le mouvement des deux miroirs est synchrone à tout moment, l'influence est négligeable. Par contre, si les miroirs montrent un mouvement qui est différent de seulement 10 %, nous trouvons le bruit de phase observé.

Les analyses font suite à deux modifications techniques du dispositif expérimental. Premièrement, des faisceaux Raman sont guidés à l'enceinte à vide en utilisant deux fibres séparées pour réduire les fluctuations en polarisation. Aussi, le diamètre des faisceaux Raman est diminué pour réduire des inhomogénéités d'intensité causées par la diffraction des faisceaux sur le chemin optique relativement étroit. Deuxièmement, les miroirs de rétroréflexion du faisceaux réseau et celui des faisceaux Raman sont montés sur la même axe optique sur un support

rigide pour minimiser un mouvement différentiel des deux.

Les mesures de stabilité de fréquence dans la suite des modifications techniques montrent une réduction du bruit à court terme par un facteur 3. Nous trouvons alors une stabilité de la mesure de fréquence de Bloch de $2 \cdot 10^{-5}$ à une seconde de moyennage. Prenant en compte la force de Casimir-Polder attendue dans une distance atome-surface de 5 μm, nous obtenons une résolution à cette force de 1 % après un moyennage de 150 s.

Ascenseur atomique cohérent

Pour de futures mesures des forces à faible distance près d'une surface macroscopique, nous avons réalisé un moyen de transport cohérent des atomes dans l'enceinte à vide. Ceci permettra de réaliser des mesures de force à différentes distances de la surface. De plus, nous pouvons préparer l'ensemble atomique dans une région de l'enceinte à vide et le transporter à une autre région. Ceci permettra de maintenir une quantité de gaz résiduel négligeable dans la zone d'interférométrie et ainsi de réduire les dépots d'atomes de Rubidium sur la surface qui peuvent créer des champs électriques parasites ce qui perturbe la mesure des forces Casimir-Polder et non-Newtoniennes envisagées.

Notre «ascenseur atomique cohérent» est basé sur l'accélération et la décélération des atomes dans un réseau optique fortement accéléré. Cette configuration est adaptée d'une expérience dans laquelle est mesuré avec haute précision le recul transferé aux atomes dans ce processus. L'accélération est induite via le désaccord de deux faisceaux laser constituants l'onde stationnaire ou, réspectivement, mouvante. Pour pouvoir réaliser de grandes accélérations, il est indispensable d'utiliser des réseaux profonds pour supprimer des pertes causées par l'effet tunnel Landau-Zener. Nous choisissons alors une longueur d'onde près de la ligne D2 ce qui permet de réaliser un déplacement lumineux important pour des valeurs de puissance optique raisonnable. Le choix du désaccord est fait à partir d'un compromis entre la profondeur du réseau et la diffusion spontanée des photons du laser réseau par les atomes. Une valeur de 30 GHz nous permet de garder un taux d'émission spontanée relativement faible pour des accélérations qui mènent aux déplacements des atomes sur des centimètres pendant des dizaines de millisecondes.

Les faisceaux résaux sont générés par une seule source laser basée sur un LCE et d'amplification en configuration MOPA. La lumière est séparée sur deux chemins au long desquels nous contrôlons l'intensité et la fréquence à l'aide d'un modulateur acousto-optique (MAO) dans chaque bras. Les faisceaux sont ensuite guidés vers l'enceinte à vide et appliqués selon l'axe optique du réseau vertical en utilisant les éléments optiques des faisceaux Raman qui ont la même longueur d'onde. L'un des deux faisceaux est appliqué par le bas et l'autre par le haut. Dans cette configuration, nous contrôlons directement la fréquence relative des faisceaux de l'ascenseur via la radio-fréquence appliquée sur les MAO.
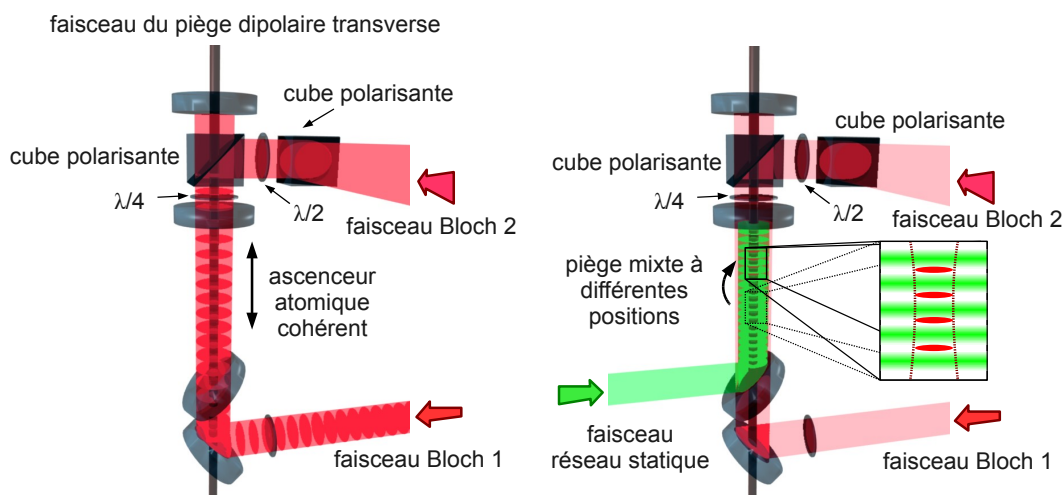
Figure 9: Ascenseur atomique cohérent. *A gauche :* Les faisceaux du réseau accérléré sont appliqués sur le chemin optique des faisceaux Raman. *A droite :* L'ascenseur atomique permet de réaliser le piégeage dans le piège mixte à différentes positions selon l'axe optique du réseau verticale statique à longueur d'onde de $\lambda_l = 532$ nm.

Un processus de déplacement consiste en une accélération, une phase de chute libre et une décélération des atomes. Nous choisissons le protocole suivant pour réaliser un ascenseur atomique : la rampe de fréquence relative des deux faisceaux du réseau est choisie d'une telle manière que le réseau suit l'accélération gravitationnelle des atomes provenant de la mélasse. Les faisceaux sont allumés avec une rampe d'intensité pour charger les atomes adiabatiquement dans le réseau. Une fois atteint la profondeur maximale, une rampe de fréquence est appliquée qui produit une accélération du réseau. Ensuite, une rampe de fréquence identique à la première est appliquée pour encore suivre l'accélération des atomes en chute libre et une rampe d'intensité décroissante sert à relâcher les atomes adiabatiquement. Pendant la phase de chute libre, les atomes se déplacent à la vitesse choisie par la pente et la durée de la rampe d'accélération, typiquement à une vitesse de quelques mètres par seconde. La phase de chute libre est suivie par la phase de décélération qui consiste en l'allumage adiabatique du réseau, la rampe de décélération et la coupure adiabatique de l'intensité des faisceaux du réseau, similaire à la phase d'accélération.

Nous étudions l'efficacité du transport cohérent en détectant les atomes par le système de détection de l'interféromètre atomique. Ceci nous permet d'observer les différents ensembles atomiques arrivants dans la zone de détection à différents moments en fonction de la séquence d'accélération. Nous pouvons ainsi distinguer entre des atomes qui ne sont pas accélérés par le réseau, ceux qui sont accélérés mais pas décélérés et ceux qui ont suivi toute la séquence de l'ascenseur. En réalisant un ascenseur descendant sur une distance de 5,5 cm, nous observons que

les atomes qui ont été accélérés, sont décélérés avec grande probabilité. L'efficacité est alors surtout limité par le recouvrement du profil d'intensité des faisceaux du réseau. Cette conclusion est confirmée par une étude d'une séquence d'un ascenseur ascendant. Nous le réalisons pour différentes valeurs de pentes d'accélération et décélération. Ici, la durée de la pente de décélération est choisie telle que les atomes ont une vitesse finale nulle. Ceci nous permet de piéger les atomes ensuite dans le réseau statique de longueur d'onde de $\lambda_l = 532$ nm. L'accélération maximale dans cette configuration est donnée par $100v_r$ par milliseconde ce qui correspond à $1,18 \cdot 10^3$ m/s^2. De plus, nous observons un taux d'émission spontanée d'environ 2 % par milliseconde.

Conclusions et perspectives

Cette thèse présente les études de stabilité d'un gyromètre atomique et celle d'un interféromètre piégé dans un réseau unidimensionnel et vertical.

Une étude détaillée des sources de dérive du signal de rotation à long terme nous a permis d'atteindre une stabilité de $2 \cdot 10^{-8}$ rad/s après une durée de moyennage de 4000 s. La prochaine étape pour l'augmentation de la sensibilité est de baisser le bruit à court terme. Ceci peut être, par exemple, réalisé en agrandissant la surface entourée par les bras des interféromètres basée sur la technique de double diffraction Raman. De plus, l'amélioration de l'alignement des miroirs de rétroréflexion Raman et la réduction des fluctuations de position des sources atomique permettra d'obtenir une meilleure stabilité intrensèque du signal de rotation à long terme.

La stabilité de la mesure de force dans le réseau vertical atteinte dans les travaux de recherche présentés dans cette thèse correspond à une incertitude statistique d'une mesure de la force de Casimir-Polder dans une distance atome-surface de 5 μm de 1 % après une intégration de 150 s. Pour réaliser une telle mesure, deux démarches doivent être prises : augmenter la résolution spatiale en utilisant des ensembles atomiques d'une plus grande densité et placer le miroir de rétroréflexion du réseau sous vide pour réaliser une mesure près de sa surface. L'ascenseur atomique cohérent servira dans ces mesures pour amener les atomes près de la surface macroscopique et pour des mesures quasi-différentielles en différentes distances de la surface.

CONTENTS

CHAPTER 1

Introduction

Interferometry is applied in various applications that are employed in fundamental and applied science, high technology, and everyday life. It makes use of interference appearing when two or more waves are superimposed: They interfere constructively or destructively depending on their relative phases. The read out of the wave intensities then allows to deduce the relative phase of the interfering waves.

A textbook example for interferometry is a light interferometer based on the work of Michelson and Morley from 1887 [1]. In the set-up of this interferometer type, which is depicted in figure 1.1, a light wave is split onto two paths using a beam splitter, retro-reflected on each of the paths, and superimposed on the same beam splitter. The intensity on the interferometer output port is then modulated as a function of the relative optical path lengths. The set-up of Michelson and Morley is nowadays used in prominent examples for interferometers of much larger experimental scale that are designed to detect gravitational waves [2].

A slightly different interferometer geometry was introduced by Mach [3] and Zehnder [4] (see figure 1.1). Here, the light waves are split on one beam splitter and, after redirection of each of the two resulting interferometer paths, recombined on a second beam splitter. The enclosed area in the Mach-Zehnder geometry is key for today's most precise rotation measurements. In 1913, Sagnac demonstrated that the phase of an interferometer scales with the product of the enclosed area and the rotation of the device [5]. Based on this so-called Sagnac effect it was possible to develop laser gyroscopes, devices in which a light wave is split, guided around an area, and brought to interference. This describes a passive light gyroscope. The same principle is used in active gyroscopes based on ring laser cavities enabling today's most precise local rotation measurements as realized in the ring laser gyroscope Grossring G [6]. These are only two examples for the many applications of light based interferometry in fundamental and applied science.

While it is possible to describe light interference by electromagnetic fields for sufficiently high light intensity, this description fails for example for interferometry
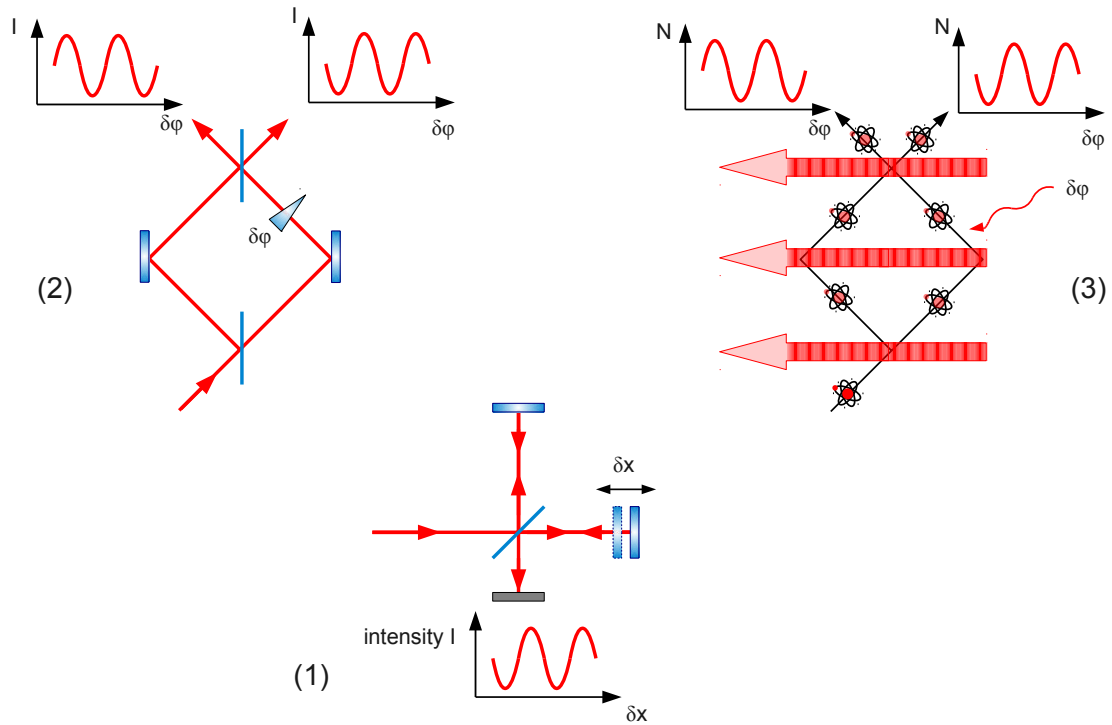
Figure 1.1: Michelson and Mach-Zehnder interferometer. The Michelson (1) and Mach-Zehnder (2) interferometer geometries are depicted as examples for light interferometry. The output intensities vary as a function of the interferometer phase $\delta\varphi$, which is induced by a difference in path length in the Michelson interferometer. Neutral atoms can be diffracted on standing light waves which enables the realization of a matter-wave analog to the Mach-Zehnder interferometer (3). The atom interferometer signal is encoded in the relation of the output state populations, which is found by counting the atoms on the two exit ports.

with minimal intensities where light reveals its quantum nature [7]. Here, a quantum mechanical picture is employed describing light as a flux of single particles, namely photons. This context is commonly known as wave-particle dualism. An important consequence of the dualism principle was predicted by de Broglie in 1923 and 1924. He assumed that it is also possible to describe massive particles as waves [8]. Since that time, matter-wave interference has been demonstrated for electrons [9], neutrons [10], atoms [11], for molecules such as fullerenes [12], and even hydrocarbon molecules with masses exceeding 10^3 atomic mass units (AMU) [13]. The emergence of matter-wave interference becomes visible, for example, in spatial fringe patterns. In the mentioned experiments, bulk crystals, material absorption gratings and, in recent works, optical ionization gratings have been used to induce matter-wave interference.

For neutral atoms, a precise control of two or more atom interferometer paths

can be realized using coherent off-resonant light fields which leads to a matter-wave analog to, for example, the Mach-Zehnder geometry as depicted in figure 1.1. Such interferometers have been demonstrated by the use of light phase gratings inducing Raman-Nath [14] and Bragg diffraction [15]. In the two cases, the phase gratings are standing light waves that are realized by the use of two counter-propagating laser beams. In the particle picture, the atomic diffraction process can be understood as an absorption of one photon from one beam and an emission of a photon into the other beam. Momentum conservation requires the atom to gain a momentum of twice the photon recoil momentum $2\hbar k$. As this process is coherent and the photon recoil direction and absolute value are known, this results in diffraction into multiple orders of $2\hbar k$ in the Raman-Nath case and in coupling of two well defined momentum states in the Bragg case [16]. If now a relative detuning of the two light fields is chosen such that an atomic transition can be addressed, so-called stimulated Raman transitions are realized that are eponymous for Raman interferometry [17]. In this case, the coupling between two momentum states coincides with an internal state coupling. This so-called state labeling [18] allows to read out the momentum state population, and thereby the interferometer signal, via the determination of the internal state populations.

Within the last two decades, Raman and Bragg type interferometers based on alkali atoms have evolved to powerful tools in metrology. Using these type of interferometers high precision measurements of the gravitational constant G [19, 20] with a statistical relative uncertainty of $1.7 \cdot 10^{-3}$ [20] could be performed. Also high precision measurements of the fine structure constant α via the ratio of Planck's constant and the atomic mass h/m_a [21, 22] could be shown with a best relative uncertainty for α of $6.6 \cdot 10^{-10}$ [22]. Furthermore, it was possible to demonstrate high resolution inertial sensors for measurements of the local gravitational acceleration [23] and the Earth rotation [24]. The best atom interferometry based absolute gravimeters show resolutions and accuracies that are competitive with state-of-the-art falling corner-cube absolute gravimeters [25]. This was for example demonstrated in the case of the cold atom gravimeter (CAG01) [26] of the Laboratoire national de métrologie et d'essais, which was the first atom gravimeter – and still the only one – to participate to international comparison campaigns [27].

While [24] presents an atomic beam gyroscope, the same interferometer geometry has been employed in gyroscopes based on laser-cooled atoms leading to much more compact set-ups [28, 29]. Such a cold atom gyroscope experiment is realized at the Institut für Quantenoptik at Leibniz Universität Hannover. The CASI ("Cold Atom Sagnac Interferometer") experiment is introduced in section 1.1. It is the first of two objects of research in this work.

The atom interferometers mentioned above all base on the interference of free-falling atoms. The measurement is realized on atomic beams, as well as on dropped or launched cold atomic ensembles. This limits the interrogation time of the atoms and thereby the interferometer scaling factor. Recent developments have led to the

extension of the total time of the atom's free fall in atom interferometers that are run in drop tower experiments [30], on parabola flights [31], and in large scale atomic fountains [32].

A development that is complementary to enlarging the interferometer size is given by trapped interferometers, which are not limited by the free-fall time and furthermore allow for measurements with high spatial resolution. It is possible to trap the atoms in a spatial superposition for example in a compact magnetic [33], or a dipole double well [34] or lattice potential [35]. The interference that occurs when recombining the two partial wave packets depends on the local potential gradient along the atomic separation baseline. In [36] a beam splitter technique on an atom chip in a radio frequency (RF) dressed potential is presented. This allows to create a spatial superposition in an effective double-well potential and thereby to realize an atom interferometer in a magnetically trapped configuration. The work presented in [37] consists in trapping atoms in an optical vertical 1D-lattice. Here, so-called Bloch oscillations occur as a quantum interference effect, which leads to a measurement of the local gravitational acceleration via the determination of the frequency of these oscillations. A combination of atomic Raman beam splitting in free fall and trapping in an optical lattice is studied in [38]. A pair of two beam splitting pulses results in a spatial superposition which is then trapped in a stationary optical lattice and recombined in free fall after a certain holding time. This allows once again for a measurement of local gravity. It can be shown that creating such a superposition is also possible by inducing tunneling in a vertical 1D-lattice using a probe light field [39]. This led to the proposal of trapped atom interferometry based on tunneling induced by stimulated Raman transitions in such a lattice [40]. The experiment based on this concept is realized at SYRTE ("SYStèmes de Références Temps Espace") in the Observatoire de Paris under the name FORCA-G ("CAsimir FORCe and Gravitation at short range"). It is the object of research in the second part of this thesis and will be introduced in section 1.2.

1.1   Rotation measurements and the CASI experiment

Before introducing the CASI experiment, possible gyroscope applications are introduced. This is followed by an overview of gyroscope technologies.

1.1.1   Rotation measurements

An important application of rotation measurements is navigation. If the six moments of inertia of a vehicle, which are rotation and acceleration in all three directions, are tracked during the movement of the vehicle, it is possible to deduce its

position relative to a given starting position at any time without external information (e.g. by the Global Positioning System, GPS). The demanded performance of the rotation measurement depends on the type of movement in, for example, aircrafts, ships, or submarines. The best resolutions are in the range of 10^{-6} rad/s to 10^{-8} rad/s. Furthermore, this type of application sets high demands on the robustness of the measurement device and requires a large dynamic range.

Rotation measurements of typically smaller dynamics but higher precision are desirable in the field of geodetics and geophysics. Here, measurements of Earth rotation variations in orientation (polar motion) and magnitude (Length-Of-Day, LOD fluctuations) give an insight into tidal effects of the Earth as a whole and into internal dynamics of the body of our planet. Relative changes of 10 ppb of the Earth rotation rate of $\Omega_E = 7.27 \cdot 10^{-5}$ rad/s demand for rotation resolutions in the regime of 10^{-12} rad/s and below [41].

An even higher sensitivity is required for the measurement of the Lense-Thirring effect [42]. This so-called frame dragging effect was deduced by Lense and Thirring from general relativity. It predicts a rotation rate induced by rotating masses such as the Earth. On a satellite in an Earth orbit, this effect is expected to induce a rotation rate in the range of 10^{-15} rad/s.

1.1.2 Gyroscope technologies

The first demonstration of an Earth rotation measurement was realized in 1861 by Foucault. It consisted in showing the rotation of the plane of a pendulum's oscillation. It was also Foucault who invented and constructed the first **mechanical gyroscope**, based on the work of Bohnenberger [43]. Such a device makes use of the conservation of angular momentum. The rotation axis of a rotating body suspended in a gimbal mount serves as a stable reference axis. This technique was used in navigation in order to track the orientation of e.g. ships and submarines over long times. By tracking the deduced trajectory it is then possible to determine the ship's position without external reference. The technology has been pushed to its limits in the realization of superconducting magnetically suspended spherical gyroscope bodies in the Gravity Probe B project. Here, it was possible to measure the a drift rate induced by the Lense-Thirring effect with an uncertainty of 19 % [44].

The Sagnac effect observed in 1913 enables the realization of gyroscopes based on interferometry. This effect describes the influence of rotations on the output phase of an interferometer featuring an area **A** that is enclosed by the interferometer paths. While this was first shown for light coming from a mercury arc lamp by Georges Sagnac one century ago [5], this effect occurs for a wave of any nature. The phase shift on the output of the interferometer scales directly with the projection of a rotation $\boldsymbol{\Omega}$ onto the enclosed interferometer area as well as with

the particle energy E

$$\Phi_{\mathbf{\Omega}} \;\; = \;\; \frac{4\pi E}{hc^2}\mathbf{\Omega} \cdot \mathbf{A}. \tag{1.1}$$

Here, h is the Planck constant and c is the speed of light. Based on this effect it was possible to develop passive and active **laser gyroscopes** [45]. **Passive** laser gyroscopes are nowadays typically realized in fiber spools. This allows for a large enclosed area and thereby for a large interferometer scaling factor in a relatively compact device. Fiber gyroscopes with resolutions in the lower 10^{-6} rad/(s$\sqrt{\text{Hz}}$) regime and high long term stabilities are today employed in so-called IMUs ("Intertial Measurement Units"). These devices consist of three of these gyroscopes and a three-axis accelerometer. They are used in navigation of, for example, aircrafts and rockets. An even higher resolution is reached using **active** ring laser gyroscopes. Typical resolutions of some 10^{-7} rad/(s$\sqrt{\text{Hz}}$) are realized for transportable instruments. Quasi-transportable instruments for the use in submarines even reach sensitivities of a few 10^{-8} rad/(s$\sqrt{\text{Hz}}$). For their application in geodesy and geophysics, these kind of devices are scaled up to a maximum enclosed single-loop area of 834 m^2 [46]. A resolution of $5 \cdot 10^{-10}$ rad/s is reached within one second of measurement time, but the resolution is limited by scaling factor instabilities. The highest resolution of a large ring laser gyroscope is up to date the measurement of the annual wobble and the Chandler wobble of Earth with the aid of the Grossring G [47]. The best sensitivity was reported in [48] for this device with 16 m^2 enclosed area of $2 \cdot 10^{-11}$ rad/(s$\sqrt{\text{Hz}}$).

The development of **atom interferometers** enabled the realization of gyroscopes based on the interference of neutral atoms. The striking argument for the use of this technology is given by the Sagnac phase (1.1). The comparison of the photon energy for a laser wavelength $\lambda = 633$ nm and an atomic rest mass of a ^{87}Rb atom results in a factor of

$$\frac{\Phi_{atom}}{\Phi_{light}} \;\; \approx \;\; 10^{11}. \tag{1.2}$$

This advantage is put into perspective as it is much more demanding to realize large enclosed areas in atom interferometers compared to light interferometers. Also, the effective atom flux is typically much lower than the used effective photon flux. Nonetheless, atom interferometry enables rotation measurements with gyroscopes that enclose much smaller areas while keeping a scaling factor comparable to light interferometry. The first and up to now most sensitive realization of an atomic gyroscope based on two atom interferometers with counter-propagating atomic beams and an area of 22 mm^2 enclosed by each interferometer was built at Stanford University. The resolution of this device was demonstrated to be as good as $6 \cdot 10^{-10}$ rad/(s$\sqrt{\text{Hz}}$) and $2 \cdot 10^{-11}$ rad/s after 2000 s of integration [49]. However, the use of thermal beams required a large apparatus. The separation of the first and

last beam splitter application amounted to 2 m. A much more compact device was constructed at SYRTE in Paris where cesium atoms were trapped and cooled in magneto-optical traps prior to be launched on parabolic trajectories. The slow atomic forward velocity on steep parabolas enabled the application of all beam splitter light field pulses within the width of one laser beam with a diameter of 48 mm. For an enclosed area of 3.8 mm^2 the sensitivity of this cold atom gyroscope was $2.4 \cdot 10^{-7}$ rad/(s$\sqrt{\text{Hz}}$) and, after an integration of approximately 1000 s, $1 \cdot 10^{-8}$ rad/(s$\sqrt{\text{Hz}}$) [29]. A second gyroscope at Stanford University is based on laser-cooled atoms in a vertical fountain configuration with a pulse sequence that requires the gravitational acceleration to form the atomic trajectories. For this device, a sensitivity of $8.8 \cdot 10^{-8}$ rad/(s$\sqrt{\text{Hz}}$) was derived with an enclosed area of about 19 mm^2 [50]. A similar vertical fountain gyroscope is currently under construction at SYRTE. The project aims for areas as large as 11 cm^2 and for resulting sensitivities in the range of 10^{-9} rad/(s$\sqrt{\text{Hz}}$).

1.1.3   The CASI experiment

In the framework of the CASI ("Cold Atom Sagnac Interferometer") project, a cold atom gyroscope consisting of two atom interferometers has been constructed. The project is motivated by the HYPER proposal [51], which aimed for the application of atomic gyroscopes for the measurement of the Lense-Thirring effect in a spaceborne device. Moreover, the compact design featuring an interferometer baseline of below 15 cm with an enclosed interferometer area of 19 mm^2 makes the device suitable for high resolution local rotation measurements for applications in geophysics.

The two interferometers are based on the interference of laser-cooled ^{87}Rb atoms on their free fall on flat parabolic trajectories using stimulated Raman transitions. As depicted in figure 1.2, these transitions are induced by phase stable laser fields that are applied in a counter-propagating configuration in three spatially separated interaction zones. The experiment has been presented in previous works [52, 53, 54, 55, 56]. Key to realizing the large area is the control of the relative pointing of the beam splitter light field in the three interaction zones. A technique for the relative pointing alignment is presented in [56, 57]. This led to the realization of the two atom interferometers with an enclosed area of 19 mm^2 each. The short term rotation sensitivity of $5.3 \cdot 10^{-7}$ rad/(s$\sqrt{\text{Hz}}$) was found to be limited by environmental perturbations, and by the noise of the interferometer signal detection.

In this work, the implementation of a rotation measurement based on alternating area orientation is presented. Such a technique was reported e.g. in [49]. In combination with an ellipse fit method, this allows to study the long term stability of the gyroscope signal. The relative wave front alignment coupled with mismatches in the overlap of the two interferometers is identified as main drift source.
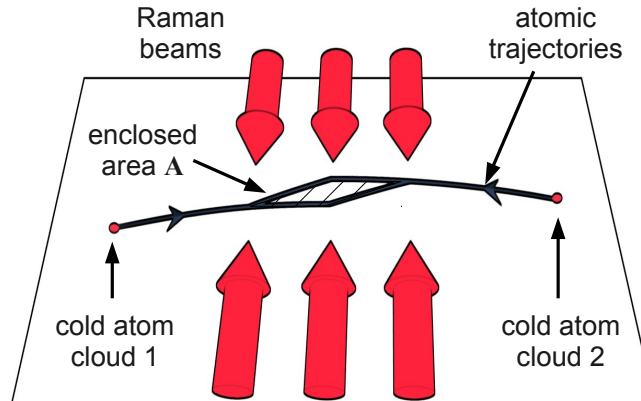
Figure 1.2: Cold Atom Sagnac Interferometer. The interferometer geometry is depicted with the laser fields used to drive the stimulated Raman transitions for atomic beam splitting. The cloud overlap is idealized in this representation.

We have employed a monitoring technique for tracking the cloud overlap in one dimension enabling an effective improvement of the rotation sensitivity of more than one order of magnitude after integration, which is presented in chapter 3.

1.2   Short range forces and the FORCA-G experiment

In this section, the field of application of the FORCA-G experiment is introduced before giving some examples for short range force measurement experiments. A brief introduction to the FORCA-G experiment is given thereafter.

1.2.1   Atom-surface interactions

The scope of the FORCA-G experiment is the measurement of forces between an atom and a macroscopic surface in ranges of atom-surface separations below the millimeter, which are difficult to access with measurement techniques based on macroscopic bodies. In this regime, deviations from the Newtonian gravitational potential are predicted by theories that aim for a unification of the standard model and gravitation [58]. These deviations are generally parametrized by a Yukawa type potential of the form

$$U \;=\; U_N \left(1 + \alpha \mathrm{e}^{r/\lambda}\right) \tag{1.3}$$

with U_N the Newtonian gravitational potential, α the strength and λ the typical range of the deviation. Measurements in the range of tens of μm down to several
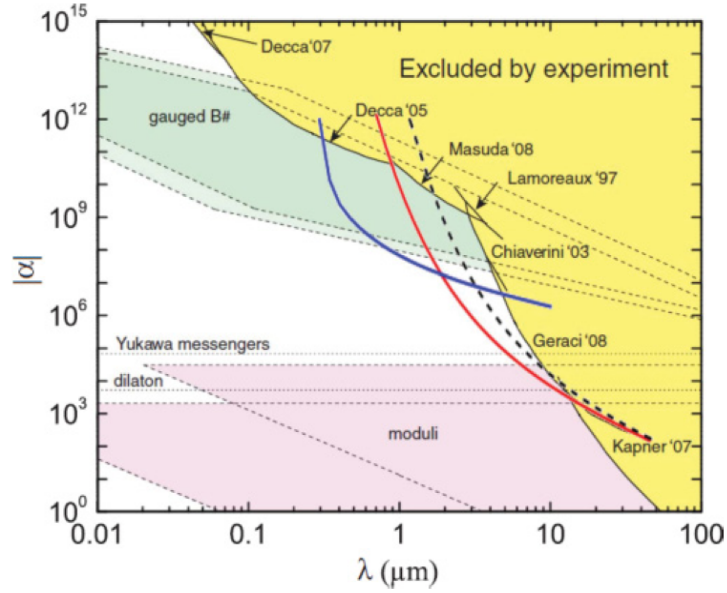
Figure 1.3: Deviations from Newtonian gravity (graph taken from [59]). The graph depicts the parametrization of possible deviations from the Newtonian gravitational potential in the Yukawa type parametrization as a α-λ-plane. The yellow area represents the region excluded by experiments. In [59], the exclusions of deviations are predicted for our experiment for particle-surface separations of about 1 μm *(blue line)*, 10 μm *(red line)*, and almost 20 μm *(black dashed line)*.

hundreds of nm may give new insights on the predicted models by either measuring a deviation from the Newtonian potential or setting new limits on such deviations and thereby excluding regions on the α-λ-plane of the Yukawa parametrization as depicted in figure 1.3.

The challenge in the detection of such deviations is the domination of electrodynamic forces in this regime which, up to now, have not been measured with an uncertainty of better than a few percent. These forces arise from the dipole-dipole interaction of an atom close to a conducting surface with its image charge. At very small distances, this interaction is instantaneous and results in the so-called Van-der-Waals-London (VdWL) force. In slightly larger distances, the so-called Casimir-Polder (CP) effect appears [60], which is the retardation effect of this dipole-dipole interaction. Assuming a perfectly conducting surface, the force is given by [61]

$$F_{CP} = \frac{3\hbar c \alpha_0}{2\pi d^5},$$
(1.4)

where α_0 is the static polarizability of the atom and d is the atom-surface distance. The transition between these two regimes can be understood via the Heisenberg

uncertainty relation $\Delta E \Delta t \leq \hbar/2$: The size of the Van-der-Waals-London potential ΔE_{VdWL} sets a limit onto the travel time of the electromagnetic interaction photon between the atom and the surface. Inserting an interaction photon energy $\hbar \omega_{DD}$ and $\Delta d = c\Delta t$ (d being the atom-surface separation distance) into the uncertainty relation formula yields a maximum distance in the range of the interaction wavelength. For the ^{87}Rb atom in the vicinity of a perfectly conducting surface, the transition from the VdWL force scaling with d^{-4} to the CP regime scaling with d^{-5} is found around 100 nm [62]. Furthermore, at distances of one order of magnitude larger, thermal effects result in a third regime, in which the force scales as in the VdWL case with d^{-4}.

1.2.2   Short range force measurements

The direct measurement of VdWL and CP forces between neutral atoms and macroscopic surfaces has been carried out so far in different ways. For example, it is possible to determine the CP potential by reflecting matter-waves on a macroscopic surface. This so-called **quantum reflection** is demonstrated in [63] for metastable neon atoms reflected on a silicon and a BK7 glass surface in grazing incidence and in [64] for ultra-cold ^{23}Na atoms in normal incidence on a silicon surface showing qualitative agreements with the predicted force as a function of the atom-surface separation. The possibility of a quantitative measurement the Casimir-Polder force is reported in [65] for quantum reflection of ^{3}He atoms on the surface of a gold single-crystal resulting in resolutions for Casimir-Polder forces of a few percent.

Quantitative measurements of the Van-der-Waals interaction were realized with a technique involving the reflection of atoms on a short range potential that is shaped by the use of an **evanescent wave**. In [66], the reflection of ^{85}Rb atoms that are dropped from a magneto-optical trap onto a mirror surface is investigated. The evanescent wave that allows to add a repulsive potential to the attractive CP potential, is created by total reflection of a laser beam inside the mirror. This experiment showed an uncertainty of 30 %, a clear agreement with the exact quantum electrodynamic (QED) or the electrostatic calculation could not be determined. A similar set-up recently led to the measurement of Casimir-Polder forces in distances of 160 to 230 nm [67]. An ultra-cold ^{87}Rb ensemble was accelerated in a combined magnetic-dipole trap and reflected on an evanescent wave on a glass prism. The results showed best agreement with the full QED calculation in the transition regime between the CP and VdWL regimes.

A slightly different approach was presented in [68]. A Bose-Einstein condensate (BEC) of ^{87}Rb is trapped in a magnetic trap near a dielectric surface. By tracking the **center of mass motion** of the **BEC** oscillating in the magnetic trap, it is possible to measure CP forces in atom-surface separation distances of 6 to 12 μm with an uncertainty of down to 10 %. The impact of thermal black body radiation

in this regime was already mentioned in [68] and later demonstrated in [69].

The first demonstration of the measurement of atom-surface interactions via the phase shift in an atom interferometer is presented in [70] for distances of down to 10 nm. One arm of a Mach-Zehnder type **interferometer** based on diffraction of Na atoms on material gratings is guided through a narrow dielectric cavity. The measurement of short range forces in distances of several μm is approached, among others, by trapped atom interferometry in a vertical unidimensional **optical dipole lattice**. The acceleration of this lattice given by the local gravitational acceleration induces so-called Bloch oscillations predicted by quantum mechanics (see chapter 2). The frequency of this process, the so-called Bloch frequency, scales with the acceleration. Measuring this frequency therefore allows for a local acceleration measurement and, if carried out in the vicinity of a macroscopic surface, for a measurement of perturbations of the acceleration induced by short-range forces. The acceleration measurement far from a surface has been realized in different ways. In [37] this is done via the determination of the atomic momentum after release from the potential, which consists in a direct measurement of the Bloch oscillation frequency by releasing the atoms after different holding times. A different approach is presented in [71], where the lattice depth is modulated and the spread of the atomic cloud is measured in-situ. This enabled a measurement of the local gravitational acceleration with a resolution of parts in 10^{-7} within a measurement time of about 1 h. In all cases, the 1D-lattice is created via the retro-reflection of a laser beam. The realization of the acceleration measurement close to the surface of the mirror used for retro-reflection results in a good control for the mapping of short range forces in multiples of the spatial lattice periodicity.

1.2.3 The FORCA-G experiment

Within the FORCA-G project a measurement of short range forces will be realized based on Raman atom interferometry. Laser-cooled ^{87}Rb atoms are trapped in the anti-nodes of a vertical dipole lattice with a periodicity of $\lambda_l/2 = 266$ nm. This gives access to measurements far from the mirror surface, in the regime of a few μm and even below the μm. The target precision of CP measurements in the range of a few μm is below the percent. This would allow for exclusions of non-Newtonian forces in the α-λ-plane as depicted in figure 1.3.

The measurement principle is an atom interferometer measurement on an atomic spatial superposition of two different lattice sites as depicted in figure 1.4. This superposition is created by coherently inducing tunneling between lattice sites using stimulated Raman transitions. After a certain evolution time, the two lattice sites can be coupled again resulting in an atomic interference. The phase of this trapped atom interferometer then depends on the potential difference between the two lattice sites. In the realization far from the mirror surface, the potential gradient is given by the gravitational acceleration. In the vicinity of the mirror surface,
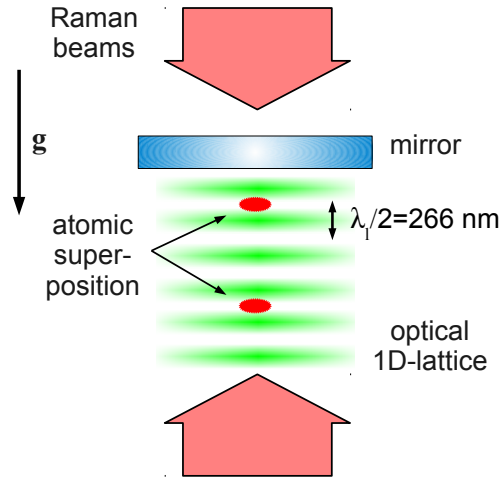
Figure 1.4: FORCA-G measurement principle. The idealized measurement principle consists in the creation of a superposition of an atomic wave packet in two lattice sites that is created and recombined using stimulated Raman transitions. The measurement in the vicinity of the lattice mirror surface allows to measure short range forces with high spatial resolution and good control of the atom-surface separation distance.

the short range forces are measured as a perturbation of the latter.

Subject of this work is the demonstration of the process of Raman induced tunneling in our vertical 1D-lattice in a proof-of-principle experiment. The interferometer measurements that are realized far from the mirror surface allow to study the short and long term stability of the acceleration measurement leading to an estimation of the interferometer resolution for short range force measurements.

The Raman laser induced tunneling process far from the mirror surface was first demonstrated in [72] and described in more detail in [73]. Spectroscopic properties of the tunneling process were then studied in [74] and the realized atom interferometer measurements were presented in [75]. The experimental studies presented in this work were mostly obtained during the year of my research stay within the framework of the jointly supervised PhD program. A detailed description of the interferometer measurements realized after my stay are presented in another dissertation [76].

1.3 Outline

This dissertation is organized as follows. First, the process of momentum state and Wannier-Stark state coupling using stimulated Raman transitions is introduced in **chapter 2**. The description is then used to evaluate the phase shifts in Raman interferometers based on free-falling and trapped Rubidium atoms. This chapter

also comprises the description of the sensitivity function formalism for the analysis of the noise processes of the atom interferometer measurements. In **chapter 3** the CASI gyroscope experiment is presented. After a short introduction to the rotation measurement method using the two interferometers, and to the impact of the alignment of the spatially separated Raman light fields, the experimental set-up and the measurement procedure are described. A subsequent analysis of the drift sources allows to identify the wave front impact as the dominant effect and to demonstrate an improvement of the long term stability by the use of a post-correction scheme. **Chapter 4** presents the FORCA-G experiment. The Introduction to the local acceleration measurement via the determination of the Bloch frequency is followed by a description of the experimental realization and measurement cycle. Next, the tunneling process and the resulting Wannier-Stark spectroscopy is presented before discussing the studies of the influences of differential light shifts induced by the Raman and trapping light fields as well as the impact of vibrations of the mechanical structure of the optical set-up of the apparatus. These studies motivate technical modifications that allow for an improved measurement stability, which is presented thereafter. For future measurements close to the mirror surface, the atoms will be prepared in one section of the vacuum chamber and transferred to the interferometer measurement section. This will be realized using a coherent transport mechanism based on a strongly accelerated optical lattice. The principle, set-up, and first realization of this transport mechanism in our experiment are presented in the end of the chapter. **Chapter 5** gives a short outlook for the two experiments.

Theoretical tools for atom interferometry

In this chapter, mathematical tools are introduced which enable the theoretical treatment of the coherent processes employed in our atom interferometers based on free-falling and trapped atoms. In both cases, the manipulation of atomic wave packets is performed using stimulated Raman transitions induced by two counter-propagating light fields. We introduce a model of stimulated Raman transitions based on a simple three-level system. This system can be under some conditions approximated by a two-level atom interacting with an effective laser field. Extending this model to external degrees of freedom allows to describe the interferometer states and their coupling for both, atoms in free fall and atoms trapped in a vertical lattice. This results in a description of the time evolution of the states which enables us to calculate the interferometer phase shift in the different interferometer sequences.

In addition, the sensitivity function formalism is introduced, which allows not only to calculate the interferometer phase shifts, but also to evaluate the influence of noise sources. This is followed by the introduction of the important features of the used ^{87}Rb atom involving the dominant frequency shifts of the internal atomic state transition. In the end, the interferometer signal is introduced and the expected interferometer phase shifts are discussed for both experiments.

2.1 Beam splitting with stimulated Raman transitions

Raman scattering describes inelastic scattering of light by atoms. If an atom absorbs a photon with energy $\hbar\omega_1$, the internal energy changes by the same amount

given that the internal structure allows for this transition. The relaxation of the internal atomic state results in a re-emission of the photon by the atom. If now the atom relaxes to a state that has an energy difference with respect to the initial state of $\hbar\omega_{int}$, the photon energy changes to $\hbar\omega_2 = \hbar\omega_1 - \hbar\omega_{int}$ due to energy conservation[1]. If two light fields of frequencies ω_1 and ω_2 are applied to the atom at the same time, the atom can undergo a two-photon process, a so-called stimulated Raman transition. If the two-photon scattering is the dominant process, the system of atom and light can be approximated by a two-level system with an electromagnetic field with a frequency $\omega_1 - \omega_2$.

In the following, the time evolution of the two-level system is derived. Then, the stimulated Raman process is introduced enabling the extension of the two-level time evolution to the case of momentum and Wannier-Stark state coupling in the subsequent sections.

2.1.1 Two-level system

Let us consider an atom with two internal states, a ground state $|g\rangle$ and long lived excited state $|e\rangle$, that have an energy difference $E_{eg} = \hbar\omega_{eg}$. The quantum state of this two-level system reads

$$|\Psi(t)\rangle = a_g(t)|g\rangle + a_e(t)|e\rangle, \tag{2.1}$$

which is normalized with $|\langle\Psi(t)|\Psi(t)\rangle|^2 = 1$. The probability amplitudes to find the atom in the ground and excited state, $a_g(t)$ and $a_e(t)$, respectively, can undergo so-called Rabi oscillations when an electromagnetic field with the angular frequency $\omega_{eg} = E_{eg}/\hbar$ is present. The Rabi formula describing this process was derived many times, for example in [77]. The derivation of the two-level system is briefly outlined here.

Finding the time evolution of this system consists in solving the Schrödinger equation

$$i\hbar|\dot{\Psi}(t)\rangle = \hat{H}|\Psi(t)\rangle \tag{2.2}$$

for the arbitrary quantum state $|\Psi(t)\rangle$. The Hamiltonian $\hat{H}$ of the system takes into account the internal energies $\hbar\omega_g$ and $\hbar\omega_e$, and the coupling given by the electro-magnetic field $\mathbf{E} = \mathbf{E}_0 \cos(\omega t + \phi)$ and the atomic dipole moment $\mathbf{d}$

$$\hat{H} = \hbar\omega_e|e\rangle\langle e| + \hbar\omega_g|g\rangle\langle g| - \mathbf{d}\cdot\mathbf{E}. \tag{2.3}$$

Equating coefficients results in a pair of coupled differential equations. The choice of

$$a_e(t) = c_e(t)\mathrm{e}^{-i\omega_e t} \tag{2.4}$$

$$a_g(t) = c_g(t)\mathrm{e}^{-i\omega_g t} \tag{2.5}$$

---

[1]We will neglect the photon recoil for now, which allows us to neglect momentum conservation at this point.

and the subsequent application of the rotating wave approximation allows to only consider slowly varying terms. We then find a pair of coupled differential equations

$$i\dot{c}_e(t) = \frac{\Omega_{eg}}{2}e^{-i(\delta t+\phi)}c_g(t) \tag{2.6}$$

$$i\dot{c}_g(t) = \frac{\Omega_{eg}^*}{2}e^{i(\delta t+\phi)}c_e(t), \tag{2.7}$$

in which $\delta = \omega - \omega_{eg}$ is the detuning of the electro-magnetic field to the atomic resonance. In this, the Rabi frequency

$$\Omega_{eg} = -\frac{\langle e|\mathbf{d}\cdot\mathbf{E}_0|g\rangle}{\hbar} \tag{2.8}$$

is the interaction matrix element and represents the coupling strength. The system can be represented in a spin-1/2 representation noting

$$|\Psi'(t)\rangle = \begin{pmatrix} c_e(t) \\ c_g(t) \end{pmatrix}. \tag{2.9}$$

Using (2.6) and (2.7), the time dependent Hamiltonian can then be written as

$$\hat{H} = \frac{\hbar}{2}\begin{pmatrix} 0 & \Omega_{eg}e^{-i(\delta t+\phi)} \\ \Omega_{eg}^*e^{i(\delta t+\phi)} & 0 \end{pmatrix}. \tag{2.10}$$

A further transformation into a frame rotating with the detuning δ results in a stationary Hamiltonian

$$\hat{H}_r = \frac{\hbar}{2}\begin{pmatrix} -\delta & \Omega_{eg}e^{-i\phi} \\ \Omega_{eg}^*e^{i\phi} & \delta \end{pmatrix}. \tag{2.11}$$

The time evolution of $c_e(t)$ and $c_g(t)$ is then derived by first finding the eigenstates of (2.11) and then projecting $|\Psi'(t)\rangle$ onto the latter. Transforming back to the non-rotating frame the time evolution is given by

$$\begin{pmatrix} a_e(t_0+\tau) \\ a_g(t_0+\tau) \end{pmatrix} = M(t_0,\tau,\Omega_{eg},\delta,\phi)\cdot\begin{pmatrix} a_e(t_0) \\ a_g(t_0) \end{pmatrix} \tag{2.12}$$

with the matrix

$$M(t_0,\tau,\Omega_{eg},\delta,\phi) =$$
$$\begin{pmatrix} e^{-i\alpha_{11}}\left[\cos\left(\frac{\Omega_r\tau}{2}\right)+i\frac{\delta}{\Omega_r}\sin\left(\frac{\Omega_r\tau}{2}\right)\right] & -ie^{-i\alpha_{12}}\frac{\Omega_{eg}}{\Omega_r}\sin\left(\frac{\Omega_r\tau}{2}\right) \\ -ie^{i\alpha_{21}}\frac{\Omega_{eg}}{\Omega_r}\sin\left(\frac{\Omega_r\tau}{2}\right) & e^{i\alpha_{22}}\left[\cos\left(\frac{\Omega_r\tau}{2}\right)-i\frac{\delta}{\Omega_r}\sin\left(\frac{\Omega_r\tau}{2}\right)\right] \end{pmatrix} \tag{2.13}$$

and the phases α_{ij}

$$
\begin{aligned}
\alpha_{11} &= (\delta + 2\omega_e)\tau/2 \\
\alpha_{12} &= (\delta + 2\omega_e)\tau/2 + (\delta + \omega_e - \omega_g)t_0 + \phi \\
\alpha_{21} &= (\delta - 2\omega_g)\tau/2 + (\delta + \omega_e - \omega_g)t_0 + \phi \\
\alpha_{22} &= (\delta - 2\omega_g)\tau/2.
\end{aligned}
\tag{2.14}
$$

Here, the generalized Rabi frequency for a small detuning is given by $\Omega_r = \sqrt{\Omega_{eg}^2 + \delta^2}$. The quantum state vector is represented in the spin notation

$$
|\Psi(t)\rangle = \begin{pmatrix} a_e(t) \\ a_g(t) \end{pmatrix}.
\tag{2.15}
$$

We can now determine the time evolution for an arbitrary initial state, Rabi frequency and detuning using (2.13). In the following, we will consider a system that is prepared in the ground state, where $a_g(t_0) = 1$ and $a_e(t_0) = 0$. The transition probability of the system to the excited state is then found by the projection of the final quantum state onto the excited state as

$$
\begin{aligned}
P_e(t) &= |\langle e|\Psi(t)\rangle|^2 \tag{2.16} \\
&= |a_e(t)|^2. \tag{2.17}
\end{aligned}
$$

For a finite pulse of duration τ, we find the well known Rabi oscillations in the formula

$$
P_e(\tau) = \frac{1}{2}\left(\frac{\Omega_{eg}}{\Omega_r}\right)^2 [1 - \cos(\Omega_r\tau)].
\tag{2.18}
$$

The transition probability is shown in figure 2.1 for different detuning values. While the Rabi oscillations show maximum amplitude for vanishing detuning, they are faster and show less amplitude for a finite detuning. Vice versa, for a fixed length of a square shaped pulse $\tau_\pi = \pi/\Omega_{eg}$, the transition probability can be rewritten as

$$
P_e(\delta) = \frac{\pi^2}{4}\operatorname{sinc}^2\left(\frac{\pi}{2}\sqrt{1 + \frac{\delta^2}{\Omega_{eg}^2}}\right).
\tag{2.19}
$$

This results in the typical spectrum of a square pulse as depicted in figure 2.1. The spectral full-width-half-maximum (FWHM) of such a Rabi pulse is here found to be

$$
\delta_{FWHM} \approx 1.6\pi/\tau_\pi.
\tag{2.20}
$$

Using the matrix (2.12), the time evolution can be studied not only for finite pulses, but also during a free evolution between subsequent pulses, where no coupling is
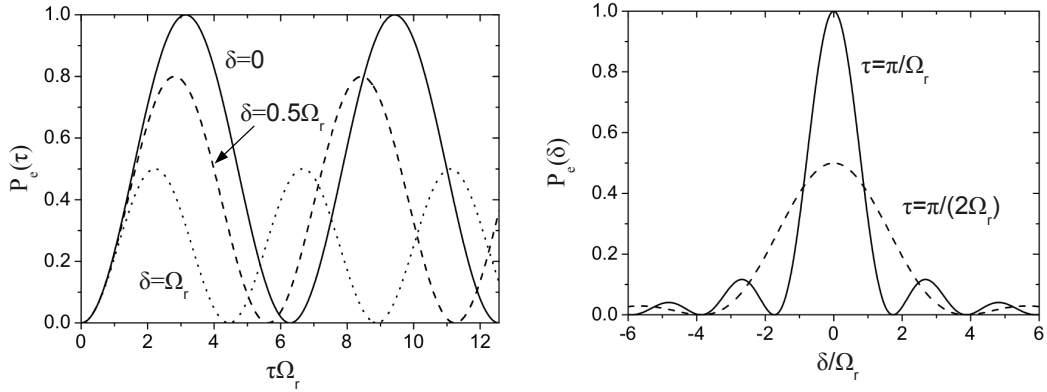
Figure 2.1: Rabi oscillations. The time evolution of the two-level system is given by Rabi oscillations between the two states with an efficiency depending on the detuning δ *(left)*. Scanning the detuning allows to find the resonance frequency, which is found to maximize P_e for the adequate choice of $\tau_\pi = \pi/\Omega_{eg}$ *(right)*.

present. Choosing the appropriate pulse duration, this results in the so-called $\pi/2$- and π-pulses that are represented by matrices

$$
\begin{align}
M_{\pi/2} &= M(t_0, \pi/(2\Omega_{eg}), \Omega_{eg}, \delta, \phi) \tag{2.21}\\
M_\pi &= M(t_0, \pi/\Omega_{eg}, \Omega_{eg}, \delta, \phi). \tag{2.22}
\end{align}
$$

The free evolution during a time T is then found by choosing zero coupling as

$$
M_T = M(t_0, T, 0, \delta, \phi). \tag{2.23}
$$

Multiplying such matrices parametrizes an arbitrary pulse sequence and, if the initial state is known, calculates the system's output state.

2.1.2 Coherent coupling with stimulated Raman transitions

The two-level system can be used to describe the time evolution in the stimulated Raman transition. For this purpose, we will consider a system of three internal atomic states and two electromagnetic fields. The two light fields have a large common detuning Δ with respect to the single-photon resonances. In addition to that, the difference of the two light field frequencies has to be resonant to the difference of two states. Thus, the two-photon transition is dominant and the system can be approximated by a two-level system with an effective electromagnetic field. The level scheme in figure 2.2 illustrates this situation. The intermediate state $|i\rangle$ is not populated, while Rabi-oscillations can be driven between the states $|g\rangle$ and $|e\rangle$. This can be shown by introducing the Hamiltonian that also incorporates
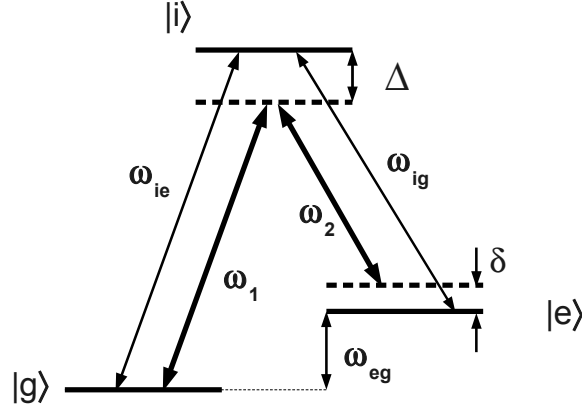
Figure 2.2: Stimulated Raman transition. The two electro-magnetic fields with angular frequencies ω_1 and ω_2 couple the states $|g\rangle$ and $|e\rangle$, if the detuning Δ is large against the effective coupling strength Ω_{eff} and the Raman detuning δ.

the intermediate state $|i\rangle$ and its energy as well as an electric field consisting of two frequencies ω_1 and ω_2. If the global detuning Δ is large against the effective coupling, which is given by the effective Rabi frequency

$$\Omega_{\text{eff}} \;=\; \frac{\Omega_e^* \Omega_g}{2\Delta}, \tag{2.24}$$

an adiabatic elimination of the intermediate state is possible. This allows to neglect populations in this state. Here, Ω_e and Ω_g are the coupling strength of the ground and excited state to the intermediate state given by (2.8). Furthermore, each of the light fields induces an AC-Stark shift on the atomic ground and excited energy level, which read

$$\Omega_e^{AC} \;=\; \frac{|\Omega_e|^2}{4\Delta} \tag{2.25}$$

$$\Omega_g^{AC} \;=\; \frac{|\Omega_g|^2}{4\Delta}. \tag{2.26}$$

These shifts combine to a differential light shift of the two-photon process

$$\delta_{AC} \;=\; \Omega_e^{AC} - \Omega_g^{AC}. \tag{2.27}$$

The description introduced here will be extended to external degrees of freedom of the atom n the following two sections. This will lead to the calculation of the time evolution of momentum and Wannier-Stark states and allow for calculating the interferometer phase shifts in the respective Raman interferometer geometries.
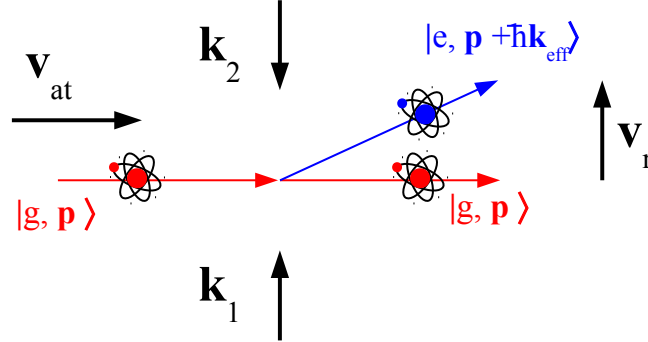
Figure 2.3: Momentum state coupling using stimulated Raman transitions. Counter-propagating Raman light fields allow for coupling of two well-defined momentum states that are distinguishable via the internal atomic state. After beam splitting, the partial wave packets separate with a velocity $\mathbf{v}_r = \hbar\mathbf{k}_{\text{eff}}/m_a$.

2.2 Coupling momentum states

During the two-photon stimulated Raman process, a momentum is transferred to the atom interacting with the light fields. The simple picture is, that the atom absorbs a photon which virtually populates the intermediate state. As the light field of the complementary frequency is also present, the atom is induced to emit a photon into the mode of this second field. A stimulated Raman transition takes place with a first momentum kick in the direction of the first light field propagation and a second momentum kick in the opposite direction of the second light field propagation, as the photon is emitted into its mode and momentum conservation demands that the atom recoils in the opposite direction. The momentum transfer is maximal for counter-propagating light fields. The effective momentum transferred to the atom is thus $\hbar\mathbf{k}_{\text{eff}}$ with $\mathbf{k}_{\text{eff}} = \mathbf{k}_1 - \mathbf{k}_2 \approx 2\mathbf{k}_1$, if $\omega_{eg} \ll \omega_{ie}, \omega_{ig}$. In this system, the excitation of the internal state then coincides with a momentum kick of $\hbar\mathbf{k}_{\text{eff}}$, while the inverted process is accompanied by a momentum kick of $-\hbar\mathbf{k}_{\text{eff}}$. The atom is found either in the ground state with its initial momentum $\mathbf{p}$ or in the excited state and carrying a momentum $\mathbf{p} + \hbar\mathbf{k}_{\text{eff}}$. This allows to write the eigenstates of the system as

$$
\begin{aligned}
|g\rangle \otimes |\mathbf{p}\rangle &= |g, \mathbf{p}\rangle & (2.28) \\
|e\rangle \otimes |\mathbf{p} + \hbar\mathbf{k}_{\text{eff}}\rangle &= |e, \mathbf{p} + \hbar\mathbf{k}_{\text{eff}}\rangle . & (2.29)
\end{aligned}
$$

The time evolution of this system can be studied by following the procedure given

in section 2.1 for the Hamiltonian

$$\hat{H} = \frac{\hat{\mathbf{p}}^2}{2m_a} + \hbar\omega_i \,|i\rangle\,\langle i| + \hbar\omega_e \,|e\rangle\,\langle e| + \hbar\omega_g \,|g\rangle\,\langle g| - \mathbf{d} \cdot \mathbf{E}(\mathbf{x}, t) \qquad (2.30)$$

with m_a being the atomic mass and $\mathbf{E}(\mathbf{x}, t)$ the bi-chromatic electric field vector representing the electromagnetic fields with angular frequencies ω_1 and ω_2 which reads

$$\mathbf{E}(\mathbf{x}, t) = \mathbf{E}_1 \cos(\mathbf{k}_1 \cdot \mathbf{x} - \omega_1 t + \phi_1) + \mathbf{E}_2 \cos(\mathbf{k}_2 \cdot \mathbf{x} - \omega_2 t + \phi_2). \qquad (2.31)$$

Similar to the two-level system, the time evolution is then derived with the matrix

$$\hat{H} = \frac{\hbar}{2} \begin{pmatrix} \Omega_e^{AC} & (\Omega_{\text{eff}}/2)e^{-i(\delta_{12}t+\phi_{\text{eff}})} \\ (\Omega_{\text{eff}}/2)e^{i(\delta_{12}t+\phi_{\text{eff}})} & \Omega_g^{AC} \end{pmatrix}, \qquad (2.32)$$

where $\phi_{\text{eff}} = \phi_1 - \phi_2$ is the differential phase of the two light fields and the effective detuning is given by

$$\delta_{12} = (\omega_1 - \omega_2) - \left(\omega_{eg} + \frac{\mathbf{p} \cdot \mathbf{k}_{\text{eff}}}{m_a} + \frac{\hbar|\mathbf{k}_{\text{eff}}|^2}{2m_a}\right). \qquad (2.33)$$

Here, the detuning incorporates the Doppler detuning $\delta_D = \mathbf{p} \cdot \mathbf{k}_{\text{eff}}/m_a$ and the necessary detuning of a recoil frequency $\omega_r = \hbar|\mathbf{k}_{\text{eff}}|^2/2m_a$. With this, we can derive a matrix similar to (2.13) leading to the calculation of the atomic state evolution during the beam splitter process and within the free evolution

$$M(t_0, \tau, \Omega_{\text{eff}}, \delta_{12}, \phi) = e^{-i(\Omega_g^{AC}+\Omega_e^{AC})\tau/2} \times$$
$$\begin{pmatrix} e^{-i\beta_{11}}\left[\cos\left(\frac{\Omega_r'\tau}{2}\right) + i\frac{\delta'}{\Omega_r'}\sin\left(\frac{\Omega_r'\tau}{2}\right)\right] & -ie^{-i\beta_{12}}\frac{\Omega_{\text{eff}}}{\Omega_r'}\sin\left(\frac{\Omega_r'\tau}{2}\right) \\ -ie^{i\beta_{21}}\frac{\Omega_{\text{eff}}}{\Omega_r'}\sin\left(\frac{\Omega_r'\tau}{2}\right) & e^{i\beta_{22}}\left[\cos\left(\frac{\Omega_r'\tau}{2}\right) - i\frac{\delta'}{\Omega_r'}\sin\left(\frac{\Omega_r'\tau}{2}\right)\right] \end{pmatrix} \quad (2.34)$$

with the phases β_{ij}

$$\begin{aligned} \beta_{11} &= (\delta_{12} + 2\omega_e)\tau/2 \\ \beta_{12} &= (\delta_{12} + 2\omega_e)\tau/2 + (\delta_{12} + \omega_e - \omega_g)t_0 + \phi_{\text{eff}} \\ \beta_{21} &= (\delta_{12} - 2\omega_g)\tau/2 + (\delta_{12} + \omega_e - \omega_g)t_0 + \phi_{\text{eff}} \\ \beta_{22} &= (\delta_{12} - 2\omega_g)\tau/2. \end{aligned} \qquad (2.35)$$

Here, the Rabi frequency is $\Omega_r' = \sqrt{\Omega_{\text{eff}}^2 + \delta'^2}$, and the effective detuning is $\delta' = \delta_{12} - \delta_{AC}$.

2.2.1 Mach-Zehnder like interferometer for inertial sensing

Coupling momentum states using stimulated Raman transition is employed to track rotations in our atom interferometer gyroscope presented in chapter 3 of this work. This is realized using a Mach-Zehnder like interferometer geometry. The atomic wave packet is split onto two paths using an initial $\pi/2$-pulse, reflected after a free propagation time T with a π-pulse, and superimposed after an additional time T with a second $\pi/2$-pulse. The propagation of an arbitrary interferometer input state can be evaluated using a multiplication of matrices which represent the Mach-Zehnder $\pi/2 - \pi - \pi/2$ sequence and the free propagation of duration T between the pulses. The respective pulse durations are chosen $\tau_{\pi/2} = \pi/(2\Omega_{\text{eff}})$ and $\tau_\pi = \pi/\Omega_{\text{eff}}$ for the beam splitters and the mirror, respectively. The time evolution matrices in these pulses will be denoted $M_{\pi/2}$ and M_π, respectively. The vanishing Rabi frequency $\Omega_{\text{eff}} = 0$ and $\tau = T$ results in the free propagation matrix M_T. For a resonant transition ($\delta' = 0$), the output is given by

$$\begin{pmatrix} a_e(2T + 4\tau_{\pi/2}) \\ a_g(2T + 4\tau_{\pi/2}) \end{pmatrix} = M_{\pi/2} \cdot M_T \cdot M_\pi \cdot M_T \cdot M_{\pi/2} \cdot \begin{pmatrix} a_e(0) \\ a_g(0) \end{pmatrix}. \qquad (2.36)$$

The interferometer measurement is realized for an input state with $a_e(0) = 0$ and $a_g(0) = 1$. The interferometer signal is then given by the transition probability from the internal ground state to the excited state $P_e = |a_e(2T + 4\tau_{\pi/2})|^2$, which is found to be

$$P_e = \tfrac{1}{2}\left[1 - \cos\left(\Phi\right)\right], \qquad (2.37)$$

where the interferometer phase Φ is determined by the total laser phase

$$\Phi = \Delta\phi = \phi_1 - 2\phi_2 + \phi_3. \qquad (2.38)$$

This total laser phase is composed by the respective laser phase values of the three beam splitting pulses

$$\begin{aligned} \phi_1 &= \phi_{\text{eff}}(0) \\ \phi_2 &= \phi_{\text{eff}}(T + \tau_{\pi/2}) \\ \phi_3 &= \phi_{\text{eff}}(2T + 3\tau_{\pi/2}). \end{aligned} \qquad (2.39)$$

The sensitivity of such an interferometer sequence to rotations is easily derived from the Sagnac formula via the area that is enclosed by the interferometer. This area depends on the atomic velocity in the direction perpendicular to the beam splitting process, and on the recoil velocity by which the two momentum states drift apart from each other over time. This is represented in figure 2.3. For a given atomic velocity $\mathbf{v}_{at}$ and pulse separation time T, the enclosed area is

$$\mathbf{A} = (\mathbf{v}_r \times \mathbf{v}_{at}) \cdot T^2. \qquad (2.40)$$
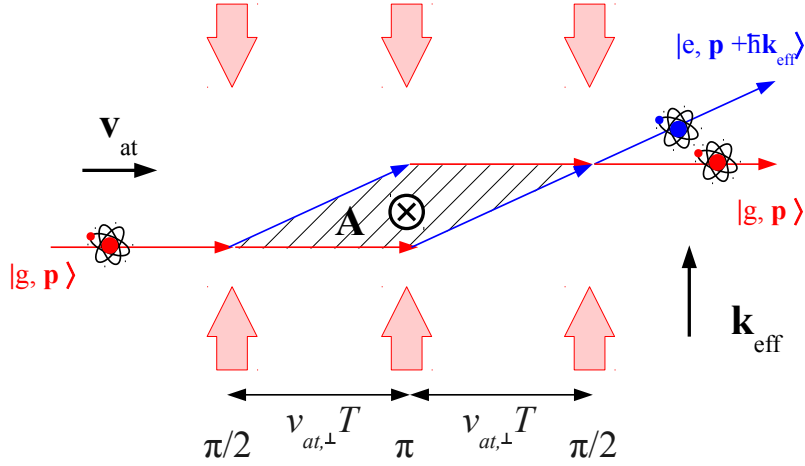
Figure 2.4: Mach-Zehnder like geometry. The application of counter-propagating Raman light fields in a $\pi/2 - \pi - \pi/2$ sequence allows to split, redirect and recombine the atomic wave packets. For a given atomic velocity $\mathbf{v}_{at}$ with non-vanishing components $v_{at,\perp}$ perpendicular to $\mathbf{k}_{\text{eff}}$, an area $\mathbf{A}$ is enclosed.

Inserting into (1.1) and replacing the recoil velocity $\mathbf{v}_r = \hbar \mathbf{k}_{\text{eff}}/m_a$ results in an expected phase shift of

$$\Phi_\Omega = 2(\mathbf{v}_{at} \times \mathbf{k}_{\text{eff}}) \cdot \mathbf{\Omega}\ T^2. \tag{2.41}$$

An exact calculation of the phase shift in the atom interferometer is provided by the $ABCD\xi$ formalism introduced by Ch. Bordé [78]. This formalism bases on the idea of the $ABCD$ matrices known from Gauss optics and provides the possibility to exactly calculate the propagation of a wave packet for systems that can be described by up to quadratic Hamiltonians. For instance, the propagation of a wave packet undergoing the beam splitter pulses and free propagation in between the pulses with external fields can be traced allowing for the interferometer phase calculation [79]. In [80], this type of calculation is presented for gravitational acceleration, gravity gradients and rotations being the external influences for a system in which the apparatus, namely the lasers and, most importantly, the Raman mirrors, are at rest. The total interferometer phase shift is here found to be

$$\Delta\Phi = \Phi_\Omega + \Phi_a + \Phi_{grad} + \phi_1 - 2\phi_2 + \phi_3 + ... \tag{2.42}$$

with inertial phase shift terms Φ_Ω arising from rotation as given in (2.41), and Φ_a due to accelerations given by

$$\Phi_a = \mathbf{a} \cdot \mathbf{k}_{\text{eff}} T^2. \tag{2.43}$$

It can be shown that (2.42) is sufficient for our considerations as for the parameters chosen in our configuration the rotation phase (2.41) induced by the Earth rotation is the leading term and higher order terms contribute to the total phase shift with a relative magnitude of of less than 10^{-6} [55]. Similarly, Φ_a will be considered to be the dominating term for the acceleration influence and impact of acceleration gradients will be neglected.

The consideration of non-inertial phase shifts in our gyroscope will be given in section 2.7.1 after the introduction of frequency shifts arising from the internal structure atomic structure of ^{87}Rb in section 2.5.

2.3 Coupling Wannier-Stark states

The situation considered in this section is an atom trapped in a vertical 1D-lattice. For an appropriate choice of the lattice depth the atom is localized and remains in the lattice for a long time compared with the duration of the experiment. The quasi eigenstates of this system consisting of a periodic potential with a superimposed uniform field are so-called Wannier-Stark states [81]. By using coherent inter-site coupling between these states, measurements of local forces can be performed using Wannier-Stark spectroscopy and interferometry.
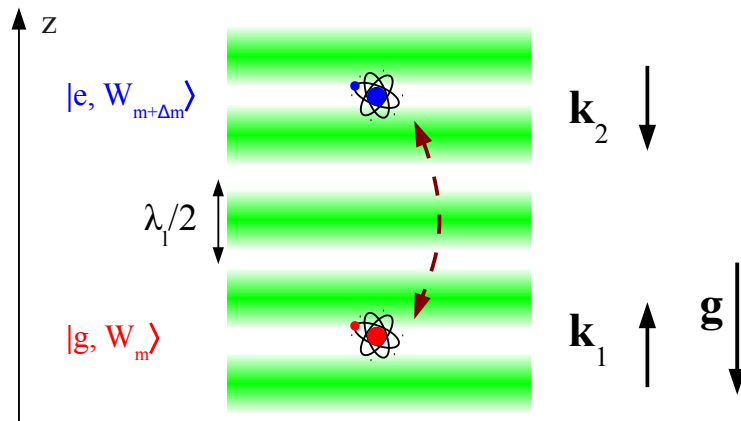
Figure 2.5: Wannier-Stark state coupling using stimulated Raman transitions. Counter-propagating Raman light fields induce coherent atomic tunneling between lattice sites. The spatial separation after beam splitting amounts to $\Delta z = \Delta m \cdot \lambda_l/2$ for a transfer from site m to site $m + \Delta m$. **g** indicates the direction of the gravitational acceleration, and $\mathbf{k}_1$ and $\mathbf{k}_2$ represent the Raman light field wave vectors.

2.3.1 Atoms in an optical 1D-lattice

For a proper description of the atom's dynamic inside the optical lattice, we consider here ^{87}Rb atoms as a three-level system ($|g\rangle$ and $|e\rangle$ are the two hyperfine ground states, and $|i\rangle$ is the $5^2P_{3/2}$ excited state, see also section 2.5) in the presence of two counter-propagating light fields. This system is described by a Hamiltonian similar to (2.30). As we want to use state labeling for the trapped interferometer measurement, we want the atoms to be trapped regardless the internal state. This is possible if the single-photon detuning of the lattice light fields is large with respect to ω_{eg}. For now, we will consider an atom initially in the ground state $|g\rangle$. The system then simplifies to a two-level atom with a dipole interaction, which reads [82]

$$\hat{H} = \frac{\hat{\mathbf{p}}^2}{2m_a} + \hbar\omega_i |i\rangle\langle i| + \hbar\omega_g |g\rangle\langle g| - \mathbf{d} \cdot \mathbf{E}(\mathbf{x}, t) \tag{2.44}$$

with

$$\mathbf{E}(\mathbf{x}, t) = \mathbf{E}_l \cos\left(\mathbf{k}_l\mathbf{x} - \omega_l t\right) + \mathbf{E}_l \cos\left(-\mathbf{k}_l\mathbf{x} - (\omega_l + \delta(t))t\right). \tag{2.45}$$

The two light fields feature a small relative detuning $\delta(t)$ and a common, global detuning with respect to the atomic resonance of $\Delta_l = \omega_l - \omega_{ig}$ with $\omega_{ig} = \omega_i - \omega_g$. The two light fields have the same wave vector $\mathbf{k}_l$ with opposed signs.

The system can be treated in a similar way as in the case of Raman transitions. For a sufficiently large detuning Δ_l, an adiabatic elimination of the excited state $|i\rangle$ allows us to rewrite the Hamiltonian to [83]

$$\hat{H} = \frac{\hat{\mathbf{p}}^2}{2m_a} + \frac{U_0}{2}\left[1 - \cos\left(2k_l\hat{z} - \delta(t)t\right)\right], \tag{2.46}$$

where $k_l = |\mathbf{k}_l|$ is the lattice wavenumber and $\hat{z}$ is the position operator along the lattice axis. As only off-resonant scattering was considered, the atom will stay in an internal ground state. However, the atom experiences a periodic dipole potential with a depth given via the AC-Stark shift of the ground state (2.26) by

$$U_0 = 4\Omega_g^{AC} = \frac{\hbar\Omega_l^2}{\Delta_l} \tag{2.47}$$

with the Rabi frequency $\Omega_l = \mathbf{d} \cdot \mathbf{E}_l/\hbar$. Hence, (2.46) represents an atom in an optical lattice given by its periodic potential with a periodicity of half the lattice laser wavelength $\lambda_l = 2\pi c/\omega_l$ and lattice depth U_0. The lattice depth is typically given in units of the recoil energy of a lattice laser photon $E_r = \hbar\omega_{r,l} = \hbar^2 k_l/2m_a$.

Such a consideration can also be made for atoms in the excited state $|e\rangle$ leading to a similar result. Indeed, for large detunings $\Delta_l \gg \omega_{eg}$ we can consider atoms in the periodic potential regardless of their internal state, which may be $|g\rangle$ or $|e\rangle$

or a superposition of both states. However, the two levels are in general shifted differently, which leads to a differential AC-Stark shift of the atomic transition frequency, which is discussed in section 2.5.1.

The Hamiltonian (2.46) is used to find a description of the atomic wave packet in an optical dipole lattice. Here, the relative detuning $\delta(t)$ can be interpreted as a Doppler shift, arising from the relative motion of the lattice lasers with respect to the atoms. We can therefore consider an accelerated lattice via a Doppler detuning increasing linearly with time, which reads $\delta(t) = k_l a t$. The Hamiltonian is then modified to

$$\hat{H} \;\; = \;\; \frac{\hat{\mathbf{p}}^2}{2m_a} + \frac{U_0}{2}\left[1 - \cos\left(2k_l\left(\hat{z} - \frac{1}{2}at^2\right)\right)\right]. \tag{2.48}$$

The system can then be transformed into the accelerated frame by applying a unitary transformation, which results in rewriting the operator to [82, 84]

$$\hat{H} \;\; = \;\; \frac{\hat{\mathbf{p}}^2}{2m_a} + \frac{U_0}{2}\left[1 - \cos\left(2k_l\hat{z}\right)\right] + m_a a\hat{z}. \tag{2.49}$$

This shows that the dynamics of an atom in an accelerated lattice is, in the reference frame of this lattice, the same as the one of an atom in a static lattice in the presence of an external force.

First, we will consider the dynamics of the atom in a non-accelerated lattice. The system simplifies to a particle moving in a periodic potential, which reads

$$\hat{H} \;\; = \;\; \frac{\hat{\mathbf{p}}^2}{2m_a} + \frac{U_0}{2}\left[1 - \cos\left(2k_l\hat{z}\right)\right]. \tag{2.50}$$

As this Hamiltonian is invariant under translations of z with multiples of half the lattice wavelength, the system can be studied using the Bloch theorem, which enables us to represent the eigenstates and eigenenergies of the system in a band structure [85]. In this representation, the energy of a particle in the periodic potential is given as a function of the particle's quasi momentum q. It is then completely described in the quasi momentum representation in the Brillouin zone reaching from $-\hbar k_l$ to $\hbar k_l$ as depicted in figure 2.6. The eigenstates of this system are given by Bloch states that feature two quantum numbers, the quasi momentum q and the band index n.

If now an acceleration is applied to the system, the quasi momentum is increased linearly in time. As the range of quasi momentum is limited to the first Brillouin zone, the linear increase results in a periodic phenomenon called Bloch oscillations [35, 86]. This process was first described for electrons in a crystal with an applied homogeneous electric field [87]. An atom described by a Bloch state experiences a cyclic quasi-momentum increase from $-\hbar k_l$ to $\hbar k_l$, while it remains in the same energy band (see figure 2.6). For a given acceleration a, these oscillations
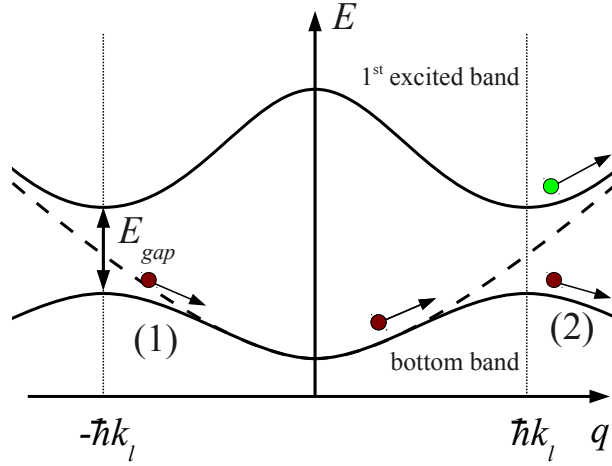
Figure 2.6: Bloch oscillations in Brillouin zone representation. The particle quasi momentum q increases under the influence of a linear acceleration. On the edge of the Brillouin zone ($q = \hbar k_l$), the atom either remains in the bottom band or, if the band gap energy E_{gap} is too small, the atom can undergo a non-adiabatic transition to the excited band. The *dashed line* depicts the free particle energy. At positions (1) and (2), the atom has identical momentum.

take place with the so-called Bloch period, which reads

$$\tau_B = \frac{2h}{m_a a \lambda_l}. \tag{2.51}$$

This process can be seen as a momentum transfer of the lattice to the atom of $2\hbar k_l$ in each of the cycles. A consequence of these repeated momentum kicks is that the atom remains in the lattice rest frame and thereby follows the movement of the accelerated lattice. However, if the band gap on the edge of the Brillouin zone is too small, the atom can undergo a non-adiabatic transition to an excited band. This process is known as Landau-Zener tunneling [88]. In practice, the atom is lost from the lattice if Landau-Zener tunneling occurs. A criterion for the atom to be trapped in the lattice is found by following considerations in [89, 90]. Here, two cases are considered, the weak binding regime in the limit of shallow lattices and the tight binding regime in the limit of deep lattices. In both cases, a probability is found for the atom still to be trapped in the lattice after a certain time as a function of the applied acceleration. The probability for the atom to be trapped after a given time T_l is found to be

$$P(T_l) = \left[1 - \exp\left(-\frac{a_c}{a} \right) \right]^{\frac{T_l}{\tau_B}}, \tag{2.52}$$

where a_c is given in the case of weak binding $(U_0 \ll 16E_r)$ by

$$a_c = \frac{a_0}{16} \left(\frac{U_0}{E_r}\right)^2, \tag{2.53}$$

and in the case of tight binding $(U_0 \gg 16E_r)$ by

$$a_c = \sqrt{2}a_0 \left(\frac{U_0}{E_r}\right)^{3/4} \tag{2.54}$$

with $a_0 = \hbar^2 k_l^3 / m_a^2$. For sufficiently deep lattices we find $P = 1$ even for long time scales, while losses increase for shallow lattices (small U_0) and large accelerations a.

In general, an atom in a lattice is not described by a Bloch state. However, the Bloch states can be used to construct (quasi-)stationary states describing the wave function of an atom localized in the periodic potential [91]. In a non-accelerated lattice, these states are degenerate in energy along the lattice axis. In the case of an accelerated lattice, the presence of the linear term breaks the translational invariance, and lifts the degeneracy, which leads to the description of the system by Wannier-Stark states derived from (2.49). A thorough description of the mathematical treatment of the Wannier-Stark states can be found in [39] and references therein [81, 92], as well as in [61].

The spatial spread of the wave function $\langle z|W_m\rangle$ of a Wannier-Stark state depends on the lattice depth. For very deep lattices, the atom is strongly localized in the m-th lattice site and the wave function is zero in the neighboring sites, while for shallower lattices the wave function spreads out over many lattice sites. In figure 2.7, the Wannier-Stark wave functions are depicted for two different lattice depth values.
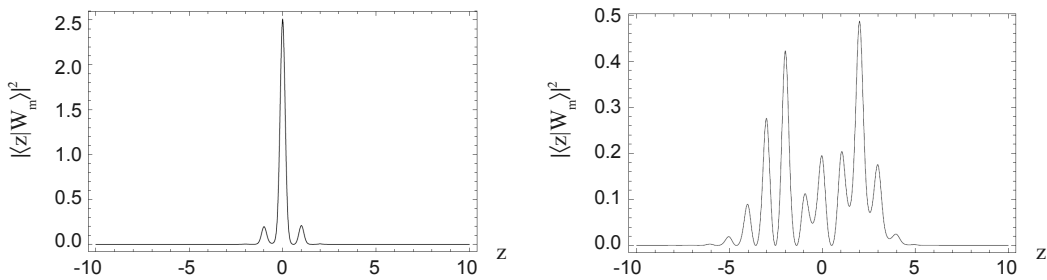

Figure 2.7: Spatial wave functions of Wannier-Stark states. In the case of $U_0 = 10E_r$ *(left)*, the atom is strongly localized, while the wave function is spread over many neighboring lattice sites in the case of a shallower lattice with $U_0 = 3E_r$ *(right)*. Here, z stands for the lattice site index with $z = 0$ representing the lattice site of index m.
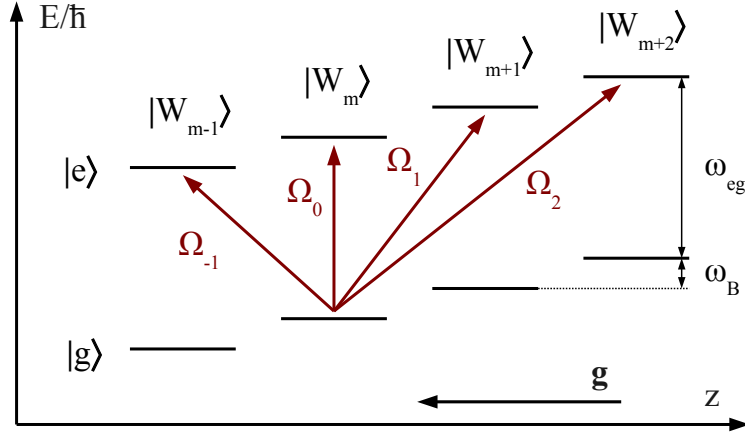
Figure 2.8: Wannier-Stark ladder. The localization of the atoms in the lattice, together with the gravitational acceleration, results in Wannier-Stark states, which, together with the internal pair of states, form a so-called Wannier-Stark ladder. The states of adjacent lattice sites are separated in energy by $\hbar\omega_B$.

2.3.2 Inter-site coupling

While stimulated Raman transition can be used to transfer a momentum kick to an atom in free space, they can also serve to couple Wannier-Stark states, which consists in inducing coherent tunneling of the atom between adjacent lattice sites. For an appropriate choice of lattice depth, Rabi frequency and of the relation of the two wavenumbers k_{eff} and k_l, two states can be coupled resulting in a basis of states

$$
\begin{aligned}
|g\rangle \otimes |W_m\rangle &= |g, W_m\rangle & (2.55) \\
|e\rangle \otimes |W_{m'}\rangle &= |e, W_{m'}\rangle . & (2.56)
\end{aligned}
$$

If only one band of the lattice is considered, this system is represented by a Wannier-Stark ladder of states (see figure 2.8) separated in energy by the difference in the gravitational potential energy between adjacent sites

$$
\Delta E = E_m - E_{m-1} = \frac{m_a g \lambda_l}{2}, \tag{2.57}
$$

where g is the gravitational acceleration. In the presence of the Raman light fields, the system is described by the Hamiltonian

$$
\hat{H} = \frac{\hat{\mathbf{p}}^2}{2m} + \hbar\omega_i |i\rangle\langle i| + \hbar\omega_e |e\rangle\langle e| + \hbar\omega_g |g\rangle\langle g| - \mathbf{d}\cdot\mathbf{E} + \hat{H}_{ext}, \tag{2.58}
$$

which consists of the free-space Raman Hamiltonian (2.30) and $\hat{H}_{ext}$ describing the trapping potential and gravitational acceleration similar to the second and third

term of (2.49). It is given by

$$\hat{H}_{ext} \quad = \quad \frac{U_0}{2}\left[1 - \cos\left(2k_l\hat{z}\right)\right] + m_a g\hat{z}. \tag{2.59}$$

Here, the lattice acceleration is given by the local gravitational acceleration $(a \equiv g)$. This system is described in the following for a single-photon transition by solving the Schrödinger equation for the Hamiltonian (2.59) and a state

$$|\Psi'(t)\rangle \quad = \quad \sum_m c_g^m(t)\mathrm{e}^{-i\omega_m t}\left|g, W_m\right\rangle + c_e^m(t)\mathrm{e}^{-i(\omega_{eg} + \omega_m)t}\left|e, W_m\right\rangle, \tag{2.60}$$

where $\hbar\omega_m$ is the quasi eigenenergy of a Wannier-Stark state $|W_m\rangle$. Equating coefficients leads to differential equations similar to (2.6) and (2.7) [39]

$$i\dot{c}_e^m(t) \quad = \quad \sum_{m'} \frac{\Omega_{eg}}{2}\mathrm{e}^{-i\delta_{m,m'}t}\langle W_m|\mathrm{e}^{ik_s\hat{z}}|W_{m'}\rangle c_g^{m'}(t) \tag{2.61}$$

$$i\dot{c}_g^m(t) \quad = \quad \sum_{m'} \frac{\Omega_{eg}^*}{2}\mathrm{e}^{i\delta_{m',m}t}\langle W_m|\mathrm{e}^{-ik_s\hat{z}}|W_{m'}\rangle c_e^{m'}(t), \tag{2.62}$$

in which Ω_{eg} is the free space Rabi frequency and $\delta_{m,m'} = \omega - \omega_{eg} + \omega_m - \omega_{m'}$ is the detuning of the coupling field to the transition $|g, W_m\rangle \to |e, W_{m'}\rangle$ on the Wannier-Stark ladder. Here, the fast oscillating terms of the internal states have again been factored out using

$$a_e^m(t) \quad = \quad c_e^m(t)\mathrm{e}^{-i\omega_e t} \tag{2.63}$$

$$a_g^m(t) \quad = \quad c_g^m(t)\mathrm{e}^{-i\omega_g t}. \tag{2.64}$$

The frequency difference of two Wannier-Stark states is found to be equal to multiples of the Bloch frequency $\Delta m\omega_B = \omega_m - \omega_m'$ with $\Delta m = m - m'$ and

$$\omega_B \quad = \quad \frac{2\pi}{\tau_B} \quad = \quad \frac{m_a g\lambda_l}{2\hbar}. \tag{2.65}$$

The effective coupling strength is given by the overlap of the Wannier-Stark wave function of the state $|W_{m'}\rangle$ and the state $|W_m\rangle$ shifted by the momentum transfer of the coupling laser with wave number k_s, which allows to write the corresponding Rabi frequency

$$\Omega_{\Delta m} \quad = \quad \Omega_{eg}\langle W_m|\mathrm{e}^{ik_s\hat{z}}|W_{m'}\rangle. \tag{2.66}$$

The set of differential equations (2.61) and (2.62) allows to consider different situations depending on the coupling strength. In the case of strong coupling with $\Omega_{m,m'} \gtrsim \omega_B$ for many sets of m and m', the atoms initially in state $|g, W_m\rangle$ couple to many states $|e, W_{m'}\rangle$. This situation is studied in detail in [93]. In the case

of weaker coupling with $\Omega_{m,m'} \ll \omega_B$, choosing the correct detuning $\delta_{m,m'}$ allows for addressing only transitions $\Delta m = m - m'$ for a fixed Δm. If we consider only linear potentials, the energy difference is independent of the initial lattice site number m and each pair of states $|g, W_m\rangle$ and $|e, W_{m'}\rangle$ can be described by a pair of differential equations independent of the initial state as

$$i\dot{c}_e^{m'}(t) = \frac{\Omega_{\Delta m}}{2}\mathrm{e}^{-i\delta_{m',m}t}c_g^m(t) \tag{2.67}$$

$$i\dot{c}_g^m(t) = \frac{\Omega_{\Delta m}^*}{2}\mathrm{e}^{i\delta_{m',m}t}c_e^{m'}(t). \tag{2.68}$$

While in the previous paragraph only single-photon transitions are considered, the same system is found for a Raman process using the procedure presented in sections 2.1 and 2.2. The time evolution for a quantum state

$$|\Psi'(t)\rangle = c_g^m(t)|g, W_m\rangle + c_e^{m'}(t)|e, W_{m'}\rangle \tag{2.69}$$

is described by the Hamiltonian

$$\hat{H} = \frac{\hbar}{2}\begin{pmatrix} \Omega_e^{AC} & (\Omega_{\Delta m}/2)\mathrm{e}^{-i(\delta_{\Delta m}t+\phi_{\mathrm{eff}})} \\ (\Omega_{\Delta m}^*/2)\mathrm{e}^{i(\delta_{\Delta m}t+\phi_{\mathrm{eff}})} & \Omega_g^{AC} \end{pmatrix}. \tag{2.70}$$

The inter-site Rabi frequency for the case of a Raman coupling is then given by

$$\Omega_{\Delta m} = \Omega_{\mathrm{eff}}\langle W_m|\mathrm{e}^{ik_{\mathrm{eff}}\hat{z}}|W_{m'}\rangle. \tag{2.71}$$

Similar to the case of momentum state coupling, the time evolution matrix for a state

$$|\Psi(t)\rangle = \begin{pmatrix} a_e^{m'}(t) \\ a_g^m(t) \end{pmatrix} \tag{2.72}$$

is found to be

$$M(t_0, \tau, \Omega_r'', \delta_{\Delta m}, \phi) = \mathrm{e}^{-i(\Omega_g^{AC}+\Omega_e^{AC})\tau/2} \times$$
$$\begin{pmatrix} \mathrm{e}^{-i\gamma_{11}}\left[\cos\left(\frac{\Omega_r''\tau}{2}\right) + i\frac{\delta''}{\Omega_r''}\sin\left(\frac{\Omega_r''\tau}{2}\right)\right] & -i\mathrm{e}^{-i\gamma_{12}}\frac{\Omega_{\Delta m}}{\Omega_r''}\sin\left(\frac{\Omega_r''\tau}{2}\right) \\ -i\mathrm{e}^{i\gamma_{21}}\frac{\Omega_{\Delta m}}{\Omega_r''}\sin\left(\frac{\Omega_r''\tau}{2}\right) & \mathrm{e}^{i\gamma_{22}}\left[\cos\left(\frac{\Omega_r''\tau}{2}\right) - i\frac{\delta''}{\Omega_r''}\sin\left(\frac{\Omega_r''\tau}{2}\right)\right] \end{pmatrix}, \tag{2.73}$$

where the phases γ_{ij} are given by

$$\begin{aligned} \gamma_{11} &= (\delta_{\Delta m} + 2\omega_e)\tau/2 \\ \gamma_{12} &= (\delta_{\Delta m} + 2\omega_e)\tau/2 + (\delta_{\Delta m} + \omega_e - \omega_g)t_0 + \phi_{\mathrm{eff}} \\ \gamma_{21} &= (\delta_{\Delta m} - 2\omega_g)\tau/2 + (\delta_{\Delta m} + \omega_e - \omega_g)t_0 + \phi_{\mathrm{eff}} \\ \gamma_{22} &= (\delta_{\Delta m} - 2\omega_g)\tau/2. \end{aligned} \tag{2.74}$$

Here, the detuning with respect to the resonant transition is

$$\delta_{\Delta m} = (\omega_1 - \omega_2) - (\omega_e - \omega_g + \Delta m\omega_B) \tag{2.75}$$

and the effective Rabi frequency is given by $\Omega_r'' = \sqrt{\Omega_{\Delta m}^2 + \delta''^2}$ with a total detuning $\delta'' = \delta_{\Delta m} - \delta_{AC}$.

Coupling strength

The inter-site coupling strength $\Omega_{\Delta m}$ from one lattice site m to another lattice site $m' = m + \Delta m$ depends on the overlap of the addressed Wannier-Stark states (2.71) which vanishes for strongly localized atoms. Hence, the choice of the lattice depth U_0 is a trade-off between the Wannier-Stark state lifetime and the spatial spread of the wave function allowing for an effective inter-site coupling. The lattice has to be sufficiently deep in order to allow for the atoms to be trapped for times that are long against the duration of an experiment, while it has to be sufficiently shallow in order to allow for a finite coupling strength between neighboring lattice sites. Besides the lattice depth, the relation of the coupling and lattice laser wavelength also has an influence on the the effective inter-site coupling strength [74]. The choice of the coupling and lattice laser wavelength and the corresponding coupling strengths are presented in the section 2.5.

2.3.3 Wannier-Stark spectroscopy and interferometry

The detuning $\delta_{\Delta m}$ given in (2.75) contains multiples of the Bloch frequency ω_B. Thus, varying the relative Raman light field detuning $\omega_1 - \omega_2$ allows to find a spectrum consisting of resonances that correspond to different orders Δm. The determination of the frequency spacing of these resonances results in the measurement of the Bloch frequency (2.65), which scales with the potential gradient given by the gravitational acceleration and possible deviations due to e.g. short range forces. For an accurate measurement, the ratio of the atomic mass m_a and the Planck constant $\hbar$, and the lattice laser wavelength λ_l need to be known with sufficiently high accuracy.

The application of this method to force measurements is studied in chapter 4 using Rabi spectroscopy and Ramsey interferometry. The Rabi interrogation consists in the application of a single pulse of duration $\tau_\pi = \pi/\Omega_{\Delta m}$, which results in coupling the states $|g, W_m\rangle$ and $|e, W_{m+\Delta m}\rangle$ as shown in figure 2.9. The spectroscopy measurement realized by measuring the internal state transition probability P_e to the excited state of an atom initially in the ground state. The transition probability is tracked for different laser detunings $\omega_1 - \omega_2$, which results in

$$P_e \;=\; \frac{\pi^2}{4}\, \mathrm{sinc}^2\left(\frac{\pi}{2}\sqrt{1 + \frac{(\delta_{\Delta m} - \delta_{AC})^2}{\Omega_{\Delta m}^2}}\right). \tag{2.76}$$

Splitting up the pulse into two and separating the resulting $\pi/2$-pulses by a time T results in the separated oscillatory field spectroscopy method introduced by Ramsey [94]. The multiplication of the corresponding matrices

$$\begin{pmatrix} a_e(T + 2\tau_{\pi/2}) \\ a_g(T + 2\tau_{\pi/2}) \end{pmatrix} \;=\; M_{\pi/2} \cdot M_T \cdot M_{\pi/2} \cdot \begin{pmatrix} a_e(0) \\ a_g(0) \end{pmatrix} \tag{2.77}$$
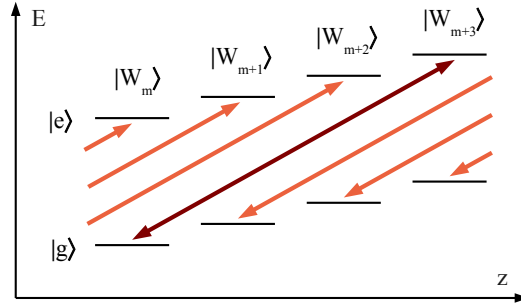
Figure 2.9: Coupling of Wannier-Stark states. Choosing the relative coupling laser frequency to $\omega_1 - \omega_2 = \omega_e - \omega_g + \Delta m \omega_B$ allows to couple each Wannier-Stark state to its Δm-th neighbor if the potential gradient is constant along the lattice site.
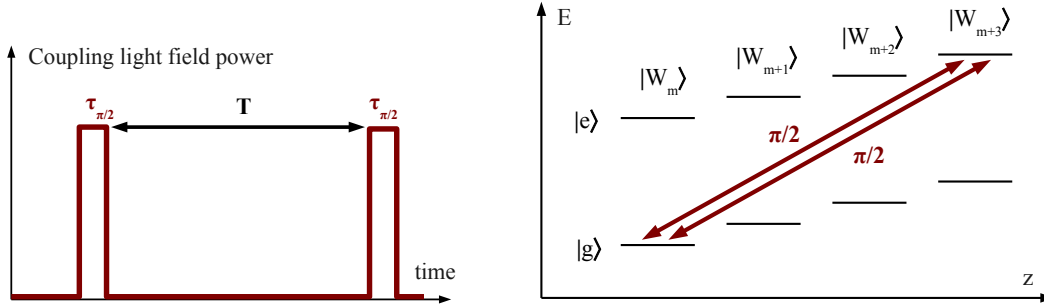

Figure 2.10: WSR interferometer. The WSR interferometer using Raman coupling of different lattice sites allows to create a superposition of Wannier-Stark states *(right)*. After an evolution time T, the Wannier-Stark states are coupled a second time *(left)*.

results in a fringe pattern with a periodicity inverse to the separation time

$$P_e = |a_e(T + 2\tau_{\pi/2})|^2 \approx \tfrac{1}{2}\left[1 - \cos\left(\delta_{\Delta m}T + \phi_1 - \phi_2\right)\right] \qquad (2.78)$$

for a given detuning $\delta_{\Delta m}$ and the effective phases ϕ_1 and ϕ_2 of the coupling light fields during the pulse application. This scheme realizes an interferometer on the two coupled Wannier-Stark ladder states. It will be referred to as Wannier-Stark Ramsey (WSR) interferometer in the following.

Given this formalism, the time evolution of the states can be calculated for an arbitrary pulse sequence. While this allows for a precise calculation of the expected interferometer output, it is more convenient in practice to use a simplified calculation based on the sensitivity function formalism presented in section 2.4. This allows to evaluate the phase in a Wannier-Stark interferometer consisting of an arbitrary pulse sequence. Furthermore, more than two states of the Wannier-Stark ladder can easily be included in the calculation. We will realize such calculations in section 2.7 for the WSR interferometer as well as for a modified WSR interferometer with internal state spin echo. Also, the use of the sensitivity function is well

adapted to the study of the response of the system to small fluctuations, which is introduced in the following.

2.4 Sensitivity function formalism

The sensitivity function formalism was initially used in the field of atomic time keeping, where it was employed for the study of noise source impacts on the frequency measurement of atomic transitions. Similarly, it can be applied to atom interferometry [95]. The formalism is based on the definition of the sensitivity function $g(t)$ via the response of the transition probability to a sudden phase jump $\delta\varphi$ in the interferometer. This is expressed as

$$g(t) = 2 \lim_{\delta\varphi\to 0} \frac{\delta P_e(\delta\varphi, t)}{\delta\varphi}, \qquad (2.79)$$

where δP_e is a variation in the transition probability induced by $\delta\varphi$. This definition is based on the assumption that the interferometer phase is generally determined in a mid-fringe measurement by choosing the total phase $\Phi = \pi/2$ [96]. The impact of a phase jump onto the interferometer phase is written in a similar way and reads

$$g(t) = \lim_{\delta\varphi\to 0} \frac{\delta\Phi(\delta\varphi, t)}{\delta\varphi}. \qquad (2.80)$$

For a given sensitivity function, the interferometer phase shift is then given by

$$\delta\Phi = \int_{-\infty}^{\infty} g(t)d\varphi(t)$$

$$= \int_{-\infty}^{\infty} g(t)\frac{d\varphi(t)}{dt}dt \qquad (2.81)$$

$$= \int_{-\infty}^{\infty} g(t)\delta(t)dt. \qquad (2.82)$$

This allows to calculate the phase shift in an interferometer arising from a time dependent frequency shift $\varphi(t)$ or a detuning $\delta(t)$, which will be employed in section 2.7 for the calculation of the expected interferometer phase shifts. Furthermore, this formalism enables the calculation of the impact of a given noise spectral density to the interferometer phase using a sequence specific transfer function, which is presented in section 2.4.1. Prior to this, the sensitivity functions for different interferometer schemes used in this work are introduced in the following. The notation is chosen similar to the one used in section 2.1, where δ is the detuning from resonance, Ω_{eff} is the Rabi frequency for zero detuning and $\Omega_r = \sqrt{\Omega_{\text{eff}}^2 + \delta^2}$ is the generalized Rabi frequency.

Rabi pulse

A Rabi sequence consists of a single interrogation pulse. The central peak frequency is determined by probing the transition probability on the half-maximum positions of the peak side slopes. For a square-shaped pulse, this corresponds to a detuning of $|\delta| \approx 0.8\Omega_{\text{eff}}$. The sensitivity function is given by [97]

$$
g(t) = \begin{cases} 0 & , t < -\frac{\tau_\pi}{2} \\ g_R(t) & , -\frac{\tau_\pi}{2} \leq t < \frac{\tau_\pi}{2} \\ 0 & , \frac{\tau_\pi}{2} \leq t, \end{cases} \tag{2.83}
$$

with

$$
g_R(t) = \frac{\delta/\Omega_{\text{eff}}}{(1 + (\delta/\Omega_{\text{eff}})^2)^{3/2}} \times
$$
$$
[\sin(\Omega_1(t))(1 - \cos(\Omega_2(t))) + \sin(\Omega_2(t))(1 - \cos(\Omega_1(t)))]. \tag{2.84}
$$

Here, the definitions for $\Omega_1(t)$ and $\Omega_2(t)$ are

$$
\Omega_1(t) = \pi\sqrt{1 + \delta^2/\Omega_{\text{eff}}^2} \cdot \left(\frac{1}{2} + \frac{t}{\tau_\pi}\right) \tag{2.85}
$$

$$
\Omega_2(t) = \pi\sqrt{1 + \delta^2/\Omega_{\text{eff}}^2} \cdot \left(\frac{1}{2} - \frac{t}{\tau_\pi}\right). \tag{2.86}
$$

This function is found to be well approximated by

$$
g(t) = \begin{cases} 0 & , t < -\frac{\tau_\pi}{2} \\ \cos\left(\pi\frac{t}{\tau_\pi}\right) & , -\frac{\tau_\pi}{2} \leq t < \frac{\tau_\pi}{2} \\ 0 & , \frac{\tau_\pi}{2} \leq t. \end{cases} \tag{2.87}
$$

Plots of both functions are depicted in figure 2.11 *(left)*.

Ramsey sequence

A Ramsey sequence is composed by two pulses of length $\tau_{\pi/2} = \tau_\pi/2$, which are separated by the Ramsey time T. The phase measurement is typically performed on the side slope of a Ramsey fringe by choosing $|\delta| = \pi/(2T)$. For $T \gg \tau_{\pi/2}$ the detuning can be considered to be small against the Rabi frequency ($|\delta| \ll \Omega_{\text{eff}}$). The sensitivity function is depicted in figure 2.11 *(right)* and is given by [97]
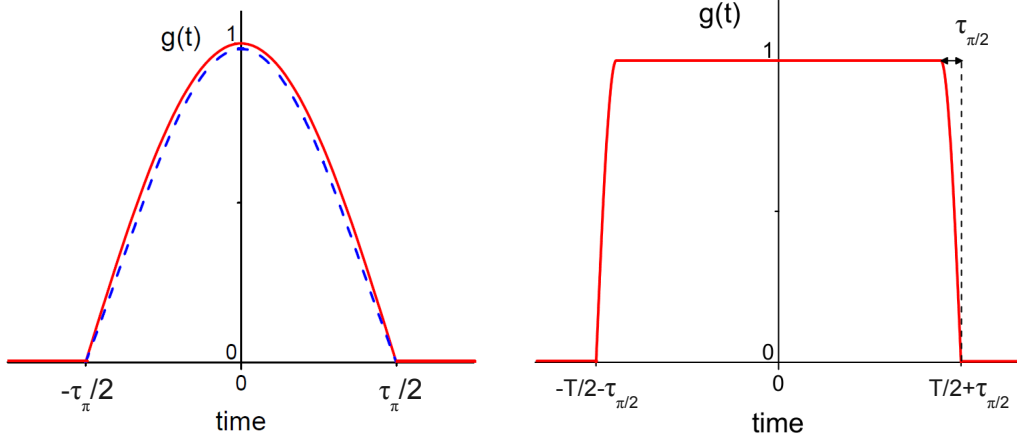
Figure 2.11: Rabi and Ramsey sequence sensitivity function. The sensitivity function is displayed in the case of a Rabi pulse *(left)* for the exact calculation (2.85) for $\delta = 0.8\Omega_{\text{eff}}$ *(dashed blue line)* and for the approximation (2.87) *(solid red line)*. The higher sensitivity of the Ramsey sequence is depicted for an interrogation on resonance *(right)*.

$$
g(t) \;=\; \begin{cases} 0 & ,t < -\frac{T}{2} - \tau_{\pi/2} \\ \cos\left(\pi \frac{t+T/2}{2\tau_{\pi/2}}\right) & ,-\frac{T}{2} - \tau_{\pi/2} \leq t < -\frac{T}{2} \\ 1 & ,-\frac{T}{2} \leq t < \frac{T}{2} \\ \cos\left(\pi \frac{t-T/2}{2\tau_{\pi/2}}\right) & ,\frac{T}{2} \leq t < \tau_{\pi/2} + \frac{T}{2} \\ 0 & ,\frac{T}{2} + \tau_{\pi/2} \leq t. \end{cases} \tag{2.88}
$$

Mach-Zehnder sequence

A Mach-Zehnder sequence consists of two subsequent Ramsey sequences, of which the central pulses are melt together to a π-pulse of duration τ_π. The sensitivity function is given by

$$
g(t) \;=\; \begin{cases} 0 & ,t < -T - \frac{\tau_\pi}{2} - \tau_{\pi/2} \\ \cos\left(\pi \frac{t+T+\tau_{\pi/2}+\tau_\pi/2}{2\tau_{\pi/2}}\right) & ,-T - \frac{\tau_\pi}{2} - \tau_{\pi/2} \leq t < -T - \frac{\tau_\pi}{2} \\ -1 & ,-\frac{T}{2} - \frac{\tau_\pi}{2} \leq t < -\frac{\tau_\pi}{2} \\ \sin\left(\pi t/\tau_\pi\right) & ,-\frac{\tau_\pi}{2} \leq t < \frac{\tau_\pi}{2} \\ 1 & ,\frac{\tau_\pi}{2} \leq t < T + \frac{\tau_\pi}{2} \\ \cos\left(\pi \frac{t-T-\tau_{\pi/2}}{2\tau_{\pi/2}}\right) & ,T + \frac{\tau_\pi}{2} \leq t < T + \frac{\tau_\pi}{2} + \tau_{\pi/2} \\ 0 & ,T + \frac{\tau_\pi}{2} + \tau_{\pi/2} \leq t. \end{cases} \tag{2.89}
$$

This function is antisymmetric with respect $t = 0$, which depicts the insensitivity to phase and frequency fluctuations that are symmetric with respect to $t = 0$ (see figure 2.12).
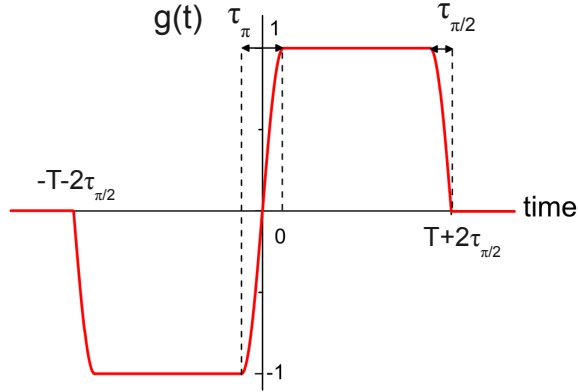

Figure 2.12: Sensitivity function for a Mach-Zehnder sequence. The Mach-Zehnder sequence corresponds to two subsequent Ramsey sequences, the first of the two being mirrored with respect to $g(t) = 0$. Hence, constant frequency shifts cancel in this sequence.

2.4.1 Interferometer noise estimation

The sensitivity function allows for the determination of frequency or phase shifts in the time domain. If these perturbations vary over time, the measured interferometer phase can fluctuate from one shot to another. In principle, this could be calculated using the sensitivity function repeated in time for weighting a perturbation that is given as a time series. An equivalent noise impact evaluation can be realized with the sensitivity function formalism in Fourier space.

Following [95], the interferometer noise can be given by the expected standard deviation from shot to shot based on a Fourier spectrum of a noise source. For uncorrelated noise, the expected interferometer uncertainty is linked to the power spectral density $S_\varphi(\omega)$ for fluctuations of the phase φ via

$$\sigma_\Phi^2 \;=\; \int_0^{+\infty} |H(\omega)|^2 S_\varphi(\omega) d\omega, \qquad (2.90)$$

where $|H(\omega)|$ is the interferometer transfer function. The latter is given by $|H(\omega)| = \omega|G(\omega)|$ with $|G(\omega)|$ being the Fourier transform of the sensitivity function

$$G(\omega) \;=\; \int_{-\infty}^{+\infty} \mathrm{e}^{-i\omega t} g(t) dt. \qquad (2.91)$$

As we consider atom interferometer measurements that are pulsed in time, the cycle rate f_c also has to be taken into account. This leads to a discrete sum

$$\sigma_\Phi^2(\tau) = \frac{1}{\tau} \sum_{n=1}^{\infty} |H(2\pi n f_c)|^2 S_\varphi(2\pi n f_c), \qquad (2.92)$$

where τ is the averaging time and $\tau \gg T_c = 1/f_c$ [95]. $\sigma_\Phi(\tau)$ is the calculated Allan standard deviation (see also appendix A) of the measured interferometer phase.

We can derive a similar expression for the expected uncertainty of a frequency measurement. For a Ramsey sequence, the relation of frequency and phase uncertainties is given by

$$\sigma_\Phi^2 = 4\pi^2 \left(T^2 + \frac{8T\tau_{\pi/2}}{2} + \frac{16\tau_{\pi/2}^2}{\pi^2} \right) \sigma_\nu^2. \qquad (2.93)$$

Presuming beam splitter pulse length that are small against the Ramsey time T, we can consider $\tau_{\pi/2} \to 0$, which results in a frequency uncertainty of

$$\sigma_\nu^2 = \frac{\sigma_\Phi^2}{4\pi^2 T^2}. \qquad (2.94)$$

Before deriving the interferometer phase shift for our two cases, free-falling and trapped interferometry, the ^{87}Rb atom will be described. We will present the internal interferometer states and introduce the most important frequency shifts on the transition between these states.

2.5 Application to the ^{87}Rb atom

The ^{87}Rb atom is an alkali atom and features a single valence electron. The atomic energy level structure results in spectroscopic properties which allows for effective magneto-optical trapping. Furthermore, the ground state hyperfine splitting provides long lived states for the realization of atom interferometry. A detailed description of the atomic structure and important numbers can be found in [98]. The level scheme of the D2-line, which is used in the presented experiments, is shown in figure 2.13. The electronic ground state $5^2S_{1/2}$ possesses two hyperfine states, one for each of the two spin orientations of the valence electron. The hyperfine states with total spin $F = 1$ and $F = 2$ have a frequency splitting of $\omega_{eg} \approx 2\pi \cdot 6.834$ GHz. Both states feature a Zeeman-splitting with sub-levels $m_F = -F, \ldots, +F$ (see figure 2.14). Applying a homogeneous magnetic field during the interferometer measurement allows for lifting this degeneracy and to address single sub-levels with the two-photon stimulated Raman process. The choice of the sub-levels used in the interferometer is motivated by the sensitivity to stray magnetic fields. With
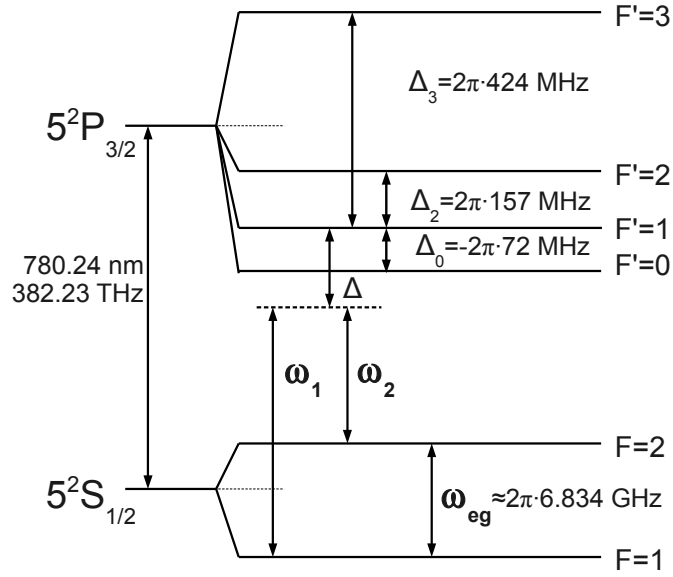
Figure 2.13: ^{87}Rb D2-line level scheme. The interferometer states are coupled with light fields of frequencies ω_1 and ω_2 with a global detuning Δ with respect to the state $|5^2P_{3/2}, F' = 1\rangle$.

the purpose of being to first order insensitive to magnetic field fluctuations during the interferometer measurement, the sub-levels with zero linear Zeeman shift are chosen. This determines the internal interferometer states

$$|g\rangle = |5^2S_{1/2}, F = 1, m_F = 0\rangle \tag{2.95}$$
$$|e\rangle = |5^2S_{1/2}, F = 2, m_F = 0\rangle . \tag{2.96}$$

These states are coupled using a stimulated Raman transition by applying two light fields with angular frequencies ω_1 and ω_2. The D2-line excited state $5^2P_{3/2}$ is used as intermediate state $|i\rangle$. For the two-photon transition coupling to the hyperfine states with total spin $F' = 1$ and $F' = 2$ needs to be taken into account. The addressed Zeeman sub-levels in the excited state are chosen by the helicity of the transition, which is depicted in figure 2.14 for a σ^+-transition.

Momentum state coupling

The application of the Raman laser light fields allows us to couple the internal atomic states and to concurrently transfer a momentum of $\hbar\mathbf{k}_{\mathrm{eff}} = \hbar(\mathbf{k}_1 - \mathbf{k}_2)$ to the atom. If the two light fields propagate in the same direction, we speak of resulting co-propagating transitions whereas applying the light fields from opposite
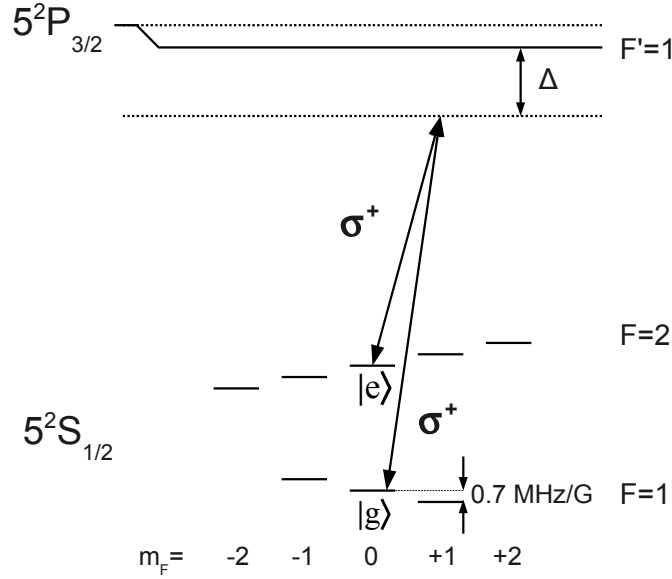
Figure 2.14: Internal interferometer states. The application of a magnetic field lifts the degeneracy, which allows only to address the interferometer states $|g\rangle$ and $|e\rangle$ via the two-photon detuning. Here, the Raman transition is depicted for the combination of two σ^+-transitions and is equivalent for σ^--transitions.

directions leads to so-called counter-propagating stimulated Raman transitions. While the momentum transfer $\hbar\mathbf{k}_\text{eff}$ is negligible in the co-propagating case, it is large enough to modify significantly the momentum of cold or thermal atoms in the counter-propagating case. In the following, the notation $\mathbf{k}_\text{eff}$ will be explicitly used for the latter case.

Wannier-Stark state coupling

In the case of laser induced tunneling in a vertical lattice, only counter-propagating light fields are considered. While the coupling strength in the case of momentum states is determined by the choice of the correct single-photon and two-photon detuning as well as the light field intensity, the Wannier-Stark state coupling strength depends strongly on the choice of the coupling and lattice laser wavelength [74]. In our case, the coupling laser effective wave number is given by $k_\text{eff} \approx 4\pi/780$ nm. This is an important criterion for the choice of the lattice laser wavelength, which is, in addition to the coupling strength, driven by several other criteria. An important parameter is the Landau-Zener tunneling rate. It is more favorable at low wavelengths. Moreover, the laser has to fulfill other criteria which are more related to the experimental realization. It has to provide single frequency continuous wave
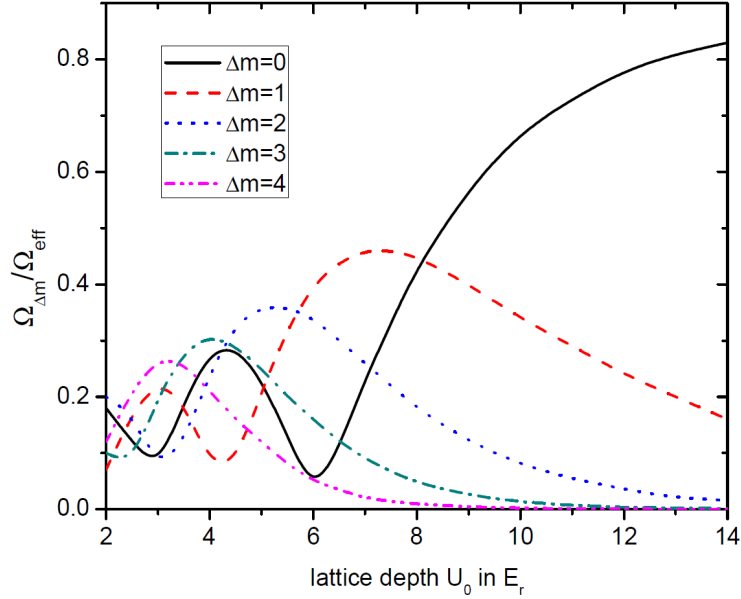
Figure 2.15: Coupling strength as a function of lattice depth. The graph shows the coupling strength $\Omega_{\Delta m}$ of the tunneling transition from a Wannier-Stark state with index m to a state of index $m' = m + \Delta m$ in relative units of the free space coupling strength Ω_{eff} and as a function of the lattice depth U_0 in units of E_r. The numerically simulated points are approximated by a spline. In the case of deep lattices, the inner-site coupling ($\Delta m = 0$) becomes dominant. For lattices with depths of $U_0 \lesssim 10 E_r$, the inter-site coupling strength shows maxima for rising values of Δm with falling lattice depth.

operation, and the output power has to be sufficiently large in order to realize sufficiently large lattice depth with a beam waist of several hundreds of μm. A laser wavelength responding to these demands is found to be $\lambda_l = 532$ nm. Figure 2.15 shows the coupling strengths between Wannier-Stark states, which are obtained in numerical evaluation of (2.71). In the experimental realization presented in this work, the lattice depths are chosen in the range of $U_0 = 1.5 E_r$ to $U_0 = 6.5 E_r$. Using (2.52) for the case of a shallow lattice and the local acceleration g, we find the losses due to Landau-Zener tunneling to be smaller than 0.5 % for a lattice depth of $U_0 = 1.5 E_r$ for trapping during 100 s.

2.5.1 Frequency shifts

The external atomic states – being the momentum states and the Wannier-Stark states in this work – are sensitive to potential gradients which allows for the measurement of the latter. As also the internal atomic state is in a superposition during the interferometer sequence, the interferometer phase is influenced by electromag-

netic fields that induce differential energy shifts of the two states. In the case of the ^{87}Rb atom with the interferometer states $|g\rangle$ and $|e\rangle$, these are the quadratic Zeeman shift and the AC-Stark shift which will be explained in the following.

Zeeman shifts

The linear Zeeman frequency shift is used to lift the degeneracy of the sub-levels in the two hyperfine states $|5^2S_{1/2}, F = 1\rangle$ and $|5^2S_{1/2}, F = 2\rangle$, which allows for addressing the desired interferometer states (see figure 2.13). While the choice of the $m_F = 0$ states for interferometry makes it possible to circumvent the deleterious effect of the linear Zeeman shift influence onto the interferometer phase, the quadratic Zeeman shift of these states, though much smaller, does also have an influence. The differential frequency shift of the interferometer states amounts to $\alpha_{qZ} = 2\pi \cdot 575.15$ Hz/G^2, which results in a frequency shift

$$\delta_{qZ}(\mathbf{x}, t) = \alpha_{qZ}|\mathbf{B}(\mathbf{x}, t)|^2. \tag{2.97}$$

AC-Stark shift

The differential AC-Stark shift arising from the beam splitting light fields is given by the difference of the AC-Stark shifts of each of the two states in (2.27). The two differential shifts cancel each other if we choose the two contributions Ω_g^{AC} and Ω_e^{AC} to be equal. This is possible for a total detuning $|\Delta| < \omega_{eg}$ as in this case, one of the beams is red detuned to both states whereas the other beam is blue detuned to the one and red detuned to the other state. The former beam induces a negative differential light shift which can be compensated by a positive shift induced by the latter light field. For given light field intensities I_1 and I_2 and a detuning Δ, the differential light shifts can be calculated taking into account the selection rules and the respective Clebsch-Gordon coefficients of the possible transitions [53, 96]. Out of this, an intensity ratio I_2/I_1 can be deduced as a function of Δ, which allows to cancel the differential AC-Stark shift induced by the coupling light fields for an intensity ratio [96]

$$\frac{I_2}{I_1} = \frac{\left(\frac{1}{60(\Delta+\omega_{eg})} + \frac{1}{4(\Delta-\Delta_2+\omega_{eg})} + \frac{2}{5(\Delta-\Delta_3+\omega_{eg})}\right) - \left(\frac{5}{12\Delta} + \frac{1}{4(\Delta-\Delta_2)}\right)}{\left(\frac{5}{12(\Delta-\omega_{eg})} + \frac{1}{4(\Delta-\Delta_2-\omega_{eg})}\right) - \left(\frac{1}{60\Delta} + \frac{1}{4(\Delta-\Delta_2)} + \frac{2}{5(\Delta-\Delta_3)}\right)}. \tag{2.98}$$

Here, Δ_2 and Δ_3 are the detunings of the fields ω_1 and ω_2 with respect to the $F' = 2$ and $F' = 3$ hyperfine levels in the intermediate state. The intensity ratio is plotted versus the detuning in figure 2.13.

The compensation is applied in interferometers based on free-falling and trapped atoms. In the case of an interferometer in a 1D-lattice, the trap light fields induce an additional differential light shift. In our case, this potential is realized using a far blue detuned optical lattice. Furthermore, lateral confinement of the atoms is
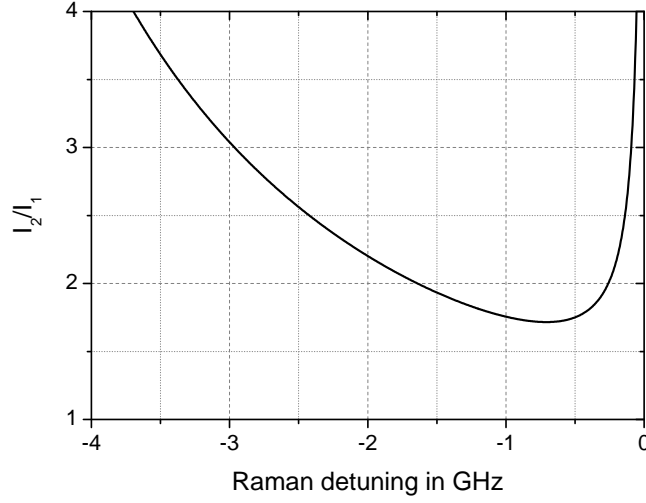
Figure 2.16: AC-Stark shift compensation. The two Raman beam splitter light fields induce a differential AC-Stark shift on the internal interferometer state transition with respectively opposed signs. The choice of the intensity ratio I_2/I_1 of the two light fields depending on the Raman detuning Δ according to the plotted line allows for an effective compensation of the shift.

realized using a far red detuned dipole trap beam (see chapter 4). Trapping in the periodic dipole potential of a lattice or in the Gaussian potential of a dipole trap is possible due to the induced AC-Stark shift of the atomic energy levels introduced in section 2.3.1. In that case, the AC-Stark shift is calculated with the assumption of a detuning that allows for the application of the rotating wave approximation. For a large detuning, the rotating wave approximation is not necessarily valid. Furthermore, coupling to several atomic resonances has to be taken into account. In the case of ^{87}Rb, these are the D1- and D2-line. For this case, we will consider a dipole potential of the form [99]

$$
\begin{aligned}
U(\mathbf{r}) \;=\; & -\frac{\pi c^2 (1 - \mathcal{P}_{g_F m_F})}{2\omega_{0,D1}^3} \left(\frac{\Gamma_{D1}}{\omega_{0,D1} - \omega} + \frac{\Gamma_{D1}}{\omega_{0,D1} + \omega} \right) I(\mathbf{r}) \\
& -\frac{\pi c^2 (2 + \mathcal{P}_{g_F m_F})}{2\omega_{0,D2}^3} \left(\frac{\Gamma_{D2}}{\omega_{0,D2} - \omega} + \frac{\Gamma_{D2}}{\omega_{0,D2} + \omega} \right) I(\mathbf{r}),
\end{aligned}
\tag{2.99}
$$

where c is the speed of light, and $\omega_{0,D1}$, $\omega_{0,D2}$ and Γ_{D1}, Γ_{D2} are the frequency and scattering rate of the ^{87}Rb D1- and D2-line. The trapping light is characterized by its frequency ω, intensity I_0 and $\mathcal{P}_{g_F m_F}$ being 0 for linearly and ± 1 for circularly polarized light. While the absolute light shift on each of the states allows for trapping, a differential light shift δ_{ACT} is induced as the trapping light field

frequencies are slightly differently detuned with respect to the ground and excited interferometer states

$$\delta_{ACT}(\mathbf{r}) \quad = \quad \frac{\omega_{eg}}{\omega_{0,D2} - \omega} \frac{U(\mathbf{r})}{\hbar}. \tag{2.100}$$

These differential light shifts cause frequency bias terms in the Bloch frequency measurement and, as the light fields are not spatially homogeneous, result in dephasing over the atomic ensemble, which is presented in chapter 4.

2.6 Interferometer signal and measurement sensitivity

The transition probability P_e describes the probability to find an atom in the state $|e\rangle$ after the interferometer pulse sequence if it was initially in state $|g\rangle$. It is given by the projection of the interferometer output state onto the excited state. In practice, an interferometer measurement is realized with many atoms at the same time, which allows to derive a statistical expression of the transition probability. This is determined via the normalized state population

$$P_e \quad = \quad \frac{N_e}{N_g + N_e} \tag{2.101}$$

$$= \quad \frac{N_e}{N}. \tag{2.102}$$

Here, N_g and N_e are the number of atoms in the ground and excited state introduced in the former section and $N = N_g + N_e$ is the total number of atoms. These numbers are measured after the interferometer sequence in a state-selective detection process. Imperfections in the beam splitting and detection process lead to a reduced interferometer contrast. We therefore express the real interferometer signal as

$$P_e \quad = \quad P_{e,0} - A \cos(\Delta\Phi) \tag{2.103}$$

$$= \quad P_{e,0} - \tfrac{1}{2} C \cos(\Delta\Phi), \tag{2.104}$$

where $P_{e,0}$, A and C respectively denote the signal offset, amplitude and contrast of the normalized signal.

2.6.1 Sensitivity, stability and noise

The sensitivity that characterize our sensors are determined by the scaling factor and the stability of the interferometer phase measurement. In our analysis we will distinguish between different time scales. In the range of seconds, we use the

expression short term stability, whereas we refer to the stability of the measurement over minutes and longer times as long term stability.

The stability of the phase measurement can be limited by different noise and drift sources. If we assume these sources to be uncorrelated, the phase noise expressed by its variance is given by the quadratic sum of the single main noise sources

$$\sigma_\Phi^2 \ = \ \sigma_{\Phi,P_e}^2 + \sigma_{\Phi,intertial}^2 + \sigma_{\Phi,non-inertial}^2 + \sigma_{\Delta\phi,laser} + \ldots \ . \quad (2.105)$$

It is composed by different terms

- σ_{Φ,P_e} is the phase uncertainty arising from the uncertainty in the determination of the transition probability P_e, which is denoted σ_{P_e}. For the point of maximal phase sensitivity – the so-called mid-fringe position – this uncertainty is related to the uncertainty of the transition probability via

$$\sigma_{\Phi,P_e} \ = \ \frac{2\sigma_{P_e}}{C}. \quad (2.106)$$

  σ_{P_e} accounts for technical noise in the determination of the atom number in the respective states and the atom number itself. The latter results in a fundamental limitation of the detection process, the quantum projection noise [100] that will be denoted with an uncertainty σ_{QPN}. It arises from the fact that a finite number of atoms only allows for a finite resolution in the transition probability. For a given transition probability value P_e, this is [96]

$$\sigma_{QPN} \ = \ \sqrt{\frac{P_e(1-P_e)}{N}} \quad (2.107)$$

  with N being the total atom number per shot.

- $\sigma_{\Phi,intertial}$ is the noise of the measured inertial forces. It is induced by vibrations of the apparatus and its environment.

- $\sigma_{\Phi,non-inertial}$ is a term arising from shifts of the internal atomic state.

- $\sigma_{\Delta\phi,laser}$ is the uncertainty of the relative phase of the two Raman light fields.

The totality of the noise sources results in an interferometer noise from one shot to another. The uncertainty of the phase measurement is then studied for a repeated phase measurement over many cycles. For uncorrelated noise, the uncertainty averages with $\tau^{-1/2}$ if τ is the total measurement time. On the contrary, slow fluctuations and drifts can lead to a different averaging behavior (see appendix A). Such long term fluctuations can be suppressed using different techniques that involve subsequent measurements with different sets of parameters. We employ such techniques in both interferometers in order to suppress the influence of fluctuations in the detection and the non-inertial frequency shifts onto the inertial phase. In the following, we will introduce the important interferometer phase shifts for both experiments.

2.7 Interferometer phase shifts

The sensitivity function formalism allows to calculate the impact of phase fluctuations and detunings onto the interferometer phase, which is discussed here for both systems. First, the phase shifts in a Mach-Zehnder interferometer with noninertial phases and frequency shifts will be considered. Then, the phase shifts are calculated for a WSR and a symmetrized WSR interferometer in the case of a trapped atom interferometer. This is done using (2.81) and (2.82) for phase and frequency impacts, respectively.

2.7.1 Non-inertial phase shifts in a Mach-Zehnder interferometer

During the Raman beam splitter light field application, the effective Raman laser phase ϕ_{eff} is imprinted onto the atoms, which is derived in section 2.2. For the Mach-Zehnder sequence, this results in a total phase shift given by (2.38). On the one hand, this allows to add an arbitrary offset to the interferometer phase by tuning the relative Raman laser phase. On the other hand, the relative phase has to be well controlled in order to suppress phase noise. Not only the phase control over time is important for the interferometer phase, the spatial phase of the Raman laser beams, the wave fronts, also have an impact on the interferometer measurement, which is introduced in section 3.2.

Other phase shifts arise from the non-inertial frequency shifts given in section 2.5, namely an imperfectly compensated differential AC-Stark shift and the quadratic Zeeman shift. An evaluation of these shifts are realized using the sensitivity function formalism, which is presented for the case of our gyroscope in [56]. The scope of this work is the study of the sensor's long term stability sighting for phase shifts varying slower than the cycle time of the experiment. This enables the application of the so-called k-reversal technique (see section 3.4.6) consisting in alternating phase measurements with opposite area orientation. This allows to reject phase shifts that are independent of the area orientation. This is the case for the AC-Stark shift and mainly for the quadratic Zeeman shift. However, a magnetic field gradient along the beam splitter optical axis is not removed using the alternating measurement scheme. This is also the case for the so-called two-photon light shift (TPLS) arising from the chosen Raman beam configuration in our set-up (see section 3.5.1).

The impacts of the Raman laser wave front, the magnetic field gradient, and the TPLS on the long term stability are studied in detail in chapter 3. The derivations for the calculation of these shifts are given in the respective sections.

2.7.2 Phase shifts in Wannier-Stark interferometry

The phase shift in Wannier-Stark atom interferometers presented in this work results from a frequency measurement. The measured frequency is determined by the energy difference of the two coupled Wannier-Stark states, namely the internal state transition frequency plus a multiple of the Bloch frequency. The interferometer is calculated in the following for a small relative detuning of the Raman laser frequency with respect to the transition frequency plus frequency shifts arising from the coupling and trap light fields. This is done for a WSR and symmetrized WSR interferometer.

In both cases, we consider a regime of a detuning that is small against the Rabi frequency ($\delta_{\pi/2}, \delta_T \ll \Omega_{\Delta m}$). With this assumption, the WSR interferometer contrast is not diminished by the Rabi envelope. The interferometer phase shift $\Delta\Phi_{WSR}$ is then calculated by inserting the respective detuning and the sensitivity function of the Ramsey sequence (2.88) into (2.82)

$$
\begin{aligned}
\Delta\Phi_{WSR} &= \left(\delta_{\Delta m} - \delta_{ACT} - \delta_{qZ}\right) T + \\
&\quad + \left(\delta_{\Delta m} - \delta_{ACT} - \delta_{ACR} - \delta_{qZ}\right) \frac{4\tau_{\pi/2}}{\pi} + \phi_1 - \phi_2.
\end{aligned} \tag{2.108}
$$

Here, δ_{ACT} and δ_{ACR} are the detunings due to the differential AC-Stark shift induced by the trapping and Raman light fields, respectively, and δ_{qZ} is the detuning induced by the quadratic Zeeman effect.

A WSR interferometer is the simplest way to realize interferometry on Wannier-Stark states. However, many different states can be coupled by choosing different relative Raman detunings during subsequent pulses. This allows to symmetrize the interferometer paths of the Ramsey sequence with respect to the evolution time in the ground and excited internal state. As a consequence, shifts of the internal state transition that are constant over the interferometer duration cancel out. This symmetrization is realized by adding two π-pulses driving the inner-site transition. The pulse separations are then chosen such that the total evolution times for both paths in the excited and ground internal state are equal. This results in the interferometer scheme depicted in figure 2.17, which will be referred to as symmetrized WSR interferometer in the following. In this sequence, the internal states can also be coupled by a one-photon process, which is realized by a microwave field with angular frequency $\omega_{MW} \approx \omega_1 - \omega_2$ in our case.

The time evolution of such an interferometer sequence can be described on a system featuring four interferometer states. Thus, the formalism introduced in section 2.3 needs to be extended to a four-dimensional basis. The phase shift can be calculated in a simpler way using the sensitivity function formalism. This calculation involves different sensitivity functions for different kinds of explicitly internal, or internal and external coupling, respectively. Doing so, we find a total
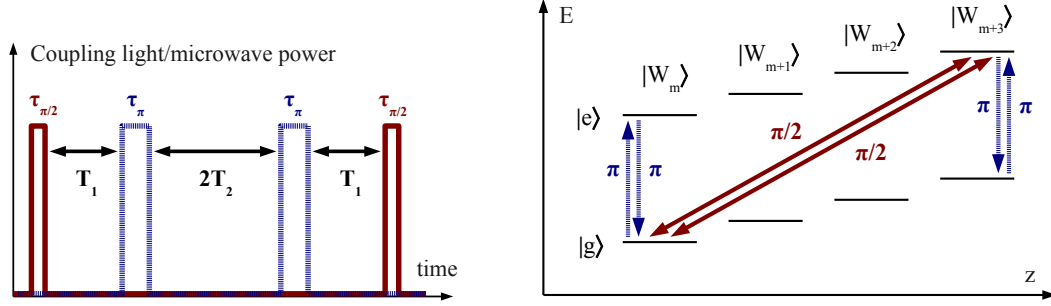
Figure 2.17: Symmetrized WSR interferometer. *Left*: timing sequence of the Raman and microwave pulses, which allows to symmetrize the internal free evolution times. *Right*: coupling of a set of four states in the symmetrized WSR interferometer. The inner-site coupling can be realized using Raman light fields or microwave fields.

phase shift in the symmetrized WSR interferometer of

$$
\begin{aligned}
\Delta\Phi_{SWSR} &= \delta_{\Delta m}\frac{4\tau_\pi}{\pi} + (\delta_{\Delta m} - \delta_{ACT} - \delta_{qZ})\,2T_1 + (\delta_{\Delta m} + \delta_{ACT} + \delta_{qZ})\,2T_2 + \\
&\quad + (\delta_{\Delta m} - \delta_{ACT} - \delta_{qZ} - \delta_{ACR})\frac{4\tau_{\pi/2}}{\pi} + \\
&\quad + \phi_1 - 2\phi_{MW,2} + 2\phi_{MW,3} - \phi_4
\end{aligned}
\tag{2.109}
$$

for arbitrary times T_1 and T_2 that define the pulse separations as depicted in figure 2.17. Here, the phases ϕ_1 and ϕ_4 are the coupling laser phases during the $\pi/2$-pulse application, and $\phi_{MW,2}$ and $\phi_{MW,3}$ are the microwave phases during the application of the π-pulses. The symmetrization of the interferometer consists in choosing the relation of T_1 and T_2 to

$$
T_2 = T_1 + \frac{2\tau_{\pi/2}}{\pi}.
\tag{2.110}
$$

The phase shift of the symmetrized WSR interferometer is then given by

$$
\begin{aligned}
\Delta\Phi_{SWSR} &= \delta_{\Delta m}T + (\delta_{\Delta m} - \delta_{ACR})\frac{4\tau_{\pi/2}}{\pi} + \\
&\quad + \phi_1 - 2\phi_{MW,2} + 2\phi_{MW,3} - \phi_4.
\end{aligned}
\tag{2.111}
$$

In this phase shift, only the differential AC-Stark induced by the Raman lasers is present. Presuming homogeneous frequency shifts, the constant contribution of the trap induced differential AC-Stark shift and quadratic Zeeman shift cancel independently.

The phase shift calculation presented here and also the theoretical tools of this chapter will be used in the study of the short and long term stability of the trapped interferometer in chapter 4.

Atom interferometer gyroscope

In this chapter, the atom interferometer gyroscope CASI is presented. After introducing the rotation measurement principle, we discuss the impact of wave front tilts on the rotation measurement. Subsequent to this, the experimental set-up and the employed interferometer sequence will be described. This is followed by the study of the main sources for drifts and slow fluctuations in the rotation measurement, and by an analysis of the present long term stability of the sensor.

3.1 Rotation measurements with the CASI gyroscope

The CASI gyroscope is composed of two Mach-Zehnder interferometers with counter-propagating, parabolic atomic trajectories (see figure 3.1). The horizontal orientation of the Raman beam splitting light fields results in a maximum sensitivity to rotations around the vertical axis. The atomic trajectories are defined by an atomic forward velocity of $v_{x,0} = \pm 2.79$ m/s and an initial vertical velocity of $v_{y,0} = 0.73$ m/s. In combination with the fixed beam splitter distance of $v_{x,0}T = 6.5$ cm, the beam splitting pulse separation time must be chosen $T = 23$ ms. The area enclosed by the interferometer paths is then $\mathbf{e}_y \cdot \mathbf{A} = 17.4$ mm^2. This results in a rotation phase shift induced by the horizontal Earth rotation projection in Hanover (52°22'N latitude) of $\Phi_\Omega = 2.74$ rad in each interferometer.

The interferometer phase is not only influenced by rotations, but also by accelerations. Although the beam splitting light fields are oriented horizontally, which results in a vanishing acceleration phase (2.43), a slight misalignment of some tens of μrad would already cause phase shifts in the same order of magnitude as the Earth rotation rate phase shift. Furthermore, the beam splitter light fields are
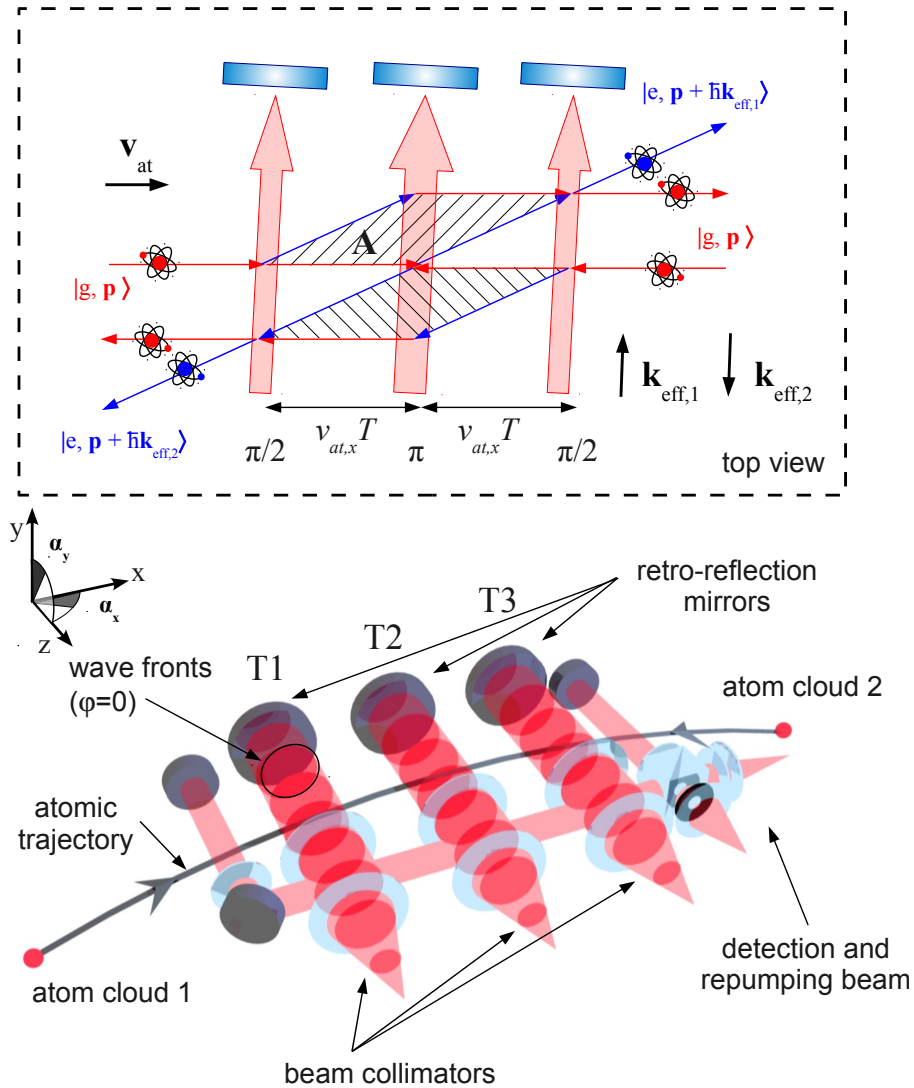
Figure 3.1: The atom interferometer gyroscope CASI. After the launch, the atoms are prepared in the interferometer ground state before being split up, redirected and recombined by the use of stimulated Raman transitions. The counter-propagating beam splitter light fields are realized using retro-reflection on mirrors, one mirror for each of the interaction zones, which are denoted T1, T2 and T3 three as depicted. The view from the top *(in dashed box)* shows the atom interferometer paths in the Mach-Zehnder configuration. The beam splitting light fields are not perfectly perpendicular with respect to the atomic forward velocity allowing for the selection of the beam splitting direction via the Doppler detuning.

realized in retro-reflection on three separate mirrors. If we presume different positions in the z-direction z_1, z_2, and z_3 for the three mirrors, we find the phase arising from the three mirror positions according to (2.42) to be

$$\Phi_{\Delta z} = k_{\text{eff}} \left(z_1 - 2z_2 + z_3 \right).$$ (3.1)

The rotation phase can be extracted from the interferometer phases by combining the two interferometer signals. The second interferometer is operated with opposed atomic forward velocity $v_{at,x}^{(1)} = -v_{at,x}^{(2)}$, and effective wave vector $\mathbf{k}_{\text{eff}}^{(1)} = -\mathbf{k}_{\text{eff}}^{(2)}$, where $^{(1)}$ and $^{(2)}$ stand for the two interferometers. While the rotation phase shift is common to both, the contributions of acceleration and relative mirror position have respectively opposed sings. Hence, the average of the two measured phases results in the rotation phase Φ_Ω and the half-difference is the acceleration phase Φ_a with an arbitrary offset

$$\Phi_\Omega = \frac{\Phi^{(1)} + \Phi^{(2)}}{2}$$ (3.2)

$$\Phi_a + \Phi_{\Delta z} = \frac{\Phi^{(1)} - \Phi^{(2)}}{2},$$ (3.3)

Before the experimental apparatus is introduced, the impact of wave front aberrations of the Raman beam splitter light fields onto the atomic gyroscope signal will be described in the following.

3.2 Impact of the Raman wave fronts on the interferometer signal

Similar to (3.1) we will consider a spatial dependence of the wave front in the directions perpendicular to the Raman beam splitter optical axis by introducing the phase arising from the effective wave fronts of the Raman beams in each interferometer pulse [101]

$$\phi_i^{WF} = \phi(x_i, y_i).$$ (3.4)

Here, (x_i, y_i) represents the lateral position of the atom within the beam splitting light field during the pulse application of the i-th pulse. In a Mach-Zehnder sequence, the total phase due to wave fronts is then given by

$$\Phi_{MZ}^{WF} = \phi(x_1, y_1) - 2\phi(x_2, y_2) + \phi(x_3, y_3).$$ (3.5)

This spatially dependent interferometer phase can influence the measurement in three ways. First, a phase shift bias is induced depending on the three positions (x_i, y_i) of the beam splitter pulse application. Second, a fluctuation of the atomic
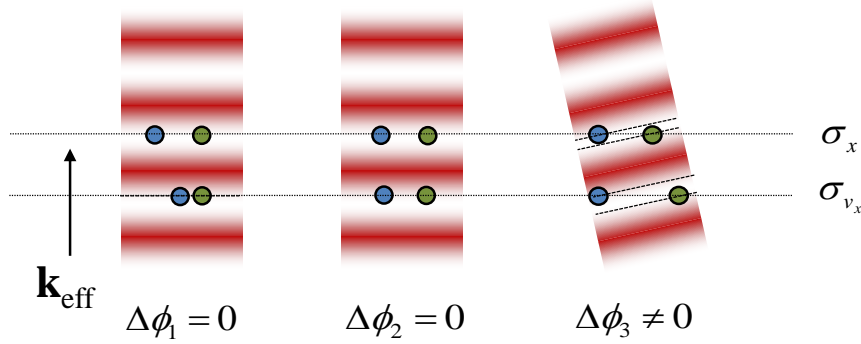
Figure 3.2: Tilt impact on single atom phases. Considering an initial position or velocity difference, two atoms acquire different interferometer phases within the Mach-Zehnder sequence given by (3.5) if the wave fronts are not perfectly plane waves or, as shown here, not parallel. The differences in phase $\Delta\phi_i$ between different atom positions lead to a phase distribution over the atomic ensemble and, for large differences, to a loss in the interferometer signal contrast.

initial position and velocity can cause the atoms to probe the laser phase on different positions in subsequent measurements resulting in a shot-to-shot noise in the interferometer signal. Third, the atomic ensemble features a certain spatial spread and expansion rate given by the initial cloud size and temperature, respectively. The total interferometer signal is detected as an average of the single atom signals. If the we consider phase variations over the expansion of the atomic cloud are large, meaning in the range of 2π and above (see figure 3.2), we find a reduction in the interferometer signal contrast. The alignment demands and the expected bias on the rotation signal arising from wave fronts are introduced in the following two sections.

3.2.1 Contrast reduction

The total interferometer signal is given as an average of the single atom interferometer signals. This can be expressed by the integration over all possible transition probabilities in dependence of the spatially dependent phase, weighted by the atomic position and velocity distribution

$$P_{e,total} = \int_{-\infty}^{\infty} P_e(\Delta\Phi^{WF}(x,y,v_x,v_y)) \cdot f(x,y) \cdot f_v(v_x,v_y) \; dxdydv_xdv_y. \tag{3.6}$$

The initial position and velocity distributions are given by

$$
f(x,y) \quad = \quad \frac{1}{2\pi\sigma_x\sigma_y}\exp\left(-\frac{(x-x_0)^2}{2\sigma_x^2}-\frac{(y-y_0)^2}{2\sigma_y^2}\right) \tag{3.7}
$$

$$
f_v(v_x,v_y) \quad = \quad \frac{1}{2\pi\sigma_{v_x}\sigma_{v_y}}\exp\left(-\frac{(v_x-v_{x,0})^2}{2\sigma_{v_x}^2}-\frac{(v_y-v_{y,0})^2}{2\sigma_{v_y}^2}\right) \tag{3.8}
$$

with cloud radii σ_x and σ_y, and velocity widths $\sigma_{v_x} = \sqrt{k_B\Theta_x/m_a}$ and $\sigma_{v_y} = \sqrt{k_B\Theta_y/m_a}$. The latter are given by the atomic temperatures Θ_x and Θ_y, the Boltzmann constant k_B, and the atomic mass m_a. The wave front is introduced via an arbitrary function $\Delta\Phi^{WF}(x,y,v_x,v_y)$ describing the spatial wave front for an arbitrary trajectory and pulse sequence. For the special case of free-falling atoms on a parabolic trajectory with **g** pointing in $-y$ direction and a wave front tilt α_x in x and α_y in y direction, the phase of a single beam splitter pulse is found to be

$$
\begin{aligned}
\phi_i(x,y,v_x,v_y) \quad = \quad & k_{\text{eff}}\left[(a_i-x-v_xt_i)\sin(\alpha_{x,i})+\left(b_i-y-v_yt_i+\tfrac{1}{2}gt_i^2\right)\sin(\alpha_{y,i})\right] \\
\approx \quad & k_{\text{eff}}\left[(a_i-x-v_xt_i)\,\alpha_{x,i}+\left(b_i-y-v_yt_i+\tfrac{1}{2}gt_i^2\right)\alpha_{y,i}\right].
\end{aligned} \tag{3.9}
$$

Here, a_i and b_i are the centers of mirror rotation, and $\alpha_{x,i}$ and $\alpha_{y,i}$ are the rotation angles around the z-axis. For a Mach-Zehnder pulse scheme, the transition probability is given by (2.37)

$$
P_e \quad = \quad P_{e,0} - A_{MZ}^{WF}\cos\left(\Delta\Phi_{MZ}^{WF}\right) \tag{3.10}
$$

with the signal offset $P_{e,0}$, the signal amplitude A_{MZ}^{WF}, and the phase shift of $\Delta\Phi_{MZ}^{WF} = \phi_1(x,y,v_x,v_y) - 2\phi_2(x,y,v_x,v_y) + \phi_3(x,y,v_x,v_y)$. Carrying out the integration (3.6) leads us to the wave front dependent signal amplitudes in the case of wave front tilts in x and y-direction [56]

$$
\begin{aligned}
A_{MZ,x}^{WF} \quad = \quad & \tfrac{1}{2}\exp\left[-\tfrac{1}{2}\left(k_{\text{eff}}\sigma_x(\alpha_{x,1-2}-\alpha_{x,2-3})\right)^2\right] \\
& \cdot\exp\left[-\tfrac{1}{2}\left(k_{\text{eff}}\sigma_{v_x}(t_1(\alpha_{x,1-2}-\alpha_{x,2-3})-2T\alpha_{x,2-3})+\chi_\Omega\right)^2\right] \tag{3.11} \\
A_{MZ,y}^{WF} \quad = \quad & \tfrac{1}{2}\exp\left[-\tfrac{1}{2}\left(k_{\text{eff}}\sigma_x(\alpha_{x,1-2}-\alpha_{y,2-3})\right)^2\right] \\
& \cdot\exp\left[-\tfrac{1}{2}\left(k_{\text{eff}}\sigma_{v_y}(t_1(\alpha_{y,1-2}-\alpha_{y,2-3})-2T\alpha_{y,2-3})\right)^2\right] \tag{3.12}
\end{aligned}
$$

with $\alpha_{x,1-2}=\alpha_{x,1}-\alpha_{x,2}$ and $\alpha_{x,2-3}=\alpha_{x,2}-\alpha_{x,3}$ being the relative angles of the mirrors T1 and T2 as well as T2 and T3, respectively. In the chosen configuration, the term of the horizontal relative beam splitter tilt $A_{MZ,x}^{WF}$ contains a term taking into account the rotation of the apparatus $\chi_\Omega = \Omega_z T^2(2-\alpha_{x,1}^2-\alpha_{x,3}^2)$, which is negligible for our parameters if the apparatus rotates with the Earth. The alignment tolerance of the respective beam splitter wave vectors is then given by the amplitude full-width-half-maximum (FWHM) values of the relative mirror
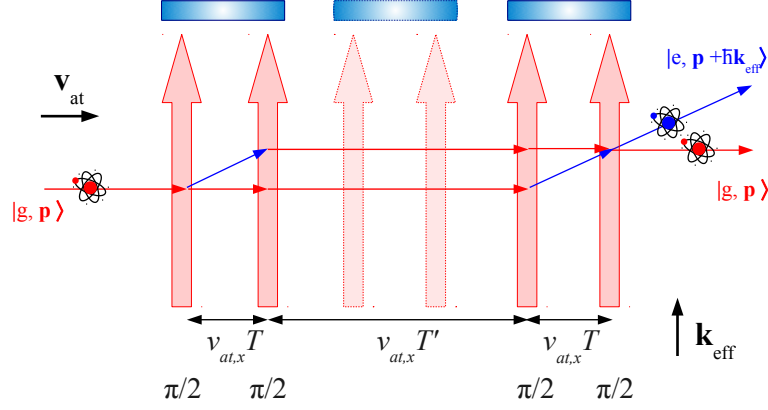
Figure 3.3: Symmetric Ramsey-Bordé geometry. Two pairs of $\pi/2$-pulses separated by a time T are applied with an additional time T' in between. If the two pulse pairs of the configuration are each applied in one interferometer zone, the interferometer signal amplitude as a function of the respective mirror orientations only depends on the atomic cloud temperature and the free evolution time T. This allows for a pairwise precise relative beam splitter mirror alignment. The arrows represent the moments of pulse application. The light fields the same as in the Mach-Zehnder interferometer case.

orientation angles. If only the central mirror is considered to be misaligned with respect to the outer mirrors, the FWHM angle reads for a vertical misalignment

$$\alpha_{y,2,FWHM} \;=\; \sqrt{\frac{8\ln(2)}{(2k_{\mathrm{eff}}\sigma_y)^2 + \left(2k_{\mathrm{eff}}\sigma_{v_y}(t_1 - T)\right)^2}}. \tag{3.13}$$

For our parameters, the alignment tolerance is found to be $\alpha_{y,2,FWHM} \approx 19 \; \mu$rad setting a high demand on the alignment of the beam splitting light fields at the position of the atoms. Therefore, we employ the symmetric Ramsey-Bordé (SRB) interferometer geometry for the alignment of the relative beam splitter light field orientation presented in section 3.4.5. This geometry consists of two pairs of $\pi/2$-pulses as depicted in figure 3.3. A calculation similar to the one leading to (2.38) can be performed for the SRB scheme which enables us to deduce to a total wave front phase taking into account (3.4)

$$\Delta\Phi_{SRB}^{WF} \;=\; \phi(x_1, y_1) - \phi(x_2, y_2) - \phi(x_3, y_3) + \phi(x_4, y_4). \tag{3.14}$$

Carrying out a calculation similar to the one in the case of the Mach-Zehnder geometry, the wave front induced signal amplitudes for tilts in x and y-direction

are found to be

$$A^{WF}_{SRB,x} = \frac{1}{4} \exp\left[-\frac{1}{2}\left(k_{\text{eff}}T\sigma_{v_x}\alpha_{x,1-3} + \chi'_{\Omega}\right)^2\right] \tag{3.15}$$

$$A^{WF}_{SRB,y} = \frac{1}{4} \exp\left[-\frac{1}{2}\left(k_{\text{eff}}T\sigma_{v_y}\alpha_{y,1-3}\right)^2\right], \tag{3.16}$$

if the two pulse pairs are each applied in one beam splitting zone as depicted in figure 3.3. Once again, the term χ'_{Ω} accounting for the apparatus rotation is small and can be neglected for our experimental parameters. We then find the alignment tolerance of the SRB scheme

$$\alpha_{y,1-3,FWHM} = \sqrt{\frac{8\ln(2)}{\left(2k_{\text{eff}}\sigma_{v_y}T\right)^2}}. \tag{3.17}$$

The scheme is suitable for a relative alignment of two Raman mirrors as it allows for scaling the alignment tolerance by choosing the pulse separation time T (see section 3.4.5).

3.2.2 Rotation phase offset

The wave front induced interferometer phase offset can be calculated using (3.6), which allows to extract the total interferometer phase offset out of a the resulting total transition probability in the form of (3.10). Once again, the case of relative beam splitter light field tilts is considered using (3.9). By introducing the center of mass position and velocity components $x \equiv x_0$, $y \equiv y_0$, and $v_x \equiv v_{x,0}$, $v_y \equiv v_{y,0}$, respectively, the phase transferred to the atoms during the i-th pulse reads

$$\phi_i \approx k_{\text{eff}}\left[\left(a_i - x_0 - v_{x,0}t_i\right)\alpha_{x,i} + \left(b_i - y_0 - v_{y,0}t_i + \frac{1}{2}gt_i^2\right)\alpha_{y,i}\right]. \tag{3.18}$$

It is easily shown that, in the case of a rotation measurement, the cloud overlap of the atom interferometers is crucial. For this, the wave front induced phase offset of the rotation phase signal

$$\Phi^{WF}_{\Omega} = \frac{\Phi^{WF(1)}_{MZ} + \Phi^{WF(2)}_{MZ}}{2} \tag{3.19}$$

is calculated similar to (3.2). Taking into account the geometry of our set-up we find

$$\begin{aligned}\Phi^{WF}_{\Omega} &= \frac{1}{2}k_{\text{eff}}\left[\Delta x\left(\alpha_{x,1} - 2\alpha_{x,2} + \alpha_{x,3}\right) + \Delta y\left(\alpha_{y,1} - 2\alpha_{y,2} + \alpha_{y,3}\right)\right]\\ &= \frac{1}{2}k_{\text{eff}}\left[\Delta x\left(\alpha_{x,1-2} - \alpha_{x,2-3}\right) + \Delta y\left(\alpha_{y,1-2} - \alpha_{y,2-3}\right)\right],\end{aligned} \tag{3.20}$$

where $x^{(2)}_0 \equiv x^{(1)}_0 + \Delta x + D$ and $y^{(2)}_0 \equiv y^{(1)}_0 + \Delta y$ with D being the nominal separation of the two atomic sources. This visualizes the wave front influence onto

the interferometer phase. If the mirrors are perfectly aligned, all angles vanish and the wave front dependent rotation phase shift is zero. However, an imperfect alignment can lead to an interferometer phase offset for an imperfect cloud overlap, and to a phase jitter and drift if the atom source positions vary over time. This effect represents the dominant drift in the rotation measurement as we shall see later in this chapter.

3.3 Experimental realization

The atom interferometer measurement is pulsed in time. The atoms are trapped, cooled and launched on well defined trajectories. After the preparation of the interferometer input state, the atoms undergo the Mach-Zehnder interferometer sequence. A hyperfine state selective detection scheme is then employed to determine the transition probability, which allows us to read out the interferometer phase and to determine the rotation signal. Figure 3.1 depicts the measurement configuration used in our atom interferometer gyroscope.

Before the experimental sequence of the atom interferometer measurement is described in section 3.4, the atom gyroscope experimental set-up will be presented including the apparatus itself, the laser sources for realization of the respective monochromatic light fields for the atomic trapping, beam splitting and detection as well as a computer real time system for control of the experimental parameter values and timing. A detailed description of the control of radio and optical frequencies can be found in [54], while the laser sources are explained in detail in [55].

3.3.1 Apparatus

A schematic of the apparatus is depicted in figure 3.4. In the following, the vacuum system, the atom sources and light detection systems will be briefly described.

Vacuum system

The atom interferometer measurement takes place in ultra-high vacuum conditions in order to suppress collisions with background gas, which would cause decoherence in the interferometer measurement. Our vacuum chamber system is described in detail in [54]. It includes pumping and atomic source sections, which are all connected to the interferometry chamber. The set-up allows for maintaining good vacuum conditions in the interferometry chamber of below 10^{-9} mbar and sufficiently high Rubidium background vapor pressure in the source parts. This is assured by differential pumping stages in the connection of the chambers of the two-dimensional magneto-optical trap (2D-MOT) and the three-dimensional
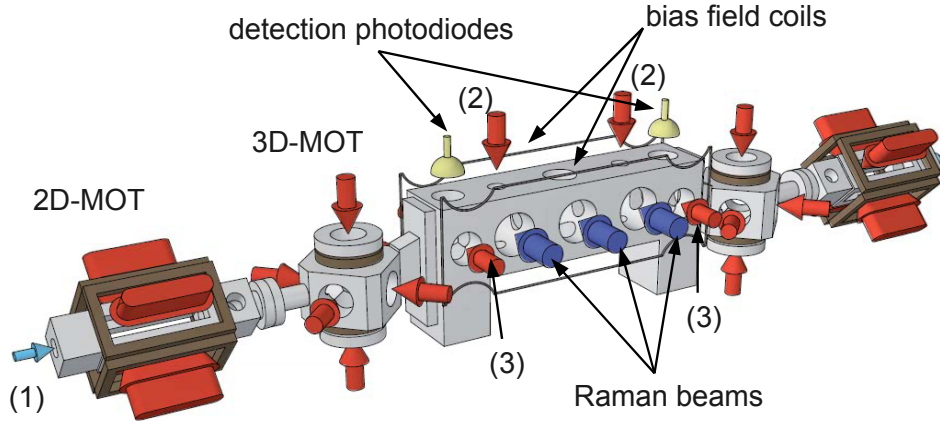
Figure 3.4: The atom gyroscope apparatus. The vacuum chamber features two source sections and one interferometer chamber common to both interferometers. The applied light fields are depicted as arrows. In addition to the MOT cooling beams, a pusher beam (1) is applied to each 2D-MOT. The 'blow away' beams (2) needed for the interferometer state preparation are applied from the top, while the detection light fields (3) are applied from the sides.

magneto-optical trap (3D-MOT) of each source. The windows giving optical access to the vacuum chamber are BK-7 substrates with anti-reflective coating and a specified surface roughness of $\lambda/10$. They are attached to the chamber using an Indium sealing technique. We employ an ion getter pump (IGP) and a titanium sublimation pump for pumping during interferometer operation. An additional valve allows us to connect a turbo molecular pump via flange for fast pumping for maintenance purposes.

Atom sources

The atom source system and its characterization is described in detail in [53]. It is based on magneto-optical trapping [102] and sub-Doppler cooling using polarization gradient cooling [103]. Both identical sources consist of a two-dimensional magneto-optical trap (2D-MOT) creating a slow atomic beam traversing the differential pumping stage which allows to load the three-dimensional magneto-optical trap (3D-MOT) in the adjacent chamber with high atomic flux. The copper coils for magnetic field generation in the 3D-MOT are directly attached to the 3D-MOT chamber. The 2D-MOT coils and the beam shaping optics for the MOT beams are fixed on mounting structures that are connected to the vacuum chamber. Two Rubidium reservoirs directly connected to the 2D-MOT chambers via vacuum valves provide the required Rubidium vapor pressure. The reservoirs are heated to around 50°C. The trapping and launching experimental sequence will be

explained in section 3.4, while the used laser sources are presented in section 3.3.2.

Bias field for atom interferometry

In order to lift the degeneracy between the Zeeman sub-levels during the interferometer sequence, we generate a well defined homogeneous magnetic field. For this purpose, a specially designed wiring board is attached directly to the interferometer section of the vacuum chamber from both sides (see figure 3.4). The typical magnetic field applied with these coils is approximately 400 mG/A.

Magnetic shielding

In order to shield the experiment from external constant and time varying magnetic fields, the whole apparatus is enclosed by a μ-metal box of a total size of $120 \times 90 \times 65$ cm^3. While the breadboard carrying the apparatus is embedded in the bottom part of the box, the upper part can be removed for maintenance purposes. The used μ-metal has a thickness of 2 mm and allows to suppress the Earth magnetic field inside the shielding by a factor of about 40 [53]. The IGP is placed inside the shielding. It is enclosed in an additional μ-metal shielding in order to reduce the stray fields originating from the magnets in the pump.

Atom monitoring and detection devices

The detection of light scattered by the atoms is of interest in two phases of the experiment: before launch and in the hyperfine state selective fluorescence detection. The scattered intensity in the 3D-MOT atom sources is collected in $4f$ configurations onto large surface photodiodes `Hamamatsu S5107`, which allows for atom number determination. Also, an image of the trapped atoms is projected on a CCD camera using a beam sampler and an appropriately configured objective.

The imaging systems used for the detection of the interferometer exit ports each consist of two convex lenses ($f = 30$ mm and $d = 30.8$ mm) and a large photodiode `Hamamatsu S5107`. The double lens collects the scattered light and focuses it onto the photodiode. The numerical aperture of the detection system is thus defined by the lens diameter and the distance to the atomic ensemble. The photodiode signal is amplified using variable gain low noise amplifiers of the type `Femto DLPCA-S`. The state selective fluorescence detection scheme realized with the aid of these photodiodes is presented in section 3.4.4.

Light fields for manipulating the atoms

The laser light fields that we employ for all experimental steps are guided to the experiment using polarization maintaining optical single-mode fibers. The collimators, mirrors and polarization optics for the Raman beam splitter process and the atom state detection are presented in sections 3.3.4 and 3.4.4, respectively.

3.3.2 Laser system

Trapping and cooling of ^{87}Rb atoms as well as coherent beam splitting and fluorescence detection is realized close to or on one of the resonances of the D2-line. This requires single frequency laser sources with a wavelength of 780 nm and typical continuous optical output power of one Watt and below. The needed laser linewidth and frequency stability are in the range of kHz to MHz. The light sources we use in our experiment are external cavity diode lasers (ECDL), combined with optical amplifiers, so-called tapered amplifiers (TA), both based on semiconductor structures. Together, these devices form master oscillator power amplifier (MOPA) systems with narrow linewidth and high output power. While a detailed description of the lasers is given in [54, 55, 56], the laser system is briefly described here.

Required light fields

The relevant frequencies of the light for all experimental steps are depicted in figure 3.5. For atomic trapping, cooling and launching, narrow linewidth single frequency light fields have to be employed to address the ^{87}Rb D2-line cooling transition $|5^2S_{1/2}, F = 2\rangle \rightarrow |5^2P_{3/2}, F = 3\rangle$ and the repumping transition $|5^2S_{1/2}, F = 1\rangle \rightarrow |5^2P_{3/2}, F = 2\rangle$ for magneto-optical trapping in the 2D- and 3D-MOT. In the 2D-MOT, an additional pusher beam featuring a blue frequency detuning relative to the cooling transition can be shined in along the atom beam axis in order to enhance the atom flux into the 3D-MOT.

Hyperfine state selective fluorescence detection is realized on a closed cooling transition for the atoms in the excited hyperfine state $|5^2S_{1/2}, F = 2\rangle$. The combination of repumping light and cooling light allows for the detection of the atoms in $|5^2S_{1/2}, F = 1\rangle$.

For coherent atomic beam splitting, two single frequency light fields are required that feature a well-defined relative frequency and phase difference in order to drive the two-photon Raman transition coherently and to control the atom interferometer phase via the relative light field phase. While the frequency difference of the two light fields needs to be close to the hyperfine transition frequency of $\nu_{eg} \approx 6.834$ GHz, the absolute laser frequencies have to be detuned with respect to the resonant cooling and repumper transitions by hundreds of MHz in order to prevent for single-photon scattering during the beam splitting process.

Laser sources

The ECDLs we use in our experiment are based on a laser diode in a linear external cavity set-up with an outcoupling mirror in cat-eye configuration. The coarse frequency selection is realized using an interference filter, while the diode current and a piezo actuator, which controls the position of the outcoupling mirror, allow for frequency fine tuning. Typical mode hop free ranges of these lasers amount
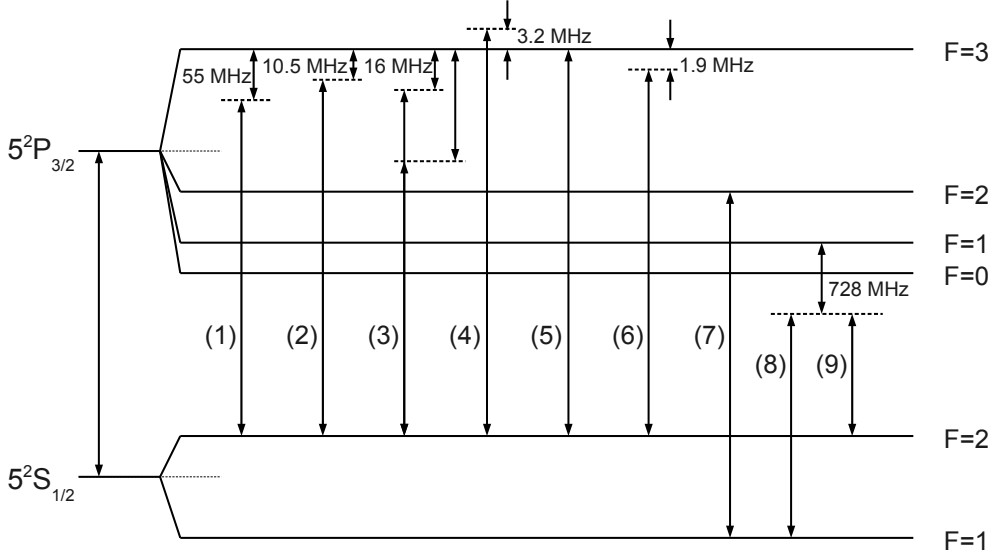
Figure 3.5: Required light fields. The purposes of the respective light fields are: (1) reference laser, locked with an offset to the $|5^2S_{1/2}, F = 2\rangle \rightarrow |5^2P_{3/2}, F = 3\rangle$-line, (2) 2D-MOT cooling light, (3) 3D-MOT cooling light with detuning for trapping and molasses cooling, (4) pusher light for loading rate enhancement in 2D-MOT, (5) 'blow away' light (-0.7 MHz), (6) detection light, (7) repumping light, (8) Raman laser 1 (ω_1), and (9) Raman laser 2 (ω_2).

to several GHz. The free-running Gaussian linewidth is below 200 kHz and the Lorentzian linewidth is in the order of 10 kHz. The continuous optical output power is up to 50 mW. The concept was first presented in [104].

Power amplification is realized using tapered amplifiers (TA), which are seeded using the ECDLs. The master oscillator power amplifier (MOPA) configuration is presented in [105]. The tapered diodes used in our configuration allow for power amplification of up to more than 20 dB while the spectral properties of the seed light are completely reproduced as the input and output facet are anti-reflection (AR) coated. We obtain continuous output powers of up to 1 W or 2 W per laser, respectively, with narrow linewidth.

Five MOPA configurations are used in our experiment as reference laser, for 3D and 2D cooling and coherent beam splitting using stimulated Raman transitions. For this, the relative phase of two ECDLs is locked onto an ultra-stable low-noise microwave reference.

In addition, we use a more compact laser set-up that provides high output power in a single-stage set-up by self-seeding a tapered amplifier diode. This diode features a finite reflectivity at the output facet, which, together with a high-reflection (HR) mirror at the input facet, forms the laser cavity. Frequency
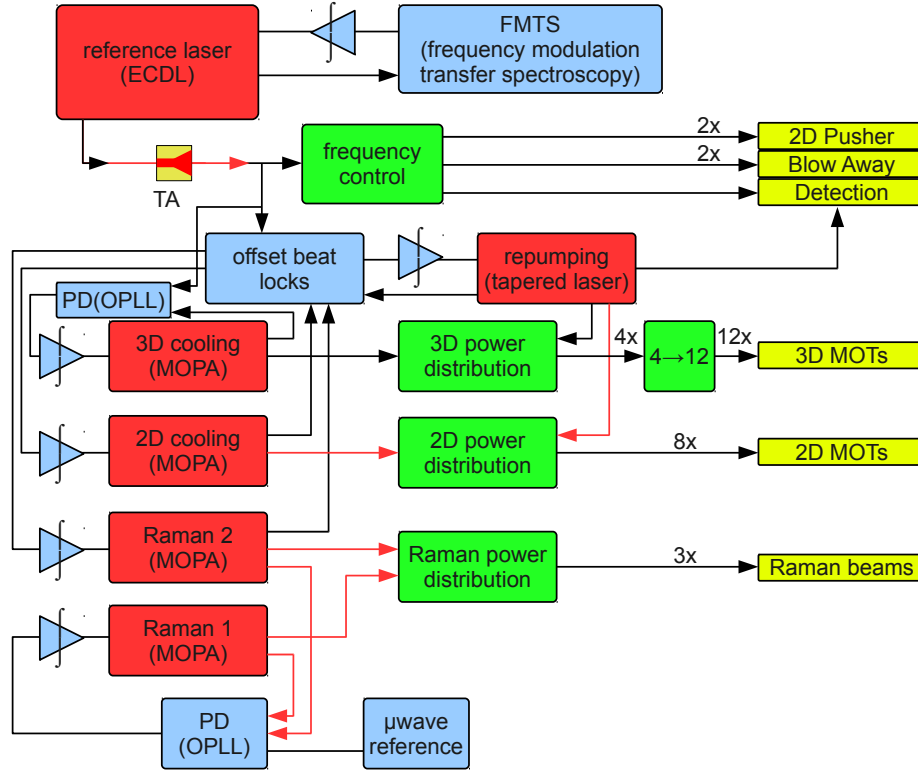
Figure 3.6: Laser set-up. *Red*: laser sources. *Blue*: beat set-ups and electronic frequency controls. *Green*: optical frequency control and power distribution using AOMs. *Yellow*: experimental purpose. The black arrows represent fiber connections while free space laser beams are depicted with red arrows. Electric connections are shown as black lines. (AOM: acousto-optic modulator, PD (OPLL): phase detector for the optical phase-locked loop, ECDL: external cavity diode laser, MOPA: master oscillator power amplifier, TA: tapered amplifier.)

selection is realized the same way as in the case of the presented ECDLs. This so-called tapered laser (TL) is characterized and compared to the ECDLs in [106]. It serves as source for repumping light in our experiment.

Light field frequency control and distribution

The laser frequencies need to be well controlled with respect to the desired atomic transition frequencies. Therefore, a reference laser system is employed which provides an absolute frequency standard using an error signal generated in a frequency modulation transfer spectroscopy (FMTS) with a Rubidium vapor cell. An uncertainty of 100 kHz is achieved with a long term stability of 92 kHz [55]. The laser sources used for cooling, repumping and beam splitting are stabilized on this laser
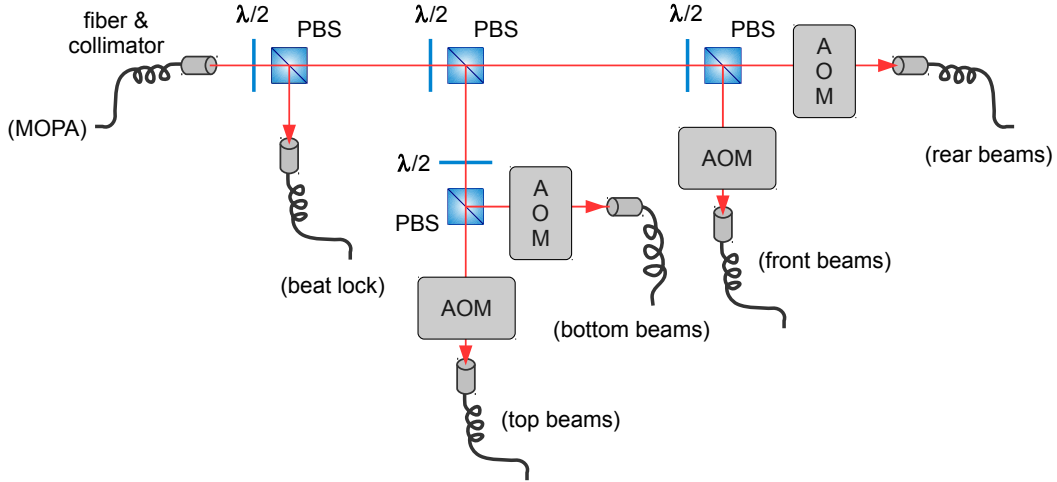
Figure 3.7: 3D-MOT light field distribution. The 3D-MOT light fields are controlled in frequency and power using AOMs. The mirrors for the alignment of the AOM passes and fiber coupling are not depicted. (AOM: acousto-optic modulator, $\lambda/2$: half-wave plate, PBS: polarizing beam splitter.)

with offset beat locking schemes. The frequency control and power distribution scheme of the employed laser system is depicted in figure 3.6. Details on the frequency control can be found in [54].

The light coming from the reference laser module can be shifted to the desired frequency for detection, pushing in the 2D-MOT, and pushing the atoms out of the interferometer zone ('blow away') using two subsequent passages through acousto-optical modulators (AOM). With these, we can switch between the fiber couplings for the different purposes and control the frequency at the same time. The 3D-MOT light fields have to be split into four frequencies, allowing for a precise control of the direction and velocity of the atomic launch using the moving molasses technique. The frequency control module is depicted in figure 3.7. After splitting the light into four beams and controlling the respective frequency detuning for the front, rear, top and bottom beams of the 3D-MOTs, the power is distributed in additional modules into four (rear and front) and two (top and bottom) fibers for the twelve 3D-MOT beams of the two atomic sources.

Raman laser 2 (emitting light with frequency ω_2) is frequency stabilized onto the reference laser using an offset lock. The relative frequency of the two Raman lasers is stabilized by realizing an optical phase-locked loop (OPLL), which locks the relative Raman laser phase onto an ultra-stable microwave reference by acting on Raman laser 1 (emitting light with frequency ω_1). The laser system is described in detail in [107]. The two needed Raman beam splitter light fields are superimposed with crossed linear polarizations. Before being guided to the experiment using
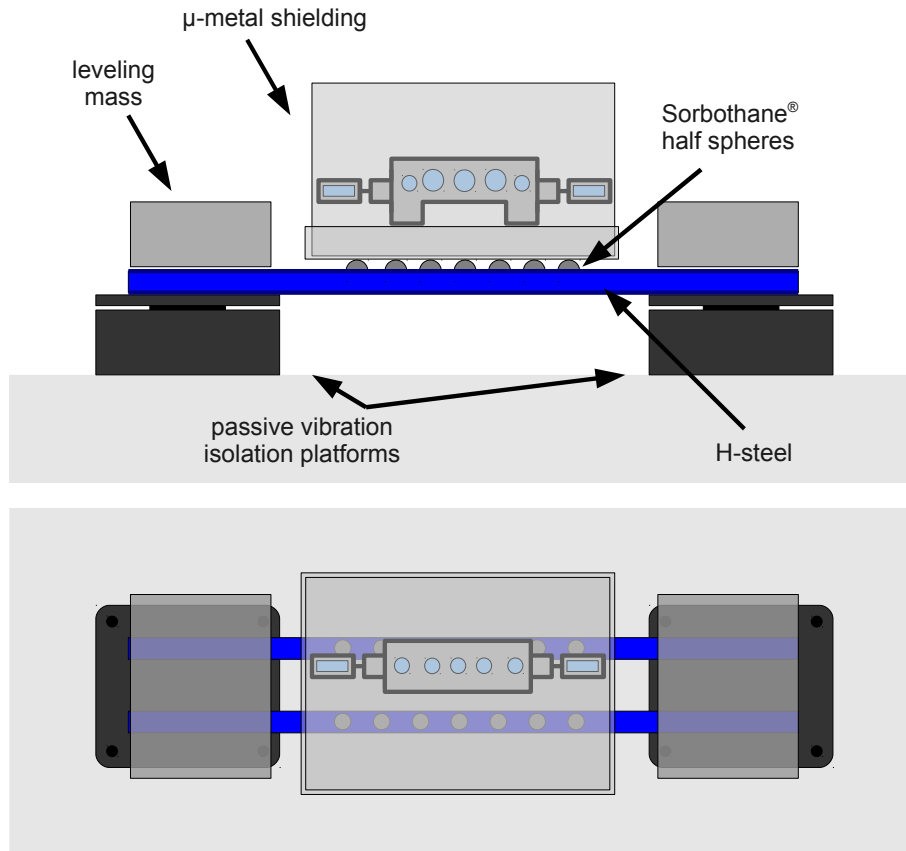
Figure 3.8: Vibration isolation platform. The vibration isolation platform set-up of the gyroscope is depicted in side view *(top)* and top view *(bottom)*. The μ-metal shield containing the apparatus mounted on a breadboard rests on two H-steel bars. The latter connect two passive isolation platforms. 14 `Sorbothane`® half spheres are introduced between the μ-metal shield and the steel bars in order to damp acoustic vibrations.

optical singe-mode fibers, a combination of a half wave-plate and a polarizing beam splitter allows us to set the intensity relation I_2/I_1 of the two Raman light fields for each interaction zone independently. The polarization is then parallel for the two beams. Switching and power control is realized with AOMs.

3.3.3 Vibration isolation platform

The experimental apparatus enclosed in the magnetic shield is placed on a vibration isolation platform in order to suppress vibrations of the reference planes, which are given by the retro-reflecting mirrors of the beam splitter light fields. The set-up is depicted in figure 3.8. It consists of two passive isolation platforms `MinusK 650BM-1`, which are rigidly coupled using two 10 cm H-steels of 2.5 m length. The

bottom part of the magnetic shield poses on 2×7 `Sorbothane`® half-spheres, which are distributed equally on the H-steels over the length of the μ-metal shielding. One leveling masses is placed above each isolation platform.

While the vibration isolation platform provides effective isolation from high frequency vibrations in vertical and horizontal direction, the orientation is not necessarily constant over long time scales. The platform tilt is monitored over time using a tilt sensor `Lippmann 1K-Plattform-Tiltmeter` over a period of about 30 hours. Typical tilts of approximately 10 μrad are observed within periods of 1000 s. Furthermore, a large tilt of up to 50 μrad is observed over long time scales (see figure 3.9).
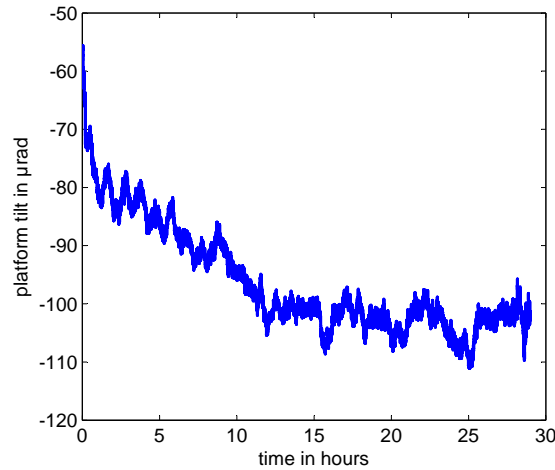

Figure 3.9: Platform tilt. The plot shows the tilt of the vibration isolation platform over time. The temperature dependence of the tilt sensor is 2.2 μrad/K and the temperature is typically stable within 1 to 2 K.

In order to exclude rotations of the isolation platform from limiting the sensor performance, the platform orientation is tracked using an optical lever. The measurement shows a periodic behavior of the platform orientation with a periodicity of about 1800 s and a peak-to-valley value of less than 1 μrad. With this, the platform orientation is found to cause rotation rates in the lower 10^{-9} rad/s regime, which will not limit our measurement.

3.3.4   Optics for the coherent manipulation of the atoms

Coherent atomic beam splitting using stimulated Raman transitions necessitates the application of two monochromatic light fields with well-controlled relative frequency and phase. The beam profile has to be large compared to the size of the atomic ensemble in order to assure a homogeneous Rabi frequency and thereby
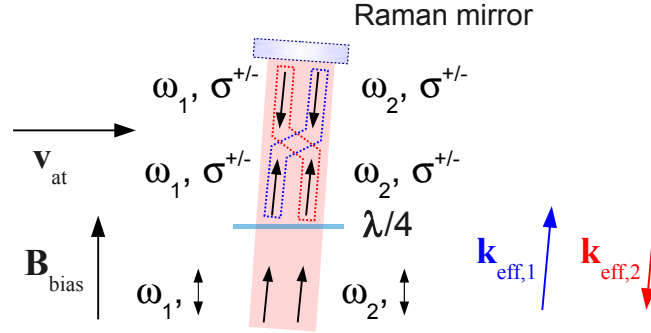
Figure 3.10: Raman beam polarization configuration. The incident parallel linear polarizations are transformed into circular polarizations, which, in combination with the magnetic bias field **B**, in light fields that allow to drive σ^+ or σ^- transitions, depending on the orientation of the quarter-wave plate ($\lambda/4$). The finite angle of the mirror surface and the atomic trajectory allows for selecting the desired effective wave vector $\mathbf{k}_{\mathrm{eff},1}$ or $\mathbf{k}_{\mathrm{eff},2}$ by choosing the respective relative Raman laser frequency $\nu_R = (\omega_1 - \omega_2)/(2\pi) = (\omega_0 \pm \omega_D + \omega_r)/(2\pi)$. The respective wave vector directions are inverted when inverting the atomic velocity $\mathbf{v}_{at}$.

an effective beam splitting. The beams of the lasers Raman 1 and Raman 2 are superimposed and then guided to the experimental set-up for the application in the three interaction zones. The light guides are three polarization maintaining single-mode fibers in which the light fields propagate with parallel linear polarization. For beam collimation we use an achromatic lens $f = 200$ mm focal length and $d = 50.8$ mm diameter for each beam. Before the beams of approximately $w_0 = 19$ mm waist pass through the interferometer section of the vacuum chamber, zero-order quarter-wave plates create circular polarizations of identical helicity for both fields.

One retro-reflective mirror for each beam allows for the creation of two pairs of counter-propagating light fields for velocity-selective Raman transitions with momentum transfer $\hbar\mathbf{k}_{\mathrm{eff}}$. The mirrors for retro-reflection of the Raman light fields (Raman mirrors) are aligned parallel to each other with regard to the effective wave front orientation in the vacuum chamber. This is described in detail in section 3.4.5. A horizontal Doppler angle between the mirror surface and the atomic forward velocity is chosen to be $\alpha_D = 3°$. This allows us to select the desired direction of $\mathbf{k}_{\mathrm{eff}}$ by tuning the relative Raman laser frequency (see section 3.4.2). The resulting pairs of Raman beams and the counter-propagating pairs inducing velocity selective stimulated Raman transitions are shown in figure 3.10.

Setting up the Raman beams in a retro-reflective configuration results in common mode rejection in the relative phase for most of the optical path from the laser to the atoms. Only the path between the atoms and the retro-reflective mirror is
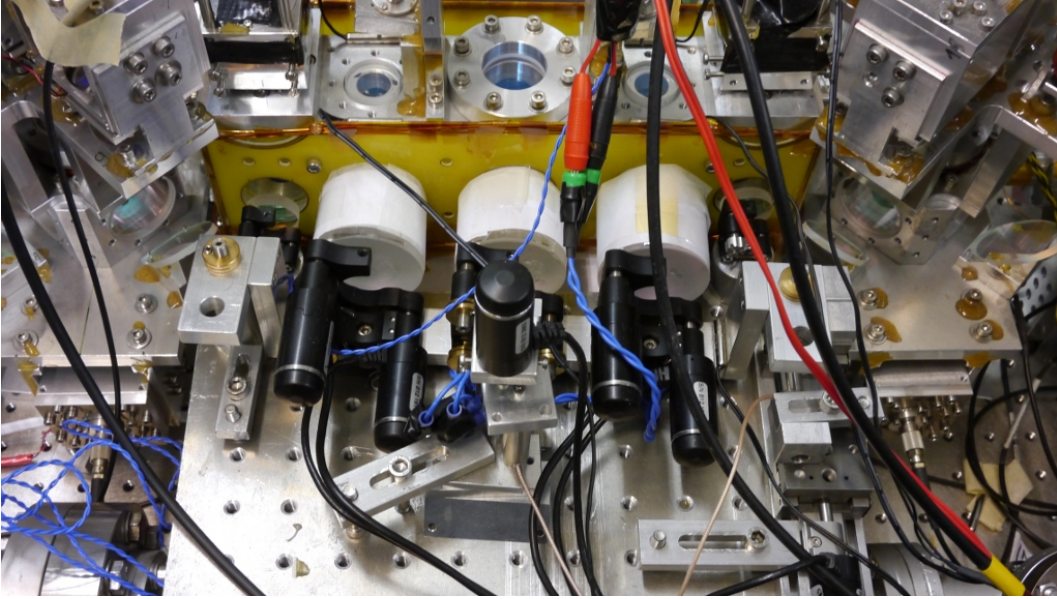
Figure 3.11: The Raman mirror bench. The Raman mirror bench carries all three mirrors used for retro-reflection of the Raman beam splitter light fields. It is stabilized in temperature using power resistors attached to the bottom. The bench itself is controlled in vertical and horizontal orientation using ultra-high resolution piezo step motors for coarse and piezo stacks for fine alignment. The two outer mirrors can be aligned using the same ultra-high resolution step motors in mirror mounts. The beam paths are isolated against air convection using paper tubes that are loosely attached to the bias field coil board.

not common to both light fields and thus induces temporal phase fluctuations due to a finite travel time coupled with relative laser phase fluctuations [108]. Also, the optical wave front of the effective beam splitting process is defined by the orientation and aberration of very few optical elements, namely the vacuum chamber windows and the retro-reflective mirror itself. In particular, the relative mirror angular alignment is crucial for the atom interferometer signal contrast [57]. Hence a good control of the respective mirror angle of a few μrad is mandatory for a stable and reliable rotation measurement.

For this purpose, we utilize a temperature stabilized and remote controllable aluminum mirror bench carrying all three $2''$-mirrors of type `Thorlabs BB2-E03` mounted on `Newport U100-A` mirror mounts (see figure 3.11). The mirrors are glued onto the mounts in order to realize a rigid compound and thus to minimize acoustic vibrations of the mirrors. The vertical and horizontal tilt alignment of the outer two mounts are remotely controlled using `Newport NanoPZ` high precision step motors, which allow for an effective angle resolution below the μrad. The mirror bench itself is remotely controlled in its vertical and horizontal orientation using `Newport NanoPZ` motors for coarse and piezo stacks for fine control. A

`Piezomechanik PSt 150/7/40` piezo stack allows for addressing a horizontal angle of 600 μrad and a `Piezomechanik PSt 150/7/20` for controlling the horizontal mirror orientation within 80 μrad by applying a voltage of 0 to 150 V to each of the piezo stacks.

The mirror mount is temperature stabilized slightly above the temperature of the structures in its proximity by heating the bottom of the aluminum structure using three power resistors, one underneath each of the mirror mounts. The temperature is read out using a NTC resistor. The NTC resistor value is read out and used for temperature stabilization with a `Newport 350 B` temperature control unit controlling the current in the power resistors. The control loop features a diode in order to only allow heating when the temperature is below the set point value[1]. The typical temperature stability of the bench is found to be better than 1 K. More importantly, the temperature is kept within this range over a long time preventing for hysteresis effects due to temperature induced expansion in the mirror mounts to cause a relative beam splitter mirror misalignment. The alignment is also retained during maintenance procedures that require the removal of the μ-metal shield although this causes harsh changes of the mirror bench surrounding.

3.3.5 Computer control and data acquisition

The experimental parameter control and timing is realized using one control computer and one real time computer featuring a field-programmable gate array (FPGA). The software architecture bases on `LabVIEW 2010`. A detailed description of the computer control can be found in [54]. As small modifications have been made compared to [54], the system is briefly described here. An overview is shown in figure 3.12.

The control computer allows for setting up the experimental parameters and timing, that are transmitted via an Ethernet connection to the real-time computer. Here, the FPGA controls the transistor-transistor logic (TTL) signals for switching, the analog output cards for experimental parameter set-point control, and the direct digital synthesizer (DDS) cards. The atom photodiode signal and auxiliary signals of the tiltmeter and temperature sensors are read in with the aid of two analog input cards in the control computer.

The 3D-MOT laser global detuning and beam power are controlled using an arbitrary wave form generator (AWG) `LeCroy ArbStudio 1104`, which is configured using the control computer. A TTL trigger allows us to synchronize the AWG output with the experimental timing. The beam power output steers voltage controlled attenuators on the four AOMs in the 3D-MOT light distribution (see figure 3.7). While the global 3D-MOT detuning is chosen by using an AWG output signal for frequency mixing in the offset lock, the front, rear, top and bottom beam

---

[1]The actual temperature value is slightly smaller than the set point due to the diode's finite threshold voltage.
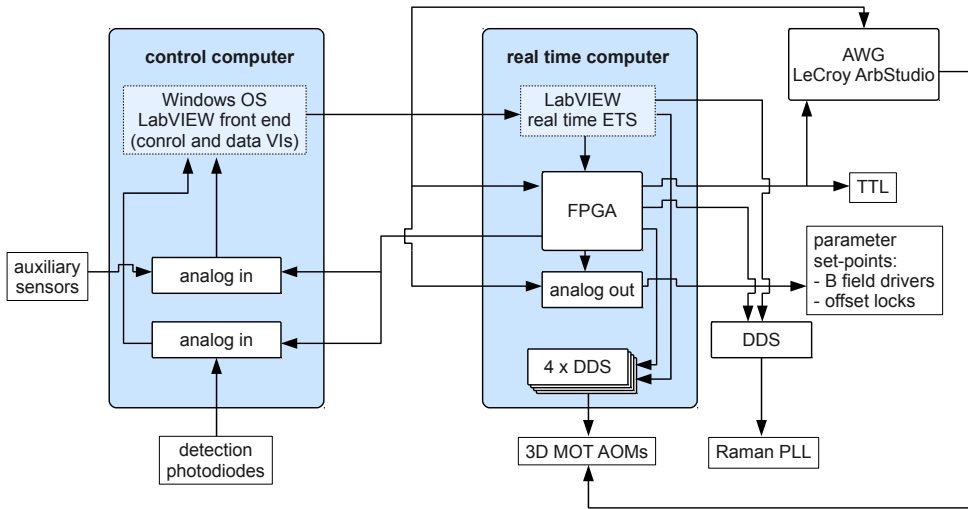
Figure 3.12: Computer control schematic. The experiment control consists of two computers, one control computer and one real time computer featuring a FPGA.

frequency detuning for the moving molasses are controlled using the AOMs with four of the DDS cards as radio frequency (RF) sources. One DDS card enables the frequency and phase control of the Raman laser phase-locked loop. This results in a direct control of the relative Raman laser frequency and phase.

The piezo motors are connected to the control computer via USB, which allows to steer the global and relative Raman mirror orientation using either the provider software or LabView®. The piezo stacks are steered by a high-voltage source Thorlabs MDT693A. We can realize modulation of the mirror bench orientation by applying an AWG signal to the modulation input of the latter.

3.4 Measurement sequence

The atom interferometer measurement is pulsed with a typical cycle time of $T_c < 0.5$ s. Each cycle can be divided in four parts. After the atoms are trapped in the magneto-optical traps, they are launched onto parabolic trajectories using the moving molasses technique. As a next step, the input state is prepared in each interferometer before the Mach-Zehnder pulse sequence is applied. The last step is the determination the transition probability in a hyperfine state selective fluorescence detection. The single steps of the experimental sequence are described in the following.

3.4.1 Atom trapping, cooling and launching

During the first part of the atom loading and launch sequence, the 2D-MOT loads the 3D-MOT with a typical loading rate of 10^9 atoms/s for 210 ms. The 2D-MOT coils have high inductance and are therefore switched off first. This initiates the timing procedure for cooling and launching shown in figure 3.13. After this, the 2D-MOT light is far detuned, which effectively switches off the 2D-MOT. At the same time, the 3D-MOT fields are switched off with a reverse voltage pulse of 0.9 ms for fast switching. While the 3D-MOT detuning is -2.7Γ during the loading sequence, it is further detuned after switching off the magnetic field. Here, $\Gamma = 2\pi \cdot 6.0666$ MHz is the ^{87}Rb D2-line linewidth. The detuning value in the case of far detuning is not exactly determined. The set-point being very far from resonance (-230 MHz) is not completely reached by the cooling laser. However, this set-point results in a reproductive and cold atomic temperature in the moving molasses mentioned hereafter.

During the launch procedure depicted in figure 3.13, the 3D-MOT light is first tuned to be -2.7Γ in order to realize an effective scattering and thereby an effective atomic acceleration. At the same time, the front, rear, top and bottom beam detunings of the 3D-MOTs are chosen such that they are compensated by a Doppler shift of atoms moving with velocities of $v_x = 2.79$ m/s ($v_x = -2.79$ m/s for the second source, respectively) and $v_y = 0.73$ m/s. This results in launching the atoms on the desired parabolic trajectories. The acceleration phase is followed by a moving molasses cooling phase, in which the 3D-MOT light is again far detuned using the same set-point mentioned above with a frequency ramp of 1 ms length. Simultaneously, the MOT beam intensities are ramped down within 2 ms. The repumping light is switched off 3.2 ms after the MOT cooling light in order to pump all atoms to the $|5^2S_{1/2}, F = 2\rangle$ manifold after launch.

3.4.2 Preparation of the interferometer state

After the atomic ensembles have left the atom sources, they are distributed over the $|5^2S_{1/2}, F = 2\rangle$ Zeeman manifold and feature an ensemble temperature of $\Theta_1 = 10$ μK and $\Theta_2 = 8$ μK. A first velocity selective Raman pulse [109] with a width of 25 μs selects an ensemble with a momentum width in the beam splitting direction corresponding to a temperature of 1.2 μK. The Doppler angle of $\alpha_D = 3°$ allows to choose between the two possible transitions driven by the two counter-propagating Raman beam pairs with the wave vector $\mathbf{k}_{\text{eff},1}$ and $\mathbf{k}_{\text{eff},2}$ as depicted in figure 3.10. For this, the Raman laser frequency difference is tuned to be resonant with $\omega_0 \pm \omega_D + \omega_r$, where ω_0 is the frequency of the Doppler insensitive transition, $\omega_D = \mathbf{v}_{at} \cdot \mathbf{k}_{\text{eff}}$ is the Doppler frequency and ω_r is the atomic recoil frequency of the two-photon transition.

After the application of the velocity selective Raman pulse, the atoms remaining in the $|5^2S_{1/2}, F = 2\rangle$-manifold are removed from the ensemble using the 'blow
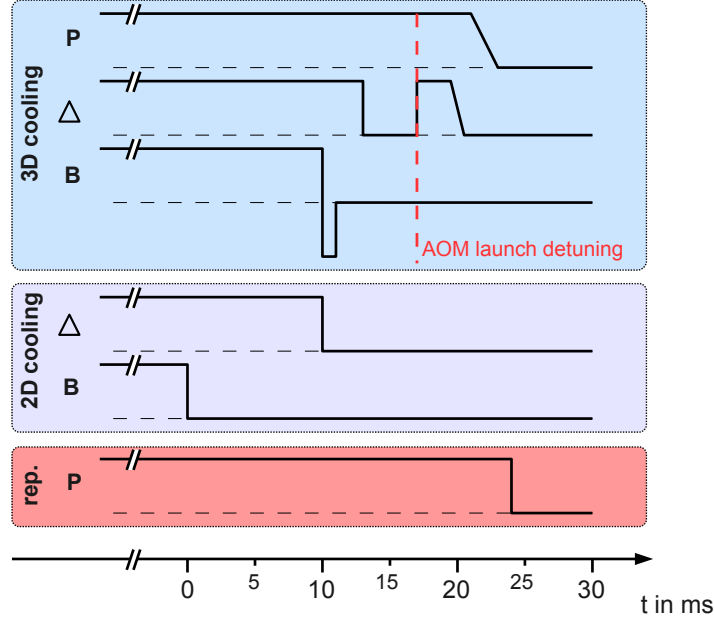
Figure 3.13: Parameter timing in the launch sequence. The schematic depicts the optical power (P) and global detuning (Δ) values for the 3D-MOT and 2D-MOT cooling lasers and the repumping laser. The magnetic fields (B) are switched off in advance such that the magnetic gradients are zero at the beginning of the atomic launch. The 3D-MOT field shut down is realized with a reverse voltage pulse.

away' beam, which leaves the velocity selected atoms in the interferometer ground state $|g\rangle$ plus a small amount of atoms in the $|5^2S_{1/2}, F = 1, m_F = \pm 1\rangle$-states: The spontaneous emission induced by single-photon transitions during the Raman pulse lead to a spontaneous decay to $m_F = \pm 1$ Zeeman sub-levels of the $F = 1$ and $F = 2$ manifold. While the atoms in the $F = 2$ manifold are removed after the preparation pulse using the 'blow away' beam, the $|5^2S_{1/2}, F = 1, m_F = \pm 1\rangle$-states remain. This creates a small background in the interferometer signal of approximately 5 % in transition probability.

3.4.3 Beam splitter pulse application

The Raman beam splitting light fields are applied when the atomic ensembles are in the center of each of the beam splitter application zones. The typical pulse duration is $\tau_{\pi/2} \approx 12$ μs in the application zones T1 and T3 for the beam splitting pulses, and $\tau_\pi \approx 15$ μs in the application zone T2 for the mirror pulse.
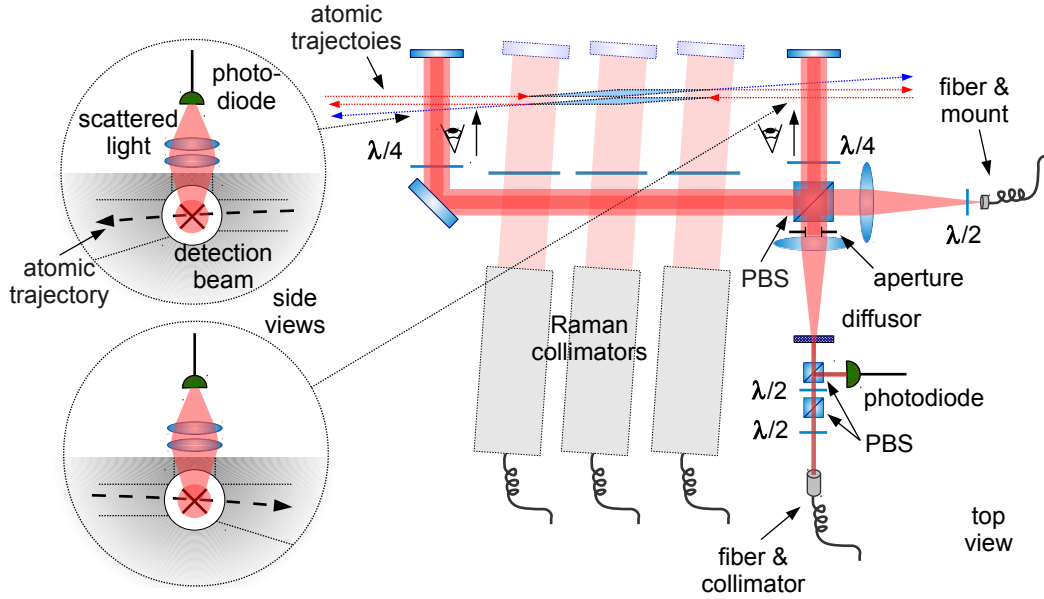
Figure 3.14: Schematic of the detection set-up. The detection and repumping light fields are common to both detection zones with opposite circular polarization. The fluoresced light is detected using a double-lens system and a large area photodiode in each interferometer. ($\lambda/2$: half-wave plate, $\lambda/4$: quarter-wave plate, PBS: polarizing beam splitter.)

3.4.4 State selective fluorescence detection

We determine the transition probability on the output of the atom interferometers using a hyperfine state selective fluorescence detection. After the atoms have been split, reflected and recombined during the Mach-Zehnder interferometer sequence, both ensembles travel trough a detection area, one for each interferometer (see figure 3.14).

The detection and repumping light fields applied to the two atomic ensembles are common to both interferometers[2]. The repumping light coming from a fiber is collimated using a single lens, whereas the detection light is collimated first, in order to realize a power monitoring on the exit of the fiber. A diffusor plate (`Thorlabs ED1-S20-MD`) is used to create a diverging beam with a flat intensity profile, which is then collimated by a single lens of focal length $f = 75$ mm. With a detection beam power of $P_{det} = 8$ mW, this results in a detection intensity of $I_{det} \approx 2.3$ mW/cm^2 $= 1.37\ I_{sat}$, where $I_{sat} = 1.669$ mW/cm^2 is the saturation

---

[2]The polarization is not the same in the two interferometers, which results in an effective driving of the $|5^2S_{1/2}, F = 2, m_F = 2\rangle \rightarrow |5^2P_{3/2}, F = 3, m_F = 3\rangle$ transition in one and of the $|5^2S_{1/2}, F = 2, m_F = -2\rangle \rightarrow |5^2P_{3/2}, F = 3, m_F = -3\rangle$ transition in the other interferometer. Taking into account the applied bias field, the frequency offset between the two transitions is approximately 3 MHz.
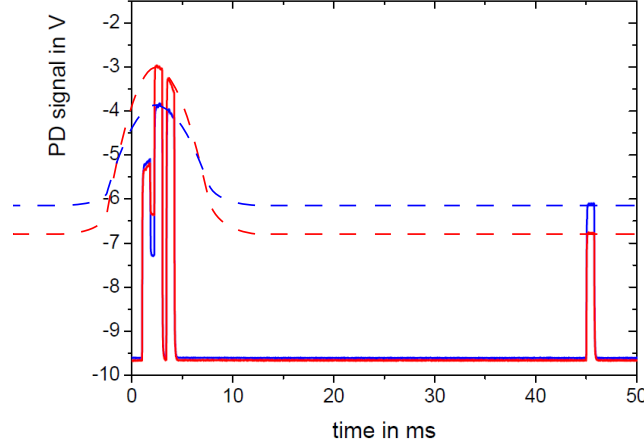
Figure 3.15: Detection signal. The photodiode signals of atom interferometers 1 *(blue)* and 2 *(red)* are depicted for a typical detection signal. An offset of -10 V is added during amplification. The *dashed lines* indicate the atomic signal for the total atom number for the case of light turned on during the whole sequence.

intensity for the $|5^2S_{1/2}, F = 2\rangle \rightarrow |5^2P_{3/2}, F = 3\rangle$ transition driven by σ-polarized light. An aperture is introduced into the detection beam in order to realize a circular, almost flat intensity profile. The aperture diameter of approximately 10 mm shows the best trade-off in the relation of light scattered by the atoms to background light. A schematic of the detection beam set-up is depicted in figure 3.14.

We detect the scattered light using the photodiodes that are mounted on the top of the vacuum chamber (see figure 3.14). The signals of the detection process with a typical atom signal are shown in figure 3.15. The profile of the scattered intensity over time results from the convolution of the spatial profile of the atomic cloud and the detection laser intensity profile, which is indicated by the *dashed lines* in the photodiode signal. The detection process consists of the following five pulses.

1. **Detection of S_e:** A detection light field pulse on the $|5^2S_{1/2}, F = 2\rangle \rightarrow |5^2P_{3/2}, F = 3\rangle$ transition with circular polarization is applied in a retro-reflected configuration with a pulse duration of 800 μs. After a few scattering processes this light field drives a closed transition being $|5^2S_{1/2}, F = 2, m_F = 2\rangle \rightarrow |5^2P_{3/2}, F = 3, m_F = 3\rangle$ (or $|5^2S_{1/2}, F = 2, m_F = -2\rangle \rightarrow |5^2P_{3/2}, F = 3, m_F = -3\rangle$). Spontaneous decay to the $|5^2S_{1/2}, F = 1\rangle$ manifold is effectively suppressed. The scattered light is detected and results in the excited-state signal S_e.

2. **Repumping:** After the first pulse, the atoms in the $|5^2S_{1/2}, F = 1\rangle$-state

are brought to the $|5^2S_{1/2}, F = 2\rangle$-state by applying a repumping pulse of 400 μs duration.

3. **Detection of S_{total}:** A second detection pulse of 800 μs duration allows to detect the total number signal of atoms in both interferometer states S_{total}.

4. **Cloud arrival time pulse S_c:** A third detection light pulse of 800 μs duration is applied with a separation to the former of 400 μs. The pulse is applied on the side slope of the detected Gaussian profile, which enables an arrival time determination using the relation of the arrival time pulse signal height to the total atom number signal.

5. **Background light detection S_{bg}:** After the atoms have left the detection zone, a last 800 μs long pulse of detection light is applied in order to determine the background light due to reflections on the apparatus itself.

From the detection signals that are given by the mean values of the temporal photodiode signal within the respective pulse period, the transition probability is derived in two steps: First, the background S_{bg} is subtracted from the signals S_e, S_{total} and S_c. The power monitoring on the fiber exit is used to correct for slow fluctuations of the detection light power that are common to the atom signal and the monitoring signal. This results in the signals N_e, N_{total} and N_c, which are proportional to the respective convolution signal, and to the excited state and total atom number, respectively. Second, the arrival time fluctuations are corrected using the information gained in the third pulse. For this, we consider the transition probability being calculated via

$$P_e \quad = \quad \frac{N_e}{N_{total}}. \tag{3.21}$$

Here, an arrival time fluctuation of the atomic ensemble results in an effective error in the determination of the transition probability. The three pulse scheme allows for a suppression of this influence. N_{total} is does not vary in the presence of small arrival time fluctuations as the timing is chosen such that this pulse is applied on the apex of the time of flight profile. The third pulse is on the slope of the time of flight signal and the changes arising from arrival time fluctuations are opposed to those of the N_e signal. We realize a compensation of the arrival time induced fluctuations in N_e in the calculation of the transition probability. The arrival time of the atomic ensemble induces a variation in the relation

$$\varepsilon_{AT} = \frac{N_c}{N_{total}}, \tag{3.22}$$

which therefore is a measure of the arrival time for small variations. If the three pulses are symmetric with respect to the detection profile center, this will be

denoted $\varepsilon_{AT,0}$. We approximate the first and third pulse signal by

$$N_e' \quad = \quad N_e \left(1 + s_e \cdot t_{AT}\right) \tag{3.23}$$
$$N_c' \quad = \quad N_c + s_c \cdot t_{AT}, \tag{3.24}$$

where s_e and s_c are the respective slopes for arrival time changes onto the signals N_e and N_c, respectively, and t_{AT} is the mean arrival time. Eliminating the arrival time results in

$$N_e \quad = \quad \frac{N_e'}{\frac{s_e}{s_c}\left(N_c' - \varepsilon_{AT,0} N_{total}\right) + 1}, \tag{3.25}$$

which is the corrected atom number in the excited state. The transition probability than reads

$$P_e \quad = \quad \frac{N_e'}{N_{total}\left[\frac{s_e}{s_c}\left(N_c' - \varepsilon_{AT,0} N_{total}\right) + 1\right]}. \tag{3.26}$$

This simplifies to (3.21) with a correction factor ε_{AT} if the pulses are perfectly centered around the center of the detected profile. The parameters s_e, s_c and $\varepsilon_{AT,0}$ are determined by introducing a delay into the experimental timing sequence before the detection sequence. The difference between detection with and without arrival time correction is qualitatively shown in figure 3.16. Here, two subsequently recorded Rabi oscillation measurements are shown for both interferometers. We have scanned the arrival time delay over 1 ms for each Raman pulse duration within the Rabi scan in order to emulate an arrival time variation. While the transition probability varies in the case without compensation, the compensated transition probability does not depend on the delay. As N_2 is slightly reduced being recorded on the side of the detection profile, the transition probability is not optimally normalized. However, the phase measurement is not harmed by this circumstance as the transition probability variations are always treated relative to the signal contrast.

3.4.5   Measurement set-up

The rotation measurement demands an adjustment of the differential AC-Stark shift, the interferometer horizontality and the relative Raman beam splitter light field orientations, which are described in the following. After that, the k-reversal technique, which allows us to suppress systematic effects and long term drifts, is introduced.

Differential AC-Stark shift compensation

The differential AC-Stark shift is compensated by adjusting the relative laser intensity of two Raman light fields in each of the interaction zones individually. For
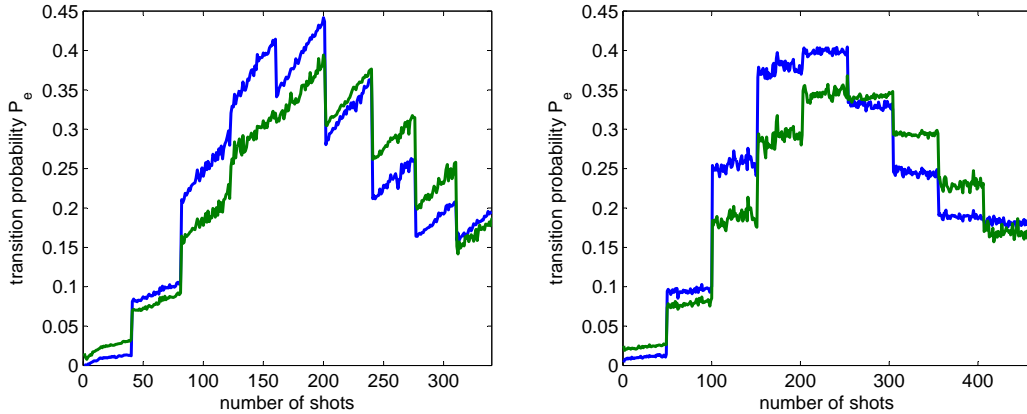
Figure 3.16: Arrival time drift compensation. Rabi oscillations with counter-propagating Raman beam splitter light fields are depicted for the detection of atom cloud 1 *(blue line)* and 2 *(green line)* (see figure 3.1). For each pulse duration value, a delay is scanned in the experimental sequence producing an effective arrival time offset with a span of 1 ms for each scan. While the transition probability changes with the arrival time in the case without compensation *(left)*, it does not in the case with compensation *(right)*.

this purpose, we apply a Mach-Zehnder sequence with small interrogation times T of 1 and 3 ms in the first and third (T1 and T3), and in the second interaction zone (T2), respectively. Between the second and third beam splitter pulse, an off-resonant Raman light field pulse is applied with a typical duration of a $3\pi/2$-pulse in the case of T1 and T3 and of a 3π-pulse in the case of T2. Switching this off-resonant pulse on and off in subsequent measurements allows for minimizing the absolute differential AC-Stark shift by minimizing the resulting relative phase offset by adjusting the Raman light field intensity ratio I_2/I_1 in each interaction zone.

The residual transition probability offset is below 10^{-2} for subsequent measurements, which results in a phase uncertainty of 20 mrad for fringe contrast of 25 %. Given a pulse duration of 30 μs, this corresponds to a residual differential AC-Stark shift of

$$\delta_{AC} \approx 2\pi \cdot 100 \text{ Hz}.$$

Interferometer horizontality

The orientation of the enclosed area relative to **g** is ensured using a long velocity selective Raman pulse for the descending atomic ensembles, meaning in the third beam splitter interaction zones of each of the interferometers. After a preparation pulse of $\tau_\pi = 25$ μs duration and a subsequent 'blow away' beam, which removes the residual atoms in the first zone, a second velocity selective Raman interroga-

tion pulse is applied in the last zone using reduced Raman light field intensity and a duration of $\tau_\pi = 50$ μs. At the moment of pulse application, the atoms have gained a vertical velocity of $v_{at} = g \cdot T = g \cdot 23$ ms ≈ 0.226 m/s, which results in an effective Doppler shift of $\nu_{Doppler} = 578$ kHz$\cdot\alpha$ with $\alpha = \cos^{-1}\left(\mathbf{k}_{\text{eff}} \cdot \mathbf{g} / (|\mathbf{k}_{\text{eff}}||\mathbf{g}|)\right)$. As the two interferometers employ effective wave vectors of opposite direction, the frequency offset has opposed signs for the two. Aligning the Raman retro-reflection mirrors' horizontality is realized by superimposing the Raman spectroscopy profiles of the two counter-propagating ensembles by changing the vertical orientation with the aid of the piezo step motor for coarse vertical alignment presented in section 3.3.4. Here, We presume other frequency offsets to be small against the offset arising from the Doppler shift. For a frequency uncertainty of 2 kHz, an uncertainty of

$$\sigma_\alpha \quad < \quad 2 \text{ mrad}$$

can be deduced for the horizontal alignment of the interferometer area. Taking into account the scaling factor of the rotation measurement, an uncertainty of below $5 \cdot 10^{-8}$ rad/s results for the absolute rotation value. This alignment is only a coarse alignment and needs to be refined for absolute accuracy studies of the rotation measurement.

Raman mirror relative alignment

The respective mirror alignment is crucial for the contrast of the interferometer signal (see section 3.2). An alignment scheme has been invented that uses the atom interferometers in different configurations in order to maximize the fringe contrast by finding the optimal relative beam splitter light field alignment [57]. The FWHM angle of the relative alignment depends on the atomic cloud initial size and temperature for a given pulse separation time T. For typical values of our experimental set-up, the alignment tolerance is in the range of tens of μrad. The alignment scheme is described in further detail in [56] and will only be briefly outlined here.

A coarse alignment of the three Raman collimation telescopes is realized using one large mirror, which has a total usable aperture of 170×40 mm^2 and a specified surface flatness of $\lambda/20$. The Raman beam pointing is aligned by maximizing the amount of light coupled back into the optical fibers. In a second step, the mirror is replaced by three single mirrors on the Raman mirror bench. The latter is depicted in figure 3.11. By maximizing once again the coupling efficiency back into the fiber, the mirrors are aligned parallel to each other. This technique allows for high precision in the relative vertical and horizontal tilt alignment of the three retro-reflective mirrors. However, the optimal alignment for the atom interferometer is different from the perfect parallel alignment as the vacuum windows are slightly
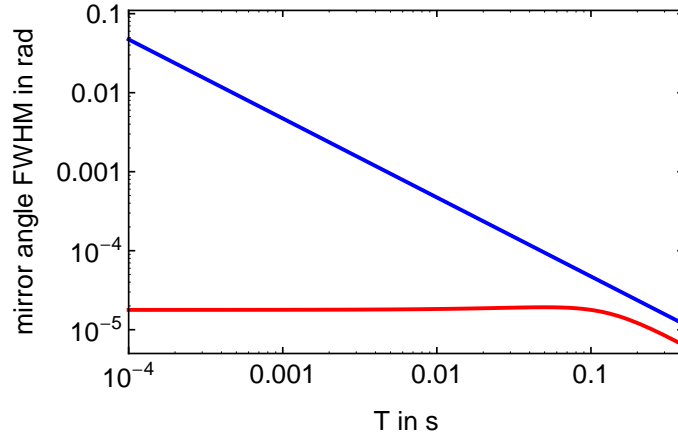
Figure 3.17: Vertical relative mirror alignment tolerance. The graph depicts the vertical relative mirror alignment tolerance as FWHM values for the signal contrast in dependence of the relative mirror angle for a Mach-Zehnder *(red line)* and a SRB geometry *(blue line)*. In the case of the Mach-Zehnder geometry, the second mirror angle in relation to the first and third mirror is considered. The two pairs of $\pi/2$-pulses of the SRB scheme are considered to be applied each on one mirror. The parameters used for the calculation are the atomic temperature $\Theta = 10 \ \mu K$, the initial cloud size of $\sigma_y = 3.8$ mm and the time of the application of the first pulse $t_1 = 50$ ms.

wedged in order to prevent for etalon effects. Therefore, the optimal relative mirror orientations are found using the atom interferometer signal itself. This allows for a parallel alignment of the wave fronts at the position of atom-light interaction.

The Mach-Zehnder interferometer scheme alignment tolerance is defined by the initial cloud size and temperature as well as the pulse separation time T. Whereas a SRB scheme consisting of four $\pi/2$-pulses is only sensitive to the cloud temperature and to the separation time of the first and second (third and fourth) pulse if the two pairs are each applied on a single mirror (see section 3.2.1). Furthermore, the pulse separation time can be chosen in the range from 0 up to 8 ms in our apparatus. The alignment tolerance is depicted as FWHM-angle for the contrast for a Mach-Zehnder and a SRB geometry in figure 3.17.

The alignment procedure consists in maximizing the interferometer signal contrast for a SRB scheme for increasing times T. This is applied on the first and second interaction zone of each of the atom interferometers. The FWHM decreases with growing T and allows for a more and more precise relative vertical and horizontal tilt mirror alignment of the mirrors T1 and T3 with respect to T2 using the interferometer signal contrast of interferometer 1 and 2, respectively. If this accuracy is not sufficient for the realization of a Mach-Zehnder interferometer, an additional SRB scheme with pulse applications of the first and last pulse on the outer mirrors and the second and third pulse on the central mirror can be em-

ployed. This scheme shows the same sensitivity to the initial cloud size as the Mach-Zehnder scheme. However, T can be chosen slightly smaller than the minimal separation time T in a Mach-Zehnder geometry corresponding to a larger angular alignment tolerance.

The final alignment step is realized using the contrast of the Mach-Zehnder geometry. For this, it can be shown that the optimal contrasts of the two interferometers only coincide with respect to the relative mirror angles if the wave fronts are parallel [56]. A beam walk like technique on the four angles of mirrors T1 and T3 allows for the fine alignment. The residual uncertainty is in the low μrad regime.

3.4.6   Rotation phase read out

From the determined transition probability P_e the phase measured in each interferometer can be deduced within an interval of $[0, \pi]$

$$
\begin{align}
P_{e,i} &= P_{0,i} + A_i \cdot \cos\left(\Phi_i\right) \tag{3.27} \\
\Rightarrow \Phi_i &= \cos^{-1}\left(\frac{P_{e,i} - P_{0,i}}{A_i}\right). \tag{3.28}
\end{align}
$$

Here, $P_{0,i}$ and A_i are the offset and amplitude of the interferometer signal. A so-called mid-fringe measurement consists in a repeated transition probability measurement for deliberately applied phase offset value chosen such that the mean transition probability corresponds to $P_{e,i} \approx P_{0,i}$. The measured phase for each interferometer cycle is then determined using (3.28). This phase read out faces two problems in the experimental realization. First, the platform tilt is not stable over longer time scales. A typical variation of tens of μrad of the platform tilt can cause fluctuations on the interferometer phases exceeding $\pi/2$. Second, drifts in the transition probability offset and amplitude can mimic phase fluctuations over time.

The platform tilt can be compensated using the mirror bench. This allows for locking the horizontality to one of the two interferometer signals, such that the acceleration phase is constant for both interferometers. At the same time, phase fluctuations caused by rotations can still be extracted via the average of the two phase values. Offset and amplitude fluctuations can be compensated using a more sophisticated measurement scheme employing not only measurements on the mid-fringe position, but also those closer to the top and bottom positions of the fringe. Fitting a fringe pattern to the obtained transition probabilities then allows for the determination of the interferometer phase as well as the fringe amplitude and offset.

In correlated interferometers, a parametric representation $(P_{e,1}, P_{e,2})$ forms an ellipse. The relative phase of the two interferometers is encoded in the orientation of the ellipse and can be extracted using an ellipse fit method. This is employed in

the cases of atomic gradiometry [110, 111] where the correlated shot-to-shot noise of the interferometers is large resulting in ambiguities in the phase read out via the fringe method. The ellipse fit method not only rejects correlated fluctuations in each shot and over longer time scales, but it also is insensitive to slow signal offset and amplitude variations. Although the sensitivity from shot to shot is reduced using this method, it is a useful, simple and robust tool for our case as the horizontal orientation varies slowly over time and the effective projected acceleration measurement of gravity acceleration causes the interferometer phases to fluctuate slowly.

Ellipse fitting with controlled phase modulation

While ellipse fitting is usually applied for phase read out in interferometers with strongly correlated noise, the same situation can be achieved using a modulation of the anti-correlated phase in order to determine the correlated phase (or vice versa). In our case, it is possible to apply a well controlled acceleration phase by slightly modulating the horizontal alignment of the beam splitting light fields and thereby the projection of $\mathbf{k}_{\text{eff}}$ onto the gravitational acceleration $\mathbf{g}$. For the pulse separation time of $T = 23$ ms and an angle of $\Delta\alpha = 75$ μrad we find an acceleration phase shift of $\Delta\Phi_a = 2\pi$ using (2.43). This allows us to apply large phase offsets on the acceleration signal of the correlated interferometers while modulation the rotation phase by a negligible amount. The latter can be seen as a variation of the projection $\mathbf{n}_A \cdot \mathbf{\Omega}_{Earth}$ with $\mathbf{n}_A = \mathbf{A}/|\mathbf{A}|$, which results in estimated fluctuations in the measured rotation rate and rotation phase values using (2.41) of

$$\Delta(\mathbf{n}_A \cdot \mathbf{\Omega}_{Earth}) \approx 1.2 \cdot 10^{-9} \, \frac{\text{rad}}{\text{s}}$$
$$\Delta\Phi_\Omega \approx 0.16 \text{ mrad}.$$

Besides the direct modulation of the rotation value due to the modulation of the area projection, the rotation phase measurement can experience an exceed in noise due to two effects. First, the rotation axis is not necessarily perfectly aligned to the mean axis of the first and second beam splitter. In this case, the angular modulation can induce an effective rotation phase modulation. Second, the modulation of the mirror bench can induce a movement of the whole experimental platform. This effect is most likely to come into play when the modulation frequency is close to a mechanical resonance frequency of the vibration isolation platform.

In order to exclude an increase in rotation noise due to the angular modulation of the Raman mirrors, the modulation is realized for different modulation frequencies. Indeed, an increased rotation phase noise level is observed for modulation frequencies as high as $\omega_{mod} = 2\pi \cdot 10$ Hz. However, the noise level for $\omega_{mod} = 2\pi \cdot 1$ Hz and $\omega_{mod} = 2\pi \cdot 100$ mHz is drastically smaller and does not diminish for lower frequencies. We use an angular modulation of $\alpha(t) = \alpha_0 \cos(\omega_{mod})$

with $\alpha_0 \approx 75 \ \mu$rad and $\omega_{mod} = 2\pi \cdot 100$ mHz for the realization of an ellipse fit each 10 s.

The ellipse fit method is chosen following the considerations in [110]. Here, the parametric representation $(P_{e,1}, P_{e,2})$ of the two transition probability signals

$$
\begin{aligned}
P_{e,1} &= P_{0,1} + A_1 \cos\left(\Phi\right) &&(3.29)\\
P_{e,2} &= P_{0,2} + A_2 \cos\left(\Phi + \Delta\Phi\right) &&(3.30)
\end{aligned}
$$

is fitted by the conic form of an ellipse

$$
\mathbf{u} \cdot \mathbf{x} \;=\; Ax^2 \;+\; Bxy \;+\; Cy^2 \;+\; Dx \;+\; Ey \;+\; F \;= 0 \qquad (3.31)
$$

with $\mathbf{x} = (x^2, xy, y^2, x, y, 1)$ and $\mathbf{u} = (A, B, C, D, E, F)^T$. A least squares (LSQ) fit method in a `Matlab`® routine allows to determine the parameters of the conic representation, and thereby to extract the phase difference from these parameters via

$$
\Delta\Phi \;=\; \cos^{-1}\left(\frac{-B}{2\sqrt{AC}}\right). \qquad (3.32)
$$

In our case, the rotation phase is determined by

$$
\begin{aligned}
\Phi_\Omega &= \frac{\Delta\Phi}{2}\\
&= \frac{1}{2}\cos^{-1}\left(\frac{-B}{2\sqrt{AC}}\right). &&(3.33)
\end{aligned}
$$

For the use of this fit method with the given modulation period of 10 s, we find a good trade-off of temporal resolution and fit uncertainty for a number of 15 shots for each fit (see figure 3.18). The fit uncertainty is not diminished for longer intervals.

In order to evaluate the influence of the ellipse fit method on the short term sensitivity, the shot-to-shot sensitivity of the sensor can be extrapolated assuming a $1/\sqrt{\tau}$ averaging behavior to find the expected standard deviation at 1 s measurement time. The ellipse fit method shows slightly higher short term noise than a mid-fringe measurement. First, the method itself yields a factor of $\sqrt{2}$ as points of lower sensitivity are taken into account in the measurement. Second, the detection noise plays an important role. The relative phase in a mid-fringe measurement can be chosen such that correlated detection noise in both interferometers cancels if the fringe contrast is equal for both interferometers. In contrast to that, the relative phase of the two interferometers changes drastically in the ellipse method. Hence, correlated, anti-correlated and non-correlated detection noise have the same effect on the fit uncertainty of the ellipse, detection noise does not cancel.

In the measurements presented in the following section the detection noise and the intrinsic fit uncertainty of the used routine cause an enhancement of the
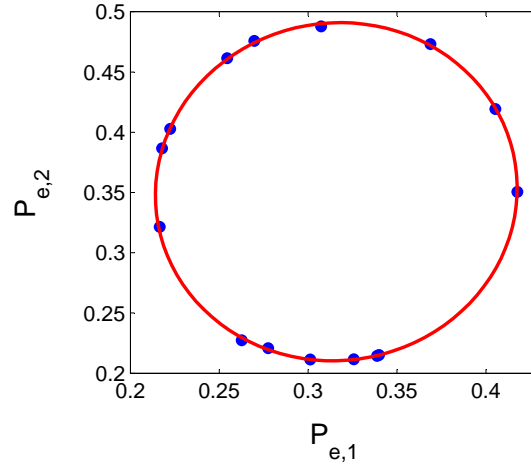
Figure 3.18: Ellipse fit example. A set of 15 shots with results $(P_{e,1}, P_{e,2})$ *(blue dots)* is plotted parametrically and fitted by an ellipse *(red line)*, which allows to extract the common phase of the two correlated interferometers.

short term noise by a factor of almost 1.5. While the mid-fringe sensitivity is $\sigma_\Omega \approx 5.5 \cdot 10^{-7}$ rad/(s$\sqrt{\text{Hz}}$) as given in [56], the extrapolation of the ellipse fit method yields a slightly decreased sensitivity of $\sigma_\Omega \approx 8.5 \cdot 10^{-7}$ rad/(s$\sqrt{\text{Hz}}$). The method's overestimation factor of the short term noise has been verified numerically using reproduced datasets with the same characteristics.

k-reversal technique

The Doppler shift allows for the realization of interferometers using $\mathbf{k}_{\text{eff},1}$ and $\mathbf{k}_{\text{eff},2} = -\mathbf{k}_{\text{eff},1}$ with areas featuring respectively opposed normal vectors. Phase offsets arising from the quadratic Zeeman and the AC-Stark effect have the same magnitude and sign for the opposite directions of the beam splitting process. Contrary to this, the inertial phase shift due to rotations only keeps the same magnitude while flipping the sign with the sign of the wave vector $\mathbf{k}_{\text{eff}}$. If the phase shifts that do not depend on the sign of $\mathbf{k}_{\text{eff}}$ vary slower than an experimental cycle, they can be removed from the measurement by performing a so-called k-reversal measurement. This consists in a repeated measurement of the interferometer phase while alternating between $\mathbf{k}_{\text{eff},1}$ and $\mathbf{k}_{\text{eff},2}$ and extracting the rotation phase as half difference of subsequent measurements. We will denote the respective effective wave vector configurations as k_1 and k_2 in the following.

In practice, the combination of ellipse fit and k-reversal technique is realized as follows. The k_1 and k_2 measurements are realized alternately. The phase for each of the two resulting datasets is then read out using the ellipse fit method employing 15 points for each phase value. Taking into account our experimental cycle frequency of $f_c = 2.12$ Hz and an alternating measurement in the k-reversal

technique, an ellipse with 15 points is obtained for each k_i. Thus, we obtain a rotation phase value every 14.3 s. Up to now the rotation phase denoted the half sum of the phases of the two interferometers. In the following, the rotation phase is considered to be the result of the combination of ellipse fit phase read out and k-reversal technique.

The k-reversal technique results in an effective suppression of constant and slowly varying phase shifts that are not dependent on the direction of beam splitting. This is the case for the residual differential AC-Stark shift and for the quadratic Zeeman shift presuming negligible magnetic field gradients. Phase shifts from other effects, namely the wave front, the two-photon light shift, and magnetic field gradients along the beam splitting light fields are not rejected by the k-reversal technique. This can lead to long term fluctuations of the rotation phase which will be considered in the following section.

3.5   Long term stability

We use a k-reversal measurement employing the modulation of the gravity acceleration projection for testing the long term stability of the rotation phase. This technique suppresses phase drifts that do not depend on $\mathbf{k}_{\text{eff}}$ are effectively suppressed if the variations are slow against the cycle time of the experiment. Moreover, amplitude and offset drifts of the interferometer signal do not influence the phase measurement as the ellipse fit method can be used to deduce the interferometer phase shift. For this, it is necessary that the time constant of the fluctuation is large compared to the modulation period.

In the next section possible drift sources, which were investigated, are descried. The main cause for drifts was the fluctuation of the cloud overlap of the two interferometers. With the use of a post-correction scheme, an integration measurement on the rotation rate results in an effective improvement of the sensitivity of our sensor of one order of magnitude compared to the previous status [56], which is presented in the end of this section.

3.5.1   Drift sources

We consider three drift sources in the following, which are not suppressed using the presented measurement scheme including the k-reversal technique. Besides the wave fronts of the beam splitting light fields introduced in section 3.2, these are the magnetic field gradient along the beam splitting light field optical axis as well as the two-photon light shift.
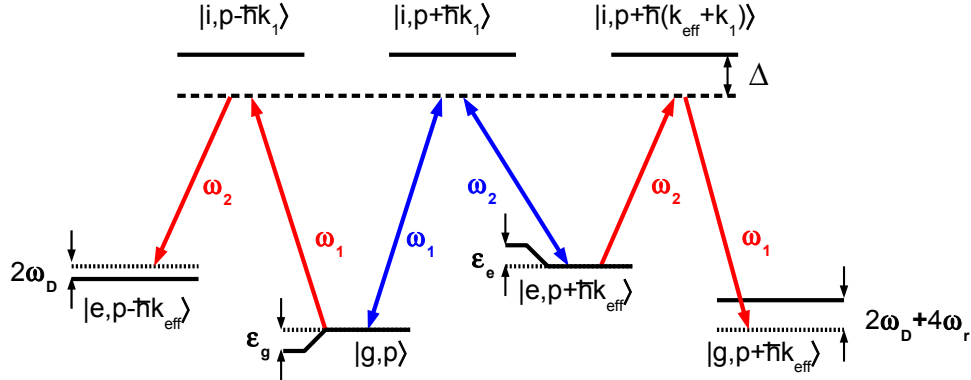
Figure 3.19: Two-photon light shift. The shift of the off-resonant two-photon transition using $\mathbf{k}_{\text{eff},2}$ is depicted for the case of a $\mathbf{k}_{\text{eff},1}$-transition. The energy level shifts ε_g and ε_g of the two interferometer states $|g, \mathbf{p}\rangle$ and $|e, \mathbf{p} + \hbar\mathbf{k}_{\text{eff}}\rangle$ result in a differential shift of $\delta\omega^{cp}_{TPLS,+} = (\varepsilon_e - \varepsilon_g)/\hbar$ in this case.

Two-photon light shift

Besides the differential AC-Stark shift, the beam splitting light fields induce a so-called two-photon light shift (TPLS), which arises in the retro-reflective Raman beam configuration. In our case, the two Raman beam splitting light fields are shined in in the same direction with parallel linear polarization. Before interacting with the atoms, the beams pass through a quarter-wave plate. This results in circular polarizations, which, in combination with the magnetic field, provides the needed σ-polarized light fields in both counter-propagating transitions. As the two light fields have the same polarization, the co-propagating transition can also be driven with the fields in our set-up. Choosing one of the Raman transitions via Doppler selection results in an effective detuning on the other possible transitions. These off-resonant two-photon couplings induce frequency shifts on the addressed transition. This is depicted in figure 3.19 for the choice of $\mathbf{k}_{\text{eff},1}$ and the effective shifts of the $\mathbf{k}_{\text{eff},2}$-transition onto the interferometer states. In our configuration, the two shifts induced by the present light fields are [112]

1. the shift of the counter-propagating transition of opposite $\mathbf{k}_{\text{eff}}$, which is shifted out of resonance by $2\omega_D$. The effective TPLS is given by

$$\delta\omega^{cp}_{TPLS,\pm} = \frac{\Omega_{\text{eff}}{}^2}{\pm 8\omega_D} + \frac{\Omega_{\text{eff}}{}^2}{4(\pm 2\omega_D) + 4\omega_r}. \tag{3.34}$$

2. the shift arising from the co-propagating transition, which is shifted out of resonance by ω_D, induces an effective frequency shift of

$$\delta\omega^{co}_{TPLS,\pm} = \frac{1}{4}\frac{\Omega_{cp}{}^2}{\pm\omega_D + \omega_r}, \tag{3.35}$$

where the Rabi frequency of the Doppler insensitive transition is experimentally determined to be $\Omega_{cp} \approx 1.4\Omega_{\text{eff}}$.

In both cases, $+$ applies for $\mathbf{k}_{\text{eff},1}$ and $-$ for $\mathbf{k}_{\text{eff},2}$. Given these frequency shifts, the phase in the interferometer caused by TPLS is calculated using (2.82) to

$$\Phi_{TPLS,\pm} \quad = \quad \int g(t)\delta\omega_{TPLS,\pm}(t)dt, \tag{3.36}$$

where $\delta\omega_{TPLS,\pm} = \delta\omega_{TPLS,\pm}^{cp} + \delta\omega_{TPLS,\pm}^{co}$ and $g(t)$ is the sensitivity function (2.89). For constant light intensities and detuning, the interferometer phase shift is found to be

$$\Phi_{TPLS,\pm} \quad = \quad \frac{\delta\omega_{TPLS,\pm}^{(1)}}{\Omega_{\text{eff}}^{(1)}} - \frac{\delta\omega_{TPLS,\pm}^{(3)}}{\Omega_{\text{eff}}^{(3)}} \tag{3.37}$$

with $^{(1)}$ and $^{(3)}$ denoting the first and last Raman beam splitting pulse. In the case of large fluctuations in the beam splitting light field intensity, we find a modified interferometer phase arising from TPLS taking into account imperfect $\pi/2$-pulses [112]

$$\Phi_{TPL,S\pm} \quad = \quad \frac{\delta\omega_{TPLS,\pm}^{(1)}}{\Omega_{\text{eff}}^{(1)}}\tan\left(\frac{\Omega_{\text{eff}}^{(1)}\tau_{\pi/2}}{2}\right) - \frac{\delta\omega_{TPLS,\pm}^{(3)}}{\Omega_{\text{eff}}^{(3)}}\tan\left(\frac{\Omega_{\text{eff}}^{(3)}\tau_{\pi/2}}{2}\right), \tag{3.38}$$

where $\tau_{\pi/2}$ is the $\pi/2$-pulse duration. For the evaluation of the impact on our rotation signal, we have to take into account that the two interaction zones T1 and T3 are traversed in opposed order by the atomic wave packets in the two interferometers. Therefore, the phase shift arising from TPLS has opposed signs for the two interferometer if we presume an ideal interferometer overlap. The influence of TPLS will be suppressed in the rotation signal as the rotation phase extracted via ellipse fitting corresponds to the half sum of the two interferometer phases. A mismatch in cloud overlap on the other hand could induce a rotation phase bias and, when fluctuating, a slowly varying spurious rotation signal.

A detailed experimental analysis has not been carried out. While the main drift source is identified to be the atom source position uncertainty coupled with an imperfect beam splitter light field alignment (see section 3.5.2), the TPLS can not be excluded from being a source of fluctuations over long time scales found in the measurement presented in section 3.5.3. Nevertheless, the impact will be small compared to what is found in the case of the wave front considerations.

If we assume a mismatch in Rabi frequencies in T1 and T3 of $\Omega_{\text{eff}}^{(3)} = 0.8\Omega_{\text{eff}}^{(1)}$, a phase of $\Phi_{TPLS,+} \approx 36$ mrad is estimated for each interferometer. If the mismatch of the cloud overlap is such that the beam splitting pulses in T1 and T3 are applied on the center of the Gaussian beam profiles for one interferometer and
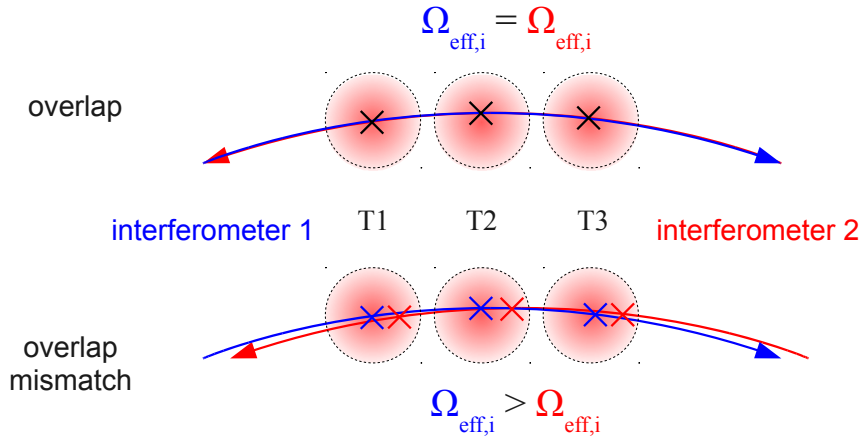
Figure 3.20: TPLS phase shift and cloud overlap mismatch. The schematic depicts a side view on the trajectories of interferometers 1 *(blue)* and 2 *(red)*. The beam splitting light fields Gaussian beam profiles are indicated in the single interaction zones T1, T2 and T3. While the Rabi frequencies $\Omega_{\text{eff,i}}$ are identical for both interferometers in the case of a perfect overlap in the x-y-plane *(top)*, an overlap mismatch induces different effective Rabi frequencies in the two *(bottom)*. This results in a TPLS phase offset in the rotation phase (see text).

at a position 10 mm off-center for the other, the effective Rabi frequencies in the second interferometer are reduced by 10 % with respect to the first. This would induce an effective phase offset on the rotation phase of $\Phi_{\Omega,TPLS,+} \approx 1$ mrad. If the overlap varies over time, phase fluctuations can occur resulting in a spurious rotation signal of $2 \cdot 10^{-8}$ rad/s. These fluctuations are small to which is found to be caused by a misalignment of the beam splitter light fields. This will be presented later in this chapter.

Although the fluctuations arising from the TPLS are considered to be small, it is desirable to further reduce their impact on the rotation signal for future measurements. This can be accomplished by technical modifications that are discussed in section 3.6.

Magnetic field gradient

The magnetic field induces a quadratic Zeeman shift on the resonance frequency of the two-photon Raman transition used for atomic beam splitting (see section 2.5.1). The magnetic field gradient along the atomic trajectory induces an effective phase shift in our set-up as the frequency shifts along the first and second half of the Mach-Zehnder sequence do not cancel each other. The phase offset is estimated to be 5.6 rad [56]. Nevertheless, this phase shift does not depend on the direction of the beam splitting process. It is therefore equal in both measurements using $\mathbf{k}_{\text{eff,1}}$

and $\mathbf{k}_{\text{eff},2}$, respectively. It is therefore suppressed in the k-reversal measurement. Contrary to this, a magnetic field gradient along the beam splitting light field direction induces a phase shift of opposite sign for the two beam splitting directions. Here, we will investigate the drift impact of such shifts on the measured rotation phase.

For the calculation of the phase shift induced by a magnetic field gradient we consider a magnetic field along the beam splitting direction of

$$B_z(\mathbf{x}) \quad = \quad B_{z,0}(x,y) + \frac{\partial B_z(\mathbf{x})}{\partial z}z. \tag{3.39}$$

For small field gradients, it is possible to approximate the frequency shift (2.97) with

$$\delta_{qZ}(\mathbf{x}) \quad \approx \quad \alpha_{qZ}\left(B_{z,0}(\mathbf{x})^2 + B_{z,0}(\mathbf{x})\frac{\partial B_z(\mathbf{x})}{\partial z}\Delta z\right). \tag{3.40}$$

The first term scaling with $B_{z,0}(\mathbf{x})^2$ allows to consider field gradients along the atomic trajectory canceling in the k-reversal technique (see above). The second term accounts for field gradients along the beam splitting light field optical axis and results in a phase shift for each interferometer, which can be calculated using (2.82)

$$\Phi_{qZ,\nabla} \quad = \quad \alpha_{qZ}\int_{-\infty}^{\infty} g(t)B_{z,0}(\mathbf{x}(t))\frac{\partial B_z(\mathbf{x}(t))}{\partial z}\Delta z(t)dt. \tag{3.41}$$

Assuming a perfect overlap of the atomic trajectories, $\Phi_{qZ,\nabla}$ has the same absolute value but opposite sign for the two interferometers. This phase would therefore be suppressed in the rotation phase. However, the overlap of the atomic trajectories is not perfectly known and the phase bias in the rotation phase is difficult to estimate. A resulting bias in the rotation phase would not be suppressed in the k-reversal measurement. Nonetheless, fluctuations arising from the magnetic field gradient can be excluded experimentally by performing measurements with different offset field values for $B_{z,0}$. In such a measurement, $\Phi_{qZ,\nabla}$ should show different fluctuations for different $B_{z,0}$ if it is a dominant source for fluctuations and drifts.

A long term measurement is performed for alternating magnetic offset field values $B_1 \approx 0.12$ G and $B_2 \approx 0.85$ G. This results in an effective measurement with a set of four parameter pairs being (k_i, B_j) for $i,j = 1,2$. The two pairs (k_i, B_1) and (k_i, B_2) allow us to determine the rotation phase value for the two different magnetic bias field values. The differential phase of the two measurements results in a fluctuation over time, that is only due to magnetic field fluctuations. The Allan standard deviation of the differential phase shift depicted in figure 3.21 does not reveal drifts or oscillations over time. This excludes the magnetic field from being the dominant source for slow fluctuations and drifts in this measurement.
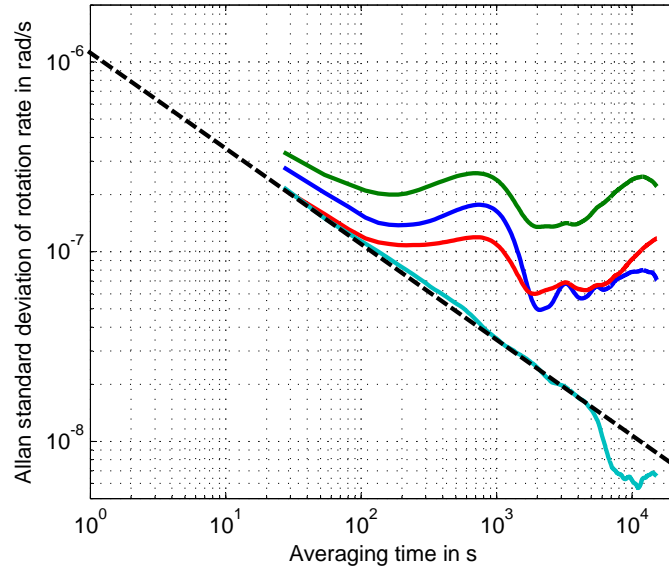
Figure 3.21: Allan standard deviation plot of magnetic field drift influence. The Allan standard deviation is depicted for the rotation rates measured with the respective magnetic field values B_1 *(blue)* and B_2 *(green)*. Combining the two measurements leads to an effective rotation rate fluctuation *(red)* and a differential rotation rate *(cyan)* of subsequent measurements with different magnetic field values.

Wave fronts

Similar to the cases of TPLS and a magnetic field gradient considered above, a misalignment of the three beam splitter light fields leads to an offset in the rotation phase given an interferometer overlap mismatch (see section 3.2.2). A slow fluctuation or drift either of the relative alignment or in the cloud overlap can lead to a slowly varying spurious rotation signal. The fluctuation in the overlap can be caused by variations in the initial position of the magneto-optical traps or of the atomic velocity if the resulting displacement is not common to both interferometer trajectories.

Using the alignment technique presented in section 3.4.5 for the relative Raman mirror angular alignment, the wave fronts in the separated beam splitting light zones are parallel with an uncertainty in the lower μrad regime. Taking into account a relative position drift of the two atom sources of a few hundred μm, we find the typical phase fluctuation in the rotation measurement to be in the range of tens of mrad using (3.20). This corresponds to a limitation for the sensitivity to rotations of several 10^{-7} rad/s. The wave front drift influence due to imperfect alignment is considered in further detail in the following section.
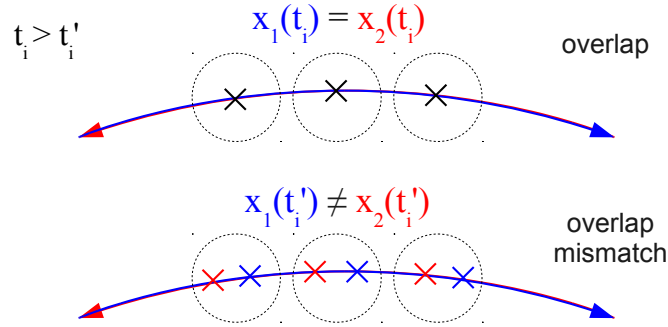
Figure 3.22: Induced pulse application mismatch. The picture shows the atomic trajectories and the three interaction zones seen from the side. For an optimal timing, the Raman pulse application positions are superimposed for both interferometers *(top)*. Adding a delay before the application of the Mach-Zehnder sequence induces a mismatch of the pulse application position overlap in the two interferometers *(bottom)*.

3.5.2   Relative beam splitter alignment and cloud overlap

The influence of an imperfect relative Raman wave front alignment on the rotation phase is investigated here. As the phase offset scales with the cloud overlap mismatch, it can be observed when varying the cloud overlap by adding a time delay to the interferometer timing sequence before the application of the Mach-Zehnder pulse sequence. As presented in figure 3.22, this induces an effective, mostly horizontal mismatch of the cloud overlap. This mismatch can be tracked using the arrival time information of our detection scheme, which is explained in detail in section 3.4.4. Realizing such a measurement, we find a clear coincidence of phase offset changes with the deliberately varied cloud overlap. Figure 3.23 depicts the rotation phase variation and the respective arrival time variations of the two interferometers for the application of delays Δt of up to 400 μs, which correspond to a MOT displacement of $\Delta x = 2v_{at}\Delta t$ of up to 2.3 mm. Applying the timing offset after the Mach-Zehnder pulse sequence allows for validating this method. The arrival time changes as before while the rotation phase value stays constant within the errors.

   The influence of the cloud overlap in horizontal direction can be quantitatively investigated by tracking the rotation phase over a varying timing delay. This results in a mapping of the resulting wave front seen by the interferometer and allows for an estimation of the relative mirror alignment uncertainty using the presented alignment scheme. Figure 3.24 represents the result of such a mapping measurement. Approximating the rotation phase measurements with a linear fit, the total phase offset is found to be 324 mrad, which corresponds to an effective
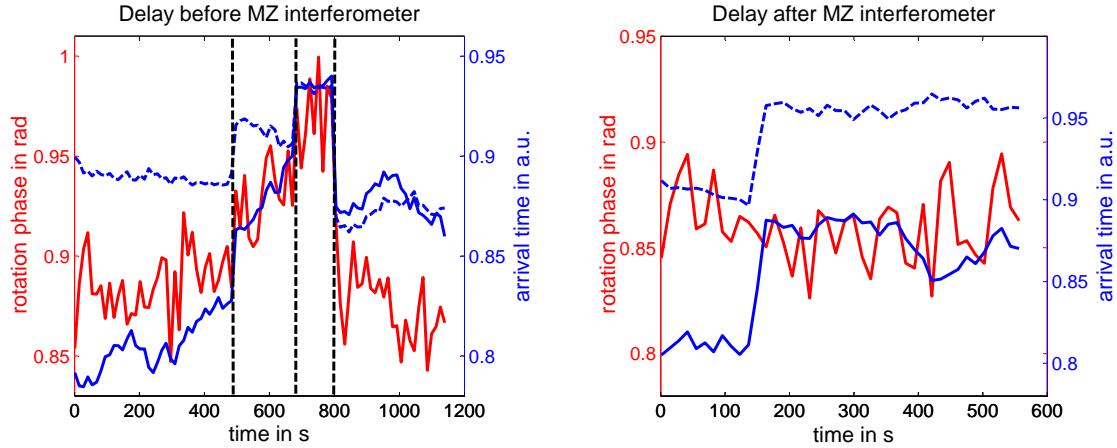
Figure 3.23: Rotation phase offset due to deliberate cloud overlap mismatch. The graphs depict the rotation phase and the arrival time measurement in the interferometer 1 *(blue, solid line)* and 2 *(dashed blue line)* for a deliberate timing delay added before *(left)* and after *(right)* the Mach-Zehnder (MZ) pulse sequence application. The vertical *dashed lines* indicate the moment in which the timing delay is changed to $\Delta t = -200$ μs, $\Delta t = -400$ μs and back to $\Delta t = 0$ μs. In the case of the delay being applied after the Mach-Zehnder pulse sequence, the applied time delay is $\Delta t = 400$ μs, which results in the step in arrival time at about 130 s measurement time.

misalignment of $\alpha_{x,1-2} - \alpha_{x,2-3} = 7$ μrad. Furthermore, we gain information about the shape of the wave front aberration out of this measurement. The linearity as a function of overlap mismatch allows us to deduce that a wave front tilt is the dominating wave front aberration.

   The same measurement is realized for different angles of one of the Raman mirrors, namely the third mirror seen by the interferometer 1, mirror T3. As depicted in figure 3.25, the rotation phase shows a different slope for different mirror angles, which indicates an effectively improved alignment for a small slope. In fact, this only indicates that the relative mirror tilts compensate one for each other ($\alpha_{x,1-2} - \alpha_{x,2-3} = 0$). However, the influence of a varying imperfect cloud overlap should be strongly diminished. The corresponding mirror alignment is suitable for an accurate and stable rotation measurement. This measurement not only allows for an improved mirror alignment, but also for an estimate of the cloud overlap. The intersection of the three phase slopes for different mirror angles indicates the correct timing for an optimal cloud overlap to be $\Delta t \approx -200$ μs. We can conclude that taking into account the residual phase uncertainties of ± 75 mrad, we can estimate an residual alignment uncertainty to about 3 μrad.

   In the following, the resulting rotation phase drift or variation arising from wave fronts will be estimated. Given the alignment uncertainty, the influence on the rotation phase can be estimated for an overlap mismatch. A cloud overlap mismatch can have different reasons. Besides the initial MOT position, which results
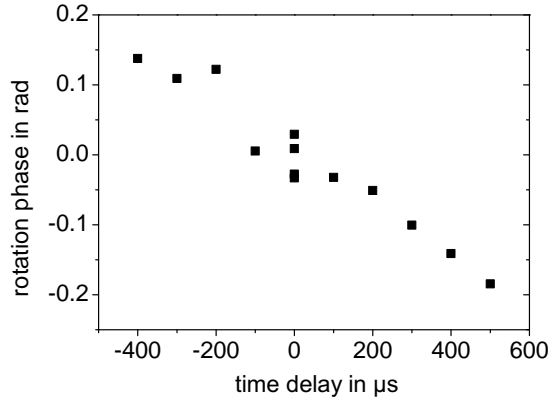
Figure 3.24: Overlap dependent rotation phase offset. The graph shows the rotation phase values for different interferometer overlaps. The overlap is controlled by introducing a timing offset before the interferometer sequence, which is represented on the horizontal axis. The measurements are not taken in order and the zero delay measurement realized several times to test the reproducibility and drift behavior. While the statistical errors are in the order of 10 mrad and therefore in the size of the symbols, the repeated measurement for zero delay allows us to deduce a typical error of ± 75 mrad over the time it takes to record the whole measurement set.

directly in an overlap mismatch if the displacement is not common to both sources, the atomic velocity can vary. This would also lead to an effective displacement of the cloud position during the beam splitter process. However, the velocity is well defined by the relative detuning applied to the front and rear molasses beams during the launch sequence. On the contrary, the initial position of the atomic ensemble, namely the MOT position, is mainly defined by the intensity balance of the MOT beams, which can show variations over time.

Launch velocity fluctuations

The launch velocity fluctuations are measured employing a SRB geometry using the outer two mirrors. In this geometry, the wave front induced interferometer phase offset due to wave front tilts does not depend on the initial cloud position. This allows to only consider velocity fluctuations when employing the SRB sequence. The single interferometer wave front phase shift in a SRB geometry for relative beam splitter light field misalignment is found using (3.14) and reads

$$\Phi_{SRB}^{WF} = k_{\text{eff}} T v_{0,x} \alpha_{x,1-3}. \tag{3.42}$$

Here, T is the pulse separation time in each of the two $\pi/2$ pulse pairs, $v_{x,0}$ is the forward launch velocity and $\alpha_{x,1-3}$ is the relative wave front alignment of the
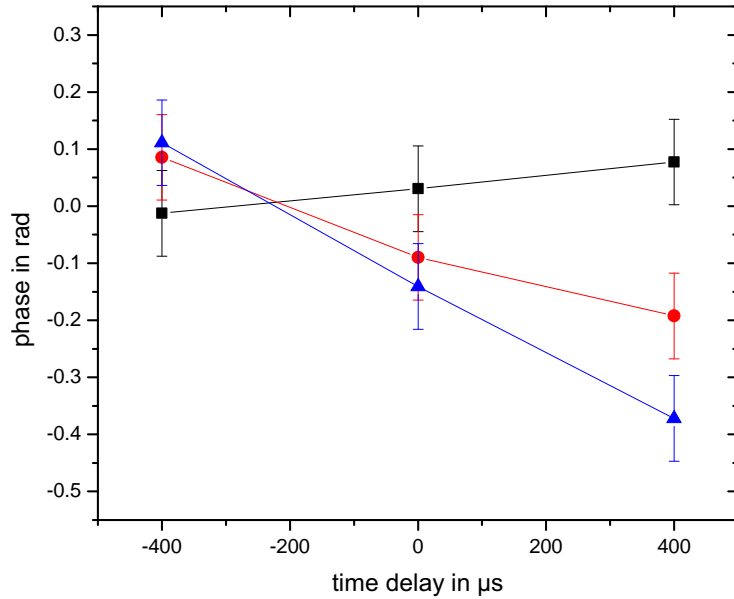
Figure 3.25: Overlap and tilt dependent rotation phase offset. The graph depicts rotation phase values as a function for the induced cloud overlap mismatch for three different horizontal tilt angles of the Raman mirror T3. The error bars take into account the phase error between subsequent measurements due to slow fluctuations, which is deduced from the measurement presented in figure 3.24. The statistical uncertainty on each point is below 20 mrad.

two outer beam splitter application zones. It is apparent that the wave front phase offset only depends on the atomic velocity and not on the atom source position. We expect a variation in the launch velocity to cause a phase shift directly proportional to the misalignment angle of the two mirrors of

$$\Delta\Phi_{SRB}^{WF} \quad = \quad k_{\text{eff}}T\Delta v_{0,x}\alpha_{x,1-3}. \tag{3.43}$$

The phase fluctuations are measured for the optimal alignment, and for an angle of $\alpha_{x,1-3} \approx 1$ mrad with a pulse separation time of $T = 3$ ms. The alignment in the optimal case is estimated to be better than 10 μrad for the three mirrors as we obtain good contrast in a Mach-Zehnder interferometer sequence. In both measurements, we deduce peak-to-valley fluctuations over long times of $\Delta\Phi^{SRB} < 10$ mrad. This allows us to deduce an upper bound for slow launch velocity fluctuations of

$$\frac{\Delta v_{x,0}}{v_{x,0}} \quad < \quad \frac{\Delta\Phi_{SRB}}{\Phi_{SRB}^{WF}(\alpha_{x,1-3} = 1 \text{ mrad})}$$
$$= \quad 7 \cdot 10^{-5}.$$

The upper bound for phase fluctuations in a Mach-Zehnder geometry being

$$\Delta\Phi_{MZ}^{WF} \quad = \quad k_{\text{eff}}\Delta v_{x,0}T\left(\alpha_{x,1-2} - \alpha_{x,2-3}\right) \tag{3.44}$$

can therefore be estimated for the given velocity fluctuations to be

$$\Delta\Phi_{MZ}^{WF} \quad < \quad 1.5 \text{ mrad}$$

with a respective mirror misalignment of $(\alpha_{x,1-2} - \alpha_{x,2-3}) = 10$ μrad. This corresponds to a spurious rotation rate fluctuation of $3 \cdot 10^{-8}$ rad/s.

Atom source position fluctuations

In order to determine the atom source position fluctuations over time, the MOT position is measured directly before launch by reading an image with the MOT monitoring camera. Several horizontal and vertical lines are extracted from each image after subtracting the background image. Each of the lines is approximated using a Gauss fit, which yields a value for the center of mass of the atomic ensemble. The center of mass positions of in total seven image lines is used to determine the MOT position in the x- and z-direction. These are the directions of the horizontal projection of the atomic trajectory and the horizontal direction perpendicular to the latter, respectively. The short term stabilities of [113] being $\sigma_x = 23$ μm and $\sigma_z = 8.5$ μm are found still to be valid. We find $\sigma_x = 22$ μm and $\sigma_z = 5$ μm. The fluctuations over long times are an order of magnitude larger than the short term variations, in the range of 300 μm over several minutes in the case of the x-direction (see figure 3.26). However, these fluctuations can be tracked using the arrival time information. This is possible as the arrival time fluctuations are found to be dominated by the MOT position fluctuation as depicted in figure 3.26. Taking into account the velocities in x- and y-direction in the moment of detection, we can furthermore consider the influence of the MOT position in y-direction onto the arrival time measurement to be a factor of 10 smaller than the one arising from the MOT position in x-direction. This motivates the application of the arrival time as a measure of the initial horizontal cloud position and, thereby, of the horizontal position of the atomic ensemble during the beam splitting process.

From typical arrival time fluctuations we deduce a MOT position variation in the order of 0.5 mm peak-to-valley over one cycle of the laboratory air conditioning with a period of about 1000 s. As the arrival time is anti-correlated for the two atom sources, this results in a total variation of the cloud overlap mismatch of up to $\Delta x \approx 1$ mm. Using (3.20), this results in potential rotation phase fluctuations with peak-to-valley values of

$$\Delta\Phi_{\Omega}^{WF,x} \quad = \quad 24 \text{ mrad}.$$

The resulting spurious rotation rate amounts to $5 \cdot 10^{-7}$ rad/s.
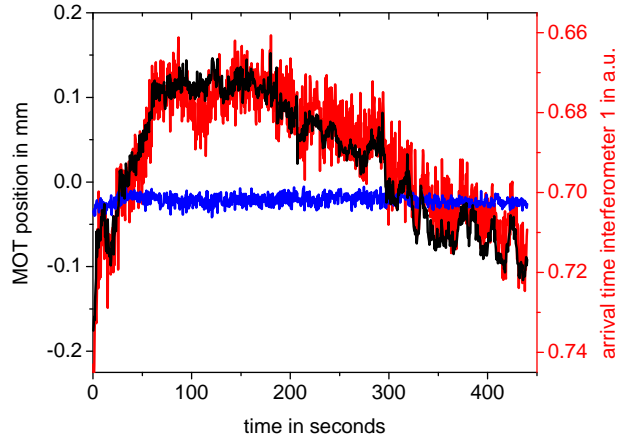
Figure 3.26: Correlation of MOT position and arrival time. The *x-(black)* and *z-*component *(blue)* of the MOT position of atom source 1 and the atomic arrival time of interferometer 1 *(red)* are depicted. The offsets of the MOT position are arbitrary. The MOT position in *x*-direction show a correlation which motivates to use the arrival time as monitoring for the initial MOT position in *x*-direction.

MOT beam power fluctuations

The MOT position fluctuations are found to be caused by power balance fluctuations in the MOT beams, namely by the power distribution using the four AOMs for top, bottom, front and rear beam frequency control. The power fluctuations measured in the MOT telescopes are well correlated with the power fluctuations of the distribution modules realizing the splitting from four to twelve fibers (see figure 3.6). This is the reason for the fluctuations in *z*-direction to be much smaller than the ones in *x*-direction. The fluctuations mainly result in imbalances between the horizontal red and blue detuned beams as each of the pairs being controlled by one AOM. The imbalance between the two red detuned beams is much smaller, which is also valid for the blue detuned beams.

The same behavior is discovered for the vertical MOT beams. The bottom and top beams show relative power fluctuations, which can result in a vertical displacement of the two MOTs. However, this displacement is common to both traps and does therefore not induce a mismatch in the cloud overlap Δy. The overlap fluctuations in forward velocity can therefore be considered to be dominant.

While a more stable power balance could not yet be realized, the MOT position fluctuations can be tracked via the atomic arrival time using the three pulse detection scheme. The cloud overlap is a linear combination of the two positions, which is used in the following section to correlate the rotation measurement fluctuations to the MOT positions. Having identified the position fluctuations coupled with
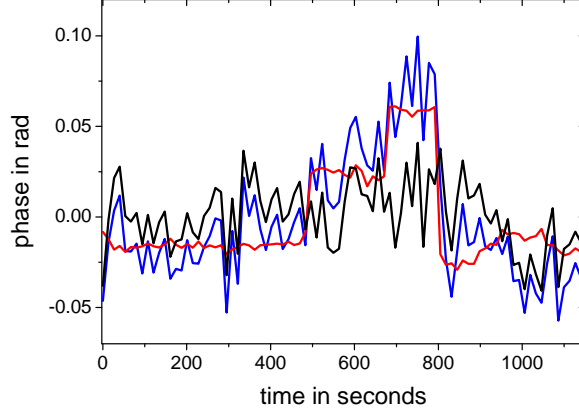
Figure 3.27: Rotation rate post-correction. The rotation phase *(blue)* is plotted over time with three deliberate changes in the cloud overlap. The expected rotation phase *(red)* as a linear combination of the arrival time values allows to remove the cloud overlap impact from the rotation phase. The difference of both curves is the corrected rotation rate *(black)*.

the Raman beam splitter misalignment as the main drift source then allows for a data post-correction and, thereby, to an effectively improved rotation sensitivity.

Rotation phase post-correction

We track the arrival time of both atom interferometers with the three pulse detection scheme. This provides the relations of the second and third detection pulse signals

$$\varepsilon_{AT,1} \quad = \quad \frac{N_{c,1}}{N_{total,1}} \tag{3.45}$$

$$\varepsilon_{AT,2} \quad = \quad \frac{N_{c,2}}{N_{total,2}} \tag{3.46}$$

for interferometers 1 and 2. As shown above for the case of interferometer 1, these coefficients are correlated with the initial atom source position in x-direction, which allows us to use them as an effective measure of the initial atom source position and, when combining the two, for the cloud overlap Δx. The resulting rotation phase fluctuations could than be given as a linear combination of the two arrival time values

$$\Phi_{\Omega}^{WF_x} \quad = \quad a_1 \varepsilon_{AT,1} + a_2 \varepsilon_{AT,2} + c, \tag{3.47}$$

where a_1, a_2, and c are fitted parameters. For n interferometer cycles, we find a dataset of expected rotation phase values $\Phi_{\Omega,i}^{WF_x}$ with $i = 1 \ldots n$ corresponding
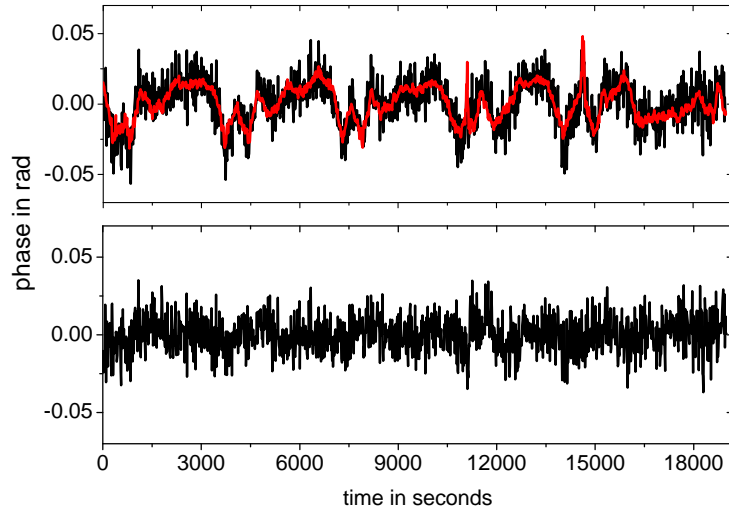
Figure 3.28: Rotation rate averaging measurement. *Top:* The rotation phase *(black)* is plotted with the time series of expected rotation phase values $\Phi_{\Omega,i}^{WF_x}$ *(red)*. The coefficients for the latter are found in a fit of a linear combination of the atomic arrival times to the rotation signal. *Bottom:* Subtracting the expected phase values results in a suppression of the wave front influence on the rotation phase. The offsets have been removed.

to a dataset of measured rotation phase values $\Phi_{\Omega,i}$. The fitting parameters are the result of a LSQ fit in which the sum of the pairwise quadratic deviations $\sum_{i=1}^{n}(\Phi_{\Omega,i}^{WF_x} - \Phi_{\Omega,i})^2$ is minimized.

The post-correction of the rotation phase is then realized using expected rotation fluctuation values. Such a post-correction is shown in figure 3.27 for the rotation phase measurement in which we deliberately induced a cloud mismatch.

3.5.3   Atom gyroscope sensitivity

In order to study the long term stability of our cold atom gyroscope we track the measured rotation phase over time. We use the ellipse fit method to extract the rotation phase values from a dataset that is obtained by modulating the atom interferometer acceleration phase. We analyze the time series of rotation phase values depicted in figure 3.28. This is an extraction from the dataset of the full run of in total 150,000 shots. The data point intervals $(1; 70,000)$ and $(110,000; 150,000)$ are rejected due to cooling laser malfunctions leaving the interval $(70,000; 110,000)$ for data analysis.

The rotation phase shows slow variations in the range of 50 mrad over typically 60 minutes. Using the fitting procedure of the post-correction method, we deduce
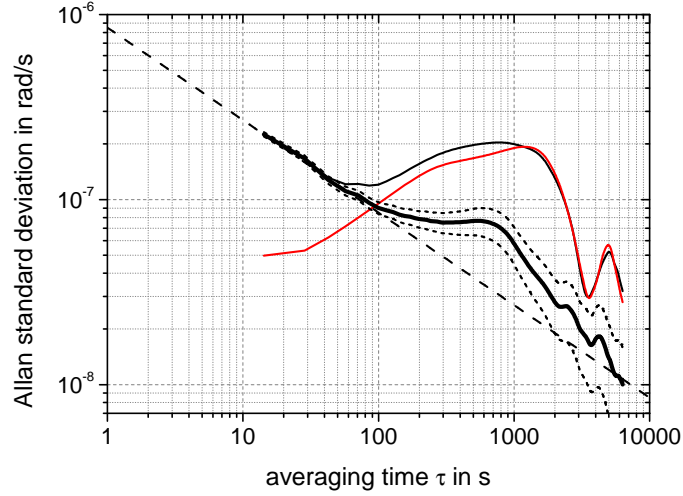
Figure 3.29: Rotation signal averaging measurement Allan standard deviation. The Allan standard deviation is depicted for the measured rotation signal *(thin black line)* and the expected spurious rotation signal *(red line)*. A post-corrected rotation rate is found by subtracting the expected spurious rotation signal from the measured one, which results in an improved averaging behavior of the gyroscope *(bold black line)*. The statistical errors on the Allan standard deviation are plotted in *short dashed black lines*. The *dashed line* depicts an averaging of $8.5 \cdot 10^{-7} \mathrm{rad}/(\mathrm{s}\sqrt{\mathrm{Hz}})$.

the expected rotation phase values from the atom cloud arrival time measurements. The expected and measured rotation phase values show good agreement over the whole duration of the measurement.

We use the dataset of expected rotation phase values to correct for long term fluctuations that arise from impacts of the wave front misalignment coupled with an imperfect cloud overlap. In order to deduce the long term stability of the rotation phase, we subtract the datasets of the expected and measured rotation rate. The two datasets and their difference are shown in time series in figure 3.28, and corresponding Allan standard deviation is given in figure 3.29.

As seen before, the short term sensitivity is reduced using the ellipse fit method. The extrapolated rotation measurement uncertainty at one second measurement time is

$$\sigma_\Omega(\tau) \quad \approx \quad 8.5 \cdot 10^{-7} \, \frac{\mathrm{rad}}{\mathrm{s}\sqrt{\mathrm{Hz}}}.$$

Over longer times, the signal starts to show a periodic behavior, which is also seen in the atomic arrival time signals. The MOT positions fluctuate slowly and the positions of the pulse application move one to each other. A residual angle of a few μrad translates this cloud overlap mismatch into a phase offset, which varies over

time. The periodic behavior manifests in a sinc-like curve on the Allan standard deviation. Removing the signal that we infer to be caused by wave front influence, the rotation phase averages into the lower 10^{-8} rad/s regime. A residual periodic fluctuation results in a plateau of $7.5 \cdot 10^{-8}$ rad/s between 200 and 800 s, while for an averaging time of 4000 s, we deduce a sensitivity to rotations of

$$\sigma_\Omega = 2 \cdot 10^{-8} \; \frac{\text{rad}}{\text{s}} \; (\text{at } 4000 \text{ s}).$$

The long term fluctuations are reduced by a factor of up to 3 using the post-correction method. Possible reasons for the residual fluctuations imperfections in the post-correction. These can be inferred small fluctuations of the respective mirror alignment that can modify the impact of the cloud overlap mismatch. Moreover, the influence of the vertical MOT position can cause fluctuations in the arrival time signal that do not cause a rotation phase shift if the fluctuation is common to both atomic sources. In the following, technical modifications are discussed that will allow to further reduce the long term fluctuation and, given an improved short term stability, for a further increase in sensitivity.

3.6 Conclusions

The sensitivity of our atom interferometer gyroscope has been studied over long integration times using an acceleration modulation technique and an ellipse fit method for rotation signal read out. The atom source position fluctuations coupled to imperfectly aligned wave fronts of the Raman beam splitter light fields are identified to be the main reason of long term phase fluctuations. A correction method using the atomic arrival time information allows for a reduction of this phase fluctuation by a factor of 3 resulting in a sensitivity to rotation measurements of the presented sensor of $\sigma_\Omega = 2 \cdot 10^{-8}$ rad/s after 4000 s integration time. This is an improvement of the sensor sensitivity of one order of magnitude compared to the sensitivity at one second measurement time presented in the preceding work [56].

The residual phase fluctuation is inferred to be caused by imperfections of the correction method. Also, the TPLS was not experimentally excluded from being a possible source for phase fluctuations. The latter effect can easily be suppressed by realizing a modification of the Raman light field optical set-up. The collimating telescope in T1 is removed and the light of telescope in T3 is split and guided to the interaction zone T1 using a non-polarizing beam splitter cube. Presuming a resulting Rabi frequency mismatch of Ω_3/Ω_1 of 5 % and Rabi frequency fluctuations arising from an imperfect cloud overlap of 5 %, we find a resulting rotation rate fluctuation below $5 \cdot 10^{-9}$ rad/s. Thus, we estimate minor rotation phase fluctuations induced by the TPLS even for an intensity mismatch and fluctuation which should easily be met by the use of common beam splitter light fields in T1 and T3.

The post-correction method using the arrival time measurement in the detection process enables rotation measurements with a sensitivity in the lower 10^{-8} $\frac{\text{rad}}{\text{s}}$ regime. However, it is desirable to realize an intrinsically higher stability of the measured rotation phase. The observed fluctuation in the rotation signal results from a combination of MOT position fluctuations and residual imperfections in the relative beam splitter light field alignment. An improvement of the stability can be achieved by either reducing the position fluctuations or the mirror alignment uncertainty.

We found the MOT position fluctuations to be mainly caused by relative power fluctuations in the MOT beams. The source is given by the periodically varying temperature in our laboratory causing misalignments in the laser system. The fluctuations are mainly in the 3D-MOT distribution module used for frequency and power control. An improvement of the power stability can be achieved by reducing the temperature fluctuations or the sensitivity of our optical set-up to temperature. Also, the intensity can be actively stabilized. An active intensity stabilization has been tried out and resulted in a suppression of the arrival time fluctuations by a factor of 2. Improving this intensity lock would allow for an improvement in the MOT position stability. If the slow power fluctuations of the MOT beams can be reduced to the typical short term sensitivity value, a reduction of a factor of 20 in cloud overlap fluctuations could be realized.

The relative beam splitter alignment is realized based on the signal contrast of our two interferometers. This alignment technique is estimated to allow for an alignment with uncertainties of the relative angle of the Raman beam retro-reflective mirrors of a few μrad [57]. Such an angle results not only in a signal contrast reduction but also in an interferometer offset. While this offset is rejected from the rotation phase for an ideal overlap of the atomic clouds of the two interferometers, an overlap mismatch results in a spurious rotation phase shift. By varying the cloud overlap on our flat parabolic trajectories, we find a residual total angle of the Raman mirrors of 7 μrad in the horizontal direction. A reduction of this angle with an uncertainty of about 3 μrad was achieved by alternating the cloud overlap for different relative mirror alignments. This was mainly limited by slowly varying overlaps during the alignment procedure. This alignment technique can be improved using a faster and direct rotation rate read out. For example, a rotation phase read out every 10 s results in a sensitivity of $3 \cdot 10^{-7}$ rad/s. For an induced overlap mismatch of ± 2 mm, this will allow for an alignment of the relative angle of below 1 μrad.

Taking into account the considerations in section 3.5.2 we infer maximum spurious fluctuations of the measured rotation rate caused by velocity uncertainties of below $3 \cdot 10^{-9}$ $\frac{\text{rad}}{\text{s}}$. The reduction in the atomic source position fluctuations would reduce the wave front induced fluctuations of below $1 \cdot 10^{-8}$ rad/s. The next steps that need to be taken for a full sensor analysis are discussed in section 5.1.

Atomic short range force sensor

This chapter presents the demonstrator experiment for the short range force sensor project FORCA-G, in which the Raman laser induced tunneling in a vertical 1D-lattice is employed for Raman interferometry with trapped atoms. First, the measurement principle and the experimental set-up are described. After that, the demonstration of the tunneling process is presented and the resolution of the resulting Wannier-Stark spectroscopy is discussed. This leads to the subsequently presented short and long term stability studies of the acceleration measurement based on Wannier-Stark Ramsey (WSR) and symmetric WSR interferometer schemes. At the end of this chapter, the coherent 'atom elevator' is introduced that allows for a low-loss quick coherent transport of the atoms over many centimeters. This will be employed in future short range force measurements in our experiment.

4.1   Accelerometry in a trapped atom interferometer

The sensitivity of accelerometry using our trapped atom interferometer is studied in this chapter. As the measurement takes place far from the mirror surface, the potential gradient is considered to be constant. This allows us to realize a force measurement with many atoms trapped in many lattice sites, which will all contribute to the measurement equally. A schematic of the experimental set-up is depicted in figure 4.1. The atoms are trapped in a vertical 1D-lattice, which is provided by a far blue-detuned standing light wave with a wavelength of $\lambda_l = 532$ nm. In such a trap, the atoms are not trapped in the transverse directions. In order to prevent the atoms from escaping in the horizontal directions, an additional transverse dipole trap [114] is created using a running wave far red-detuned light field with $\lambda_{dip} = 1064$ nm. This configuration will be denoted 'mixed trap' in the following. All beams used to create the mixed atomic trap and coherent beam splitting

are vertically aligned in a collinear manner. This is realized using different dichroic mirrors that provide high reflectance for one wavelength and high transmission for a different wavelength at the same time.
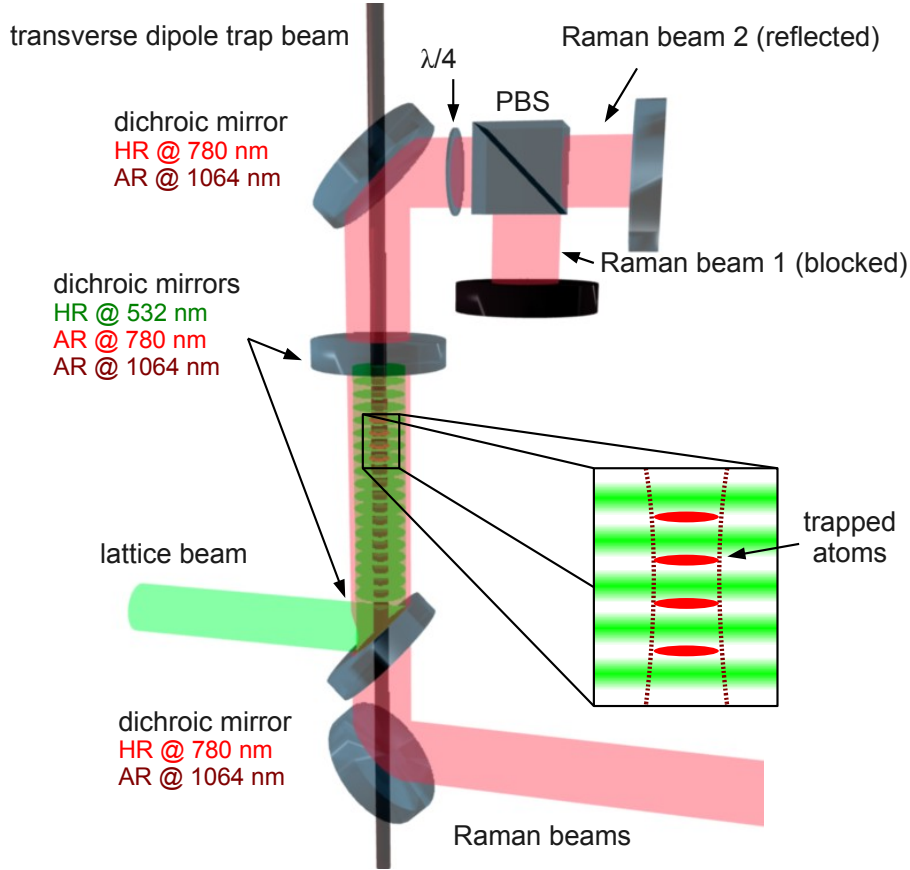

Figure 4.1: Short range force sensor schematic. The atoms are trapped in the mixed trap consisting of a vertical standing laser wave and a vertical traveling wave. Raman laser beams that are applied along the lattice optical axis allow for coupling of lattice sites that are separated up to several μm. The beam set-up is realized using dichroic mirrors. As the induction of tunneling using Raman lasers results in a state labeling, the transition probability between lattice sites can be determined by detecting the internal atomic state after release from the trap.

Within this set-up, we realize coherent tunneling of the trapped atoms by applying the Raman light fields in the depicted counter-propagating configuration. During the application of the Raman pulses, inter-site coupling appears if the relative Raman laser detuning matches the energy difference between two Wannier-Stark states plus the hyperfine transition frequency. This is equivalent to setting the total detuning $\delta_{\Delta m}$ in (2.75) to the respective Wannier-Stark resonance Δm to

zero. The resulting resonance condition for the Raman laser detuning reads

$$\nu_R \;\; = \;\; \nu_{eg} + \Delta m \nu_B, \tag{4.1}$$

where $\nu_R = (\omega_1 - \omega_2)/(2\pi)$ the relative Raman laser detuning, $\nu_{eg} = \omega_{eg}/(2\pi)$ is the internal state transition frequency, and ν_B is the Bloch frequency according to (2.65). This is now given by

$$\nu_B \;\; = \;\; \frac{m_a g \lambda_l}{2h}. \tag{4.2}$$

Here, m_a is the atomic mass, g is the local gravity acceleration and λ_l is the lattice laser wavelength. The internal state transition frequency itself can be influenced by differential shifts on the two interferometer states. These are in particular the quadratic Zeeman shift $\nu_{qZ} = \delta_{qZ}/(2\pi)$, given in (2.97), and the differential light shifts induced by the mixed trap light fields $\nu_{ACT} = \delta_{ACT}/(2\pi)$, given in (2.100), as well as by the Raman light fields $\nu_{ACR} = \delta_{ACR}/(2\pi)$.

The resonance condition (4.1) allows for a measurement of the Bloch frequency using Raman spectroscopy or interferometry. If the ratio of the atomic mass, Planck's constant, and the lattice laser wavelength value are known, this allows for the measurement of g. In the following, the experimental apparatus and the measurement sequence are introduced. Then, the inter-site coupling is demonstrated and the mixed trap influence on this process is discussed. After this, Bloch frequency measurement stability studies are presented. Identifying the limits of the stability motivates modifications in the set-up, which allow for an improved stability.

4.2 Experimental realization

For the accelerometry measurements we employ the mixed trap and Raman beam configuration depicted in figure 4.1. In the following, the experimental set-up for these experiments is introduced including the vacuum system, the laser sources, the beam set-up and detection devices. A first description can be found in [73].

4.2.1 Apparatus

The apparatus bases on similar technology as the atom gyroscope described in chapter 3. The single parts are introduced in the following.

Vacuum system

The vacuum system used for this experiment consists of a 2D-MOT chamber, and a combined 3D-MOT and interferometry chamber featuring at its bottom a detection
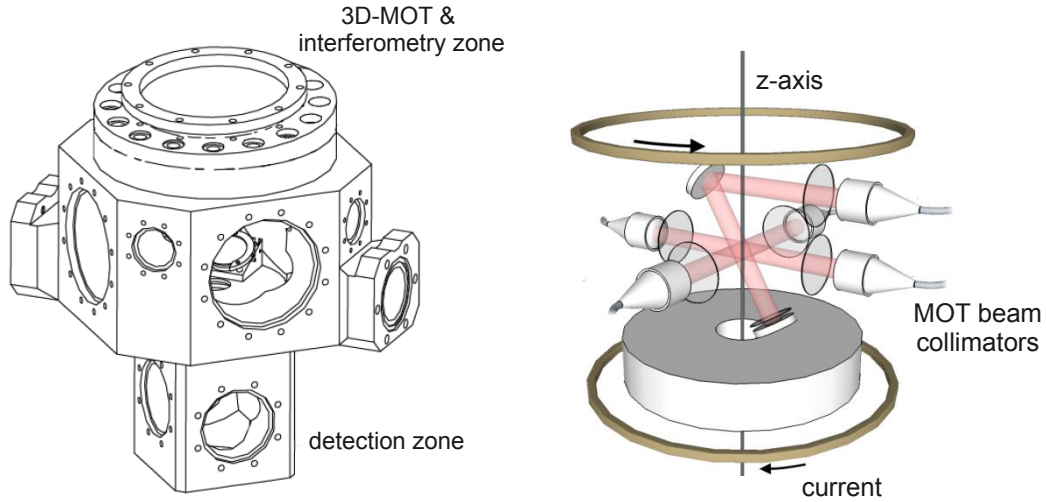
Figure 4.2: Vacuum chamber and 3D-MOT beam configuration [115]. The interferometer and 3D-MOT chamber features a detection zone on its bottom *(left)*. The 3D-MOT beam configuration is chosen such that the mixed trap beams can be applied on the vertical axis *(right)*. The magnetic quadrupole field is produced by a pair of coils oriented along the vertical axis.

region in which the atoms fall after release from the mixed trap. The vacuum conditions of below 10^{-9} mbar are maintained using an ion getter pump (IGP), which is attached to the pumping part of the vacuum system that has a connection to the interferometry chamber. The 2D-MOT section, which shows a pressure of about 10^{-8} mbar, is connected to the interferometer part via a differential pumping stage.

Atomic source

The atomic source is based on the same principles as the atomic sources in the case of the atom gyroscope. The ^{87}Rb atoms are provided by an atomic reservoir heated to a temperature between 40°C and 50°C. This source is attached to the 2D-MOT chamber in order to realize a sufficiently high Rubidium vapor pressure. The 3D-MOT is loaded by forming an atomic beam in the 2D-MOT that passes through the differential pumping stage. The magnetic quadrupole fields for magneto-optical trapping are provided using copper coils that are attached to the respective chamber parts.

Magnetic shielding

The whole system is shielded by a one-layer magnetic shield in octagon shape with a top and bottom cover. The shield features holes that allow for optical access

for atom cooling, trapping and detection. We compensate for residual magnetic fields using three pairs of copper coils mounted inside the magnetic shield, one in each of the three directions. This results in a residual field with a magnitude of approximately 1 mG [73].

Bias field for atom interferometry

During the interferometry and detection sequences, a homogeneous field in z-direction is applied. The field of 0.17 G defines the quantization axis for the atomic magnetic moment in the vertical direction. The typical differential quadratic Zeeman shift on the internal state transition amounts to 17 Hz.

Microwave antenna

A $\lambda/4$ microwave antenna is attached to the vacuum chamber, that allows for direct coupling between the two Rubidium hyperfine states using a 6.834 GHz signal delivered by an ultra-stable synthesizer. The field homogeneity allows us to perform Rabi oscillations with a contrast close to 100 %.

Atom detection set-up

Two photodiodes of type `Hamamatsu S-1337` with one common imaging lens mounted on the detection zone of the vacuum chamber collect a part of the light that is scattered from the atoms when passing through the detection zones, which allows for detecting the total atomic transition probability (see section 4.3.4). We employ optical band pass filters in front of the photodiodes in order to suppress the influence of stray light at 532 nm and 1064 nm. The two resulting electric signals are amplified and logged by the computer using an analog input card.

4.2.2 Laser system

The light fields for laser-cooling and magneto-optical trapping as well as for other processes in which resonant scattering on the ^{87}Rb D2-line is employed are provided by laser sources similar to the ones presented in section 3.3.2. The mixed optical dipole trap requires two lasers. The first one emits blue-detuned light with a wavelength of $\lambda_l = 532$ nm. The second laser is red-detuned and emits light at a wavelength of $\lambda_{dip} = 1064$ nm.

Required light fields

The light fields required for magneto-optical trapping, molasses cooling, optical pumping, detection and Raman beam splitting are depicted in figure 4.3. In addition to the cooling and trapping light as well as hyperfine selective fluorescence
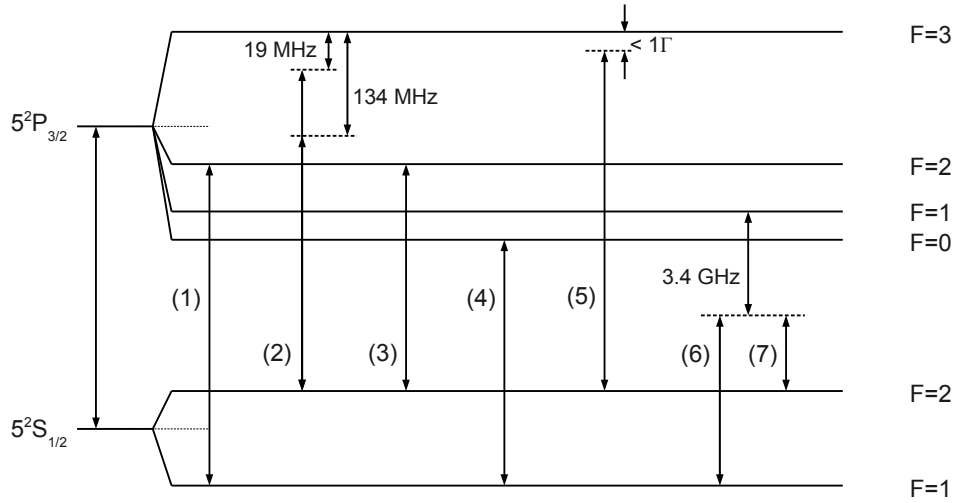
Figure 4.3: Required light fields. The used light fields are: (1) reference laser, locked 80 MHz below the repumping transition $|5^2S_{1/2}, F = 1\rangle \rightarrow |5^2P_{3/2}, F' = 2\rangle$ and, when compensated by an AOM, used for repumping (2) 2D- and 3D-MOT cooling light (3) 'depumping' light (4) optical pumping light (5) detection light (6) Raman laser 1 (ω_1) (7) Raman laser 2 (ω_2).

detection, a so-called 'depumping' light field is needed in the experimental sequence of the atomic short range force sensor. This light field serves for pumping all atoms from the $|5^2S_{1/2}, F = 2\rangle$ to the $|5^2S_{1/2}, F = 1\rangle$-state by resonantly driving the $|5^2S_{1/2}, F = 2\rangle \rightarrow |5^2P_{3/2}, F' = 2\rangle$ transition (see section 4.3.2).

Coherent tunneling in the vertical optical lattice based on stimulated Raman transitions requires two light fields stabilized in phase, similar to the free space case. The typical Rabi frequencies used in the trapped set-up have to be small compared to the Bloch frequency in order to resolve the transition orders Δm, which reduces the amount of required laser intensity. Furthermore, the coupling on the inter-site transition will be reduced with respect to the free atom case (these are depicted in figure 2.15). In order to reduce spontaneous single-photon scattering to a minimum, the global detuning is chosen to be $\Delta = -2\pi \cdot 3.4$ GHz. This value suppresses spontaneous scattering while keeping the possibility to compensate the Raman light field induced differential AC-Stark shift.

Besides the light fields for resonant single- and two-photon resonant coupling, two light fields are needed for optical trapping of atoms in the mixed trap, one blue-detuned lattice light field and another red-detuned light field for transverse confinement. The demands on the lattice laser are given on the one hand by the effective coupling strength depending on the relation of the lattice and coupling laser wavelength. The coupling strength given by (2.71) is indeed found to be small

for wavelengths close to the Raman laser wavelength, while our choice of $\lambda_l = 532$ nm allows for relatively large inter-site coupling [74]. On the other hand, the laser has to provide a single-frequency light field with high optical output power. For a large detuning, a high power is needed in order to enable the realization of lattice depths of several E_r while keeping a relatively large waist. This is important for a transverse homogeneity of the trap depth over the lateral expansion of the trapped atomic ensemble. These demands can be met by a frequency doubled solid state laser with an output wavelength of $\lambda_l = 532$ nm. The second light field needed in the mixed trap needs to feature a large red detuning with respect to the ^{87}Rb D1- and D2-line and high output power in order to efficiently trap the atoms laterally in the center of the lattice.

The transverse dipole trap light field induces a position dependent shift on the internal state transition, which results in an effective spectroscopic broadening which will be discussed in section 4.4.2. The shift can be compensated using a fairly weak light field inducing a differential shift opposed to the first. This can be realized with a light field that has a frequency close to the one of the Raman laser 1 (see figure 4.3).

Laser sources, frequency control and distribution

The laser sources at 780 nm used in the experiment are external cavity diode lasers (ECDL) [104] with tapered amplifiers (TA) for power amplification [105], similar to the lasers used in the atom gyroscope experiment. Acousto-optical modulators are employed for frequency and power control and mechanical shutters are used at appropriate positions in oder to effectively prevent for any resonant light from being coupled into the fibers during the spectroscopy or interferometer sequence. A schematic of the diode laser set-up is shown in figure 4.4, while more details on the laser system can be found in [73][1].

Four ECDLs are used in our experiment. The optical set-up is separated into two parts. One part consists of one cooling laser and one repumping laser. The other part includes Raman laser 1 and Raman laser 2.

The repumping laser is locked to the $|5^2S_{1/2}, F = 1\rangle \rightarrow |5^2P_{3/2}, F' = 2\rangle$ transition with a frequency offset of -80 MHz via a lock-in technique using an electro-optic modulator (EOM) for frequency modulation. The light coming from this laser serves as a reference for other lasers, which can thereby be stabilized using offset beat locks. Furthermore, the light is used for repumping during magneto-optical trapping and molasses cooling, as well as during detection. In both cases, the light is shifted on resonance with a 80-MHz-acousto-optical modulator (AOM). Optical pumping requires the light to be resonant with the $|5^2S_{1/2}, F = 1\rangle \rightarrow$

---

[1]Two changes have been made with respect to [73]. The so-called 'blower' light is now used as 'depumping' with a different frequency. Furthermore, the repumping light is now also used for optical pumping which is possible by shifting the frequency by an additional AOM double pass.
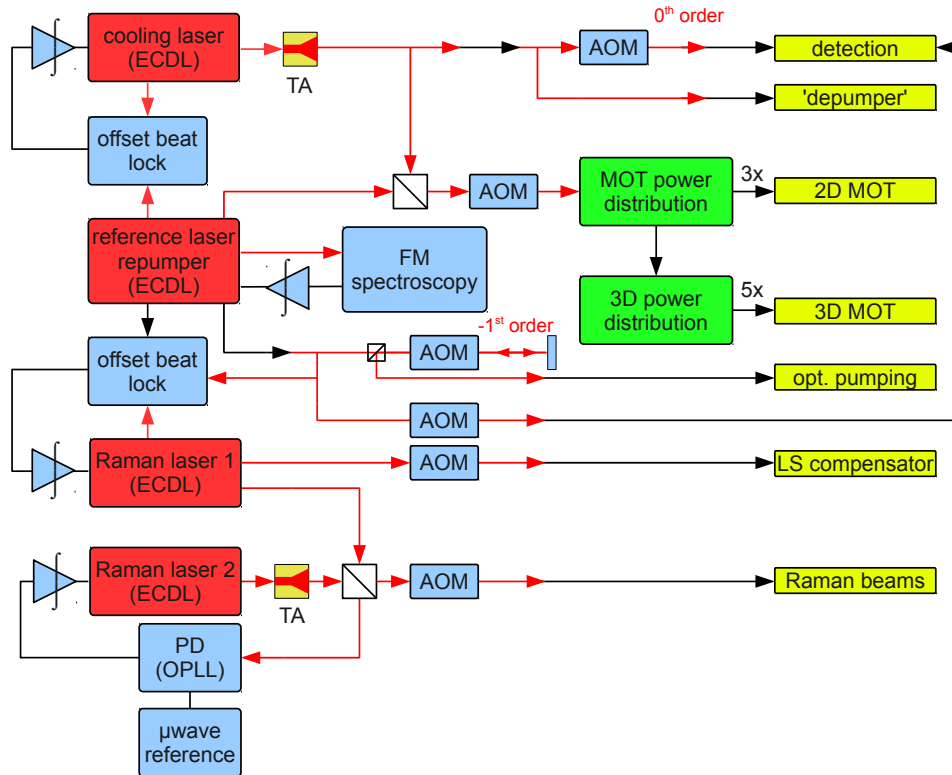
Figure 4.4: Diode laser set-up. *Red*: laser sources *Blue*: beat set-ups, electronic frequency controls, AOMs for frequency control and switching *Green*: frequency and power control using AOMs *Yellow*: experimental purpose. The black arrows represent fiber connections while free space laser beams are depicted with red arrows. Electric connections are shown as black lines. In the case of the detection, an AOM serves for power stabilization of the cooling light by diffracting a part of the light into the diffracted order. (AOM: acousto-optic modulator, PD (OPLL): phase detector for the optical phase-locked loop, ECDL: external cavity diode laser, TA: tapered amplifier, FM: frequency modulation.)

$|5^2P_{3/2}, F' = 0\rangle$ transition. This is achieved by passing through a 80-MHz-AOM double pass in the -1st order.

The cooling laser is power amplified to approximately 200 mW using a tapered amplifier and frequency locked to the repumping laser via an offset beat lock with a variable frequency offset around -6.8 GHz, which allows to drive the $|5^2S_{1/2}, F = 2\rangle \rightarrow |5^2P_{3/2}, F' = 2, 3\rangle$ transitions. We us the light of the cooling laser for magneto-optical trapping, molasses cooling, detection, and 'depumping'. The detuning needed in trapping and molasses cooling is controlled by acting directly on the beat lock frequency offset. Power control and switching is realized using an AOM. For detection, the cooling light is power controlled when passing trough an AOM in 0th order. For 'depumping', the laser frequency is tuned ex-

actly to the $|5^2S_{1/2}, F = 2\rangle \to |5^2P_{3/2}, F' = 1\rangle$ transition and the light is directly coupled into a fiber.

Two ECDLs serve as Raman lasers. The Raman laser 1 is locked to the repumping laser via an offset beat lock with a frequency offset of -3.4 GHz to the $|5^2S_{1/2}, F = 1\rangle \to |5^2P_{3/2}, F' = 2\rangle$ transition. The the relative phase of the two Raman lasers is stabilized onto an ultra-stable microwave reference using an optical phase-locked loop (OPLL). Within the OPLL, the beat note signal is first mixed with an ultra-stable signal at 6.934 GHz and, in a second step, frequency divided by 2 and compared on a phase detector to a signal coming from a 50 MHz direct digital synthesizer (DDS). Thereby, the DDS signal allows for convenient control of the relative Raman laser frequency and phase around the hyperfine frequency $\nu_{eg} = \omega_{eg}/(2\pi)$. As we need four times the optical power in Raman laser 2 compared to Raman laser 1, the light coming from Raman laser 2 is amplified using a tapered amplifier.

The optical 1D-lattice light field is provided by a solid state frequency doubled Nd:YVO^4 laser of type `Coherent Verdi V-12`, which features a chiller for heat dissipation `ThermoTek T255P`. The light field is guided to the vacuum chamber in a free-space set-up. For the realization of the transverse confinement dipole trap beam, we use a Yb-fiber laser of type `Manlight ML-CW-P-TKS` featuring a maximum optical output power of 20 W at a wavelength of 1064 nm. Switching and power control of both, the lattice and dipole trap beam, are realized using 80-MHz-AOMs.

4.2.3   Mixed trap and Raman beam set-up

The set-up depicted in figure 4.1 requires the lattice, transverse dipole trap and Raman beams as well as the differential light shift compensation beam to share a vertical optical axis. Superimposing the beams is realized by the use of dichroic mirrors, which is depicted in figure 4.5 *(right)*. The lattice and dipole trap beams are aligned vertically and onto the center of the magneto-optical trap. The alignment can easily be optimized on the total number of trapped atoms.

The lattice beam is applied from the bottom and retro-reflected on a dichroic mirror that is mounted above the vacuum chamber. This results in a standing light wave realizing the optical lattice. The upper window is slightly tilted in order to prevent for parasitic reflections. The beam waist is set to 600 μm using a Keplerian telescope before passing through the AOM. The dipole trap laser beam is shined in from the top collinear to the lattice beam and is dumped after the passage through the chamber. The beam waist of 200 μm at the position of the atomic cloud is realized by using a lens of focal length $f_{IR} = 400$ mm in a distance of 400 mm from the mixed trap position.

A counter-propagating Raman beam configuration is realized by shining in both Raman light fields from below and retro-reflecting only one of the two beams
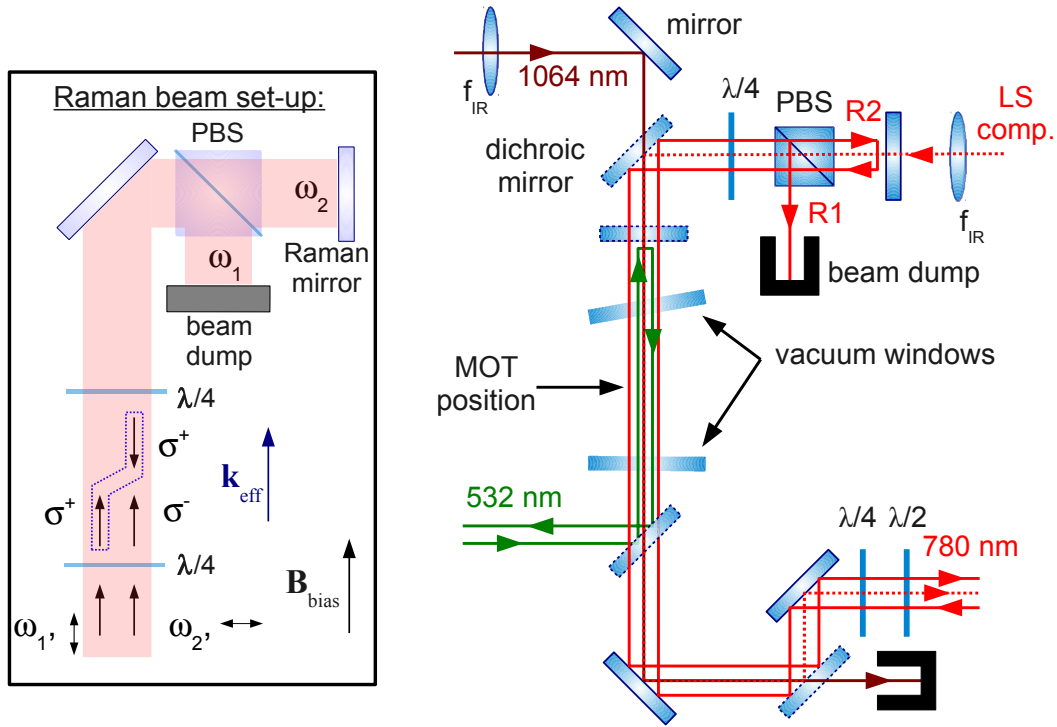
Figure 4.5: Mixed trap and Raman beam set-up. The Raman laser set-up *(left)* allows to realize a retro-reflective configuration while only choosing one momentum transfer direction. This is realized by reflecting only one of the Raman light fields while filtering out the other light field using a polarizing beam splitter cube (PBS). The trap and beam splitter set-up *(right)* is realized using dichroic mirrors *(dashed edging)* that allow to superimpose all fields on one optical axis. The arrows indicate the beam propagation directions while the actual optical axis are collinear.

as depicted in figure 4.5 *(left)*. For this, the polarizations of the two Raman light fields need to be circular and orthogonal. This allows us to choose only one pair of beams with frequencies ω_1 and ω_2 with the same polarization while the other pair is suppressed as the second beam is filtered out as depicted in figure 4.5 *(right)*. The two Raman light fields are guided to the experiment in one polarization maintaining single-mode optical fiber with orthogonal polarizations. Switching and power control are realized with an AOM before fiber coupling. After the exit of the fiber, the beam is enlarged to a collimated beam with a waist of 5.6 mm. The beam polarization is controlled using a half-wave plate and a quarter-wave plate before superimposing the Raman light fields with the mixed trap beams on dichroic mirrors. A second quarter-wave plate on the top of the experimental chamber allows to filter out the Raman beam 2 using a polarizing beam splitter cube before Raman beam 1 is retro-reflected and guided back to the mixed trap.

4.2.4 Lattice laser frequency stabilization

An accurate Bloch frequency measurement demands a precise knowledge and control of the lattice laser frequency. The stabilization of the laser frequency of a 532 nm laser on a molecular transition of bi-atomic iodine molecules has shown to be a method providing high precision and stability. I_2 features many transition lines in the visible electromagnetic spectrum thanks to rovibronic transitions, which are each split into either 15 or 21 hyperfine structure lines. Using cooled iodine vapor cells in advanced optical set-ups for modulation spectroscopy, relative frequency uncertainties in the lower 10^{-13} regime can be achieved in 1 s averaging time [116]. The accuracy can be as low as 10^{-12} in relative units [117].

The lattice laser frequency is locked using a frequency modulation transfer spectroscopy (FMTS). As the demands are moderate in our case, the lock set-up is simplified in comparison to the realizations presented in [116, 117]. Details on the frequency lock can be found in appendix B. The linewidth of the transition that is used for locking is determined to be $\delta\nu_l$=9 MHz. Considering this linewidth as the relative uncertainty of the lock leads to a relative uncertainty and accuracy in the lattice laser wavelength of below

$$\frac{\delta\nu_l}{\nu_l} = 1.6 \cdot 10^{-8}.$$

The free-running frequency stability is found to be not limiting the present measurement precision. Therefore, the lock is not used during the measurements presented in this work. Nevertheless, it serves for long term stability and accuracy studies presented in [75].

4.2.5 Computer control and data acquisition

The experimental parameters and timings are controlled using a computer. An analog output card allows for controlling experimental parameters by setting a set-point voltage for e.g. power control in AOMs, frequency and phase control of sinusoidal signals using a DDS and a synthesizer. Switching processes are controlled using TTL signals generated by the computer. An analog input card enables the high resolution read out of e.g. photodiode signals.

Besides parameter and timing control, a `C` based software allows to realize a computer based locking scheme. From shot to shot, experimental parameters can be automatically modified following control parameters that are generated based on information gained in the precedent interferometer cycle. This realizes a software based lock of the atom interferometer to, for example, a fringe slope.

4.3 Measurement sequence

We perform the spectroscopy and interferometry measurements in experimental cycles of a typical length of 1.4 s to 2 s. After trapping and cooling the atoms in the magneto-optical trap, they are loaded into the mixed trap, where the interferometer state preparation and spectroscopy or interferometer pulse sequence take place. After the completion of the pulse sequence, the atoms are released from the trap. The dropped atoms pass a detection zone in which the hyperfine state selective fluorescence detection allows to determine the transition probability via the measurement of the internal state populations.

4.3.1 Trapping and cooling

The atomic source for the trapped interferometry is realized using a 2D-3D magneto-optical trap (MOT) system. During the loading sequence of $T = 500$ ms, about 10^7 atoms are loaded into the 3D-MOT [73]. The 2D-MOT flux, and thus the loading rate, is mainly limited by a Rubidium deposit on the bottom vacuum window leading to a partial intensity imbalance between the ascending and descending 2D-MOT laser beams.

After trapping in the MOT, the atoms are cooled down in an optical molasses. While the detuning is chosen to be -3Γ during the MOT phase, the molasses is realized using a detuning of -20Γ, where $\Gamma = 2\pi \cdot 6.067$ MHz is the linewidth of the cooling transition. Parallel to the detuning ramp from -3Γ to -20Γ of 1 ms duration, the magnetic field is switched off. After 10 ms of molasses cooling, the 3D-MOT light intensity is ramped down using a shutter with typical switching times of approximately 500 μs. This leaves an ensemble of 10^7 ^{87}Rb atoms with a temperature of 2 μK.

The cold atomic ensemble is then loaded into the mixed trap consisting of the vertical 1D lattice and the superimposed optical dipole trap. For a measured power at the atomic position of $P_l = 7$ W and the given waist of $w_{0,l} = 600$ μm, we find a theoretical maximum lattice depth of $U_0 = 7.4E_r$ using (2.99). This depth corresponds to an atomic temperature of $\Theta_{at} = U_0/k_B = 2.8$ μK with k_B being the Boltzmann constant. Hence, the atoms are trapped in the vertical direction with relatively high efficiency. The lattice depth found in the experimental sequence is slightly lower. We find depths of up to $U_0 = 6.5E_r$ for optimal alignment. We typically $U_0 = 1.8E_r$ and $U_0 = 4E_r$, which corresponds to temperatures of $\Theta_{at} = 0.7$ μK and $\Theta_{at} = 1.5$ μK, respectively.

The trapping efficiency in the lateral direction is mainly limited by the relatively small trap volume. Approximately $4 \cdot 10^4$ atoms are trapped in the mixed trap that features an effective lateral radius of about 200 μm. The initial MOT size results in a vertical spread of trapped atoms of about 2.5 mm. For the two different trap depth values, we find a number of trapped atoms after $T_{trap} = 0.5$ s of $N = 18,000$
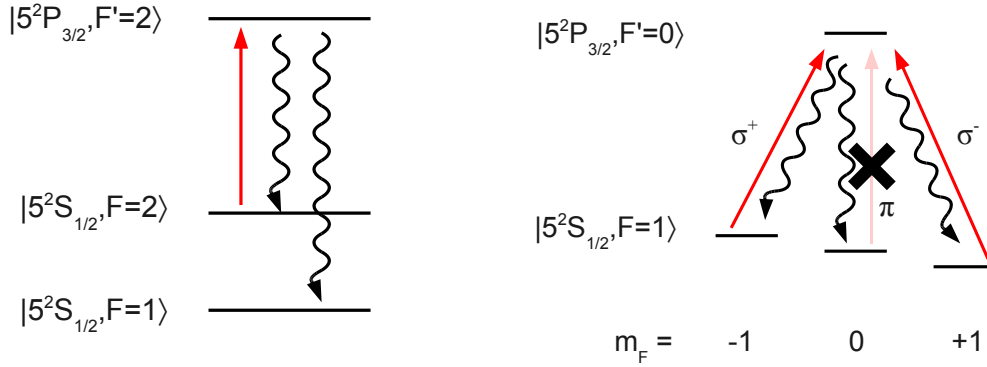
Figure 4.6: Optical depumping and optical pumping. *Left*: Optical 'depumping' pumps the atomic ensemble from the $F = 2$ to the $F = 1$-state. *Right*: Optical pumping on the $F = 1 \rightarrow F' = 0$-transition with light linearly polarized along the quantization axis results in accumulating the atoms to the interferometer ground state.

and $N = 50,000$, respectively.

4.3.2 State preparation

In order to fulfill the assumption that $P_e(t = 0) = 0$, we prepare all atoms in the interferometer ground state $|g\rangle$. After being trapped in the MOT and loaded into the mixed trap, the atoms are equally distributed over all five Zeeman sub-levels of the $|^5S_{1/2}, F = 2\rangle$-state.

The two steps of the state preparation depicted in figure 4.6 are based on optical pumping [118]. First, the atoms are brought to the $|5^2S_{1/2}, F = 1\rangle$-state using the 'depumping'[2] light field. The 'depumping' is realized by driving the $|5^2S_{1/2}, F = 2\rangle \rightarrow |5^2P_{3/2}, F = 2\rangle$ transition. The atoms are accumulated in the $|5^2S_{1/2}, F = 1\rangle$ Zeeman manifold. Second, optical pumping is performed on the $|5^2S_{1/2}, F = 1\rangle \rightarrow |5^2P_{3/2}, F = 0\rangle$ transition. The interplay of the linearly polarized light field and the magnetic field quantization axis along this polarization efficiently suppresses the π-transition. As a consequence, $|g\rangle = |5^2S_{1/2}, F = 1, m_F = 0\rangle$ represents a dark state, in which the atoms accumulate. The efficiency of this process of 95 % is limited by polarization impurities of the optical pumping beam. Applied optical power and pulse time are chosen by making a trade-off between pumping efficiency and atom loss.

A way to remove the residual $|5^2S_{1/2}, F = 1, m_F \neq 0\rangle$ atoms is given as follows. We can transfer the $|5^2S_{1/2}, F = 1, m_F = 0\rangle$ atoms to the $|5^2S_{1/2}, F = 2, m_F = 0\rangle$-

---

[2]The term 'depumping' refers to the fact that the atoms are brought from the Zeeman manifold around the excited interferometer state to the one around the interferometer ground state, which realizes a counterpart to the process described by the term 'repumping'.

state using a resonant microwave π-pulse and further shine in the optical pumping beam. The polarization impurities then would cause heating in the atomic ensemble which removes the residual atoms after a sufficiently long application time. This process could be realized in shorter time by changing the polarization of the optical pumping beam to an arbitrary one, e.g. by inserting a half-wave plate glued on a controllable lever.

4.3.3   Raman laser and microwave pulse application

The application of Raman light field pulses is realized using an acousto-optical modulator for switching and power control. The pulses show typical durations of a few ms up to more than 1 s. The maximum laser intensities used in the measurements presented in this work are $I_{1,max} = 0.25$ mW/cm^2 and $I_{2,max} = 0.54$ mW/cm^2 for typical pulse lengths of the order of 10 ms. The microwave can be used to drive the internal state transition without transferring momentum to the atoms. The intensity and frequency are controlled by the synthesizer that provides the microwave signal.

4.3.4   State selective fluorescence detection

After the release from the trap, the populations of both internal states N_g and N_e are determined in a hyperfine state selective fluorescence detection. This results in the transition probability

$$P_e \;\; = \;\; \frac{N_e}{N_g + N_e}. \tag{4.3}$$

The two atom numbers are determined via the resonantly scattered light intensity of the atoms in the respective states when falling through two light sheets underneath the mixed trap after being released from the lattice by switching off the lattice and dipole trap laser (see figure 4.7 *(left)*). The light field in these two light sheets is almost resonant with the $|5^2S_{1/2}, F = 2\rangle \rightarrow |5^2P_{3/2}, F' = 3\rangle$ transition and circularly polarized. This allows us to drive a closed transition between the $m_F = 2$ and $m'_F = 3$-states. The detection beams are applied in a retro-reflected configuration in order to minimize heating and thus maximize the number of scattered photons during the passage. The bottom part of the retro reflecting mirror is blocked, which results in heating and pushing of the detected atoms out of the second light sheet's zone of interest.

Detecting light scattered in the first sheet thus enables us to determine N_e. The atoms in the ground state do not fluoresce in the first light sheet. They are then optically repumped in a third light sheet, which is placed between the two detection light sheets. The subsequent detection in the second detection light sheet results in the population number N_g.
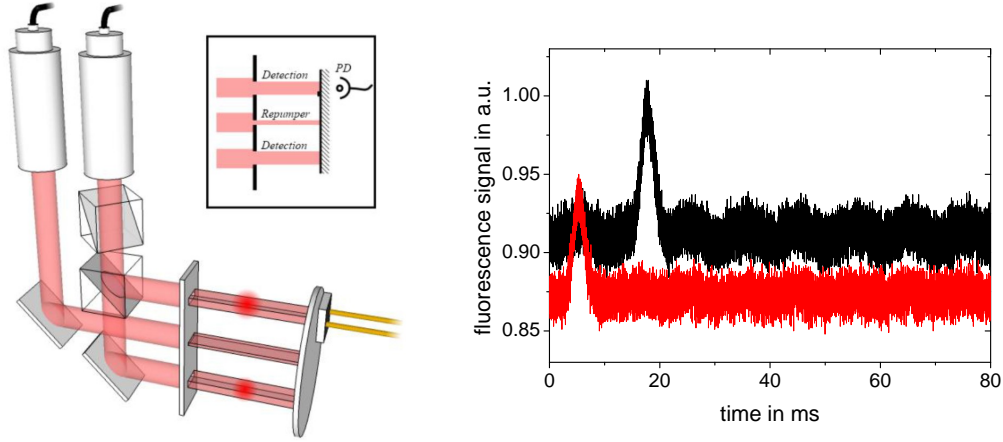
Figure 4.7: Detection scheme (left picture taken from [73]). *Left:* The population of the two internal states are measured when the atoms pass through the detection and repumping light sheets after being released from the lattice. The fluorescence signals of each sheet corresponding to the population N_e and N_g, respectively, are captured by two separate photodiodes. The detection intensity is stabilized using the residual transmission of the retro reflection mirror of the detection molasses. The light sheets are realized with apertures in front of the Gaussian beams coming from the collimators. *Right:* The fluorescence signals are integrated within the computer data treatment. The resulting value is proportional to the state population N_g and N_e, respectively. The signals show a 100 Hz modulation caused by incident the laboratory light. This is averaged out if the integration time is chosen to be a multiple of 10 ms.

Tracked over time, the two fluorescence signals result in time of flight signals representing a convolution of the light sheet's intensity profile and the spatial distribution of the atomic ensemble during detection (see figure 4.7*(right)*). After subtracting the corresponding offsets from these signals, their integrated values are proportional to the state populations N_e and N_g.

For an appropriate operation of this detection scheme, the light intensities have to be adapted. The repumping beam intensity is chosen such that the atoms are, on the one hand, sufficiently repumped in the excited state during their passage, and, on the other hand, not repumped by diffused light before entering the detection, which is the case if the intensity is too high. The detection light intensity is adjusted to be well in the saturation regime, in the order of a few mW/cm^2. This intensity is stabilized on a controllable reference voltage [73]. A photodiode measuring the residual transmission of the detection beam's retro reflection mirror provides the error signal for this stabilization (see figure 4.7*(left)*).
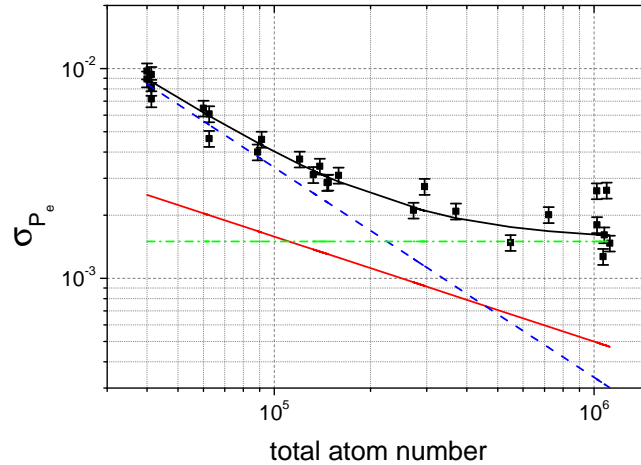
Figure 4.8: Particle number dependent detection noise. The detection noise σ_{P_e} is measured *(black squares with statistical error bars)* as a function of the total number of atoms in free-falling configuration. For this, the 2D-MOT loading time is varied in order to achieve the wanted atom number in the detection. The different regimes are given by a fit *(black line)*, representing a quadratic sum of the different regimes of $1/N$ *(blue dotted line)*, $1/\sqrt{N}$ *(red solid line)* and constant noise *(green dashed line)*.

Detection noise

As the transition probability detection shows an intrinsic noise σ_{P_e}, it potentially limits the signal-to-noise ratio of the spectroscopic and atom interferometer measurements. While the fundamental limit of the detection resolution is given by the quantum projection noise (QPN), technical limitations like amplifier noise and detection light power and frequency fluctuations are sources for detection noise. Depending on their origin, the different noise sources show different power laws with respect to the atom number N [119].

Technical noise which does not depend on the atom number scales with $1/N$. Here, these noise sources are mainly the photodiode dark current, the electric amplifier noise, and background light detected by the photodiode. QPN is a classical fundamental limitation, which scales with $1/\sqrt{N}$ [100]. Noise influences scaling with the atom number cause a noise floor, which is constant in regard to the total atom number. Noise sources of this kind are fluctuations of the detection laser frequency and optical output power.

An evaluation of the detection noise is performed in two ways, by dropping the atoms directly after the molasses phase, and by trapping the atoms in the mixed trap before release and detection, respectively. In order to determine the regime we work in and the ultimate noise limit of the detection system, when
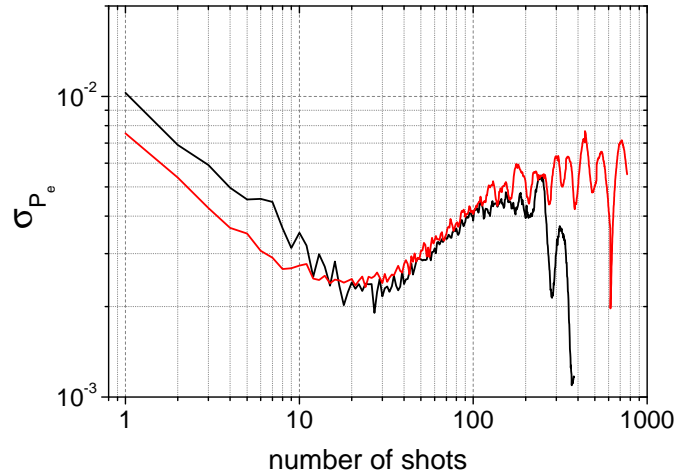
Figure 4.9: Detection uncertainty over time. The detection noise is depicted as an Allan like standard deviation over the number of shots for $3 \cdot 10^4$ atoms that are directly released after molasses cooling *(black boxes)* and for $4 \cdot 10^4$ atoms, that have been trapped in the mixed trap for 1 s *(red dots)*. The curves can be approximated by $\sigma_{P_e} = 0.75 \cdot 10^{-2}$ and $\sigma_{P_e} = 1 \cdot 10^{-2}$, respectively *(dotted lines)*. Taking into account the $1/N$ behavior, the detection noises for atoms coming from the molasses and coming from the mixed trap are found to be the same.

performing measurements in the mixed trap, we first measure the noise in the transition probability σ_{P_e} as a function of number of atoms directly dropped after molasses cooling (see figure 4.8). For this measurement, a microwave $\pi/2$-pulse with negligible power as well as frequency noise provides a transition probability with a typical working point value of $P_e = 0.5$.

In order to compare the detection noise in the two cases, the noise is measured in a time series for atoms dropping after the molasses phase and atoms being dropped after a holding time in the mixed trap of 1 s. The resulting Allan standard deviation given in figure 4.9 shows similar behavior of the detection for both cases when we suppose that the total number of detected atoms is equal for trapped and free-falling ensembles and take into account operation in the $1/N$ regime.

The working point is predetermined by the number of atoms loaded in the composed trap and the trap lifetime, resulting in typically $3 \cdot 10^4$ to $4 \cdot 10^4$ atoms at a total trap time of 500 ms to 1 s, which clearly puts the measurement in the $1/N$ regime with a typical detection noise on P_e for $N = 3 \cdot 10^4$ of

$$\sigma_{P_e} \;\; = \;\; 1 \cdot 10^{-2} \text{ per shot.}$$

4.3.5   Compensation of differential AC-Stark shifts

The presence of off-resonant electromagnetic fields induces a differential AC-Stark shift on the internal state transition of the interfering Rubidium atoms. The light fields inducing this shift are the Raman beams as well as the trapping laser beams.

The size of the Raman laser beams being much larger than the size of the mixed trap, the differential AC-Stark shift induced by the beam splitting light fields can be considered to be homogeneous over the extend of the atomic ensemble. This results in a frequency offset on the measurement that, in principle, can vary over time. For our case, it is in the order of several hundreds of Hz for π-pulses of a typical duration of 10 ms. However, the choice of an appropriate intensity ratio I_2/I_1 of the two beam splitting light fields allows for compensation of the two differential shifts induced by each of the Raman laser fields (see section 2.5.1). The compensation is optimized on an inner-site transition spectrum by using a microwave coupling pulse with a duration that is similar to the Raman coupling pulse durations typically used in our experiment. Parallel to the application of the microwave field the Raman light fields are shined in. The detuning Δ to the respective single-photon transitions stays unchanged while the two-photon detuning is chosen to several MHz with respect to the hyperfine transition frequency. With this setting, the Raman beams do not induce any coupling via a two photon transition, but the Raman light fields' differential AC-Stark shift on the internal state transition is the same as in the case of Raman coupling. This allows for a direct determination of the shift by driving the microwave transition with and without the presence of the Raman light fields. We are able to compensate the differential AC-Stark shift with an accuracy of several Hz by choosing the intensity ratio to[3] $I_2/I_1 \approx 2$.

The lattice laser induced AC-Stark shift is comparatively small as the detuning to the Rubidium D-lines is large and the atoms are trapped in the intensity minima of the laser standing wave. Also, the shift is homogeneous over the atomic ensemble as the atoms are confined in the center of the lattice laser's transverse beam profile using the dipole trap for lateral trapping. Performing a microwave interrogation for different lattice laser intensity values, the total shift is found to be 0.4 Hz for the maximum laser power and the chosen waist of $w_{0,l} = 600 \ \mu$m. The differential light shift is stable and does not cause dephasing over the atomic ensemble. It therefore has to be taken into account in accuracy studies of the measurement but is not expected to show strong fluctuations and thus can be neglected here.

The dipole trap laser beam realizing the lateral confinement induces an inhomogeneous differential AC-Stark shift on the internal state transition over the atomic ensemble. While the mean differential light shift is determined to 3 Hz/W,

---

[3]The theoretical intensity ratio for the compensation is $I_2/I_1 = 3.43$ (see figure 2.16), and therefore $I_2/I_1 = 1.72$ in our beam configuration. In reality, partial reflections on the dichroic mirrors and imperfect suppression of the retro-reflection of Raman light field with frequency ω_2 slightly changes the intensity ratio.
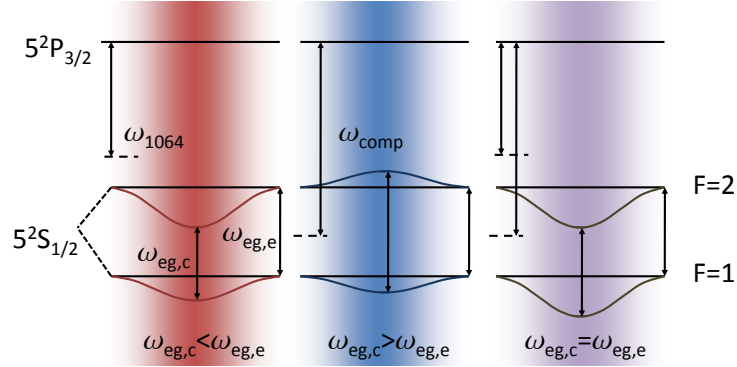
Figure 4.10: Differential light shift compensation. The schematic depicts the differential light shift of the internal state transition induced by the dipole trap laser beam *(left)*, the differential light shift compensation beam *(center)* and the compensated differential light shift when superimposing the two *(right)*, which leads to a vanishing differential AC-Stark shift. The internal state transition frequencies in the trap center $\omega_{eg,c}$ is smaller than the one on the edge of the trap $\omega_{eg,e}$ for the dipole trap beam and vice versa for the differential light shift compensation beam.

the peak broadening of the microwave transition is found to be 2 Hz/W. This leads to a broadening in a Rabi pulse spectroscopy and to contrast decay in the Ramsey measurement on the inner- and, more importantly, on the inter-site transition (see section 4.4.2). Therefore, the differential light shift is compensated using a technique presented in [120], which is similar to the idea of the differential light shift compensation in the coupling laser case. The effective red detuning of the internal state transition is counterbalanced by a weak light field, which is tuned in between the two hyperfine transition states and spatially mode-matched to the trapping beam. While this light field is blue detuned for the upper state, it is red detuned for the lower state, which results in an effectively positive differential light shift (see figure 4.10). The Raman light field coming from Raman laser 2 has the appropriate frequency. This allows us to use a part of this light for light shift compensation in the dipole trap. For this purpose, a part of the beam is picked up and coupled into a fiber after passing through an AOM. The AOM shifts the light by 80 MHz and therefore prevents for interference effects between the compensation beam and the Raman beam splitter light field. As the required intensity for this compensation beam is only in the range of a few nW in our case, the light field can be shined in via the Raman retro-reflective mirror by using the residual transmission (see figure 4.5). The beam is mode-matched to the dipole trap beam by using a lens of focal length f_{IR}. The performance of the differential light shift compensation and the optimization of the superposition with the dipole trap beam is presented in section 4.4.2.

4.4 Wannier-Stark spectroscopy and interferometry

The measurement of the Bloch frequency with high resolution using Wannier-Stark spectroscopy and interferometry necessitates coherent coupling of the Wannier-Stark states. Here, the inter-site coupling is shown in Wannier-Stark spectra for a single pulse and Ramsey interrogation scheme. After discussing the dipole trap differential AC-Stark shift as a limitation for the measurement resolution and its compensation, the limitations on the resolution of a single pulse are described.

4.4.1 Wannier-Stark spectra and coherent coupling

The transition probability pattern resulting from a scan of the relative Raman laser frequency around the internal state transition frequency is a so-called Wannier-Stark spectrum. This appears as structure of many peaks, that are separated one from another by multiples of the Bloch frequency. This spectrum is found by rewriting (2.76) to peaks of the form

$$P_{e,\Delta m} \quad = \quad \frac{\pi^2}{4}\mathrm{sinc}^2\left(\frac{\pi}{2}\sqrt{1 + \frac{(2\pi\Delta\nu_{\Delta m})^2}{\Omega_{\Delta m}^2}}\right). \tag{4.4}$$

Here, the effective frequency detuning is given by $\Delta\nu_{\Delta m} = \nu_R - \nu_{eg} - \Delta m\nu_B - \nu_{qZ} - \nu_{ACT} - \nu_{ACR}$. This is valid when the Rabi frequencies $\Omega_{\Delta m}$ are chosen to be smaller than the peak frequency separation, which is given by the Bloch frequency. Hence, the Raman laser power is chosen such that the typical pulse length is $\tau_\pi = \pi/\Omega_{\Delta m} \gg \pi/\omega_B \approx 1$ ms.

We probe the inter-site coupling by applying a single Raman pulse of a length of $\tau = 10$ ms with Raman intensities $I_{1,max}$ and $I_{2,max}$ after trapping the atoms in the mixed trap and preparing all atoms in the ground state. The recorded detected transition probability is measured subsequent to releasing the atoms after a trapping time of 500 ms. In figure 4.11, two spectra are depicted for two different lattice depths, which are realized by varying the lattice beam's optical power. We observe peaks for relative Raman detunings at multiples of the Bloch frequency values plus a small offset $\nu_R = \nu_{eg} + \Delta m \cdot \nu_B + \nu_0$. The single peaks correspond to coupling from any lattice site m to a neighbor $m' = m + \Delta m$. Here, the internal state transition frequency shift is given by $\nu_0 = \nu_{qZ} + \nu_{ACT} + \nu_{ACR}$.

The pulse duration is chosen smaller than a π-pulse duration for all transitions. Hence, the relative peak heights are a good measure of the coupling strengths as a function of Δm. Indeed, we can precisely determine the lattice depths seen by the atoms by comparing the peak heights of the respective orders Δm. Using the coupling strength plot as a function of the lattice depth in figure 2.15, we find the lattice depth values to be $U_0 = 3.9E_r$ and $U_0 = 1.6E_r$ for the two spectra depicted in figure 4.11. It can be seen clearly that coupling between further separated lattice sites is possible in shallower lattices. On the other hand, for even shallower lattices,
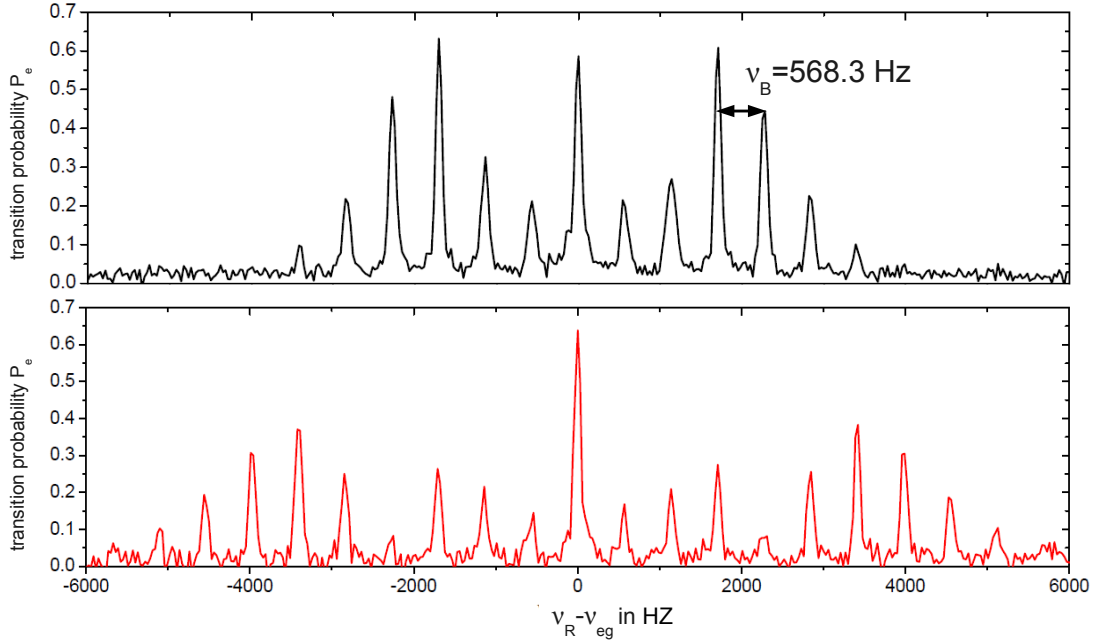
Figure 4.11: Wannier-Stark spectra. The spectra are obtained by tracking the transition probability after a single Raman pulse for atoms initially in the ground state for different relative Raman laser detuning. The relative detuning is plotted as an offset to the internal state transition frequency. The lattice depth values are found to be $U_0 = 3.9 E_r$ *(top)* and $U_0 = 1.6 E_r$ *(bottom)*.

the number of trapped atoms is strongly reduced which makes a spectroscopic measurement very noisy and even impossible. We find the trade-off that has been described in section 2.3.

Given the coupling between lattice sites, the coherence of the transition needs to be investigated. This is done by driving Rabi oscillations on single inter-site transitions. For this, the Raman frequency is chosen to be on resonance with one of the inter-site transitions and the duration of the Raman pulse is scanned from shot to shot. Rabi oscillation plots are shown in figure 4.12 for the transition $\Delta m = 3$ for the two selected lattice depth values. Indeed, the Rabi frequency is larger in the case of the deeper lattice as expected from numerics. Furthermore, the damping is stronger in the case of the shallower lattice. This can be explained by a Bloch frequency inhomogeneity. A slightly inhomogeneous coupling, which is given by a lattice depth inhomogeneity induced by the Gaussian lattice beam profile, results in an certain Rabi frequency distribution over the atomic ensemble. The width of this distribution is relatively small for a local maximum of $\Omega_{\Delta m}/\Omega_0$, while it is larger on the slope of the inter-site coupling strength with respect to the lattice depth. A small width results in a relatively homogeneous Rabi frequency over the atomic ensemble and a relatively slow damping of the Rabi oscillations.
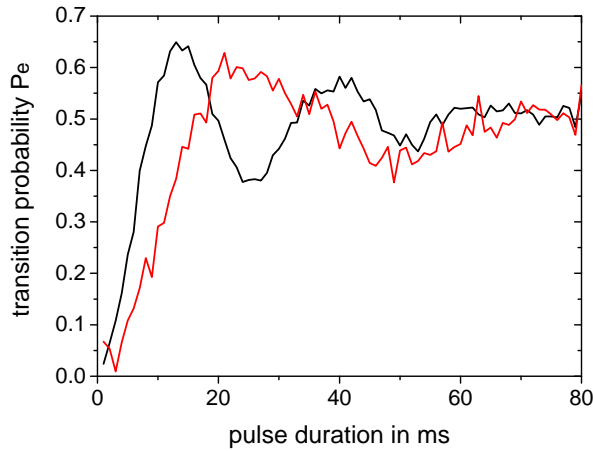
Figure 4.12: Rabi oscillations on the inter-site transition $\Delta m = 3$. The transition probability is plotted versus the duration of the single Raman pulse for $U_0 = 3.9 E_r$ *(black)* and $U_0 = 1.6 E_r$ *(red)*.

The coupling strength can be studied for different lattice depth values. The determination of Rabi frequencies for different lattice depth values for oscillations on the transitions $\Delta m = 1, 2, 3, 4$ allows to reproduce the numerical solutions of (2.71). The Rabi frequency values for different lattice depths and different diffraction orders are depicted in figure 4.13 with the free space Rabi frequency Ω_{eff} being a adjustable factor.

So far, the coherent coupling of lattice sites has been demonstrated for atoms in the same lattice band. By choosing the appropriate relative Raman laser frequency, it is possible to measure the Bloch frequency using a single pulse interrogation. However, the theoretical description is only valid for a system that only features one band of the lattice being populated [39]. Indeed, by extending the Wannier-Stark spectrum in figure 4.11 to frequencies in the order of 15 kHz in the case of the deep lattice ($U_0 = 3.9 E_r$), a broad plateau of the transition probability is found, which indicates that the atoms undergo an inter-band transition. Hence, the Raman laser interaction allows for coupling between bands. For a shallower lattice, the inter-band transition moves to lower frequency values as expected. However, only a blue sideband is observed. This suggests that no atoms are present in the excited band, as the coupling from the excited to the bottom band would necessitate a red sideband transition. Indeed, we find a rather short life time of states in the excited band of only 16 ms. Hence, atoms that are initially trapped in the excited state are lost before the moment of pulse application. This leaves us with the desired system of atoms in the bottom band of a vertical 1D-lattice.

Using the coherent coupling of the inter-site transition, a WSR interferometer
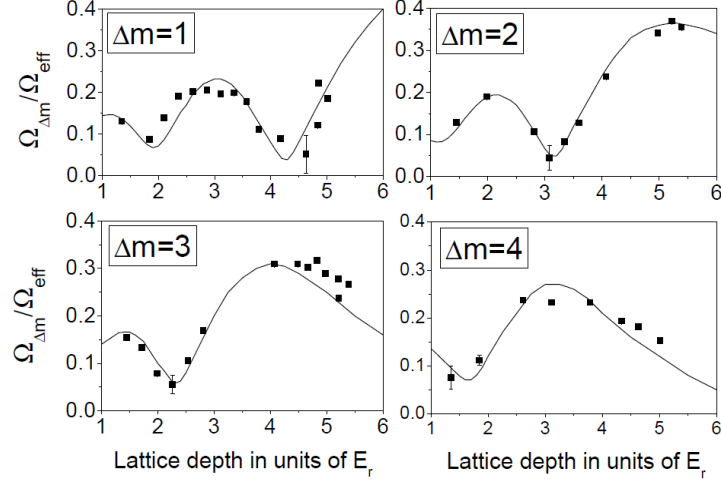
Figure 4.13: Rabi frequency mapping. The measured Rabi frequencies *(boxes)* follow the theoretical calculations *(lines)* versus the lattice depth, which is depicted for different values Δm.

can be realized. This represents a simple interferometer on the Wannier-Stark inter-site transition. Following the considerations in sections 2.6 and 2.7.2, we find the interferometer signal to be

$$P_{e,\Delta m} = P_{e,0} - \frac{C}{2}\cos(\Delta\Phi_{WSR}) \tag{4.5}$$

with a WSR phase shift given in (2.108). For a small detuning from the resonance of the Δm transition, this fringe pattern can be obtained by scanning the Raman laser frequency ν_R as in the case of the Wannier-Stark spectrum using a single-pulse interrogation. The resulting fringe pattern is then given by

$$P_{e,\Delta m} = P_{e,0} - \frac{C}{2}\cos\left(2\pi\Delta\nu_{\Delta m,R}\left(T + \frac{4\tau_{\pi/2}}{\pi}\right)\right). \tag{4.6}$$

Here, the effective detuning $\Delta\nu_{\Delta m,R}$ allows to account for the fact that the differential Raman laser AC-Stark shift is only present during pulse application. The detuning

$$\Delta\nu_{\Delta m,R} = \nu_R - \nu_{eg} - \Delta m\nu_B - \nu_{qZ} - \nu_{ACT} - \nu_{ACR}\frac{\frac{4\tau_{\pi/2}}{\pi}}{T + \frac{4\tau_{\pi/2}}{\pi}} \tag{4.7}$$

then results in the resonance condition for the relative Raman laser frequency

$$\nu_{\Delta m,R} = \nu_{eg} + \Delta m\nu_B + \nu_{qZ} + \nu_{ACT} + \nu_{ACR}\frac{\frac{4\tau_{\pi/2}}{\pi}}{T + \frac{4\tau_{\pi/2}}{\pi}}. \tag{4.8}$$
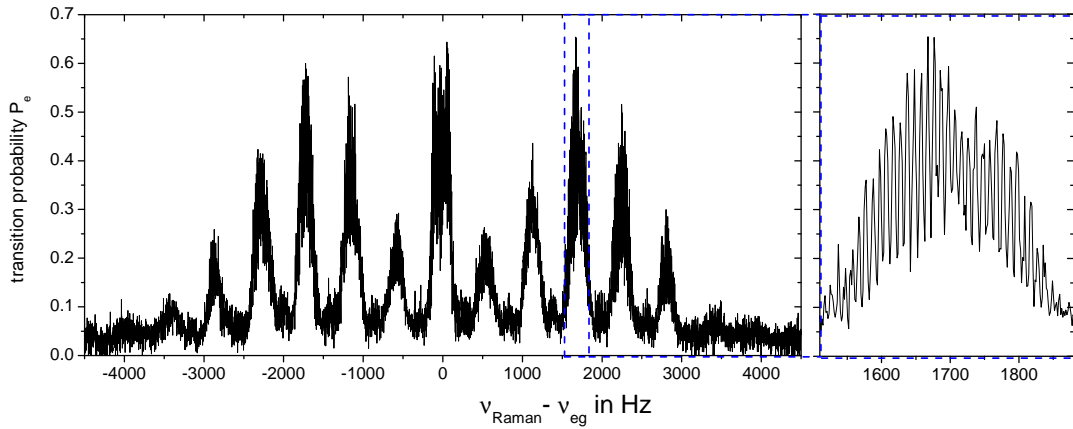
Figure 4.14: WSR spectrum for $U_0 \approx 3.9\ E_r$. The transition probability is plotted against the relative Raman laser frequency minus the internal state transition frequency. A zoom on the transition $\Delta m = 3$ is depicted within the blue dashed box.

The same frequency scan as employed in the single pulse configuration results in maxima around the values for zero detuning $\Delta\nu_{\Delta m,R} = 0$. The spectrum for a Ramsey sequence with pulse durations of $\tau_{\pi/2} = 5.5$ ms and a Ramsey time of $T = 100$ ms is depicted in figure 4.14 for the case of a lattice depth of $U_0 = 3.9 E_r$. It shows the WSR fringes with Rabi envelopes for large detuning. A zoom of the pulse on the transition $\Delta m = 3$ is depicted in the same figure, which shows the expected fringe spacing of $1/(T + \frac{4\tau_{\pi/2}}{\pi}) \approx 10$ Hz as well as a fringe contrast of approximately 30 %.

4.4.2   Influence of the transverse optical dipole trap

The lateral confinement of the atoms in the center of the intensity profile of the lattice laser beam using the transverse dipole trap has consequences on the Wannier-Stark spectroscopy and interferometry. The Gaussian intensity profile of the dipole trap determines the shape of the potential the atoms are trapped in. Classically speaking, the atoms oscillating in the transverse dipole trap potential have different maximum deflection from the trap center depending on their total energy. Quantum mechanically speaking, the dynamics in the dipole trap can be described by a harmonic oscillator if the potential can be approximated by a parabola [121]. The atoms populate many of the eigenstates depending, once again, on their total energy. The modes of the harmonic oscillator are separated in energy by $h\nu_{dip}$ with ν_{dip} being the trap frequency. States with higher energies have larger position uncertainty, which is the equivalent to the classical average deflection from the

center. The total energy is determined by the positions and velocities in x- and y-directions at the moment the atoms are trapped in the dipole trap.

The transverse profile of the dipole trap beam results in a position dependent differential AC-Stark shift. The differential light shift profile is given by the Gaussian beam profile of the dipole trap beam with maximum light shift in the center. This leads to a different differential light shift for atoms with different kinetic energies in the transverse directions. The atoms with higher energy have a larger average position spread and therefore experience a smaller total differential light shift. The actual position and energy distribution of the atoms in the dipole trap result in a differential light shift distribution profile. In the case of a single spectroscopy pulse, the width of this distribution translates into an effective peak broadening, while in the case of a WSR interferometer, fringe contrast is strongly reduced due to an effective dephasing of the atomic ensemble. We counteract on these effects with the differential AC-Stark shift compensation beam. This light field induces a differential light shift that is exactly opposite to the one of the dipole trap laser beam. The performance of the compensation is investigated for the Rabi and WSR case. As this is a pure internal state effect, the study is realized using a microwave inner-site coupling.

A second effect of the transverse confinement onto the Wannier-Stark spectrum is given by coupling of the harmonic oscillator states. The eigenstates of the harmonic oscillator in transverse direction can be coupled during the stimulated Raman transition. If the transverse component of $\mathbf{k}_{\text{eff}}$ is sufficiently large, an atom can gain or lose transverse momentum in the interaction with the Raman light fields during an inter-site transition, resulting in a change of the vibrational state. This leads to sidebands on the spectroscopic line as we shall see below.

Rabi peak broadening

The effective broadening of a peak on the inner-site transition is studied by using a microwave pulse of variable duration. The power is adjusted for each pulse such that a π-pulse is realized. Scanning the frequency around $\nu_{MW} = \nu_{eg} + \nu_0$ allows us to realize sinc^2-like spectra. While the pulse width is found to be given by the Fourier limit for pulse durations of up to 200 ms, a limit of the finesse is observed for long interrogation times being a full-width-half-maximum (FWHM) value of 3 Hz for a dipole trap total power of 1.5 W. However, the application of the differential light shift compensation beam allows for a reduction of the peak broadening. We find the microwave spectra to be Fourier limited up to pulse durations of more than 1 s with an optimized power and mode-match adjustment of the compensation beam as depicted in figure 4.15 *(left)*. From the comparison of spectra for a pulse of 1.478 s duration with and without differential light shift compensation we can deduce not only the peak broadening, but also the average differential AC-Stark shift (see figure 4.15 *(right)*).
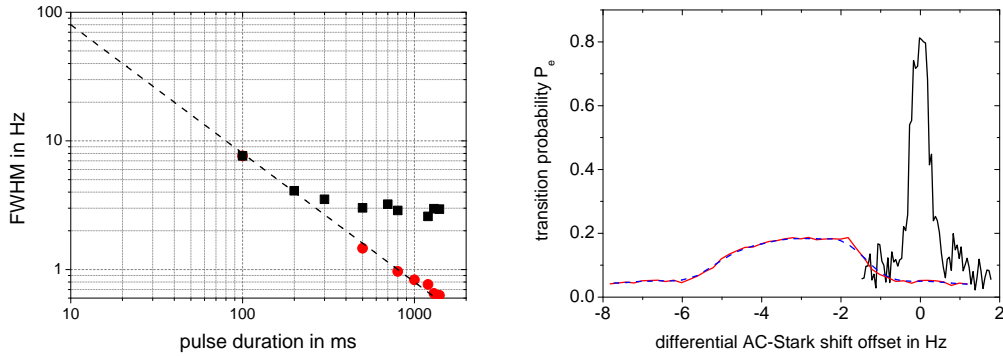
Figure 4.15: Fourier limited microwave spectroscopy. A microwave single pulse interrogation on the internal state transition allows to realize Fourier limited peaks in presence of the differential light shift compensation beam. *Left*: The FWHM values of the microwave inner-site coupling are Fourier limited *(dashed line)* for pulse durations of up to 1.5 s in the presence of the differential light shift compensation beam *(red circles)*, while a minimum peak width of 3 Hz is found without compensation *(black boxes)*. For longer interrogation times, the atom number is too low. The Fourier limit is $\nu_{FWHM} = 0.8/\tau_\pi$ as derived from (2.20). *Right*: A peak for a microwave pulse of a duration of 1.478 s is depicted with *(black)* and without *(red)* the light shift compensation beam being applied. The profile is smoothed by realizing an averaging of intervals of 5 points *(blue dashed)*.

Ramsey fringe contrast

The impact of the differential light shift distribution with finite width is given by a loss of contrast of the Ramsey and WSR fringes. This loss is induced by a dephasing of the atoms in the atomic ensemble. As the differential light shift distribution can be extracted from the broadening of the spectrum in the case of a single pulse, it is possible to predict the time behavior of the Ramsey contrast with increasing interrogation time. Using the spectrum shown in figure 4.15 *(right)*, we can derive the Ramsey fringe contrast as a function of the duration of the Ramsey interferometer by calculating the fringe pattern as an average of the single atom fringe pattern, which is weighted with the differential light shift distribution $f(\nu)$. The total transition probability is then given by an integral of the form

$$P_{e,total}(\phi) \;=\; \frac{\int_{-\infty}^{\infty} f(\nu) P_e(\nu, \phi)\; d\nu}{\int_{-\infty}^{\infty} f(\nu)\; d\nu}. \tag{4.9}$$

Here, $P_e(\nu, \phi)$ is the transition probability of a single atom as a function of the differential light shift. Scanning ϕ and finding the maxima and minima of the resulting pattern allows for a deduction of the contrast. In practice, the integral
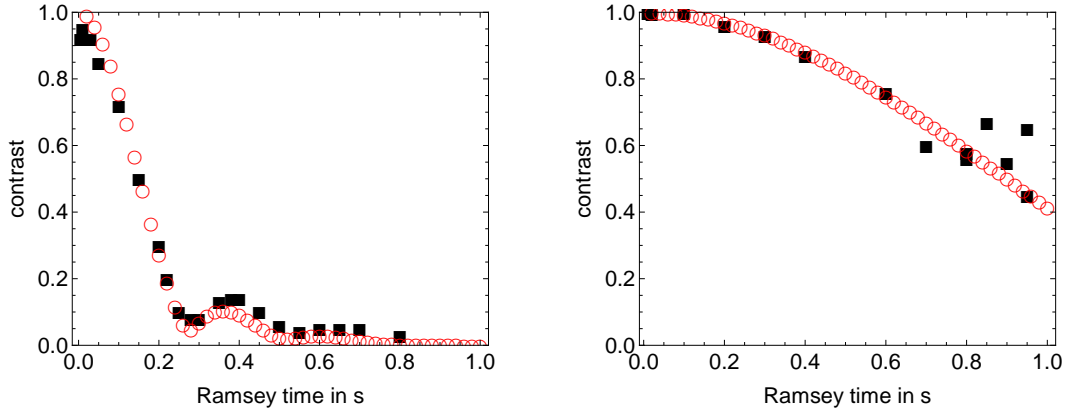
Figure 4.16: Ramsey contrast versus interrogation time. The numerically calculated *(red circles)* and measured *(black boxes)* are depicted for measurements without *(left)* and with the differential light shift compensation beam *(right)*.

can be replaced by a sum

$$P_{e,total}(\phi) \quad = \quad \frac{\sum_{i=1}^{N} f_i \cdot P_e(i \cdot \nu, \phi)}{\sum_{i=1}^{N} f_i}, \tag{4.10}$$

where f_i is the discrete frequency distribution given by the single pulse spectrum depicted in figure 4.15 *(right)*.

The measured contrast of the Ramsey fringe pattern is determined by recording a Ramsey fringe pattern with pulse durations of $\tau_{\pi/2} = 0.5$ ms and varying interrogation time T. The resulting fringe contrast shows good agreement with the numerical predictions as shown in figure 4.16. The actual fringe contrast is slightly underestimated for longer Ramsey interrogation times. This is due to the fact that the measured distribution is a convolution of the Fourier width of the probe pulse and the actual differential light shift distribution. More importantly, both distributions show a revival of the fringe contrast after a certain time.

The Ramsey contrast can be increased for longer interrogation times by applying the compensation beam. The calculation we employed before can now be used for an estimation of the residual effect of the differential light shift. For this, the frequency width of the measured distribution is numerically reduced. We find a good agreement of calculated and measured contrast values. From this we can deduce a residual peak broadening of less than 0.5 Hz.

Transverse mode coupling

The Raman beam splitter effective wave vector $\mathbf{k}_{\text{eff}}$ is aligned along the lattice laser beam optical axis. An imperfect alignment results in a non-vanishing projection of $\mathbf{k}_{\text{eff}}$ onto the x- and y-axis. This results in the possibility to couple different
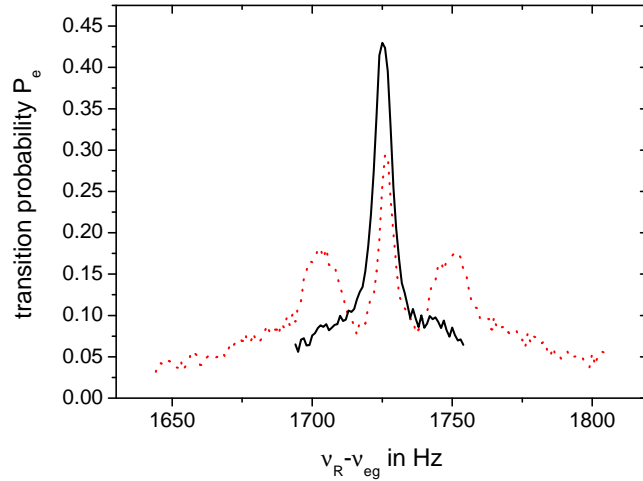
Figure 4.17: Transverse mode coupling. The Wannier-Stark spectrum is shown for transition $\Delta m = 3$ for perfect collinear alignment of the Raman and lattice laser *(black line)* and for a slight misalignment *(red dashed line)*. The red and blue sidebands are clearly visible with a spacing to the carrier peak of approximately 23 Hz.

harmonic oscillator modes of the transverse dipole trap. Depending on the Raman frequency, the transition can be an excitation or disexcitation, which visualize in a blue and red sideband on the Wannier-Stark transition peak. The separation of the sidebands with respect to the carrier is given by the trap frequency ν_{dip}. The spectrum around the Wannier-Stark peak $\Delta m = 3$ is depicted in figure 4.17 for imperfect alignment with two different dipole trap frequencies and for the case of a good alignment. The trap frequency for the typically used dipole laser power is found to be $\nu_{dip} \approx 20$ Hz.

For pulse durations $\tau_{\pi/2} > 1/\nu_{dip}$, these sidebands can be resolved and have, in principle, no effect on the Bloch frequency measurement. However, for short pulses as used in a Ramsey sequence, the sidebands result in an effective damping of the Rabi oscillations and thus in a reduced fringe contrast. We have to align the Raman and lattice laser beam optical axes to assure a high WSR fringe contrast.

4.4.3   High resolution Bloch frequency measurements

Single pulse Wannier-Stark spectroscopy and the realization of a WSR interferometer on an inter-site transition allows for the determination of the Bloch frequency ν_B and thereby the potential gradient between the involved lattice sites. The Bloch frequency is derived from the position of the center of a resonance curve. For optimal sensitivity, we alternate measurements on both sides of the resonance, by
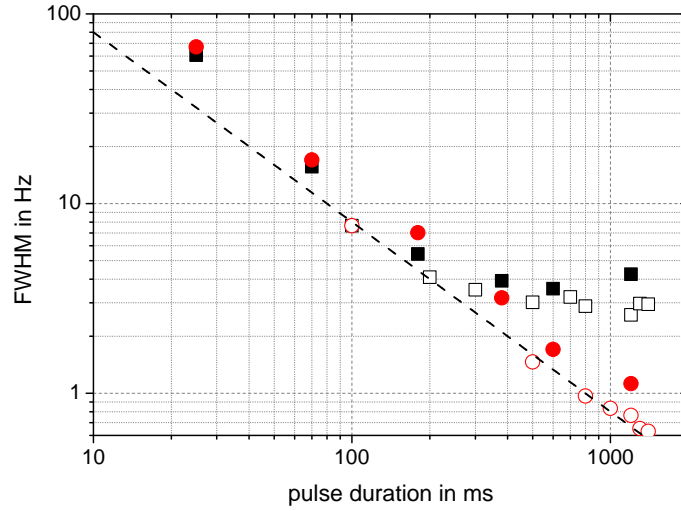
Figure 4.18: Raman spectroscopy resolution. The FWHM values of the single-pulse interrogation is plotted for the inter-site transition $\Delta m = 3$ with *(red circles)* and without *(black boxes)* differential light shift compensation beam. The microwave interrogation is plotted for comparison *(open symbols)*. The Raman interrogation is about a factor of 2 above the Fourier limit *(dashed line)*, which is $\nu_{FWHM} = 0.8/\tau_\pi$ as derived from (2.20).

adjusting the detuning of the Raman lasers. From the difference between two consecutive measurements, we derive an error signal which we use to lock the Raman frequency difference onto the center of the resonance.

The signal to noise ratio of this repeated frequency measurement is potentially limited by the slope of the resonance curve. A steep slope results in a large change of the signal for a given frequency fluctuation resulting in a high signal-to-noise ratio. This demands a narrow, high peak in the case of Rabi spectroscopy and a large contrast for large interrogation times in the case of a WSR interferometer.

The presented set-up involving the differential AC-Stark shift compensation enables high resolution Wannier-Stark spectroscopy using a single Rabi pulse. The resolution is studied for long pulses in a similar way as for the microwave transition. Here, the frequency scan of the Raman frequency around the resonance of the inter-site transition $\Delta m = 3$ is employed to determine the FWHM values of the Wannier-Stark transition for varying pulse durations. The resulting FWHM values are depicted in figure 4.18. While the peak width decreases with $1/\tau_\pi$ as expected, we find a peak broadening with respect to the Fourier limit by a factor of 2. As this broadening does not depend on the pulse length, we infer this constant factor to a differential light shift inhomogeneity over the atomic ensemble caused by intensity inhomogeneities on the Raman beam profiles.

In the case of a WSR interferometer, we find relatively high contrast even for

T_{trap}	$U_0 \approx 4E_r$ $\Delta m = 3$	$U_0 \approx 1.8E_r$ $\Delta m = 7$
0.5 s	$N \approx 50,000$ $\sigma_{P_e} \approx 0.6\ \%$	$N \approx 18,000$ $\sigma_{P_e} \approx 1.7\ \%$
1 s	$N \approx 25,000$ $\sigma_{P_e} \approx 1.2\ \%$	$N \approx 9,000$ $\sigma_{P_e} \approx 3.3\ \%$

Table 4.1: Detection noise levels. The detection noise scales with the inverse of the total detected atom number. Here, the detection noise levels are given for different measurement configurations resulting in different total atom numbers N. The mixed trap holding times T_{trap} define the maximum total length of the realized Rabi pulse or WSR interferometer. The interrogation on $\Delta m = 3$ allows for a deeper lattice of typically $U_0 \approx 4E_r$ whereas it is necessary to lower the lattice depth to $U_0 \approx 1.8E_r$ for measurements on transitions between further separated lattice sites, here $\Delta m = 7$. The shallower lattice leads to a smaller number of trapped atoms.

long interrogation times of up to 1 s. In the following, typical interrogation times of $T = 400$ ms are employed, for which we find contrast values of about $C = 35\ \%$.

4.5 Bloch frequency measurement stability

The short and long term stability of the Bloch frequency measurement determines the sensitivity to inertial forces along the lattice laser optical axis. The stability of such a measurement is studied for the case of a WSR interferometer with a separation time of $T = 400$ ms in the following. Potential noise and drift sources are identified and their impact on the measurement stability is evaluated.

A Bloch frequency measurement consists of tracking a multiple of the Bloch frequency $\Delta m \cdot \nu_B$ in a repeated frequency measurement on the inter-site transition Δm. The computer control allows us to realize a feedback loop and thereby to track the resonance frequency $\nu_{\Delta m,R}$ given in (4.8). As the uncertainty of the detection process averages down with $\tau^{-1/2}$ on short time scales and only shows drift behavior for longer time scales (see section 4.3.4), this prevents slow fluctuations and drifts of the detection process from limiting the measurement.

In order to suppress the influence of internal state transition shifts on the Bloch frequency measurement, the frequencies $\nu_{\Delta m,R}$ and $\nu_{-\Delta m,R}$ are measured alternately. If the internal state transition frequency fluctuations are slow compared

to the cycle time, the multiple of the Bloch frequency is then given by the half difference

$$
\begin{aligned}
\nu_{B,\Delta m} &= \frac{\nu_{\Delta m,R} - \nu_{-\Delta m,R}}{2} \\
&= \Delta m \cdot \nu_B.
\end{aligned}
\tag{4.11}
$$

The typical set of four measurements is taken within time scales of less then 10 s.

Although perturbations in the detection are suppressed on longer time scales, they can be the limiting noise source from shot to shot, which is not suppressed by the alternating measurement on the two side slopes of the fringe. The transition probability noise σ_{P_e} depends on the number of detected atoms. In table 4.1, four different noise values are given for typical measurement configurations. These are defined by the trap time in the mixed trap T_{trap} and the chosen lattice depth, which is in each case optimized for coupling the transition $\Delta m = 3$ or $\Delta m = 7$, respectively. For a Ramsey interrogation, the short term noise of the frequency measurement resulting from detection noise is then given by

$$
\sigma_{\nu,det} = \frac{\sigma_{P_e}}{\pi C \left(T + 4\tau_{\pi/2}/\pi \right)}.
\tag{4.12}
$$

The described measurement is realized for $\Delta m = -7$. With the alternating measurement of $\nu_{-7,R}$ and $\nu_{+7,R}$ and a cycle time of $T_c = 1.4$ s, this results in one Bloch frequency value every 2.8 s. Figure 4.19 shows the Allan standard deviation for the frequency values $\nu_{-7,R}$ and $\nu_{B,7}$. The Allan standard deviation values for small times is characteristic for the feedback loop and has no metrological meaning. The short term stability value can be found by approximating the Allan standard deviation curve with $\sigma(\tau = 1 \text{ s})/\sqrt{\tau\text{Hz}}$, where τ is the averaging time. At short time scales, the measurements show the same stability. A factor of $\sqrt{2}$ between the single noise of the interrogation on one and alternating on both sides arises due to the fact that the determination of $\nu_{B,7}$ includes both, the measurement of $\nu_{-7,R}$ and $\nu_{+7,R}$.

For averaging times longer than 30 s, we observe a drift on the $\nu_{-7,R}$ value, whereas the measurement of the Bloch frequency multiple $\nu_{B,7}$ shows an averaging behavior of $\tau^{-1/2}$. The Allan standard deviation plot can be approximated with $0.23 \text{ Hz}/\sqrt{\tau\text{Hz}}$, which results in a measured frequency short term stability of

$$
\sigma_{\nu_{B,7}} = 0.23 \frac{\text{Hz}}{\sqrt{\text{Hz}}}.
$$

For the Bloch frequency measurement, the resulting relative stability is then

$$
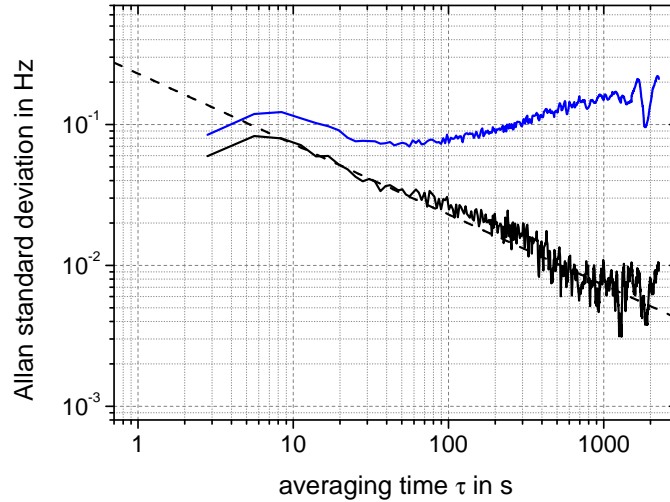\frac{\sigma_{\nu_B}}{\nu_B} = 5.8 \cdot 10^{-5} \frac{1}{\sqrt{\text{Hz}}}.
$$

Figure 4.19: Allan standard deviation of the WSR Bloch frequency measurement on $\Delta m = +7$ and $\Delta m = \pm 7$. The Allan standard deviation is plotted versus the integration time τ for the tunneling transition $\Delta m = \pm 7$ *(black line)* and $\Delta m = -7$ *(blue line)*, respectively. The frequency resolution for both measurements can be approximated by $0.23\,\mathrm{Hz}/\sqrt{\tau \mathrm{Hz}}$ *(dashed line)*.

While the frequency measurement on the two transitions $\Delta m = \pm 7$ show a drift after 30 s integration time, the effective Bloch frequency measurement that is realized by alternating on the two transitions averages down over the full measurement time. After an averaging over 2000 s we find a relative uncertainty of

$$\frac{\sigma_{\nu_B}}{\nu_B} \;\; = \;\; 1.3 \cdot 10^{-6}.$$

The long term stability of a measurement of $\nu_{\Delta m}$ is clearly limited by the drift of ν_0. In the following, the potential limitations of the short term stability are investigated. In principle, the fluctuations of the measured frequency can arise from fluctuations of the Bloch frequency itself, from an unstable shift of the internal state transition frequency, or from fluctuations of the Raman laser phase.

Bloch frequency fluctuations can be induced by a fluctuating lattice laser wavelength or by vibrations of the whole apparatus, which results in a noise on g. These uncertainties are expected to scale with the frequency value and, in particular, with Δm. In order to investigate the potential limitation of the measurement by these fluctuations, the measurement described above is realized for $\Delta m = 3$. The resulting stability is depicted as Allan standard deviation in figure 4.20. As the short term stability is found to be equal for both measurements, we can exclude Bloch frequency fluctuations from being the dominant noise source.
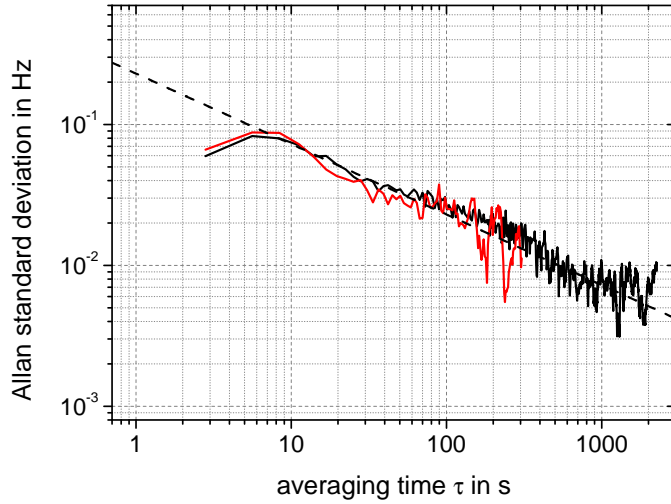
Figure 4.20: Allan standard deviation of the WSR Bloch frequency measurement on $\Delta m = \pm 7$ and $\Delta m = \pm 3$. The Allan standard deviation is plotted versus the integration time τ for the tunneling transition $\Delta m = \pm 7$ *(black line)* and $\Delta m = \pm 3$ *(red line)*, respectively. The frequency resolution for both measurements can be approximated by $0.23 \text{ Hz}/\sqrt{\tau \text{Hz}}$ *(dashed line)*.

For both measurements, the detection noise influence is calculated using (4.12). This results in frequency noise values of $\sigma_{\nu,det} \approx 3.5 \cdot 10^{-2} \text{ Hz}/\sqrt{\text{Hz}}$ ($N = 23,000$, $C = 35$ %) for the measurement on the transition $\Delta m = 7$, and $\sigma_{\nu,det} \approx 1.6 \cdot 10^{-2} \text{ Hz}/\sqrt{\text{Hz}}$ ($N = 50,000$, $C = 35$ %) in the case of $\Delta m = 3$. Hence, the detection noise is not the dominant noise source in the two measurements.

In the following, the differential light shift will be investigated as possible noise source. In order to exclude Raman phase perturbations and Bloch frequency fluctuations from the measurement, a Ramsey type sequence is realized using microwave pulses to drive the internal state transition. By using only the microwave interrogation, the influence of the mixed trap differential light shift can be studied independently from frequency and phase fluctuations arising from the interaction with the Raman laser fields. Furthermore, the Raman laser differential light shift is investigated by simultaneously applying a microwave pulse and an off-resonant Raman laser pulse of identical length as described in section 4.3.5. For the stability studies using the microwave inner-site coupling, a higher lattice depth of $U_0 \approx 4E_r$ is chosen in order to trap a large number of atoms.
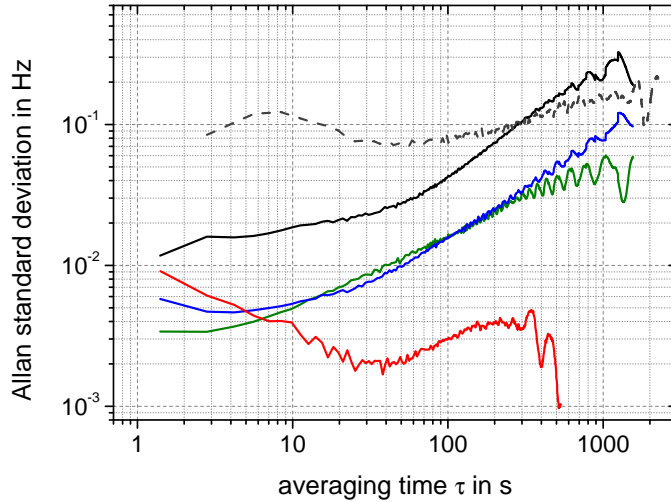
Figure 4.21: Mixed trap differential light shift influence. The Allan standard deviation values are plotted for the frequency deviation in a Ramsey measurement: Ramsey frequency measurement using microwave pulses *(black)*, the calculated frequency influence of the power fluctuations of the dipole trap laser *(green)* and the differential light shift compensation beam *(blue)*. The detection noise on the frequency is calculated taking into account the fringe contrast and Ramsey time *(red)*. The Allan standard deviation of the frequency measurement $\nu_{-7,R}$ is plotted for comparison *(gray dashed line)*. The drift observed in the microwave Ramsey measurement is stronger than in the WSR interferometer measurement, which we infer to a slightly varying drift rate. This can be due to a different temperature fluctuation in the laboratory or to a different alignment quality in the second measurement.

4.5.1   Mixed trap differential light shift fluctuations

Here, the influence of the fluctuations of the differential light shift of the dipole trap laser and the differential light shift compensation light field are studied. The influence of the lattice laser is considered to have a smaller effect. We investigate the impact on the WSR measurement using a microwave Ramsey scheme with an interrogation time $T = 400$ ms and pulse durations $\tau_{\pi/2} = 0.7$ ms. The obtained fringe pattern shows a typical contrast of $C \approx 90$ %. During this measurement the optical power of the dipole trap and differential light shift compensation beam are recorded with photodiodes. The frequency shift of the dipole trap and compensation laser power is directly calibrated on a Ramsey frequency measurement. This allows to evaluate the power fluctuation measurement by calculating the frequency shift of each interferometer cycle using the photodiode signal that is recorded during the Ramsey sequence.

Comparing the Allan standard deviations depicted in figure 4.21, the differen-

tial light shift is found not to be dominant of the Bloch frequency measurement on short time scales. The drift on the long term measurement shows good agreement for the inter-site and the microwave Ramsey interrogation. However, as the fluctuations are slow, alternating on the Δm and $-\Delta m$ can effectively suppress the differential light shift influence of the mixed trap beam set-up. The microwave Ramsey measurement itself is limited by the detection noise.

Comparing the microwave Ramsey measurement with the calculated frequency fluctuations caused by intensity drifts of the dipole trap and differential light shift compensation beam, we find the microwave Ramsey signal to show a stronger drift than it is derived from the intensity fluctuations. From this we infer the drift mainly to be caused by a slowly varying relative misalignment of the dipole trap and differential light shift compensation beams. Indeed, the pointing of the beams was tracked in a similar study using quadrant-photodiodes. Although we could not find a clear correlation between calculated and measured frequency fluctuations, the pointing instabilities were found to result in frequency fluctuations of the observed magnitude.

4.5.2 Raman laser differential light shift fluctuations

In order to study the Raman laser differential light shift influence, an off-resonant Raman pulse is applied during the duration of the microwave $\pi/2$-pulse application. The microwave power and timing as well as the Raman beam power is adjusted to a pulse duration of $\tau_{\pi/2} = 5$ ms. The fringe contrast is $C \approx 70$ % in this case. The microwave Ramsey averaging measurement is then realized for two situations. First, all Raman laser beams are shined in. Second, the retro-reflection of the Raman laser is misaligned such that only the ascending Raman beams are present during the microwave pulse. The differential AC-Stark compensation of the Raman laser beams shift and the mode matching of the differential light shift compensation beam are optimized for each of the measurements.

The measurements are compared using the Allan standard deviation values shown in figure 4.22. On time scales in the range of tens of seconds, the Ramsey measurement is limited by fluctuations of the differential AC-Stark shift of the Raman laser beams. These fluctuations are stronger in the presence of all three Raman light fields. Furthermore, the short term stability is slightly decreased with respect to the detection noise in the presence of the Raman beams. This is even more the case if all Raman beams are present. We infer this fluctuations to the polarization instabilities of the Raman light fields. These are guided to the experiment using one polarization maintaining single-mode optical fiber with crossed polarizations. Although the polarization is maintained when the light passes through the fiber, the polarization axis orientation of the light fields in the experiment can rotate by a few degrees. In our chosen beam configuration (see figure 4.5), this fluctuation translates into power fluctuations of the retro-reflected
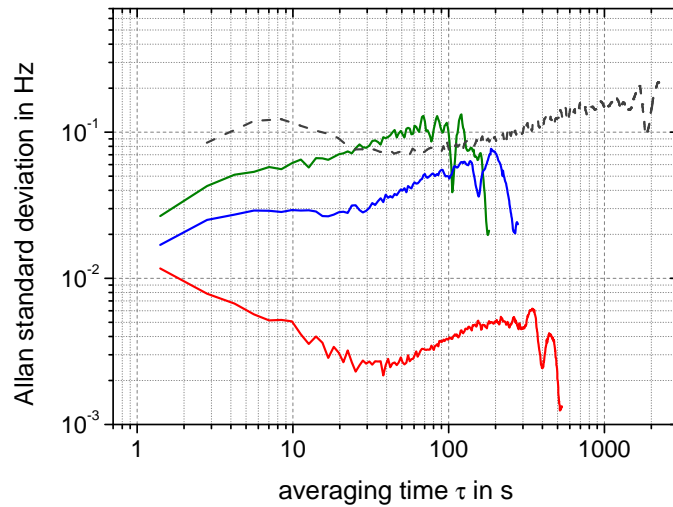
Figure 4.22: Raman laser differential light shift influence. The Allan standard deviation values are plotted for the frequency deviation in the Ramsey measurements using microwave pulses and off-resonant simultaneously applied Raman laser pulses. This is shown for the presence of all Raman beams *(green)*, and of only the ascending beams by misaligning the retro-reflection *(blue)*. The detection noise on the frequency is calculated taking into account the fringe contrast and Ramsey time *(red)*. For comparison, the Allan standard deviation of the frequency measurement $\nu_{-7,R}$ is plotted *(gray dashed line)*. The drift rate in the microwave Ramsey measurement is again found to be stronger than in the WSR Interferometer measurement. This can arise from a varying drift rate due to different temperature fluctuations or a slightly different suppression factor of the Raman induced differential AC-Stark shift in the two measurements.

Raman laser beam. In addition, the suppression of the retro-reflection of the second beam becomes imperfect.

For measurement times that are large against the experimental cycle time, the instability of the Raman laser induced differential light shift can be suppressed using the procedure of alternating measurements on the transitions Δm and $-\Delta m$. On short time scales, it is found not to be the dominating noise source. Nevertheless, the short term noise is significantly higher then the detection noise, which motivates the technical modification of the Raman laser beam set-up presented in section 4.6.

4.5.3   Symmetrized WSR interferometer

A different way to distinguish between the influence of the differential light shift of the Raman beam splitter light fields and the mixed trap is to use the symmetrized Ramsey sequence introduced in section 2.7.2. This scheme allows to symmetrize the
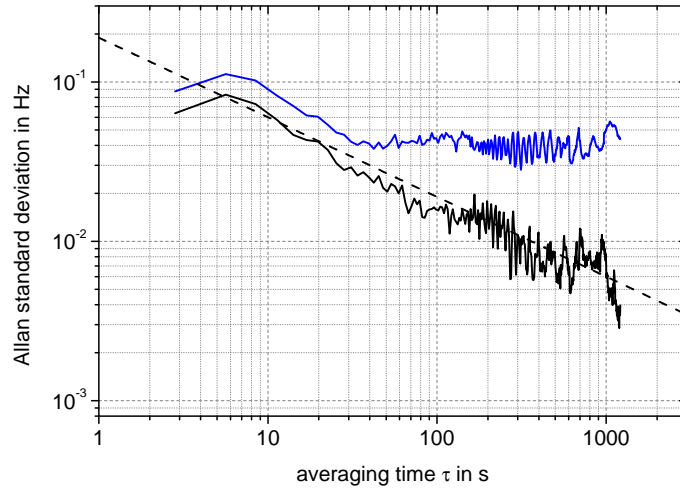
Figure 4.23: Bloch frequency measurement stability for the symmetrized Ramsey scheme. The Allan standard deviation of the symmetrized Ramsey scheme frequency measurement is shown for the frequencies $\nu_{+3,R}$ *(blue line)* and $\nu_{B,3}$ *(black line)*. Extrapolation of the frequency uncertainty at 1 s measurement time is possible with 0.19 $\mathrm{Hz}/\sqrt{\tau\,\mathrm{Hz}}$ *(dashed black line)*.

duration of the time evolution in the internal ground and excited state. Therefore, the mixed trap induced differential light shift cancels out and leaves only the Raman light field differential light shift in the interferometer phase.

A symmetrized Ramsey scheme is realized on the transition $\Delta m = 3$. While the first and last coupling pulse consist in a Raman coupling, the π-pulses for inner-site coupling are realized using the microwave field. The timing is chosen to be $\tau_{\pi/2} = 5.5$ ms, $\tau_{\pi} = 1.2$ ms, $T_1 = 96.7$ ms and $T_2 = 99.4$ ms. This meets the symmetrization condition (2.110) with a mismatch of 0.8 ms for T_2. Hence, we expect the differential light shift influence of the mixed trap to be suppressed by a factor of about 100.

We realize a Bloch frequency measurement by software-locking the Raman laser frequency on the fringes of the transitions $\Delta m = \pm 3$. Indeed, we find no influence of changes in the mixed trap differential light shift. When changing the light shift by 30 %, we would expect a change in the measured frequency of more than 1 Hz. Doing so, we do not find a significant change of the measured frequency which stays in a range of 0.2 Hz over the whole measurement period of 4 min duration. Also, this change in trap power would lead to a contrast loss due to the increased inhomogeneity of the differential light shift which is not observed in this measurement.

The long term stability of a Bloch frequency measurement using the symmetrized WSR interferometer is realized alternately on the transitions $\Delta m = \pm 3$.

The Allan standard deviation plot is depicted in figure 4.23 for the measured frequency values $\nu_{+3,R}$ and $\nu_{B,3}$. The long term stability of the interrogation on only the transition $\Delta m = 3$ appears to be more stable over long time scales. Although the uncertainty around 100 s is slightly lower compared to the measurement using the microwave Ramsey scheme presented in section 4.5.2, the Raman light fields are still found to limit the measurement at a level of about $4.5 \cdot 10^{-2}$ Hz uncertainty. The short term stability if found to be the same as for a WSR measurement in the beginning of this section.

4.5.4   Vibrations of the apparatus

Vibrations of the apparatus influence the measured frequency value in two ways. First, the measured quantity itself, the Bloch frequency, changes. This is true for accelerations of the whole apparatus for which the movement of all components, especially mirrors, is common. Furthermore, vibrations of the apparatus can induce vibrations of the mirrors in the experimental set-up. In particular, the Raman retro-reflection mirror and the lattice mirror can show a relative movement. This relative distance fluctuation induces a phase fluctuation of the Raman laser phase at the position of the coupled lattice sites and, therefore, a phase noise in the measurement.

For both kind of vibration influences we can evaluate the phase noise of the measurement by using the interferometer transfer function as described in section 2.4.1. The vibrations of the apparatus are measured using a seismometer of type `Lennartz LE-1DV`, which is placed on the top of the retro-reflection part of the optics set-up. From the acceleration measurement, we deduce a power spectral density of the vibration $S_a(\nu)$. The measured power spectral density for accelerations is depicted in figure 4.24.

The vibration influence is calculated as an Allan standard deviation value at $\tau = 1$ s averaging time using (2.92). For the case of common vibrations, the resulting phase noise power spectral density is given by the Bloch frequency perturbation, which results in a phase noise spectral density that reads

$$
\begin{aligned}
S_\varphi(\omega) &= \frac{S_\omega(\omega)}{\omega^2} \\
&= \left(\frac{m_a \lambda_l \Delta m}{2\hbar} \right)^2 \frac{S_a(\omega)}{\omega^2}.
\end{aligned}
\tag{4.13}
$$

The calculation of the vibration influence in the case of relative vibrations demands the knowledge of the relative position of the two mirrors during the Ramsey interrogation. The realization of such a measurement is a technically complex task. In order to estimate the influence of a relative mirror vibration, we consider the following. One of the mirrors is considered to be stationary whereas the other mirror follows the accelerations that are given by the measured vibration. This
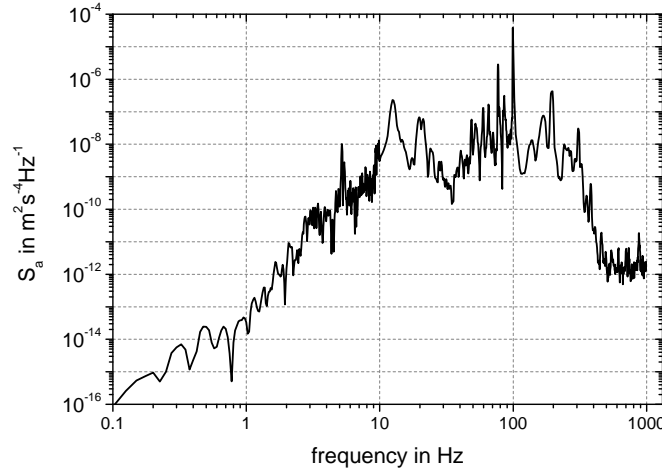
Figure 4.24: Acceleration power spectral density. The spectrum is measured on the top of the experimental apparatus using a seismometer.

assumption is even more motivated by the fact that one of the mirrors is mounted with an angle of 90°. The vibrations of the mirrors are caused by vibrations in different directions. With this assumption, the phase noise spectral density is then given via the spatial Raman phase $\delta\varphi = \mathbf{k}_{\text{eff}} \cdot \delta\mathbf{x}$ by

$$
\begin{aligned}
S_\varphi(\omega) &= k_{\text{eff}}^2 S_x(\omega) \\
&= k_{\text{eff}}^2 \frac{S_a(\omega)}{\omega^4}.
\end{aligned}
\tag{4.14}
$$

The respective phase and frequency noise standard deviations for the Ramsey sequence. We consider the pulse duration to be negligible versus the total Ramsey interrogation time. The calculated values for $T = 400$ ms and $\tau \to 0$ are given in table 4.2. Here, the frequency standard deviation is calculated using (2.94) and the relative standard deviation is given for an interrogation on the inter-site transition $\Delta m = 7$.

As the Bloch frequency and its fluctuations scale directly with the order Δm, the vibration induced Bloch frequency noise would induce an exceed in the short term measurement uncertainty when comparing repeated frequency measurements on different transition orders Δm. This reasoning already allowed us to exclude the vibration of the whole apparatus from being the dominant noise source by realizing a Bloch frequency measurement on the transitions $\Delta m = 3$ and $\Delta m = 7$ (see above). Indeed, the calculated influence of vibrations of the whole retro-reflection part of the Raman and lattice beams is found to be one order of magnitude below the observed short term stability of the Bloch frequency measurement.

mirror vibrations	σ_Φ	σ_ν	σ_{ν_B}/ν_B
common	$5.6 \cdot 10^{-2}\ \frac{\text{rad}}{\sqrt{\text{Hz}}}$	$2.2 \cdot 10^{-2}\ \frac{\text{Hz}}{\sqrt{\text{Hz}}}$	$5.5 \cdot 10^{-6}\frac{1}{\sqrt{\text{Hz}}}$
relative	$4.86\ \frac{\text{rad}}{\sqrt{\text{Hz}}}$	$1.93\ \frac{\text{Hz}}{\sqrt{\text{Hz}}}$	$4.8 \cdot 10^{-4}\frac{1}{\sqrt{\text{Hz}}}$

Table 4.2: Vibration induced noise. The Allan standard deviation values are given for the interrogation on the transition $\Delta m = 7$. Common and relative vibrations of the Raman and lattice retro-reflective mirrors are considered. The standard deviation is given in units of phase σ_Φ, frequency σ_ν, and in relative units σ_{ν_B}/ν_B. The latter is calculated here for the Bloch frequency multiple $\nu_{B,7} = 7 \cdot \nu_B$.

The impact of vibrations of only one of the two mirrors leads to an estimate of the impact of relative displacements of the Raman and lattice laser retro-reflection mirrors. Assuming that only one of the mirrors follows the measured vibrations, we find a vibration induced short term noise of $\sigma_{\nu_B}/\nu_B = 4.8 \cdot 10^{-4}\ 1/\sqrt{\text{Hz}}$, which is one order of magnitude above the measured value. Hence, a relative mirror vibration inducing only 10 % of this movement is sufficient to cause the observed short term noise on the Bloch frequency measurement. This motivates the modification of the apparatus set-up on the retro-reflection optical bench on the top of the experimental apparatus introduced in the following section.

4.6   Set-up modifications and stability improvement

In the former section, the short and long term stability of the Bloch frequency measurement have been presented. The long term stability of measurements of up to 1000 s is found to be limited by drifts of the internal state transition frequency induced by differential light shift variations. The drift can be effectively suppressed by alternating the Bloch frequency measurement on transitions $\pm\Delta m$, which allows for an averaging over 2000 s resulting in a statistical uncertainty of $1.3 \cdot 10^{-6}$. The short term stability amounts to $5.8 \cdot 10^{-5}\ 1/\sqrt{\text{Hz}}$. Two potential limitations of the short term stability have been identified. We infer the main part of the short term noise to mechanical instabilities of the mirror mounting of the Raman and lattice beam retro-reflection mirrors. A second source for short term noise and for drifts on time scales of tens of seconds is given by the Raman laser induced differential AC-Stark shift. In the following, the realized modifications of the experimental
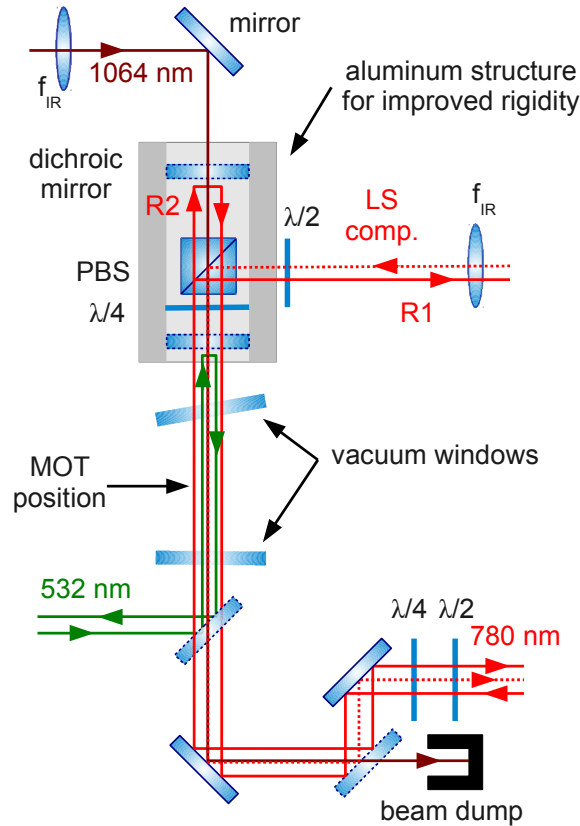
Figure 4.25: New beam set-up. The lattice and Raman mirrors are both oriented horizontally in the new configuration. The two mirrors and the polarizing beam splitter are mounted on a robust aluminum structure.

set-up are described, and the resulting improved Bloch frequency measurement stability is presented.

4.6.1 Modifications

Two modifications are realized in order to improve the short term stability of the Bloch frequency measurement. The first concerns the mounting of the two mirrors that serve for retro-reflecting the lattice laser beam and one of the two Raman light fields, respectively. A more rigid set-up is chosen.

The second modification is in the guidance of the Raman light fields from the laser sources to the experimental chamber. The two light fields are brought to the experiments using separate fibers in order to allow for good control of the single beam power and polarization.

Mechanical rigidity

The mounting of the Raman and lattice beam retro-reflection mirrors is modified in order to reduce relative movements of the two mirrors induced by vibrations of the apparatus. For this, the second dichroic mirror on the top of the apparatus is used as Raman mirror by choosing its orientation to be parallel to the lattice mirror. The polarizing beam splitter cube (PBS) and the quarter-wave plate are placed in between the two dichroic mirrors as depicted in figure 4.25. This allows to apply the differential light shift compensation beam directly via the beam splitting cube from the side. An additional half-wave plate serves for power control of the compensation beam.

Furthermore, the rigidity of the retro-reflection optical bench that is mounted above the experimental chamber is increased. The new construction is based on four instead of three pillars with larger diameter. The mounting of the retro-reflection mirrors is replaced by a breadboard with a massive aluminum structure carrying the two retro-reflection mirrors and the optical elements for the dipole trap beam set-up. The Raman and the lattice mirror are mounted using lockable mirror mounts in order to allow for a higher stiffness and to suppress mirror vibrations.

Raman light fields

The set-up of the phase-locked Raman lasers is depicted in figure 4.4. The beat measurement for the optical phase-locked loop is realized on the optical bench on which the two ECDL lasers used for the generation of the Raman light fields are mounted. The two Raman beams are then guided to the experiment using one polarization maintaining single-mode fiber.

The modification applied to the optical set-up involves two changes. First, the two Raman light fields are guided to the experiment separately using two fibers of the same type. On the output of each of the fibers, the polarization is controlled using a half-wave plate and a polarizing beam splitter cube on each. The beat measurement is realized after the optical fibers. Also, the AOM for switching and power control is now moved onto the optical bench of the experimental apparatus.

The second modification is the change of the beam size of the Raman beams by a factor of 2 to a beam waist of 2.8 mm. This reduces intensity profile inhomogeneities of the Raman light fields due to diffraction caused by the restricted diameter of the optical path of the Raman laser beams. Such a beam waist reduction potentially leads to larger Rabi frequency inhomogeneities due to the Gaussian beam profile. However, this could not be observed when studying the Rabi oscillations realized in the modified set-up. The smaller beam waist also results in a larger beam intensity. The optical power emitted by the ECDL is now sufficient to realize the needed intensities. This allows us to remove the tapered amplifier used for power amplification in the Raman laser set-up.
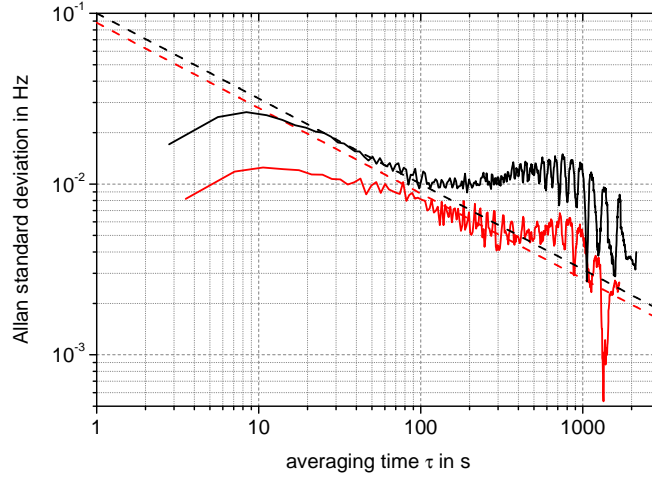
Figure 4.26: Improved WSR interferometer Bloch frequency measurement. The Allan standard deviation is depicted for a measurement with $\tau_{\pi/2} = 10$ ms and $T = 400$ ms *(black line)* and for a measurement with $\tau_{\pi/2} = 120$ ms and $T = 850$ ms *(red line)*. The frequency resolution for the two measurements approximated with 0.1 Hz$/\sqrt{\tau \text{Hz}}$ *(dashed black line)* and $8.8 \cdot 10^{-2}$ Hz$/\sqrt{\tau \text{Hz}}$ *(dashed red line)*, respectively.

4.6.2 Improved Bloch frequency measurement stability

During the time of my research work on this experiment the Bloch frequency studies presented up to this point have led to the two presented modifications. Here, three frequency measurements will be presented that have been recorded after the realization of the modifications.

In order to study the improvement in the short term stability a WSR interferometer is realized on the inter-site transition $\Delta m = 7$ similar to the one presented in section 4.5. The Raman pulses have a duration of $\tau_{\pi/2} = 10$ ms, and the Ramsey time is chosen to $T = 400$ ms. By extrapolation of the Allan standard deviation plot of the measured frequency $\nu_{B,7}$ we find a short term stability of

$$\sigma_{\nu_{B,7}} \;\; = \;\; 0.1 \; \frac{\text{Hz}}{\sqrt{\text{Hz}}}.$$

For the Bloch frequency measurement, the improved relative stability is then

$$\frac{\sigma_{\nu_B}}{\nu_B} \;\; = \;\; 2.5 \cdot 10^{-5} \; \frac{1}{\sqrt{\text{Hz}}}.$$

A similar measurement has been carried out employing a longer Ramsey interrogation time and longer beam splitter pulses. With a scheme featuring $\tau_{\pi/2} = 120$ ms

and $T = 850$ ms, an integration measurement was realized alternating once again on the transitions $\Delta m = \pm 7$. The corresponding Allan standard deviation allows to extrapolate a frequency stability at 1 s of

$$\sigma_{\nu_{B,7}} \;\; = \;\; 8.8 \cdot 10^{-2} \; \frac{\mathrm{Hz}}{\sqrt{\mathrm{Hz}}}.$$

This results in an improved relative Bloch frequency measurement stability of

$$\frac{\sigma_{\nu_B}}{\nu_B} \;\; = \;\; 2.2 \cdot 10^{-5} \; \frac{1}{\sqrt{\mathrm{Hz}}}.$$

Further details on the second of these measurements are given in [75] and [76].

A similar Bloch frequency measurement is realized using a Rabi interrogation scheme with a single pulse of a duration of $\tau_\pi = 0.98$ s. A four-pulse software-lock scheme is employed similar to the one used for integration measurements using the WSR interferometer scheme. In this case, the alternating measurements on each of the peaks of the transitions $\Delta m = \pm 3$ are realized on the half maximum frequency values on the two side slopes. The short term stability is found to be comparable to the one found with a WSR interferometer.

In general, the short term stability of a Rabi interrogation is expected to be reduced in comparison with the Ramsey measurement [94]. The equality of the two stability values is explained by the dominating noise source, the detection noise. While the Rabi interrogation is expected to show a short term stability σ_{ν_B} that exceed the stability of the measurement employing a WSR interferometer by a factor of almost 2, the peak height of the Rabi spectrum shows the same factor in comparison with the WSR interferometer signal fringe contrast. Therefore, the slopes on which the repeated measurements are realized have the same steepness. This leads to the same impact of the detection noise onto the two measurements.

In both cases, we find a relative short term stability of the Bloch frequency measurement of

$$\boxed{\frac{\sigma_{\nu_B}}{\nu_B} = 2 \cdot 10^{-5} \; \frac{1}{\sqrt{\mathrm{Hz}}}.}$$

An integration over a total measurement time of $\tau = 300$ s allows to increase the stability to

$$\boxed{\frac{\sigma_{\nu_B}(\tau = 300s)}{\nu_B} = 1.2 \cdot 10^{-6}.}$$

Before concluding on the realized Bloch frequency stability at the end of this chapter, the coherent atom elevator for future short range force measurements is introduced in the following section.

4.7 Coherent atom elevator

For future Bloch frequency measurements close to the surface of the mirror that retro-reflects the lattice laser beam, it will be necessary to transport the prepared atomic ensemble over distances in the cm regime. This would allow us to realize the measurements in different atom-mirror distances in order to enable controlled spatial mapping of atom-surface-interactions. In addition, such a technique comprises the possibility for preparing the atomic ensemble in one part of the experimental chamber and realizing the interferometer measurement itself in a different part. This is a promising way to reduce Rubidium deposit on the mirror surface, which can induce parasitic electric fields and thus induce systematic effects in the measurement of Casimir-Polder forces [122].

The technique of choice is acceleration and deceleration of atoms in periodic potentials based on Bloch oscillations [123]. This has been refined for the case of neutral ^{87}Rb atoms and employed for a high precision measurement of the photon recoil, which allows for a determination of the ratio h/m_{Rb} and thus of the fine structure constant α using single pulse [124] or Ramsey type velocity selective Raman interrogation of the atomic ensemble velocity [125]. These measurements have been realized with a present relative uncertainty for α as good as $6.6 \cdot 10^{-10}$ [22]. The control of the atomic position presented here is based on the process used in the preparation cycle described in [125]. In addition to this, the technique of accelerated lattices also allows for the realization of so-called large momentum transfer (LMT) beam splitters combining Raman [126, 127] or Bragg type [128] beam splitting techniques (for Cs atoms in [128]) with an enhanced momentum, which leads to an increase in the sensitivity of atom interferometers.

In the following, the principle of coherent transport using Bloch oscillations will be briefly described and the potential limitations are introduced. After that, the technical realization of the required laser configuration will be presented. This set-up allows us to transport atoms along the vertical 1D-lattice, which is described thereafter.

4.7.1 Coherent atomic transport using Bloch oscillations

In the trapped accelerometry measurement presented in this work, the atoms are trapped in a vertical 1-D-lattice. As discussed in section 2.3.1, Landau-Zener tunneling is effectively suppressed for a sufficiently deep lattice and small accelerations. This enables us to trap the atoms for long times and therefore to measure accelerations by realizing the trapped Raman atom interferometer.

An atom in a vertical lattice is equivalent to an atom in an accelerated lattice (see section 2.3.1). The lattice acceleration can be realized by e.g. accelerating the retro-reflection mirror. As a consequence, the standing light wave would move with the velocity of the mirror. The relative movement of the lattice to the atom

results in an effective Doppler shift. The system starts to perform Bloch oscillations and, once again, for sufficiently deep lattices and sufficiently small accelerations, the atom follows the lattice movement. When the lattice light is switched off (adiabatically) after the acceleration, the atom moves with the final velocity of the mirror surface as it adiabatically followed the movement of the lattice. This results in an effective acceleration process. As the process of Bloch oscillations is coherent, this acceleration process in principle does not induce heating of the atomic ensemble or decoherence due to inelastic scattering.

Rather than using a retro-reflective configuration, the two light fields can be directly shined in in a counter-propagating way as shown in figure 4.27 *(left)*. The movement of the lattice is then controlled by setting a frequency difference between the two light fields. This results in a moving lattice for a constant detuning and, if we chirp this frequency difference over time, in an accelerated lattice. With this, we can realize a 'coherent atom elevator' consisting in an effective displacement of atoms using the following sequence (see also figure 4.27 *(right)*):

1. **loading** of the atoms into a standing wave

2. application of a frequency chirp, which realizes the **acceleration** of the lattice

3. **release** of the atoms from the moving lattice

4. **free fall** of the atoms

5. **loading** of the atoms into the co-moving lattice

6. application of a frequency scan of opposite sign in order to **decelerate** the atoms

7. **release** of the atoms from the lattice at zero momentum.

This sequence is realized by switching the laser power of the lattice beams and controlling the relative detuning of the two fields

$$\Delta \nu = \nu_1 - \nu_2, \tag{4.15}$$

where $\nu_1 = \omega_1/(2\pi)$ and $\nu_2 = \omega_2/(2\pi)$ are the frequencies of the counter-propagating light fields. For vanishing initial relative motion of the atom in the laboratory rest frame, the initial frequency detuning is chosen to be $\Delta \nu = 0$. The acceleration process then consists in applying a frequency scan to the relative detuning. After a linear frequency ramp from $\Delta \nu(t = 0) = 0$ to $\Delta \nu(T_a)$ over a certain time T_a, the atoms will move at a velocity
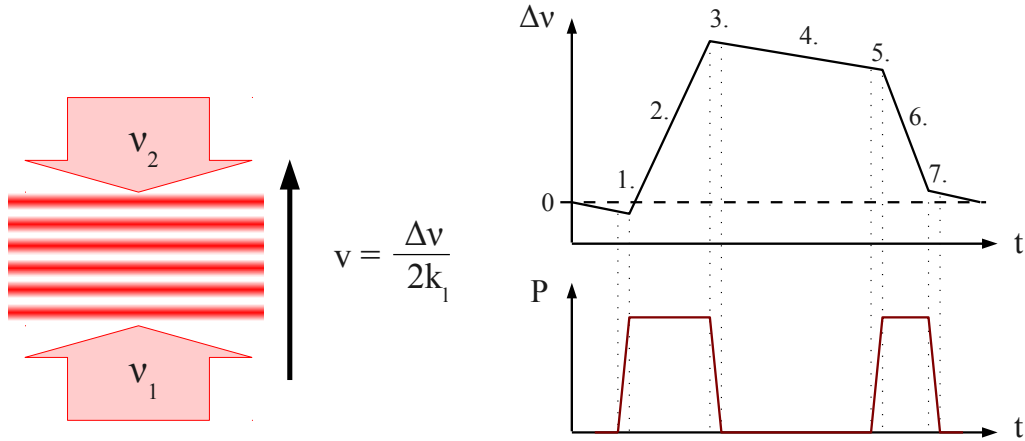
$$v(T_a) = \frac{\Delta \nu(T_a)}{2k_l}, \tag{4.16}$$

Figure 4.27: Bloch lattice transport. *Left*: Two counter-propagating light fields are applied with a frequency difference of $\Delta\nu$. This results in an effective movement of the resulting optical lattice with a velocity of $v_l = \Delta\nu/(2k_l)$. *Right*: Scanning $\Delta\nu$ over time with arbitrary ramps allows for arbitrary atomic trajectories of atoms trapped along the lattice axis. The sequence for the frequency difference and the laser power P depicted here corresponds to a coherent atom elevator.

where k_l is the lattice laser wavenumber of the counter-propagating light fields. This process is then realized with an opposite slope, which decelerates the atoms. The sequence depicted in figure 4.27 *(right)* is a displacement upwards. The frequency slope outside the acceleration and deceleration ramps is applied so that the lattice follows the atoms being accelerated by gravity.

While the atom follows the lattice movement, the system performs Bloch oscillations with a period given by (2.51). Seen from the laboratory rest frame, the atom gains a momentum of $2\hbar k_l$ and a velocity of $\Delta v_{r,l} = 2\hbar k_l/m_a$ during each Bloch oscillation cycle. The corresponding frequency difference, which has to be applied to the relative detuning, is found by considering a Doppler detuning of

$$\Delta\nu_{DBO} = \frac{2\hbar k_l^2}{\pi m_a}. \tag{4.17}$$

The acceleration can then be expressed as a multiple of n Bloch oscillations, which results in a final velocity of $v_a = n \cdot v_{r,l}$ if we apply a total frequency sweep of

$$\Delta\nu = n \cdot \Delta\nu_{DBO} = \frac{2n\hbar k_l^2}{\pi m_a}. \tag{4.18}$$

Losses in the acceleration process

The acceleration has to be performed adiabatically. This means that for a given lattice depth, the acceleration may not be too large. Otherwise, the atoms can not

follow the lattice as they undergo Landau-Zener tunneling (see section 2.3.1). The probability to find an atom in a lattice accelerated by a after a duration $T_l = T_a$ is given by (2.52). For the limit of a deep lattice, which will apply for our case, we find the criterion to find an atom in the lattice after $n = T_a/\tau_B$ Bloch oscillations to be

$$P = \left[1 - \exp\left(-\frac{a_c}{a} \right) \right]^n, \tag{4.19}$$

where the critical acceleration reads

$$a_c = \sqrt{2} a_0 \left(\frac{U_0}{E_r} \right)^{3/4} \tag{4.20}$$

with $a_0 = \hbar^2 k_l^3/m_a^2$. Hence, in order to efficiently accelerate the atom, we have to choose a deep lattice, as intuitively expected.

A large lattice depth can be achieved using high laser intensity or small lattice detuning Δ_l (see (2.47)). However, not only the lattice depth is increased but also single-photon processes can take place. The single-photon scattering rate is generally given by [98]

$$\gamma_{sp} = \left(\frac{\Gamma}{2} \right) \frac{I/I_{sat}}{1 + 4(\Delta_l/\Gamma)^2 + (I/I_{sat})}. \tag{4.21}$$

Here, I is the total lattice laser intensity, I_{sat} is the saturation intensity of the atomic transition, and Γ is the linewidth of the transition. In the limit of large detuning, we can rewrite this expression to

$$\gamma_{sp} = \frac{I}{I_{sat}} \frac{\Gamma^3}{8\Delta_l^2}. \tag{4.22}$$

With the Rabi frequency

$$\Omega = \sqrt{\frac{I}{I_{sat}}} \frac{\Gamma}{\sqrt{2}} \tag{4.23}$$

and (2.47), we find the spontaneous emission as a function of the lattice depth and lattice detuning Δ_l that reads [89]

$$\gamma_{sp} = \frac{1}{2} \frac{U_0}{\hbar} \frac{\Gamma}{\Delta_l}. \tag{4.24}$$

This formula applies for a homogeneous light field. However, the detuning is chosen $\Delta > 0$, such that the lattice is effectively blue detuned and the atoms are trapped in the intensity minima. This reduces the effective spontaneous emission, which then is given by [84]

$$\gamma_{sp,blue} = \frac{1}{2} \sqrt{\frac{E_r}{U_0}} \frac{U_0}{\hbar} \frac{\Gamma}{\Delta_l}. \tag{4.25}$$

As it can be seen from (2.47), the lattice depth U_0 scales with Δ_l^{-1}, while the scattering rate $\gamma_{sp,blue}$ scales with Δ_l^{-2}. Hence, losses due to spontaneous scattering are reduced when increasing the detuning. As the lattice depth on the other hand also diminishes for increasing detuning, the choice of the detuning for a given laser intensity is then made as a trade-off between single-photon scattering losses and lattice depth.

Up to now, we have neglected the loading process of the atoms into the optical lattice. This process has to be realized adiabatically in order to prevent for a loading into excited bands of high order. The adiabaticity criterion for the case of tight binding is given by [90]

$$\frac{d}{dt}\frac{U_0}{E_r} \ll 16\sqrt{2}\frac{E_r}{\hbar}\left(\frac{U_0}{E_r}\right)^{3/2}. \qquad (4.26)$$

4.7.2 Experimental realization

We aim for a coherent transport of cold atoms over distances in the range of many cm in order to transport the atoms to positions close to or far from the mirror. Even more, the technique will be employed to transport an atomic ensemble from one section of the apparatus to another. This process is meant to be realized within a time of several ms. These demands are matched by the acceleration and deceleration process based on the parameters presented in [84, 89]. Namely, we aim for a lattice depth of $U_0 \approx 100E_r$ for a detuning of $\Delta_l \approx 2\pi \cdot 30 \ldots 40$ GHz, and a beam waist of $w_0 \approx 1$ to 2 mm.

The detuning Δ_l is chosen with respect to the ^{87}Rb D2-line cooling transition. Thus, the lattice lattice laser wavelength is in this case $\lambda_l \approx 780$ nm, and the recoil velocity transferred to an atom during one Bloch oscillation is given by the Raman beam splitter recoil momentum $v_{r,l} \approx v_r = \hbar k_{\text{eff}}/m_a$. Taking into account (4.19) and (4.20), we can estimate that the expected lattice depth enables us to realize $n = 300$ Bloch oscillations within $T_a = 3$ ms, which is equivalent to an acceleration of $a = 300v_r/T_a = 1.18 \cdot 10^3$ m/s^2. This results in a final velocity offset during the free fall of $v = 300v_r = 3.54$ m/s.

Laser source

In [84, 89], the demands in laser power are met by Ti:sapphire lasers. In this work, the light field generation is realized using a simpler and less expensive laser system based on the same technique as used for cooling, trapping, and coherent beam splitting in the atomic short range force sensor and the atom gyroscope. The laser system is a MOPA system based on an ECDL with a TA for power amplification. The complete system delivers 1 W output power in free space. The optical set-up comprising the ECDL and the TA is depicted in figure 4.28.
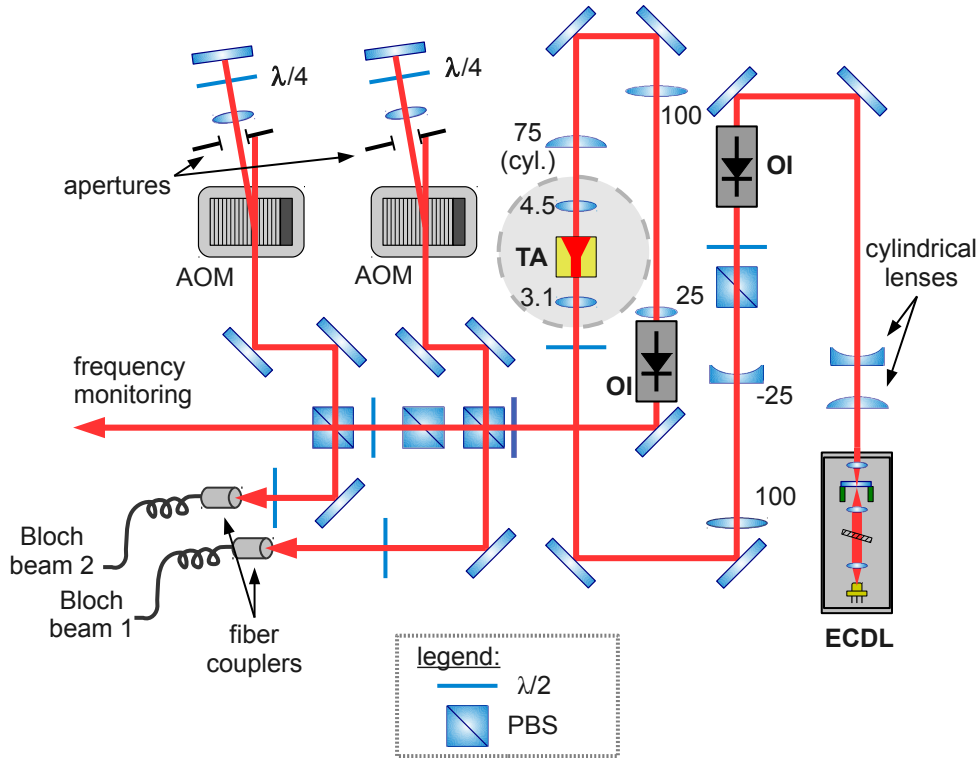
Figure 4.28: Bloch laser bench. The light coming from the ECDL is amplified, controlled in frequency and power using AOMs, and coupled into polarization maintaining fibers that guide the light fields to the experiment. After the ECDL and after power amplification in the TA, two OIs prevent light from being reflected into the TA and ECDL. The focal lengths are depicted for the important lenses in mm. (AOM: acousto-optic modulator, ECDL: external cavity diode laser, OI: optical isolator, TA: tapered amplifier, $\lambda/2$: half-wave plate, $\lambda/4$: quarter-wave plate, PBS: polarizing beam splitter.)

Power and frequency control

The two required light fields are generated out of a single laser source. For the generation of the two light fields featuring a frequency difference in the range of MHz, the light coming from the MOPA system is split, and the two resulting beams are controlled individually in power and frequency. The ECDL itself is not stabilized in frequency. Using a grating spectrograph, the frequency is set to a relative detuning of $\Delta_l \approx 2\pi \cdot 30$ GHz. Even over longer times, the frequency is stable within at most 1 GHz. The free-running absolute frequency stability is sufficient for the realization of a coherent transport. If better control of the lattice global detuning is needed, an active stabilization can be realized using an offset beat note or a transfer cavity [129].

Frequency and power of the single Bloch laser beams are controlled with an
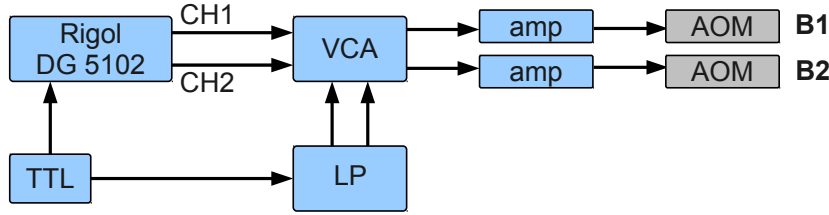
Figure 4.29: Bloch laser frequency control. The RF signal generated in the AWG is power controlled using voltage controlled attenuators (VCA) before being amplified (amp). The TTL serves for timing of the frequency sequence and for power switching. For this, the TTL signal is filtered by a low pass filter (LP) in order to create an effective intensity ramp. The resulting RF signal is applied to the two AOMs.

acousto-optical modulator (AOM) in double-pass configuration for each light field. For the control of the relative Bloch laser frequency, we apply $\nu_{AOM,1} = 80$ MHz and $\nu_{AOM,2} = \nu_{AOM,1} + \Delta\nu/2$ to the two AOMs. In the double-pass configuration, this results in a common frequency shift of the two Bloch laser beams of 160 MHz and a detuning of $\Delta\nu$. The radio frequency (RF) signals at around 80 MHz are created using an arbitrary waveform generator (AWG) of type `Rigol DG 5102`. Channels 1 and 2 of this device are used to generate the frequencies $\nu_{AOM,1}$ and $\nu_{AOM,2}$. Channel 1 emits a constant frequency output, while channel 2 is set to generate a programmed arbitrary waveform. This waveform is created using a homemade `C` program, which writes a chain of voltage values composing the waveform into a `CSV`-file. This file is loaded onto the AWG. The playback of the arbitrary waveform is triggered using a TTL signal, coming from the experiment's control computer.

The Bloch beam power is controlled via the RF power level in the two AOMs. The RF signals coming from the AWG are controlled in power using voltage controlled attenuators (VCA) before an amplification stage with standard RF power amplifiers of type `AA electrooptics AMPA-B-30` (see figure 4.29). The VCAs allow to create a power ramp of variable slope using a tunable low-pass filter allowing for the realization of intensity ramps for an adiabatic loading of the accelerated Bloch lattice.

After frequency and power control in the AOMs, Bloch light fields 1 and 2 with frequencies ν_1 and ν_2, respectively, are guided to the experimental chamber using polarization maintaining fibers. The Bloch beams have to be aligned along the common optical axis of the 1D-lattice, the optical dipole trap beam and the Raman laser beams. As the Bloch laser wavelength is the same as for the Raman light fields, the Bloch beams are shined in via the optical path of the Raman beams. This is realized as follows. The Bloch beam 1 comes from the bottom of the chamber. It is superimposed with the Raman beams in the AOM, which we use for power control and switching of the Raman beams (see figure 4.30).
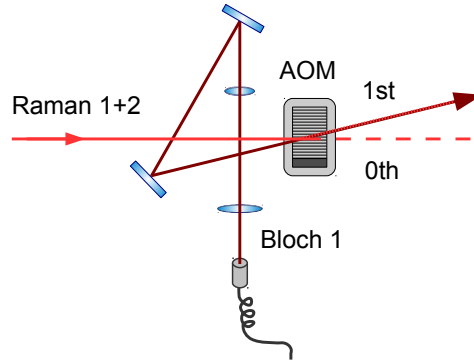
Figure 4.30: Bloch beam 1 application. The Raman beams are switched and power controlled using an AOM in the modified configuration (see section 4.6.1). The Bloch beam 1 is superimposed to the first diffraction order of the Raman beams.

Reducing the beam waist by a factor of 2 before aligning the Bloch beam 1 with the Raman beams we obtain a final waist of $w_0 = 1.4$ mm after the telescope of the Raman beams. Bloch beam 2 is applied from the top (see figure 4.31). For this, an additional polarizing beam splitter cube (PBS) is used, on which the differential light shift compensation beam and the Bloch beam 2 are superimposed. The half-wave plate between the two PBS is oriented in its rotation such that the reflection of the Bloch beam is almost maximal[4]. The waist of the Bloch beam 2 is set to match the waist of Bloch beam 1 using a Galilean telescope.

The total power in each beam is found to be typically $P_1 = P_2 = 70$ mW. With this set-up, we can realize a lattice depth of $U_0 = 108 E_r$ for a detuning of $\Delta_l = 2\pi \cdot 30$ GHz. The losses due to single-photon scattering are calculated to be 21.27 % for a total transport duration of 10 ms and atoms initially in the $|5^2 S_{3/2}, F = 2\rangle$-state.

Inconveniently, for the presented beam configuration, the Bloch beam 1 is retro-reflected by the Raman retro-reflection mirror. This increases slightly the single-photon scattering rate as seen at the end of the following section.

4.7.3   First results

The acceleration and deceleration used for the coherent transport is first studied for a transport downwards using a detuning and power scheme as depicted in figure 4.32 *(left)*. First, an acceleration process is demonstrated for a total number of 300 Bloch oscillations within 3 ms. The Bloch laser beams are switched on and off adiabatically with intensity ramps of $\tau_{ramp} = 500$ μs duration. The corresponding

---

[4]The low demand in optical power for the differential light shift compensation beam allows to choose the reflection of this beam on the second PBS almost minimal.
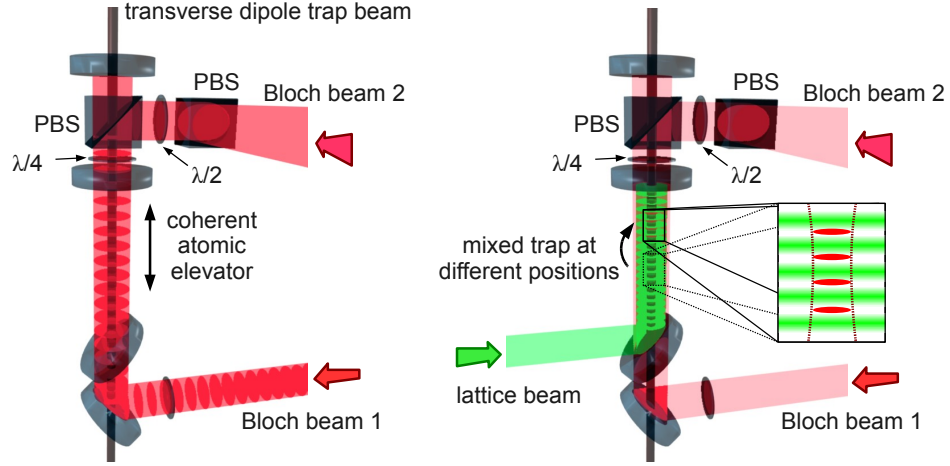
Figure 4.31: Bloch laser beam set-up. The Bloch laser beams are aligned along the mixed trap optical axis. Bloch beam 1 is applied via the Raman beam optical path. Bloch beam 2 is shined in via the Raman beam splitter cube in the retro-reflection part. The coherent transport in the Bloch lattice *(left)* allows to trap the atoms at different positions in the mixed trap *(right)* by loading from the Bloch lattice into the lattice with
$$\lambda_l = 532 \text{ nm}.$$

time-of-flight (TOF) measurement in the detection zone is depicted in figure 4.32 *(right)*. Second, a deceleration process is added after a free fall of 12 ms. Once again, the intensity is switched on and off adiabatically. Applying a ramp in the opposite direction with respect to the acceleration ramp allows us to transfer a momentum of the same amount in the opposite direction. After this deceleration process, the atoms move as fast as the atoms that did not undergo the elevator process, but with an effective displacement of approximately -5.5 cm. In the TOF signals, we can see that the acceleration process leaves behind slightly more than half of the atoms. The narrow TOF profile of the accelerated atoms is due to the fast movement of the cloud leading to a narrower convolution with the detection light sheet. The deceleration is found to be highly efficient. Only a small part of the atoms stays at full velocity.

A first quantitative characterization of the coherent transport efficiency is realized using the scheme depicted in figure 4.27 *(right)*. After the molasses cooling phase, the atoms are trapped in a lattice that is accelerated in the same way as the atoms are in an adiabatic loading process with an intensity ramp of $\tau_{ramp} = 500 \ \mu$s. Then, the lattice is accelerated upwards during 1 ms and the atoms are released from the lattice by switching of the light fields adiabatically within $\tau_{ramp} = 500 \ \mu$s. After a time of free fall of 11 ms, the lattice is switched on again. A second frequency sweep brings the atomic velocity back to almost zero. The timing is adapted such that, after adiabatically switching off the lattice in the end, the
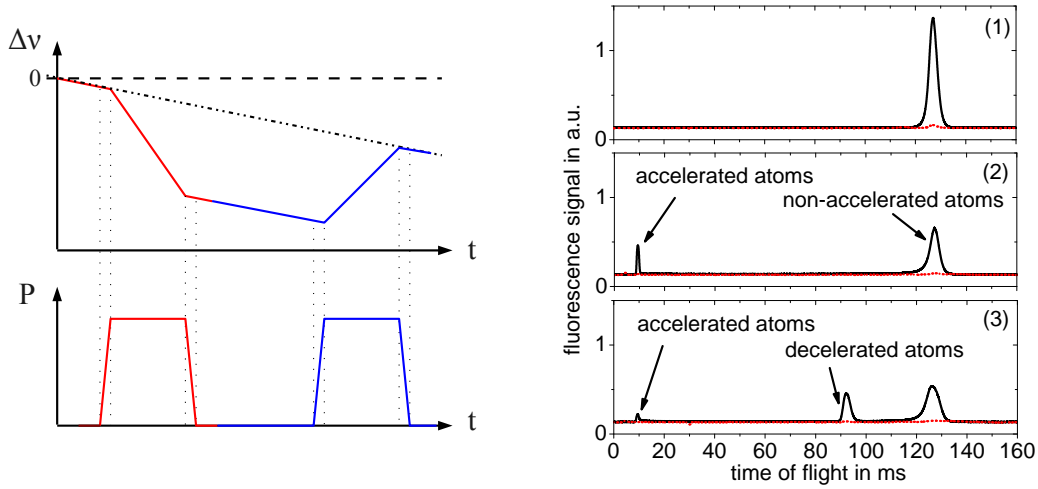
Figure 4.32: Acceleration and deceleration using Bloch oscillations. *Left*: The accelera-tion process is demonstrated by a descending acceleration *(red line)*. The full transport process is completed when adding an ascending acceleration *(blue line)*. This process follows the gravitational acceleration *(dashed dotted black line)*. *Right*: The resulting time-of-flight signals in our detection are depicted for the case of no acceleration (1), only acceleration (2), and acceleration and deceleration (3). The fluorescence signal of the upper *(black line)* and lower detection photodiode *(red dotted line)* are depicted.

atoms have zero vertical velocity after the whole process. In this moment, the mixed trap is switched on and the atoms are loaded into the far-detuned lattice with $\lambda_l = 532$ nm. The efficiency of this process is then given by the ratio of the initial number of atoms and the number of atoms which, due to the vertical displacement and subsequent trapping, arrive later in the detection zone.

The resulting efficiency is plotted against the number of Bloch oscillations, which is depicted in figure 4.33. We find a saturation for a transport efficiency of 27 % when trapping the atoms in the mixed trap after the transport. We also compare on that figure the measured efficiency with calculations performed for three different depths: $U_0 = 80E_r$, $U_0 = 100E_r$, and $U_0 = 120E_r$. The actual lattice depth is slightly lower than the predicted value. The reason for the limited efficiency even for lower acceleration values is found when repeating the same measurement without subsequent trapping. In this case, the efficiency increases even for lower accelerations. This is due to atoms in regions of lower lattice depth on the edge of the lateral Gaussian intensity profile. These atoms are accelerated only in the case of low accelerations and counted in the case without subsequent trapping. On the contrary, these atoms are not trapped in the mixed trap in any case and therefore do not limit the transport efficiency for the case of our
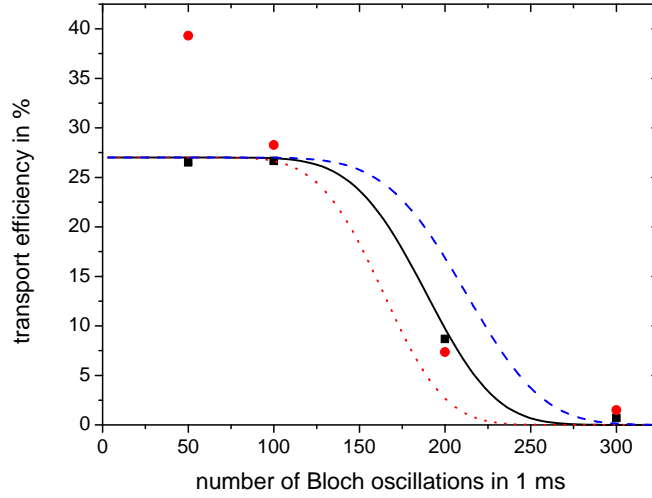
Figure 4.33: Atom displacement efficiency. The measured transport efficiency is plotted directly after the transport process *(red circles)* and for subsequent trapping in the mixed trap *(black boxes)*. For comparison, the theoretical efficiency is plotted for $U_0 = 80E_r$ *(red dotted line)*, $U_0 = 100E_r$ *(black line)*, and $U_0 = 120E_r$ *(blue dashed line)* and normalized to 27 % efficiency.

application. With this, we find a maximum velocity for the transport process of

$$a_{max} \approx \frac{100v_r}{10^{-3} \text{ s}}.$$

In order to evaluate the losses induced by single-photon scattering, we load the atoms into the lattice for varying durations. The detuning $\Delta\nu$ is chosen such that the lattice follows the free fall of the atoms after the release from the optical molasses. Starting in the $F = 2$ Zeeman manifold, we can quantify the single-photon scattering losses by tracking the number of atoms in the $F = 1$ Zeeman manifold in the detection zone. Taking into account the possible excitations to the $|5^2P_{3/2}\rangle$ hyperfine states and subsequent spontaneous relaxation into the $F = 1$ and $F = 2$-state, we expect one third of the excited atoms in the $F = 1$-state. Indeed, the application of the Bloch laser beams results in a transition probability from the $F = 2$ to the $F = 1$-state of approximately 7 % after a total application time of 10 ms as depicted in figure 4.34. This results in a total loss due to single-photon scattering of approximately

$$\eta_{sp} \quad \approx \quad \frac{2 \text{ \%}}{10^{-3} \text{ s}}.$$
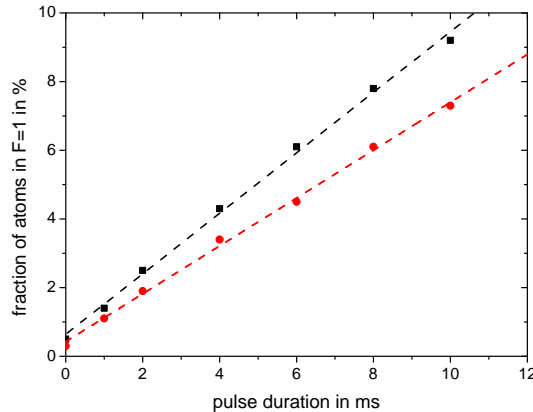
Figure 4.34: Single-photon scattering in the transport process. The fraction of atoms in the $F = 1$-state is measured after varying trapping time of free-falling atoms in a co-moving lattice. The measurement is realized for only ascending Bloch beam 1 and descending Bloch beam 2 *(red circles)*, as well as for ascending and descending Bloch beam 1 and descending Bloch beam 2 *(black boxes)*. For small times, the losses can be approximated linearly *(dashed lines)*.

This set-up will enable coherent transports of atomic ensembles along the 1D-lattice for measurements in different positions. For this, the acceleration duration is slightly enlarged as presented in the first measurement. With an application of 300 Bloch oscillation cycles within 3 ms and a free-fall time of several tens of ms, a transport over several tens of cm can be realized with low losses.

4.8   Conclusions

In this chapter, a trapped atomic accelerometer based on Raman induced tunneling in a vertical optical 1D-lattice has been presented. It serves as a test-ground for the stability studies of Bloch frequency measurements in the vertical lattice. This type of measurements will be used in a similar set-up for the measurement of short range forces in the vicinity of the lattice retro-reflection mirror.

After the introduction of the experimental set-up and the measurement sequence, we have demonstrated the Raman laser induced tunneling process allowing for Wannier-Stark spectroscopy, which leads to a measurement of multiples of the Bloch frequency. The characteristics of tunneling process has been proven to show good agreement with the theoretical predictions. By the use of a differential light shift compensation beam that is mode-matched with the optical dipole trap beam that serves for transverse confinement, we are able to show a Wannier-Stark spectroscopy resolution exceeding the fundamental Fourier limit by only a factor

of 2. This residual broadening was inferred to be caused by intensity inhomogeneities of the Raman beam splitter light fields resulting in a differential light shift inhomogeneity.

We have employed two types of interferometer sequences with the demonstrated inter-site coupling: a WSR interferometer and a WSR type interferometer that is symmetrized with respect to the internal atomic state using microwave inner-site transitions. The best short term stability was found to be $5.8 \cdot 10^{-5} \ 1/\sqrt{\text{Hz}}$. We have realized interferometers with a lattice site separation of up to seven, which corresponds to a spatial separation of almost 2 μm. Based on vibration measurements on the retro-reflection optical set-up and the evaluation of the impact on the interferometer phase using the sensitivity function formalism, we estimated the short term stability to be limited by the relative vibration of the lattice and Raman retro-reflective mirrors. Studies of the long term stability have been carried out using a microwave Ramsey sequence to analyze the impact of the trapping and Raman light fields on the stability of the Bloch frequency measurement. The imperfect mode-match of the dipole trap and differential light shift compensation beam was inferred to be the dominant source for long time drifts of frequency measurements on a single inter-site transition. These long term fluctuations could be suppressed by alternating the frequency measurement on the inter-site transitions in opposite directions along the lattice in subsequent interferometer measurements.

The presented analysis led to two modifications in the experimental set-up. First, the retro-reflection optical bench was replaced by a more stable structure and the lattice and Raman retro-reflection mirrors were installed on the same optical axis in a robust mounting structure. Second, the Raman light fields were independently guided to the experiment. This allows for better polarization control of each of the two light fields. Furthermore, the beam diameter was reduced in order to avoid diffraction on the Raman light fields caused by the limited aperture on the optical path. After the application of these modifications, the short term stability was improved by a factor of 3 to about $2 \cdot 10^{-5} \ 1/\sqrt{\text{Hz}}$.

From the Bloch frequency measurement, we can deduce the local acceleration that acts on the atoms. In the presented measurements far from the mirror surface, this is the gravitational acceleration. Taking into account the stable lattice laser frequency we can deduce a sensitivity to the gravitational acceleration given by

$$\frac{\delta g}{g} \;\; = \;\; 2 \cdot 10^{-5} \ \frac{1}{\sqrt{\text{Hz}}}.$$

This is a factor of 2 above the value reported in [71]. The sensitivity of $\delta g/g = 1 \cdot 10^{-7}$ is in this case obtained within a measurement time of approximately 1 hour in a Bloch frequency measurement realized by modulating the lattice depth.

The sensitivity to accelerations allows for an estimate of the resolution of short range force measurement. These short range forces will be measured as a perturbation of the gravitational acceleration. By performing subsequent Bloch frequency

measurements close to or far from the mirror surface, a quasi-differential measurement of short range forces can be realized. Taking into account the Casimir-Polder force value that can be deduced using (1.4) we can estimate the limitation of our atom interferometer for the Casimir-Polder force measurement. For a distance of 5 μm between Rubidium atoms and a perfectly conducting surface we find a resolution of

$$\frac{\delta F_{CP}}{F_{CP}} \;\; = \;\; 1 \; \%$$

after 150 s of integration. The steps that have to be taken to realize such a measurement will be briefly discussed in section 5.2.

In addition, we have implemented a coherent atomic transport based on strongly accelerated lattices. This will serve for transporting the atoms between the source section of the vacuum chamber and the interferometer chamber. Furthermore, it will allow to transport the atoms to positions in variable distances to the retro-reflection mirror surface in order to realize a mapping of forces along the lattice optical axis. We have demonstrated a high transport efficiency for our targeted acceleration values.

Subsequent to the presented work, detailed studies on different Wannier-Stark interferometer sequences have been carried out. Furthermore, a study on systematic effects of the Bloch frequency measurement has been realized [75]. This will be presented in more detail in [76].

Outlook

5.1 Atom interferometer gyroscope

In chapter 3, the long term stability of our cold atom gyroscope was analyzed leading to an improvement in sensitivity of one order of magnitude. However, for the full characterization of the apparatus, several additional parameters, such as the bias and the factors reducing the short term stability, need to be further analyzed. The studies of this thesis started out with a short term sensitivity of $5.5 \cdot 10^{-7}$ rad/(s$\sqrt{\text{Hz}}$) determined in a mid-fringe measurement. Using an ellipse fit method to extract the rotation phase, which is robust against acceleration perturbations, we find a short term sensitivity of $8.5 \cdot 10^{-7}$ rad/(s$\sqrt{\text{Hz}}$). With this method, it was possible to demonstrate a rotation sensitivity of $2 \cdot 10^{-8}$ rad/s after 4000 s of integration. Key to this was the monitoring of the overlap between the atomic trajectories in the longitudinal direction which was employed for post-correction of the rotation signal. A suppression by a factor of 3 was achieved for the dominant sources of slow fluctuations: (i) the relative wave front misalignments and (ii) an imperfect interferometer overlap. The tools developed in the presented study will allow to improve the long term stability of our gyroscope below 10^{-8} rad/s, and even the lower 10^{-9} rad/s regime is within reach.

In this work estimates, of the rotation signal bias are given, but the experimental determination was beyond the scope of this thesis. It necessitates a further reduction of the drift rate of less than $1 \cdot 10^{-8}$ rad/s over hours. An improvement of the short term stability would permit to reduce the integration time to reach the range of 10^{-9} rad/s. Therefore, an analysis of the sources causing the present short term stability is crucial. The factors suspected to reduce the sensitivity are (i) the vibrations induced by acoustic perturbations, (ii) the residual rotational vibrations of the apparatus, and (iii) the signal-to-noise ratio.

Acoustic vibrations couple to the experiment mostly via the air. The upper side of the μ-metal shield shows vibrational resonances in the range of tens of Hz. These vibrations are transferred to the apparatus, and in particular to the Raman mirrors. This can excite modes in the mirror mount that have a non-vanishing rotation component. These vibrations will be strongly suppressed with an acoustic isolation box that is currently being designed.

Environmental vibrations are strongly reduced with the aid of the employed vibration isolation platform. Nevertheless, the level of residual vibrations are in a range that potentially limits the current short term sensitivity of the gyroscope. In the case of cold atom gravimeters, a post-correction technique based on the auxiliary measurement if vibrations using a broadband seismometer is employed. This method has shown to reduce the devices' short term vibrational noise by a factor of 3 [130]. A similar technique can be employed for our atom interferometer gyroscope. Two of these seismometers can be used that are separated by a baseline of about 1 m length. The instantaneous rotation of the platform can then be determined via the differential signal of the two seismometers allowing for a direct correction of the rotation signal measured in our atom gyroscope. However, it is not clear to what extend this technique can suppress small environmental vibrations. The transfer functions and the sensitivities of the two seismometers as well as cross talk effects from different axes have to be identical in the two sensors. This will be subject to studies in the near future. In any case, these studies will be beneficial for possible future field applications for atom gyroscopes in environments of higher seismic background in which an increase of the dynamic range is of high interest [50].

A way to avoid environmental vibrations rather than realizing a post-correction is to move to a laboratory environment that has a low seismic background. Such can be found in the basements of the LNQE (Laboratorium für Nano- and Quantenengineering) in Hanover and will in near future be available in the planned HiTec facility (Hannover Institut für Technologie). An even lower seismic background level can be found in laboratories far from human-made vibrations. This kind of environment exists in the Fundamentalstation in Wettzell. Also, it would be of high interest to perform comparison measurements to the Grossring G ring laser gyroscope at this site. Nevertheless, it is necessary to increase the signal-to-noise ratio of our sensor for such a comparison.

A fundamental limitation of the signal-to-noise ratio is given by the quantum projection limit. For the atom number used in our interferometers, this limits the sensitivity to about $3 \cdot 10^{-8}$ rad/(s$\sqrt{\text{Hz}}$) for a signal contrast of 30 %. However, the technical noise in the state selective fluorescence detection is expected to be larger, in the range of higher 10^{-8} rad/(s$\sqrt{\text{Hz}}$) to $1 \cdot 10^{-7}$ rad/(s$\sqrt{\text{Hz}}$) for our present scaling factor for rotations. For the application in a calm environment it will then be useful to further increase the signal-to-noise ratio by increasing the scaling factor of our gyroscope. A promising way to achieve this is via the use of so-

called Raman double-diffraction. This beam splitting technique couples one initial zero momentum state to two symmetric states with momenta $\pm\hbar\mathbf{k}_{\text{eff}}$. A pulse scheme similar to the Mach-Zehnder like geometry can be realized leading to an effective increase of the enclosed area of a factor of 2. This has been demonstrated in a cold atom gyroscope at SYRTE [131]. The double-diffraction scheme provides an additional advantage arising from the fact that the two interferometer paths are at any time in the same internal state. As a consequence, systematic effects due to spatially homogeneous frequency shifts of the internal states are suppressed. This reduces not only the bias terms in the rotation signal, but also jitters and drifts. Furthermore, the interferometer phase in a double-diffraction geometry is insensitive to laser phase fluctuations arising from noise in the phase-locked loop. Although the internal state is the same for both interferometer paths, it is still possible to read out the interferometer state using a state selective fluorescence detection. This makes double diffraction, in principle, applicable in our gyroscope.

A drawback of this technique is the high demand set on the atomic ensemble temperature. In order to realize splitting in both directions at the same time, the Doppler angle is chosen to be zero such that diffraction in both directions can take place in the presence of all four Raman light fields. This results in a diffraction to higher orders, which reduces the diffraction efficiency into the desired states. The atoms in the unwanted order can be pushed out of the system as they feature an internal state that is opposite to the interferometer paths. However, the atom number in the interferometer is reduced. In order to suppress higher order diffraction, the pulse length needs to be increased with respect to our parameters. For the case of ^{87}Rb, double diffraction has been applied in a cold atom gravimeter [132]. The pulse lengths for beam splitting and mirror pulses are $\tau_{BS} = 18$ μs and $\tau_M = 36$ μs, respectively. Indeed, performing a numerical calculation following the considerations in [133], we find drastically decreasing diffraction efficiency to the desired orders for shorter pulses. The increase in pulse length compared to the presently used ones results in the selection of a narrower velocity class. This has two consequences for the application in our gyroscope. First, the number of atoms in the interferometer decreases by a factor of two compared to the current status. Second, the narrower velocity selection increases the relative number of atoms that undergo spontaneous emission processes and scatter to the magnetically sensitive Zeeman sub-levels. This increases the background and therefore reduced the effective interferometer signal contrast. However, we can counteract on the latter effect by increasing the global Raman detuning. This method is therefore applicable in our gyroscope with a slight reduction in atom number, which will presumably not increase the detection noise.

The double-diffraction offers an additional possibility to increase the area of our gyroscope by applying a larger number of pulses that diffract the atoms to momentum states $\pm 2\hbar\mathbf{k}_{\text{eff}}$ and higher [131]. While the influence of most of the considered frequency shifts can be effectively suppressed in the double-diffraction

scheme, this is not the case for wave fronts. Even more, the magnitude of the wave front offset scales with the order of the diffraction process. Increasing the area therefore also leads to the increase of wave front influences. It will therefore be crucial for an increase in short and long term stability of our sensor to find a way to circumvent the necessity of the alignment of the laser beams. This could be achieved using one large mirror of high flatness for all three interaction zones that is put into the vacuum chamber. The mounting of such a mirror needs to be designed such that the stress on the bulk substrate is minimized in order to prevent for deformations.

In conclusion, presuming a total factor of 4 in the area increase for a contrast comparable to the present status and a detection noise level of $1 \cdot 10^{-7}$ rad/(s$\sqrt{\mathrm{Hz}}$) for our present scaling factor, we would find a sensitivity of $2.5 \cdot 10^{-8}$ rad/(s$\sqrt{\mathrm{Hz}}$) in a seismically quiet environment. With the effective rejection of most of the systematic effects, and with a reduction in the wave front impact, we can expect an integration to the lower 10^{-9} rad/s level and below within averaging times of hundreds of seconds.

5.2   Atomic short range force sensor

In chapter 4, the proof-of-principle demonstrator for an atom short range force sensor has been presented. We have demonstrated for the first time Raman laser induced tunneling in a vertical optical 1D-lattice which corresponds to coupling Wannier-Stark states. The spectroscopy of transitions between these states is then studied in detail resulting in a resolution of a factor of 2 above the Fourier limit. Using the Wannier-Stark state coupling, we have realized a WSR interferometer. This allows to measure the Bloch frequency which, for a known lattice laser wavelength, corresponds to an acceleration measurement. The noise and drift sources of such a Bloch frequency measurement have been studied in detail, which identified the vibrations of the apparatus as dominant short term limitation. Differential light shifts induced by the Raman and mixed trap light fields were found to be the main source for long term fluctuations. Two technical modifications have been realized that led to an improvement of the relative stability of the Bloch frequency measurement of $2 \cdot 10^{-5}$ $1/\sqrt{\mathrm{Hz}}$. This corresponds to a measurement resolution for Casimir-Polder forces in a 5 μm atom-surface separation distance of 1 % after 150 s of integration.

In order to realize Casimir-Polder measurements in the vicinity of the surface of the lattice retro-reflection mirror with our trapped Raman interferometer, we will (i) enhance the spatial resolution of the interferometer measurement and (ii) place the mirror insight the vacuum chamber. Thus, the next step towards the measurement of Casimir-Polder forces is the increase in atomic density. For now, the measurements have been realized with 15,000 to 50,000 atoms that are distributed along the lattice over a length of about 2.5 mm. Reducing this spatial

spread while keeping a high atom number will be achieved preparing an ultra-cold atomic ensemble using evaporative cooling in a horizontal crossed dipole trap. This will not only decrease the spread along the lattice, but also increase the number of trapped atoms. The loading was up to now limited by the transverse spatial overlap of the mixed trap and the atomic distribution after MOT trapping and molasses cooling. The vacuum chamber has already been replaced by a new chamber featuring the necessary optical access ports. A fiber laser source at a wavelength of 1070 nm and an output power of 100 W for the generation of the dipole trap beams is currently being installed. The experimental implementation of trapping and evaporative cooling is expected to be achieved shortly.

Once the atom number per lattice site is increased, we want to select only a few or even a single lattice site in order to achieve the maximal spatial resolution. This can be achieved by the combination of two tools. First, an additional standing light wave with a wavelength close to the lattice laser wavelength of $\lambda_l = 532$ nm (e.g. $\lambda_{l2} = 515$ nm) can be superimposed to our lattice which leads to a spatial modulation of the lattice depth with a characteristic periodicity of 8 μm. The atoms are then trapped in a periodic pattern of the same periodicity. In a second step, the atoms are prepared in a magnetically sensitive state ($m_F \neq 0$) such that the Zeeman shift can be used for selecting atoms in the lattice sites of one of the super-lattice antinodes. While the resonance frequency was the same for all lattice sites up to now, we can lift this degeneracy by applying a magnetic field gradient. By choosing the appropriate frequency, a transition on the Wannier-Stark ladder can be induced only in a few lattice sites. As the atoms also change their internal state during the tunneling process, it is possible to remove the unwanted atoms from the mixed trap by inducing heating with a resonant light field. We can, in principle, achieve single-site selection using a strong magnetic field gradient in this method [134].

The following step is to perform the atom interferometer measurement close to the mirror surface. It has been shown that deposited Rubidium atoms on the mirror surface can, in the interaction with their image charges, produce electrostatic fields that perturb the Casimir-Polder measurement [122]. In order to avoid this, we will prepare the atomic ensemble in one experimental chamber section and transport it to another section where the short range force measurement is performed. This will be realized using the coherent transport based on an accelerated lattice presented in this work. Casimir-Polder forces can then be measured in a differential way alternating measurements close to the surface in the range of 5 μm to 10 μm and in distances of several mm. Subtracting the two measured values will result in the Casimir-Polder force value. In these distances, the Casimir-Polder potential can be considered as a perturbation to the gravitational acceleration. Measurements in shorter atom-mirror separation distances demand for different considerations. It has been shown in [59], that the wave function of the Wannier-Stark states strongly changes in distances below 1 μm and the perturbation calculation is no more valid.

We target for a precision in the Casimir-Polder measurement of below 1 %. The measured value will then be compared to the full quantum electrodynamic (QED) calculation. A dominant source for uncertainties in these calculations is the exact knowledge of the dielectric function of the interacting surface, which limits the precision of the calculations mentioned in [67]. This will play an important role in the ongoing selection process of the used mirror material.

If a good agreement is found with high precision, new constrains can be set for non-Newtonian forces in the range of several μm. In shorter distances, the prediction of the interaction is more demanding. In these regions, different methods can be used to strongly reduce the QED interactions and to directly validate or falsify possible non-Newtonian gravity. The considerations from [40] will be briefly described in the following. For example, a disc made out of a material that is transparent at both, the lattice and, more importantly, the interaction wavelengths could be inserted between the mirror surface and the atoms. Its position could be tracked with a light interferometer between the disc and the lattice mirror. A different method would be to realize a differential measurement using ^{85}Rb and ^{87}Rb atoms. On the one hand, this results in a reduction of the sensitivity to gravitational forces by a factor of 10^{-2}. On the other hand, QED interactions are effectively suppressed by a factor of 10^{-6}, which will allow to set new limits on non-Newtonian gravity.

Allan standard deviation

The Allan standard deviation is introduced following the description in [135]. Here, a frequency measurement is considered to be realized in finite time intervals with a certain duration T_{meas}, which results in measurement values

$$y_i \;=\; \frac{1}{T_{meas}} \int_{t_i}^{t_i+T_{meas}} y(t)dt. \tag{A.1}$$

The scattering in the consecutive measurements enables to evaluate the uncertainty with which the measured quantity can be determined, usually as mean value $\bar{y} = 1/N \sum_{i=1}^{N} y_i$ of the measurement results. While the standard deviation s_y is defined by its square, the variance

$$s_y^2 \;=\; \frac{1}{N-1} \sum_{i=1}^{N} (y_i - \bar{y})^2 \tag{A.2}$$

gives us an information about the total uncertainty of one set of N measurements, it does not take into account correlations between the single measurements corresponding to fluctuations of different time constants and spectral properties. A tool for studying the temporal behavior of noise processes is the Allan variance. The Allan variance value at a time τ is given by the mean of all pairwise quadratic deviations of consecutive measurements values $\bar{y}$ and $\bar{y}'$ that are obtained in an averaging process over a time τ and reads

$$\sigma^2(\tau) \;=\; \tfrac{1}{2} \left\langle (\bar{y}' - \bar{y})^2 \right\rangle. \tag{A.3}$$

The mean is typically taken over all possible consecutive pairs in a total measurement time with arbitrary length $\tau_{total} \gg \tau$. The Allan standard deviation is then defined as the square root of the variance.

In fact, the determination of the Allan variance necessitates the knowledge of the measurement value at any time for an arbitrarily long measurement interval. In particular, this demands a vanishing dead time, which can not be fulfilled by the data taken in the atom interferometer measurements. The Allan variance can in practice be replaced by an average of the two-sample variance for a measurement time $\tau = m \cdot T_c$ following [135], which reads for example

$$\sigma_y^2(m \cdot T_c) \;\; = \;\; \frac{1}{N - 2m} \sum_{i=1}^{N-2m} \frac{1}{2} \left(\frac{1}{m} \sum_{j=i}^{i+m-1} y_j - \frac{1}{m} \sum_{j=i+m}^{i+2m-1} y_j \right)^2 . \quad (A.4)$$

The square root of such an expression $\sigma_y(\tau)$ will be referred to as Allan standard deviation in this work neglecting the dead time of the measurement. This is a good approximation for our case, in which an averaging of $\tau^{-1/2}$ for times $\tau > T_c$ is observed [136].

For white noise of the measured frequency y, the averaging process scales as $\tau^{-1/2}$. This scaling is typically found in the measurements presented here. With this, the Allan standard deviation allows to determine the uncertainty of the measurement for different integration durations, which results for example in an uncertainty value per shot, per second and on longer integration times. The value per shot is given by the value of $\sigma_y(\tau = T_c)$, whereas the uncertainty at 1 second integration time is typically determined via an extrapolation of the Allan standard deviation curve with $\sigma_y(\tau = 1 \text{ s})/\sqrt{\tau \text{Hz}}$.
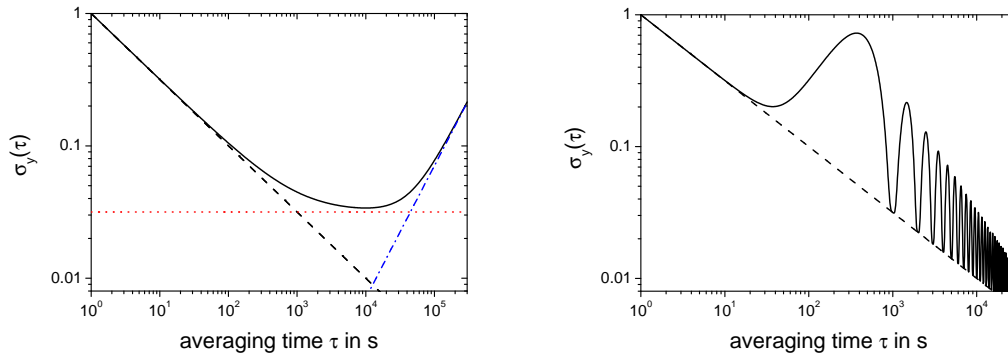
Figure A.1: Averaging behaviors. The Allan standard deviations are depicted for an repeated measurement of a frequency value with a harmonic modulation *(right)* and without modulation *(left)*. Typical noise types are white noise showing a $\tau^{-1/2}$ averaging *(dashed black)*, flicker noise causing the constant so-called flicker floor *(dotted red)* and a linear drift causing an increase of the Allan standard deviation linear with τ *(dashed dotted blue)*.

Frequency fluctuations with different time constants and different spectral properties can be identified using the Allan standard deviation [135]. While an aver-

aging over a time τ would allow for a reduction of the uncertainty with $\tau^{-1/2}$ over arbitrarily long times, the spectral properties of the measured quantities typically feature a so-called flicker noise. The Allan standard deviation for this noise is constant against the averaging time, which is depicted by the so-called flicker floor. Even more, the measured quantity can show drifts over longer time scales. A linear change with $a(t) = a \cdot t$ results in an increase of the Allan standard deviation value over time with $\sigma_y(\tau) = a\tau/\sqrt{2}$. For a modulation with a frequency $f_m \ll 1/T_c$, which is given by

$$y(t) \quad = \quad \frac{\Delta\nu_0}{\nu_0} \sin(2\pi f_m t), \tag{A.5}$$

the Allan standard deviation is found to be [137]

$$\sigma_y(\tau) \quad = \quad \frac{\Delta\nu_0}{\nu_0} \frac{\sin^2(\pi f_m \tau)}{\pi f_m \tau}, \tag{A.6}$$

which becomes zero for $\tau = n/f_m$ and shows maxima for $\tau = (2n+1)/(2f_m)$ for $n \in \mathbf{N}$. The respective Allan standard deviations for the presented noise types are depicted in figure A.1.

Lattice laser frequency stabilization

In this appendix, the lattice laser absolute frequency measurement and the frequency stabilization on a I_2 hyperfine transition line are presented. Three rovibronic lines of I_2 can be detected within the frequency scanning range of the lattice laser using the frequency modulation transfer spectroscopy (FMTS) set-up featuring an acousto-optical modulator (AOM) for frequency modulation and an iodine vapor cell at room temperature. An additional wavemeter measurement of the wavelength with an absolute accuracy of approximately 1 pm allows for identification of these lines and thus for an absolute wavelength measurement only limited by the linewidth of the FMTS.

B.1   Experimental realization

The lattice laser is a solid state intra-cavity frequency doubled ring laser providing single-mode and single-frequency laser light at a wavelength of 532 nm and a continuous wave output power of 12 W. It is a turn-key scientific laser source based on a diode pumped Nd:YVO$_4$ gain medium and a LBO crystal for frequency doubling. The frequency can be scanned by applying a voltage onto the PZT, which permits us to modulate the position of one of the cavity mirrors and thus the cavity length. Two stages featuring electric capacities of 100 pF (fast entrance) and 500 pF (slow entrance) can be employed applying voltages in the range of 0 to 100 V to two BNC connectors on the backside of the laser head corresponding to the two stages. The producer strongly recommends not to apply any voltage below 0 V or above 100 V. The attained frequency scanning ranges are 0.75 GHz and 7.5 GHz, respectively. The fast PZT can be modulated up to 20 kHz. Within this range, we find a mechanical resonance at about 2.7 kHz.
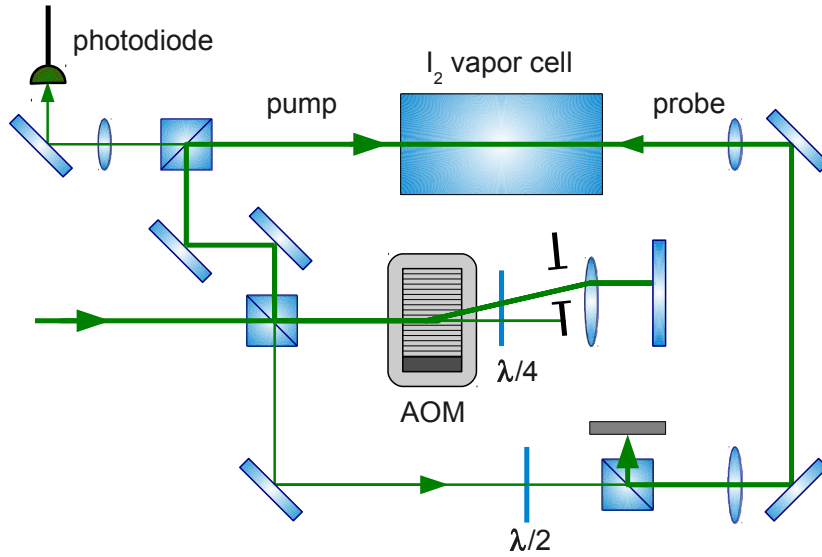
Figure B.1: Lattice laser lock set-up. The FMTS is based on a room temperature iodine cell. The pump beam is shifted by 160 MHz and modulated at 100 kHz using an AOM in double-pass configuration.

The voltage is supplied by a homemade PZT driver, which is supplied by a `TTi EX752M` voltage source. This driver is designed to only deliver voltages in the range of 5 V to 95 V, in order not to destroy the PZT stack. It provides two modulation inputs and an offset-control.

We realize the frequency modulation of the pump beam using an AOM of type `MT80-1,5A-VIS` from `AA optoelectronic`, which is supplied with a modulated radio frequency (RF) signal around 80 MHz. This RF signal is produced by a voltage controlled oscillator `POS-150`, which can be adjusted manually and at the same time modulated with a sensitivity of 8.6 MHz/V. This signal is amplified by a RF power amplifier `AMPA-B-30` from `AA optoelectronic`. The modulation signal of $U_{mod}(t) = U_{mod,0}\cos(\omega_{mod}t)$ with $U_{mod,0} \approx 2$ V and $\omega_{mod} = 2\pi \cdot 100$ kHz is furnished by a homemade lock-in box providing also the demodulation circuit featuring an offset and phase-offset control.

The FMTS is realized as shown in figure B.1. A beam of about 200 mW is taken from the laser output beam using a polarizing beam splitter cube (PBS). This beam is then split into a pump beam (160 mW) and a probe beam (20 mW) with the aid of a half-wave plate and another PBS. The pump beam modulation with the AOM is set up in a double-passage to suppresses pointing modulations that would cause an amplitude modulation of the absorption signal due to spatial fluctuations of the molecular excitations in the vapor probe region. The modulated probe beam (85 mW) traverses the iodine cell and is dumped after the cell in order
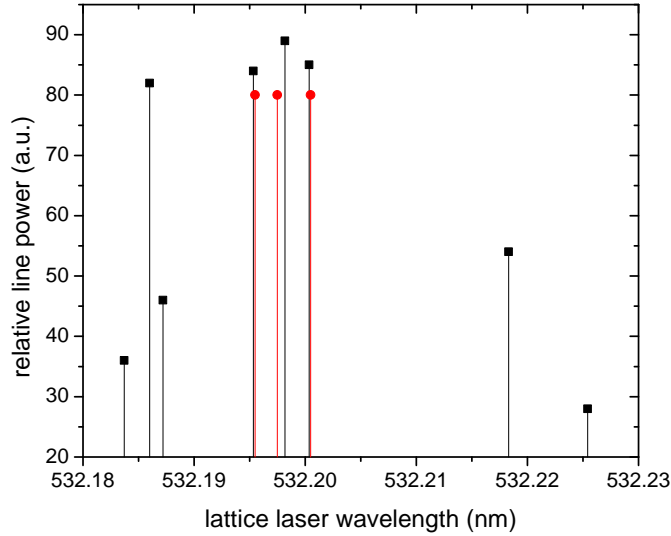
Figure B.2: Measured rovibronic I_2 lines. Taking into account a tolerance of 10 pm, the three lines R(85)33 (1114), R(55)32 (1115), and P(52)32 (1116) (from left to right) are found to be the detected lines *(red lines and dots)* when comparing to the literature values *(black lines and squares)*.

PZT voltage (V)	λ_l (nm)	ν_l (GHz)	k_l (cm^{-1})	line no.	λ (nm)
24.4	532.199	563309	18789.996	1114	532.200
50.8	532.196	563312	18790.06	1115	532.198
67.8	532.194	563315	18790.1	1116	532.195

Table B.1: Main absorption lines of the lattice laser light in the I_2 vapor cell.

to avoid interference effects after a complete round trip in the set-up.

The probe beam power is adapted (7.5 mW) and the polarization is filtered by a half-wave plate and a PBS. The beam is reduced in size by a factor 2 and superimposed with the pump beam in the iodine vapor cell. After the passage through the cell, it is focused onto a photodiode. The absorption signal detected by the photo diode is filtered by a band pass filter for 100 kHz before being demodulated. This demodulation results in the error signal depicted in figure B.3.

For the absolute frequency determination, a wavemeter `EXFO-WA1000` is employed and read out with a pc oscilloscope and a homemade software counting the fringes realized in the wavemeter measurement. These fringes are measured using a two-color Michelson interferometer. In this, an internal highly stable Helium-Neon (HeNe) laser serves as a frequency reference. The fringes of the HeNe light at 633 nm are counted in the same interferometer and using the same mirror po-
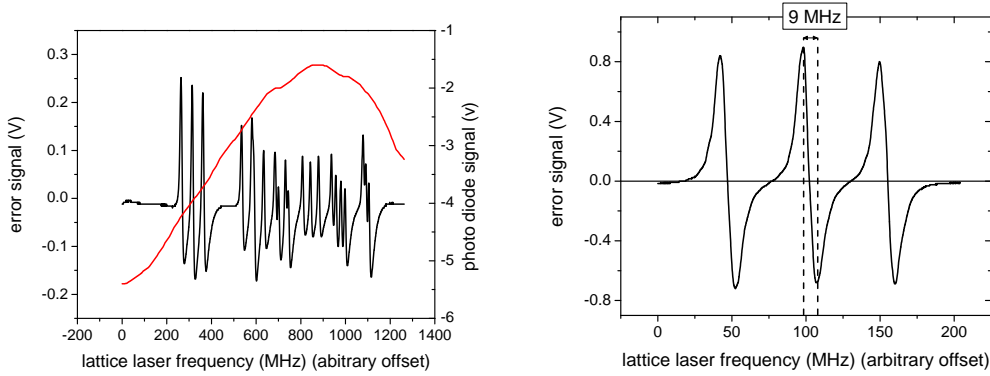
Figure B.3: Resolution of line R(85)33 (1114). The error signal *(black line)* of the FMTS is depicted for a full scan over the line *(left)* and for a zoom on a triplet of hyperfine lines *(right)*. The photodiode signal is depicted as *red line*.

sition modulation of the corner cube mirrors as for the laser light that is to be measured. The latter is injected via a fiber input and automatically aligned to the interferometer. Modulating the position of the corner cube allows for the creation of interference fringes for the two lasers on one photo diode for each beam. The pc oscilloscope reads these fringe signals which makes them accessible for a computer. On this, a homemade software counts the fringes and directly gives the frequency and wavelength value of the measured laser light using the formula

$$\nu_l = \frac{N_l \cdot \nu_{HeNe}}{N_{HeNe}}, \tag{B.1}$$

where ν_l is the measured frequency, ν_{HeNe} is the known HeNe laser frequency, and N_l and N_{HeNe} are the respective decimal numbers of counted fringes. Here, no correction factor for humidity or air pressure is applied to the measurement. Presuming a linear dispersion for the measured frequency, a correction factor can be obtained measuring stabilized light of the MOT cooling beam at 780 nm. Here, we find a value of $\lambda_{cooling} = 780.245$ nm, which results in a deviation of 4 pm on the measured wavelength. This would lead to an error of approximately 3 pm on the measured wavelength in the 532 nm range. For the absolute wavelength determination, we thus presume an error of 10 pm.

B.2   Achieved frequency stability and accuracy

We measure the absolute frequency of the lattice laser using the absorption signal and the absolute frequency measured with the wavemeter. For the peak absorption in the FMTS, which are meant to be the center of the rovibronic absorption

lines, the PZT voltage offset values as well as the measured wavelength values are determined (see B.1). With the aid of the found frequency values and taking into account the presumed error of 10 pm, the lines can be found by using literature values taken from [138]. The only lines that are found in the interval in question are the lines R(85)33 (1114), R(55)32 (1115), and P(52)32 (1116) (see figure B.2).

By using the demodulated signal of the three lines we can find the expected 21 hyperfine structure lines for the first two and 15 hyperfine structure lines for the last, respectively. The line 1114 is shown in figure B.3 *(left)*.

The frequency lock is realized with the aid of one of the hyperfine structure line's error signals, here on the line R(85)33-2 is chosen. An upper bound for this linewidth can be derived directly from the measured spectrum, as shown in figure B.3 *(right)*. The extrema of the error signal can be seen as the lock capture range, and thus, as the frequency range the laser will be locked on. The stability and accuracy are then limited by this quasi-linewidth of 9 MHz. This results in a relative accuracy and stability of

$$\frac{\delta \nu_l}{\nu_l} = 1.6 \cdot 10^{-8}.$$

BIBLIOGRAPHY

[1] A. A. Michelson and E. W. Morley.
On the Relative Motion of the Earth and of the Luminiferous Ether.
Sidereal Messenger, **6** 306–310, 1887.

[2] A. Abramovici, W. E. Althouse, R. W. P. Drever, Y. Gürsel, S. Kawamura,
F. J. Raab, D. Shoemaker, L. Sievers, R. E. Spero, K. S. Thorne, R. E.
Vogt, R. Weiss, S. E. Whitcomb, and M. E. Zucker.
LIGO: The Laser Interferometer Gravitational-Wave Observatory.
Science, **256(5055)** 325–333, 1992.

[3] L. Mach.
Über einen Interferenzrefraktor.
Z. für Instrumentenkunde, **12** 89–93, 1892.

[4] L. Zehnder.
Ein neuer Interferenzrefraktor.
Z. für Instrumentenkunde, **11** 275–285, 1891.

[5] M. G. Sagnac.
Sur la preuve de la réalité de l'éether lumineux par l'expérience de
l'interférographe tournant.
Compt. Rend. des Sc. d. l'Acad d. Sc., **157** 1410–1413, 1913.

[6] K.U. Schreiber, T. Klügel, A. Velikoseltsev, W. Schlüter, G.E. Stedman, and
J.-P.R. Wells.
The Large Ring Laser G for Continuous Earth Rotation Monitoring.
Pure Appl. Geophys., **166(8-9)** 1485–1498, 2009.

[7] P. Grangier, G. Roger, and A. Aspect.
Experimental Evidence for a Photon Anticorrelation Effect on a Beam Split-
ter: A New Light on Single-Photon Interferences.
Europhy. Lett., **1(4)** 173, 1986.

[8] L. de Broglie.
Waves and Quanta.
Nature, **112** 540, 1923.

[9] C. Davisson and L. H. Germer.
Diffraction of Electrons by a Crystal of Nickel.
Phys. Rev., **30** 705–740, 1927.

[10] H. Rauch, W. Treimer, and U. Bonse.
Test of a single crystal neutron interferometer.
Phys. Lett. A, **47(5)** 369 – 371, 1974.

[11] D. W. Keith, C. R. Ekstrom, Q. A. Turchette, and D. E. Pritchard.
An Interferometer for Atoms.
Phys. Rev. Lett., **66(21)** 2693–2696, 1991.

[12] M. Arndt, O. Nairz, J. Voss-Andreae, C. Keller, G. v. d. Zouw, and
A. Zeilinger.
Wave-particle duality of C60 molecules.
Nature, **401** 680, 1999.

[13] P. Haslinger, N. Dörre, P. Geyer, J. Rodewald, S. Nimmrichter, and
M. Arndt.
A universal matter-wave interferometer with optical ionization gratings in
the time domain.
Nat. Phys., **9** 144–148, 2013.

[14] E. M. Rasel, M. K. Oberthaler, H. Batelaan, J. Schmiedmayer, and
A. Zeilinger.
Atom Wave Interferometry with Diffraction Gratings of Light.
Phys. Rev. Lett., **75(14)** 2633–2637, 1995.

[15] D. M. Giltner, R. W. McGowan, and S. A. Lee.
Atom Interferometer Based on Bragg Scattering from Standing Light Waves.
Phys. Rev. Lett., **75** 2638–2641, 1995.

[16] P. Meystre, *Atom Optics.*
Springer, 2001.

[17] M. Kasevich and S. Chu.
Atomic interferometry using stimulated Raman transitions.
Phys. Rev. Lett., **67** 181–184, 1991.

[18] C.J. Bordé.
Atomic interferometry with internal state labelling.
Phys. Lett. A, **140(1,2)** 10–12, 1989.

[19] J. B. Fixler, G. T. Foster, J. M. McGuirk, and M. A. Kasevich.
Atom Interferometer Measurement of the Newtonian Constant of Gravity.
Science, **315(5808)** 74–77, 2007.

[20] G. Lamporesi, A. Bertoldi, L. Cacciapuoti, M. Prevedelli, and G. M. Tino.
Determination of the Newtonian Gravitational Constant Using Atom Inter-
ferometry.

Phys. Rev. Lett., **100** 050801, 2008.

[21] H. Müller, S.-W. Chiow, Q. Long, C. Vo, and S. Chu.
A new photon recoil experiment: towards a determination of the fine structure constant.
Appl. Phys. B, **84(4)** 633–642, 2006.

[22] R. Bouchendira, P. Cladé, S. Guellati-Khélifa, F. Nez, and F. Biraben.
New Determination of the Fine Structure Constant and Test of the Quantum Electrodynamics.
Phys. Rev. Lett., **106** 080801, 2011.

[23] A. Peters, K. Y. Chung, and S. Chu.
Measurement of gravitational acceleration by dropping atoms.
Nature, **400** 849–852, 1999.

[24] T. L. Gustavson, P. Bouyer, and M. A. Kasevich.
Precision Rotation Measurements with an Atom Interferometer Gyroscope.
Phys. Rev. Lett., **78** 2046–2049, 1997.

[25] T. M. Niebauer, G. S. Sasagawa, J. E. Faller, R. Hilt., and F. Klopping.
A new generation of absolute gravimeters.
Metrologia, **32(3)** 159, 1995.

[26] S. Merlet, Q. Bodart, N. Malossi, A. Landragin, F. Pereira Dos Santos, O. Gitlein, and L. Timmen.
Comparison between two mobile absolute gravimeters: optical versus atomic interferometers.
Metrologia, **47(4)** L9, 2010.

[27] E. Felicitas Arias et al.
Final report of key comparison CCM.G-K1: International comparison of absolute gravimeters ICAG2009.
Metrologia, **49(1A)** 07011, 2012.

[28] B. Canuel, F. Leduc, D. Holleville, A. Gauguet, J. Fils, A. Virdis, A. Clairon, N. Dimarcq, Ch. J. Bordé, A. Landragin, and P. Bouyer.
Six-Axis Inertial Sensor Using Cold-Atom Interferometry.
Phys. Rev. Lett., **97** 010402, 2006.

[29] A. Gauguet, B. Canuel, T. Lévèque, W. Chaibi, and A. Landragin.
Characterization and limits of a cold-atom Sagnac interferometer.
Phys. Rev. A, **80** 063604, 2009.

[30] H. Müntinga, H. Ahlers, M. Krutzik, and A. et al. Wenzlawski.
Interferometry with Bose-Einstein Condensates in Microgravity.
Phys. Rev. Lett., **110** 093602, 2013.

[31] R. Geiger, V. Ménoret, G. Stern, N. Zahzam, P. Cheinet, A. Battelier, B. Villing, F. Moron, Bidel Y. Lours, M., A. Bresson, A. Landragin, and P. P. Bouyer.
Detecting inertial effects with airborne matter-wave interferometry.
Nat. Commun., **2** 474, 2011.

[32] S. M. Dickerson, J. M. Hogan, A. Sugarbaker, D. M. S. Johnson, and M. A. Kasevich.
Multi-axis inertial sensing with long-time point source atom interferometry.
Preprint arXiv:1305.1700, 2013.

[33] W. Hänsel, P Hommelhoff, T. W. Hänsch, and J. Reichel.
Bose-Einstein condensation on a microelectronic chip.
Nature, **413** 498–501, 2001.

[34] Y. Shin, M. Saba, T. A. Pasquini, W. Ketterle, D. E. Pritchard, and A. E. Leanhardt.
Atom Interferometry with Bose-Einstein Condensates in a Double-Well Potential.
Phys. Rev. Lett., **92** 050405, 2004.

[35] M. Ben Dahan, E. Peik, J. Reichel, Y. Castin, and C. Salomon.
Bloch Oscillations of Atoms in an Optical Potential.
Phys. Rev. Lett., **76** 4508–4511, 1996.

[36] P. Böhi, M. F. Riedel, J. Hoffrogge, J. Reichel, T. W. Hänsch, and P. Treutlein.
Coherent manipulation of Bose-Einstein condensates with state-dependent microwave potentials on an atom chip.
Nat. Phys., **5** 592–597, 2009.

[37] G. Roati, E. de Mirandes, F. Ferlaino, H. Ott, G. Modugno, and M. Inguscio.
Atom Interferometry with Trapped Fermi Gases.
Phys. Rev. Lett., **92** 230402, 2004.

[38] R. Charrière, M. Cadoret, N. Zahzam, Y. Bidel, and A. Bresson.
Local gravity measurement with the combination of atom interferometry and Bloch oscillations.
Phys. Rev. A, **85** 013639, 2012.

[39] P. Lemonde and P. Wolf.
Optical lattice clock with atoms confined in a shallow trap.
Phys. Rev. A, **72** 033409, 2005.

[40] P. Wolf, P. Lemonde, A. Lambrecht, S. Bize, and A. Landragin, A.and Clairon.
From optical lattice clocks to the measurement of forces in the Casimir regime.

Phys. Rev. A, **75** 063608, 2007.

[41] G. E. Stedman.
Ring-laser tests of fundamental physics and geophysics.
Rep. Prog. Phys., **60(6)** 615, 1997.

[42] J. Lense and H. Thirring.
Über den Einfluss der Eigenrotation der Zentralkörper auf die Bewegung der
Planeten und Monde nach der Einsteinschen Gravitationstheorie.
Physikalische Zeitschrift, **19** 156, 1918.

[43] J. G. F. v. Bohnenberger.
Beschreibung einer Maschine zur Erläuterung der Geseze der Umdrehung der
Erde und ihrer Axe und der Veränderung der Lage der letzteren.
Tübinger Blätter für Naturwissenschaften und Arzneikunde, **3**, 1817.

[44] C. W. F. Everitt et al.
Gravity Probe B: Final Results of a Space Experiment to Test General Rel-
ativity.
Phys. Rev. Lett., **106** 221101, 2011.

[45] W. W. Chow, J. Gea-Banacloche, L. M. Pedrotti, V. E. Sanders, W. Schleich,
and M. O. Scully.
The ring laser gyro.
Rev. Mod. Phys., **57** 61–104, 1985.

[46] R. B. Hurst, G. E. Stedman, K. U. Schreiber, R. J. Thirkettle, R. D. Graham,
N. Rabeendran, and Wells J.-P. R.
Experiments with an 834 m^2 ring laser interferometer .
J. Appl. Phys., **105** 113115, 2009.

[47] K. U. Schreiber, T. Klügel, J.-P. R. Wells, R. B. Hurst, and A. Gebauer.
How to Detect the Chandler and the Annual Wobble of the Earth with a
Large Ring Laser Gyroscope.
Phys. Rev. Lett., **107** 173904, 2011.

[48] K. U. Schreiber, A. Gebauer, and J.-P. R. Wells.
Long-term frequency stabilization of a 16 m^2 ring laser gyroscope.
Opt. Lett., **37(11)** 1925–1927, 2012.

[49] D. S. Durfee, Y. K. Shaham, and M. A. Kasevich.
Long-Term Stability of an Area-Reversible Atom-Interferometer Sagnac Gy-
roscope.
Phys. Rev. Lett., **97** 240801, 2006.

[50] J. K. Stockton, K. Takase, and M. A. Kasevich.
Absolute Geodetic Rotation Measurement Using Atom Interferometry.
Phys. Rev. Lett., **107** 133001, 2011.

[51] C. Jentsch, T. Müller, E.M. Rasel, and W. Ertmer.
HYPER: A Satellite Mission in Fundamental Physics Based on High Precision Atom Interferometry.
Gen. Rel. and Grav., **36(10)** 2197–2221, 2004.

[52] C. Jentsch.
Konzeption und Aufbau eines Experimentes zur quantenlimitierten Inertialsensorik mit lasergekühlten Rubidiumatomen.
PhD Thesis, Universität Hannover, 2004.

[53] T. Müller.
Realisierung eines Atominterferometers zur hochauflösenden Inertialsensorik mit kalten Rubidiumatomen.
PhD Thesis, Leibniz Universität Hannover, 2006.

[54] T. Wendrich.
High resolution rotation sensor based on cold atom interferometry.
PhD Thesis, Leibniz Universität Hannover, 2010.

[55] M. Gilowski.
Quantitative Analyse der Auflösungsbegrenzung eines atomaren Gyroskops.
PhD Thesis, Leibniz Universität Hannover, 2010.

[56] C. Schubert.
Grossflächiges Sagnac Interferometer mit kalten Atomen.
PhD Thesis, Leibniz Universität Hannover, 2012.

[57] G. Tackmann, P. Berg, C. Schubert, S. Abend, M. Gilowski, W. Ertmer, and E.M. Rasel.
Self-alignment of a compact large-area atomic Sagnac interferometer.
New J. Phys., **14(1)** 015002, 2012.

[58] S. Dimopoulos and A. A. Geraci.
Probing submicron forces by interferometry of Bose-Einstein condensed atoms.
Phys. Rev. D, **68** 124021, 2003.

[59] R. Messina, S. Pelisson, M.-C. Angonin, and P. Wolf.
Atomic states in optical traps near a planar surface.
Phys. Rev. A, **83** 052111, 2011.

[60] H. B. G. Casimir and D. Polder.
The Influence of Retardation on the London-van der Waals Forces.
Phys. Rev., **73** 360–372, 1948.

[61] S. Pélisson.
Etude d'états atomiques à proximité d'une surface massive - Application à l'expérience FORCA-G.
PhD Thesis, Université Pierre et Marie Curie, Paris 6, 2012.

[62] M. Antezza, L. P. Pitaevskii, and S. Stringari.
Effect of the Casimir-Polder force on the collective oscillations of a trapped
Bose-Einstein condensate.
Phys. Rev. A, **70** 053619, 2004.

[63] F. Shimizu.
Specular Reflection of Very Slow Metastable Neon Atoms from a Solid Sur-
face.
Phys. Rev. Lett., **86** 987–990, 2001.

[64] T. A. Pasquini, Y. Shin, C. Sanner, M. Saba, A. Schirotzek, D. E. Pritchard,
and W. Ketterle.
Quantum Reflection from a Solid Surface at Normal Incidence.
Phys. Rev. Lett., **93** 223201, 2004.

[65] M. DeKieviet, U. D. Jentschura, and G. Łach.
Modern Experiments on Atom-Surface Casimir Physics.
In D. Dalvit, P. Milonni, D. Roberts, and F. da Rosa, editors, *Casimir
Physics*, pages 393–418. Springer Berlin Heidelberg, 2011.

[66] A. Landragin, J.-Y. Courtois, G. Labeyrie, N. Vansteenkiste, C. I. West-
brook, and A. Aspect.
Measurement of the van der Waals Force in an Atomic Mirror.
Phys. Rev. Lett., **77** 1464–1467, 1996.

[67] H. Bender, Ph. W. Courteille, C. Marzok, C. Zimmermann, and S. Slama.
Direct Measurement of Intermediate-Range Casimir-Polder Potentials.
Phys. Rev. Lett., **104** 083201, 2010.

[68] D. M. Harber, J. M. Obrecht, J. M. McGuirk, and E. A. Cornell.
Measurement of the Casimir-Polder force through center-of-mass oscillations
of a Bose-Einstein condensate.
Phys. Rev. A, **72** 033610, 2005.

[69] J. M. Obrecht, R. J. Wild, M. Antezza, L. P. Pitaevskii, S. Stringari, and
E. A. Cornell.
Measurement of the Temperature Dependence of the Casimir-Polder Force.
Phys. Rev. Lett., **98** 063201, 2007.

[70] J. D. Perreault and A. D. Cronin.
Observation of Atom Wave Phase Shifts Induced by Van Der Waals Atom-
Surface Interactions.
Phys. Rev. Lett., **95** 133201, 2005.

[71] N. Poli, F.-Y. Wang, M. G. Tarallo, A. Alberti, M. Prevedelli, and G. M.
Tino.
Precision Measurement of Gravity with Cold Atoms in an Optical Lattice
and Comparison with a Classical Gravimeter.

Phys. Rev. Lett., **106** 038501, 2011.

[72] Q. Beaufils, G. Tackmann, X. Wang, B. Pelle, S. Pelisson, P. Wolf, and F. Pereira dos Santos.
Laser Controlled Tunneling in a Vertical Optical Lattice.
Phys. Rev. Lett., **106** 213002, 2011.

[73] X. Wang.
Gravimètres de haute résolution basés sur l'interférométrie atomique.
PhD Thesis, Université Pierre et Marie Curie, Paris 6, 2011.

[74] G. Tackmann, B. Pelle, A. Hilico, Q. Beaufils, and F. Pereira dos Santos.
Raman-laser spectroscopy of Wannier-Stark states.
Phys. Rev. A, **84** 063422, 2011.

[75] B. Pelle, A. Hilico, G. Tackmann, Q. Beaufils, and F. Pereira dos Santos.
State-labeling Wannier-Stark atomic interferometers.
Phys. Rev. A, **87** 023601, 2013.

[76] B. Pelle.
Interféromètres atomiques dans un réseau optique (in preparation).
PhD Thesis, Université Pierre et Marie Curie, Paris 6, 2013.

[77] P. R. Berman, editor.
Atom Interferometry.
Acadamic Press, 1997.

[78] C.J. Bordé.
Theoretical tools for atom optics and interferometry.
Comptes Rendus de l'Académie des Sciences - Series {IV} - Physics, **2(3)** 509 – 530, 2001.

[79] Ch. Antoine and Ch. J. Bordé.
Exact phase shifts for atom interferometry.
Phys. Lett. A, **306(5-6)** 277 – 284, 2003.

[80] Ch. Antoine and Ch. J. Bordé.
Quantum theory of atomic clocks and gravito-inertial sensors: an update.
J. of Opt. B: Quantum and Semiclass. Opt., **5(2)** S199, 2003.

[81] G. H. Wannier.
Wave Functions and Effective Hamiltonian for Bloch Electrons in an Electric Field.
Phys. Rev., **117** 432–439, Jan 1960.

[82] Gutiérrez-Medina, B.
Quantum Transport and Control of Atomic Motion with Light.
PhD Thesis, University of Texas at Austin, 2004.

[83] K. W. Madison.

QUANTUM TRANSPORT IN OPTICAL LATTICES.
PhD Thesis, University of Texas at Austin, 1998.

[84] M. Cadoret.
Application des oscillations de Bloch d'atomes ultra-froids et de l'interférométrie atomique à la mesure de h/m et à la détermination de la constante structure fine.
PhD Thesis, Université Pierre et Marie Curie, 2008.

[85] N. W. Ashcroft and N. D. Mermin, *Solid state physics*.
New York : Harcourt College Publ., 2000.

[86] M. Raizen, C. Salomon, and Q. Niu.
New Light on Quantum Transport.
Physics Today, pages 30–34, 1997.

[87] F. Bloch.
Über die Quantenmechanik der Elektronen in Kristallgittern.
Zeitschrift für Physik, **52(7-8)** 555–600, 1929.

[88] C. Zener.
Non-Adiabatic Crossing of Energy Levels.
Proc. Soc. Lond. A, **833** 696–702, 1932.

[89] P. Cladé.
Oscillations de Bloch d'atomes ultrafroids et mesure de la constante de structure fine.
PhD Thesis, Université Pierre et Marie Curie, Paris 6, 2005.

[90] M. Ben Dahan.
Transport et relaxation d'atomes de césium : oscillations de Bloch et résonance de diffusion.
PhD Thesis, Ecole Normale Supéreure, Paris, (Laboratoire Kastler Brossel), 1998.

[91] M. Glück, A.R. Kolovsky, H.J. Korsch, and N. Moiseyev.
Calculation of Wannier-Bloch and Wannier-Stark states.
Eur. Phys. J. D, **4(3)** 239–246, 1998.

[92] J. Callaway.
Optical Absorption in an Electric Field.
Phys. Rev., **130** 549–553, 1963.

[93] M.-K. Zhou, B. Pelle, A. Hilico, and F. Pereira dos Santos.
Atomic multiwave interferometer in an optical lattice.
Accepted for puplication in Phys. Rev. A, 2013.

[94] N. F. Ramsey.
A Molecular Beam Resonance Method with Separated Oscillating Fields.
Phys. Rev., **78** 695–699, 1950.

[95] P. Cheinet, B. Canuel, F. Pereira dos Santos, A. Gauguet, F. Yver-Leduc, and A. Landragin.
Measurement of the Sensitivity Function in a Time-Domain Atomic Interferometer.
IEEE Trans. Instr. Meas., **57(6)** 1141–1148, 2008.

[96] P. Cheinet.
Conception et Réalisation d'un Gravimètre à Atomes Froids.
PhD Thesis, Université Pierre et Marie Curie, Paris 6, 2006.

[97] G. J. Dick.
Calculation of Trapped Ion Local Oscillator Requirernents.
Proc. 19th Annual Precise Time and Time hklerval (PTTI) Applications and Planning Meeting, pages 133–147, 1988.

[98] D. A. Steck.
Rubidium 87 Line Data, September 2008.

[99] J. Nes.
Cold Atoms and Bose-Einstein Condensates in Optical Dipole Potentials.
PhD Thesis, Technische Universität Darmstadt, 2008.

[100] W. M. Itano, J. C. Bergquist, J. J. Bollinger, J. M. Gilligan, D. J. Heinzen, F. L. Moore, M. G. Raizen, and D. J. Wineland.
Quantum projection noise: Population fluctuations in two-level systems.
Phys. Rev. A, **47** 3554–3570, 1993.

[101] J. Fils, F. Leduc, P. Bouyer, D. Holleville, N. Dimarcq, A. Clairon, and A. Landragin.
Influence of optical aberrations in an atomic gyroscope.
Eur. Phys. J. D, **36(3)** 257–260, 2005.

[102] H. J. Metcalf and P. van der Straaten, *Laser Cooling and Crapping.*
Springer, New York, 1999.

[103] A. Aspect, E. Arimondo, R. Kaiser, N. Vansteenkiste, and C. Cohen-Tannoudji.
Laser cooling below the one-photon recoil energy by velocity-selective coherent population trapping: theoretical analysis.
J. Opt. Soc. Am. B, **6(11)** 2112–2124, Nov 1989.

[104] W. Baillard, A. Gauguet, S. Bize, P. Lemonde, Ph. Laurent, A. Clairon, and P. Rosenbusch.
Interference-filter-stabilized external-cavity diode lasers.
Opt. Comm., **266(2)** 609 – 613, 2006.

[105] D. Voigt, E.C. Schilder, R.J.C. Spreeuw, and H.B. van Linden van den Heuvell.
Characterization of a high-power tapered semiconductor amplifier system.

Appl. Phys. B, **72(3)** 279–284, 2001.

[106] M. Gilowski, Ch. Schubert, M. Zaiser, W. Herr, T. Wübbena, T. Wendrich, T. Müller, E.M. Rasel, and W. Ertmer.
Narrow bandwidth interference filter-stabilized diode laser systems for the manipulation of neutral atoms.
Opt. Comm., **280(2)** 443 – 447, 2007.

[107] P. Berg.
Analyse und Unterdrückung von Phasenrauschen in der Atominterferometrie.
Diploma Thesis, Leibniz Universität Hannover, 2009.

[108] Le Gouët, J. and Cheinet, P. and Kim, J. and Holleville, D. and Clairon, A. and Landragin, A. and Pereira Dos Santos, F.
Influence of lasers propagation delay on the sensitivity of atom interferometers.
Eur. Phys. J. D, **44(3)** 419–425, 2007.

[109] M. Kasevich, D. S. Weiss, E. Riis, K. Moler, S. Kasapi, and S. Chu.
Atomic velocity selection using stimulated Raman transitions.
Phys. Rev. Lett., **66** 2297–2300, 1991.

[110] G. T. Foster, J. B. Fixler, J. M. McGuirk, and M. A. Kasevich.
Method of phase extraction between coupled atom interferometers using ellipse-specific fitting.
Opt. Lett., **27(11)** 951–953, 2002.

[111] F. Sorrentino, Bodart Q. Bertoldi, A., L. Cacciapuoti, M. de Angelis, Y.-H. Lien, M. Prevedelli, G. Rosi, and Tino G.M.
Simultaneous measurement of gravity acceleration and gravity gradient with an atom interferometer.
Appl. Phys. Lett., **101** 114106, 2012.

[112] A. Gauguet, T. E. Mehlstäubler, T. Lévèque, J. Le Gouët, W. Chaibi, B. Canuel, A. Clairon, F. Pereira Dos Santos, and A. Landragin.
Off-resonant Raman transition impact in an atom interferometer.
Phys. Rev. A, **78** 043615, 2008.

[113] T. Müller, T. Wendrich, M. Gilowski, C. Jentsch, E. M. Rasel, and W. Ertmer.
Versatile compact atomic source for high-resolution dual atom interferometry.
Phys. Rev. A, **76(6)** 63611, 2007.

[114] R. Grimm, M. Weidemüller, and Y. B. Ovchinnikov.
Optical Dipole Traps for Neutral Atoms.
pages 95 – 170. Academic Press, 2000.

[115] The pictures are taken from the following source and modified with the author's permission:
Wang, Xiaolong.
Gravimètres de haute résolution basés sur l'interférométrie atomique.
PhD Thesis, Université Pierre et Marie Curie, Paris 6, 2011.

[116] E. J. Zang, J. P. Cao, Y. Li, C. Y. Li, Y. K. Deng, and C. Q. Gao.
Realization of Four-Pass I2 Absorption Cell in 532-nm Optical Frequency Standard.
IEEE Trans. Instr. Meas., **56(2)** 673–676, 2007.

[117] A. Y. Nevsky, R. Holzwarth, J. Reichert, Th. Udem, T. W. Hänsch, J. von Zanthier, H. Walther, H. Schnatz, F. Riehle, P. V. Pokasov, M. N. Skvortsov, and S. N. Bagayev.
Frequency comparison and absolute frequency measurement of I2-stabilized lasers at 532 nm.
Opt. Comm., **192(3-6)** 263 – 272, 2001.

[118] T. R. Caver.
Optical Pumping.
Science, **141(3581)**, 1960.

[119] G. Santarelli, Ph. Laurent, P. Lemonde, A. Clairon, A. G. Mann, S. Chang, A. N. Luiten, and C. Salomon.
Quantum Projection Noise in an Atomic Fountain: A High Stability Cesium Frequency Standard.
Phys. Rev. Lett., **82** 4619–4622, 1999.

[120] A. Kaplan, M. Fredslund Andersen, and N. Davidson.
Suppression of inhomogeneous broadening in rf spectroscopy of optically trapped atoms.
Phys. Rev. A, **66** 045401, 2002.

[121] F. Schwabl, *Quantum Mechanics*.
Springer, 2007.

[122] J. M. McGuirk, D. M. Harber, J. M. Obrecht, and E. A. Cornell.
Alkali-metal adsorbate polarization on conducting and insulating surfaces probed with Bose-Einstein condensates.
Phys. Rev. A, **69** 062905, 2004.

[123] E. Peik, M. Ben Dahan, I. Bouchoule, Y. Castin, and C. Salomon.
Bloch oscillations and an accelerator for cold atoms.
Appl. Phys. B, **65(6)** 685–692, 1997.

[124] R. Battesti, P. Cladé, S. Guellati-Khélifa, C. Schwob, B. Grémaud, F. Nez, L. Julien, and F. Biraben.
Bloch Oscillations of Ultracold Atoms: A Tool for a Metrological Determination of h/m_{Rb}.

Phys. Rev. Lett., **92** 253001, 2004.

[125] M. Cadoret, E. de Mirandes, P. Cladé, S. Guellati-Khélifa, C. Schwob, F. Nez, L. Julien, and F. Biraben.
Combination of Bloch Oscillations with a Ramsey-Bordé Interferometer: New Determination of the Fine Structure Constant.
Phys. Rev. Lett., **101** 230801, 2008.

[126] P. Cladé, S. Guellati-Khélifa, F. Nez, and F. Biraben.
Large Momentum Beam Splitter Using Bloch Oscillations.
Phys. Rev. Lett., **102** 240402, 2009.

[127] P. Cladé, T. Plisson, S. Guellati-Khélifa, F. Nez, and F. Biraben.
Theoretical analysis of a large momentum beamsplitter using Bloch oscillations.
Eur. Phys. J. D, **59(3)** 349–360, 2010.

[128] H. Müller, S.-w. Chiow, Q. Long, S. Herrmann, and S. Chu.
Atom Interferometry with up to 24-Photon-Momentum-Transfer Beam Splitters.
Phys. Rev. Lett., **100** 180405, 2008.

[129] B. G. Lindsay, K. A. Smith, and F. B. Dunning.
Control of long-term output frequency drift in commercial dye lasers.
Rev. Sci. Instrum., **(6)** 1656–1657.

[130] J. Le Gouët, T.E. Mehlstäubler, J. Kim, S. Merlet, A. Clairon, A. Landragin, and F. Pereira Dos Santos.
Limits to the sensitivity of a low noise compact atomic gravimeter.
Appl. Phys. B, **92(2)** 133–144, 2008.

[131] T. Lévèque, A. Gauguet, F. Michaud, F. Pereira Dos Santos, and A. Landragin.
Enhancing the area of a raman atom interferometer using a versatile double-diffraction technique.
Phys. Rev. Lett., **103** 080405, 2009.

[132] N. Malossi, Q. Bodart, S. Merlet, T. Lévèque, A. Landragin, and F. Pereira Dos Santos.
Double diffraction in an atomic gravimeter.
Phys. Rev. A, **81** 013617, 2010.

[133] T. Lévèque.
Développement d'un gyromètre à atomes froids de haute sensibilité fondé sur une géométrie repliée.
PhD Thesis, Université Pierre et Marie Curie, Paris 6, 2010.

[134] D. Schrader, I. Dotsenko, M. Khudaverdyan, Y. Miroshnychenko, A. Rauschenbeutel, and D. Meschede.

Neutral Atom Quantum Register.
Phys. Rev. Lett., **93** 150501, 2004.

[135] F. Riehle, *Frequency Standards*.
WILEY-VCH Verlag GmbH&Co. KGaA, Weinheim, 2004.

[136] J. A. Barnes, A. R. Chi, L. S. Cutler, D. J. Healey, D. B. Leeson, T. E.
McGunigal, J. A. Mullen, W. L. Smith, R. L. Sydnor, R. F. C. Vessot,
and G. M. R. Winkler.
Characterization of Frequency Stability.
IEEE Trans. Instrum. Meas., **IM-20(2)** 105–120, 1971.

[137] J. Rutman.
Characterization of phase and frequency instabilities in precision frequency
sources: Fifteen years of progress.
Proceedings of the IEEE, **66(9)** 1048–1075, 1978.

[138] S. Gerstenkorn and P. Luc, *Atlas du spectre d'absorption de la molécule
d'iode.*
Laboratoire Aimé Cotton, CNRS II, Orsay, France, 1982.

LIST OF FIGURES

LIST OF TABLES

Acknowledgements

Within the last four years, I've had the chance to make the experience of doing research in two different teams, on two different experiments, and, most importantly, with many great people. This great chance was offered to me by Ernst Rasel and Franck Pereira. Vielen Dank and merci beaucoup !

Already in the time of my diploma thesis, I was enjoying scientific discussion with Ernst. Since that time we had many inspiring discussions and I've learned a lot in each of them. I'm grateful not only for learning physics from Ernst, but first of all an inspiring passion and enthusiasm.

I would like to say thank you to Franck for welcoming me in his team in Paris. I had the pleasure to learn from him for one year I spent in the Observatoire de Paris and also in the time after my stay. Thank you for so many explanations and nice discussions. And thanks a lot for all your help in the organisation of my co-tutelle procedure. At the Observatoire, it was also a pleasure working in the lab with Bruno Pelle, Quentin Beaufils, Xiaolong Wang and Adèle Hilico. I would like to thank them for a great time in Atelier 2. I'm very happy to have spent a time of my PhD in the inertial sensor team at SYRTE. For this, I would also like to thank Arnaud Landragin, Sébastien Merlet, Carlos Garrido Alzar, Jean Lautier, Matthieu Meunier, and Tristan Farah. Merci à tous ! Furthermore, I would like to thank Peter Rosenbusch for a huge help in finding a flat in Paris! And merci to Ouali Acef for giving advice in setting up the frequency stabilization. Many thanks to Marine Pailler, Anne Quezel and colleagues for helping me in all that administrative and paperwork! Thanks to Laurent Volodimer, Michel Lours and José Pinto-Fernandes for explaining electronics to me with so much patience. I appreciated and enjoyed very much my stay in the Observatoire de Paris.

My time at the Institut für Quantenoptik began as a "Hiwi". I was introduced to the institute and the group of Ernst Rasel by Stefan Jöllenbeck and Temmo Wübbena, thank you for this! And special thanks to Maic Zaiser who took the decision to let me work on his experiment. Most of the time I spent in the CASI team. I would like to thank Michael Gilowski, Christian Schubert, and Thijs Wendrich for teaching me, giving me great instructions and having a good time together. Also many thanks to Peter Berg and Sven Abend. It is a great pleasure to run the gyro with them and to discuss all the small and bigger problems you have to face in the lab. There are so many other people I had great discussions with

and who helped me out. For this, I would like to thank all members of the group of Ernst Rasel, but also the members of the group of Wolfgang Ertmer and Carsten Klempt, and of the groups of Silke and Christian Ospelkaus. I would also like to acknowledge the help in paperwork and support in administrative procedures from Mrs. Göldner, Mrs. Faber, Mrs. Pfennig, and Mrs. Hünitzsch. Off course, electronics also play a very important role in our experiment, and I'm grateful for the explanations and good help by Thijs Wendrich and Kai-Martin Knaak. I'm enjoying to be in this institute.

During the time of my PhD, I had great support from my wife, Elke. Thank you so much for coming with me to Paris, for always being there for me, and for always believing in me! I want to thank my parents who supported me during my Diploma studies and also helped me out during the time of my PhD. And also my brother and sister, and Elke's family were a great help.

When typing the dissertation, I had good discussions with many people. I also want to thank Christian Schubert, Jonas Hartwig, Peter Berg, Sven Abend, Felix Kösel, Waldemar Herr, Katerine Posso-Trujillo, Sebastian Bode, and Elke for reading parts of the manuscript.

Setting up a jointly supervised PhD procedure, a co-tutelle, demands a lot of help from many people. I would like to greatfully acknowledge Prof. Pomérol and Prof. Barke, the presidents of Université Pierre et Marie Curie and Leibniz Universität Hannover, as well as Prof. Hare, director of the école doctorale ED389 and Prof. Morgner, dean of the Fakultät für Mathematik und Physik, for supporting the co-tutelle program.

I would also like to thank Prof. Dr. Markus Arndt and Dr. Jean-Claude Garreau as well as Prof. Dr. Ernst Rasel for writing a report on my dissertation. Furthermore, I thank Dr. François Nez and Prof. Dr. Klemens Hammerer for accepting to be members of my thesis defense committee.

Finally, I would like to gratefully acknowledge financial support of the Max-Planck-Gesellschaft, the Observatoire de Paris, the European Intercan network and the Deutsch-Französische Hochschule, l'Université Franco-Allemande.

List of publications

1. M. Gilowski, Ch. Schubert, T. Wendrich, P. Berg, G. Tackmann, W. Ertmer, and E. M. Rasel.
   High resolution rotation sensor based on cold Rubidium atoms.
   Procceding, EFTF-IFCS 2009, 1173-1175 (2009).

2. G. Tackmann, M. Gilowski, Ch. Schubert, P. Berg, T. Wendrich, W. Ertmer, and E. M. Rasel.
   Phase-locking of two self-seeded tapered amplifier lasers.
   Opt. Expr., Vol. 18, Issue 9, pp. 9258-9265 (2010).

3. Q. Beaufils, G. Tackmann, X. Wang, B. Pelle, S. Pélisson, P. Wolf, and F. Pereira Dos Santos.
   Laser controlled tunneling in a vertical optical lattice.
   Phys. Rev. Lett., **106** 213002 (2011).

4. G. Tackmann, B. Pelle, A. Hilico, Q.Beaufils, and F. Pereira Dos Santos.
   Raman-laser spectroscopy of Wannier-Stark states.
   Phys. Rev. A, **84** 063422 (2011).

5. G. Tackmann, P. Berg, C. Schubert, S. Abend, M. Gilowski, W. Ertmer, and E. M. Rasel.
   Self-alignment of a compact large-area atomic Sagnac interferometer.
   New J. Phys., **14** 015002 (2012).

6. B. Pelle, A. Hilico, G. Tackmann, Q. Beaufils, and F. Pereira Dos Santos.
   State-labelling Wannier-Stark atomic interferometers.
   Phys. Rev. A, **87** 023601 (2013).

Curriculum Vitae

Personal data:

Name:	Gunnar Tackmann
Born:	May 12, 1982 in Warburg (Germany)
Nationality:	German

Doctoral studies:

09/2011 – today	3rd and 4th year of doctoral studies in the group of Prof. Dr. Ernst M. Rasel at the Insitut für Quantenoptik of Leibniz Universität Hannover
09/2010 – 08/2011	2nd year of doctoral studies in the group "Interférométrie Atomique et Capteurs Inertiels" at SYRTE in the Observatoire de Paris under the direction of Dr. habil. Franck Pereira Dos Santos
09/2009 – 08/2010	1st year of doctoral studies in the group of Prof. Dr. Ernst M. Rasel at the Insitut für Quantenoptik of Leibniz Universität Hannover
09/2009 – today	PhD student in a jointly supervised PhD program (cotutelle) between Leibniz Universität Hannover (LUH) and Université Pierre et Marie Curie (UPMC), Paris 6. Supervisors: Prof. Dr. Ernst M. Rasel (LHU) and Dr. habil. Franck Pereira Dos Santos (UPMC). Thesis research subject: "Precision Raman interferometry with free-falling and trapped laser-cooled atoms".

University education:

05/2008 – 06/2009	Diplomarbeit at the Institut für Quantenoptik of Leibniz Universität Hannover in the group of Prof. Dr. Ernst M. Rasel
06/2007 – 08/2007	Internship in the Institut Français du Pétrole
09/2006 – 05/2007	Master 1 at Université Claude Bernard, Lyon 1, in the framework of the student exchange program ERASMUS
10/2005 – 06/2009	Diplom Studiengang Physik mit der Studienrichtung Technische Physik at Leibniz Universität Hannover
10/2003 – 09/2005	Vordiplom Studiengang Physik at Leibniz Universität Hannover

Community service:

08/2002– 05/2003	Göttinger Werkstätten in Hann. Münden

School education:

08/1995 – 06/2002	Grotefend Gymnasium Münden, Abitur 06/2002
08/1993 – 07/1995	Orientierungsstufe 1 in Hann.Münden
08/1989 – 07/1993	Grundschule Königshof in Hann.Münden